

T146

49656

CENTRAL LIBRARY	
TEZPUR UNIVERSITY	
Accession No. <u>49656</u>	CENTRAL LIBRARY, T. U.
Date <u>14/9/11</u>	New ACC. NO. <u>T146</u>

REFERENCE BOOK
NOT TO BE ISSUED
TEZPUR UNIVERSITY LIBRARY

**Optical Properties of Semiconductor Quantum dots,
Interacting
Quantum dots and Nanomaterial filled SHI induced
Ion tracks**

**Nabanita Dutta
Registration Number (004) of 2010**

**A thesis submitted in partial fulfilment of the requirements
for the degree of Doctor of Philosophy**

July, 2010



**School of Science & Technology
Department of Physics
Tezpur University
Napaam, Tezpur-784028
Assam, India**

Dedicated to my parents,

Pulin Dutta & Monimala Dutta

My brother Sankar Jyoti

My nephew Barnava(Googulu)

Abstract

In recent years, nanotechnology has spread its applications over all aspects of life with its dramatic quantum size effects. The attraction towards the nanostructured systems rapidly increasing day by day because of its stunning range of size dependent properties as well as properties related its large surface/volume ratio. Accordingly, there has been an explosive growth of research in the arena of nanomaterials synthesis, characterization and application. The dimension of a material can be reduced in one, two or all the three directions to obtain thin films, wires or dots, respectively. The carrier motion is restricted to different extents in these low dimensional systems and are subjected to quantum mechanical rules. Since the properties of these materials vary with size variation, a large scope of assembling new and newer materials and device components has emerged over the years. The low dimensional semiconductors occupy a special place with reference to its possible range of applications. It is necessary to explore these novel low dimensional systems from point of view of basic understanding as well as technological applications.

The growing demand towards miniaturization of devices along with higher output efficiency has led to growing technological interest. The novel devices include single electron transistors, tunnel junctions, magnetic spin valves etc. Interestingly, these devices do not have their bulk counterparts. Semiconductor quantum dots are used not only in optoelectronics but also in chemical sensors, drug delivery, solar cell etc. In this regard, the role of semiconductor coupled quantum dots also needs to be emphasized; it provides us with unique ways of storing, and retrieving information. Various procedures were identified to develop semiconductor quantum dots.

PbS is a narrow band gap semiconductor in which band gap enhancement up to ten times can be achieved. Therefore, it gives an opportunity of tuning the band gap over a wide spectrum of energy range. An apparently strong quantum confinement is observed in case of PbS because of its large excitonic Bohr radius ($a_B \sim 18\text{nm}$). In this work we present fabrication and characterization of PbS quantum dots following different synthesis paths with due attention to various aspects; size control, stability,

monodispersity and particle-particle interaction in homogeneous and heterogeneous system.

In order to obtain size controlled quantum dots we considered polyvinyl alcohol (PVOH) is the host matrix. The role of surface physics and chemistry with regard to surface capping, surface coating and surface passivation is being reported in this work. The surface coating with polyvinyl pyrrolidone (PVP) was done to obtain quality quantum dots.

Another non toxic matrix called carboxylated styrene butadiene rubber (SBR) which exhibits geometric isomerism was also used as a stabilizing media in the fabrication process. The dispersing media facilitates interaction between the quantum dots and leads to the formation of coupled quantum dots. Isolated PbS quantum dots can also be obtained using carboxylated SBR latex under suitable conditions.

The synthesis of mesoporous TiO_2 thin films of anatase phase has attracted considerable interest because of their potential applications in photocatalysis, photovoltaics and gas sensing. The thin films of nanoporous anatase TiO_2 was also used as a supporting medium for PbS incorporation in a precise manner.

The use of swift heavy ion induced track technology in nanoparticle synthesis has also become a promising aspect. The ion irradiation experiment was carried out in GPSC chamber of IUAC, New Delhi. Here, gold foil scattering is exploited to control the ion fluence and hence the number of latent tracks in PVOH films PbS quantum dots have been grown in the etched tracks of PVOH. In addition, microemulsion technique has been adapted to produce size selective PbS quantum dots. Here, sodium dioctyl sulfosuccinate (AOT) and n-heptane were used for preparing the micro emulsion.

For characterizing size as well as morphology of synthesized quantum dots we used various analytical techniques such as Transmission electron microscopy (TEM), Scanning electron microscopy (SEM), Atomic force microscopy (AFM) and X-Ray diffraction(XRD) and Energy dispersive X-Ray analysis(EDS) was also performed to study composition analysis of the desired samples.

The use of conducting polymer PVP coating has helped to make narrow size distribution of PbS quantum dots whereas the effect of acetonitrile treatment allowed adequate surface passivation along with ordering of PbS quantum dot assemblies

Nitrogen adsorption studies were carried out to substantiate incorporation of PbS molecules in the mesopores of TiO₂. Though, pore geometry, pore-size, and pore distribution were studied previously but these studies in heterogeneous/coupled system like PbS/TiO₂ have been illustrated with a special emphasis to understand various competitive mechanisms.

The photoluminescence of synthesized PbS quantum dots have been investigated in detail. The PbS quantum dots are capable of emitting light of wavelengths in the visible to the near infra red (450nm to 900nm). Note that the bulk PbS emits in the infrared (IR) region of the electromagnetic spectrum and therefore a large shifting of the emission peak towards blue indicates a significant enhancement of the energy band gap. The ample prospects of making wide range of, optical sensors, light emitting devices using only one type of material but of selective sizes can be undertaken exploring this broad photoluminescence spectrum of PbS. The excitonic emission was obtained in case of PbS quantum dots embedded in SBR latex. In this case, a well separation between the band edge emission at 573nm and excitonic emission peak at 617nm was observed. Production and interaction of excitons is very much promising from the point of view of basic understanding as well as application purposes. Charge leaking mechanism in quantum dot system through the interface state (surface states) can be applied for various optoelectronic device applications such as single electron devices, quantum point contacts and photovoltaic operation etc. Photoluminescence of the heterogeneous system was investigated to establish these interface phenomena. In this work, optical probing of the interfacial charge transfer effects in PbS/TiO₂ coupled quantum dot systems will be discussed.

An electrical measurement of PbS/TiO₂ system was performed to explore the electrical properties of the system. *I-V* measurements were carried out with the help of Keithley conductivity meter. The conductivity nature was recognized as a Pool-Frenkel type. It is an evidence of interfacial charge transfer through the interfaces of PbS and TiO₂.

The reason behind the enhancement of band gap in nanocrystal is always a crucial question to be answered. One theoretical approach on this aspect was exercised in this work. Here the band gap enhancement in nano scale (quantum dot) material evaluated with the help of three fundamental approaches of Physics ; Kronig Penny Model, Free electron theory and finally Linear combination of atomic orbital(LCAO) method. The inverse dependence of size in case of PbS nanocrystal is studied meticulously with the

help of LCAO method. Depending on arrangement /ordering of atoms and hence, corresponding to the electronic structure evolution, the bulk PbS displays both direct and indirect band gap types. The explanation behind occurrence of two kinds of band of PbS is also examined.


Significant nonlinear optical properties (NLO) can be achieved when the nanocrystal radius R is much smaller than the bulk Bohr radius of the exciton (a_B). As an important application we have investigated the NLO features of surface passivated PbS nanocrystals with respect to two photon excitation fluorescence spectroscopy(TPEF) and second harmonic generation(SHG) imaging . The Ti-Sapphire laser source fixed at a wavelength of $\sim 706\text{nm}$ (power:400mW)was used to facilitate two photon absorption(TPA) process. For imaging based on TPEF and SHG studies, confocal spectral laser scanning microscope Leica TCS SP was used.

The TPEF and SHG signals were detected in backward as well forward directions respectively. The TPEF spectra shows two distinct emission features prominent band edge emission and a broad surface trap emission. The PbS nano particle assembly was successfully imaged which is consistent with the TEM micrographs. In addition surface passivated PbS nanoparticles are capable of producing adequate SHG signals (of wavelength of 352nm). These SHG coming out of the optical section were adequately imaged. In order to make a comparison between the intensity distribution profiles of TPEF and SHG a MATLAB programme was employed which shows that SHG response is nearly 34% stronger than its TPEF counterpart. TPEF and SHG results of PbS nano particles can be promising for imaging tissues, disease infected cells and other such biological specimens.

DECLARATION

I hereby declare that the thesis entitled 'Optical Properties of Semiconductor Quantum dots, Interacting Quantum dots and Nanomaterial filled SHI induced Ion tracks' being submitted to Tezpur University, Tezpur, Assam in partial fulfilment of the requirements for the award of the Degree of Doctor of Philosophy is a record of research work done by me during the Ph. D. course. This work has not been submitted in part or full for the award of any degree, diplomã, associateship, fellowship or any other similar title or recognition from any other institute or organization.

Date: 30/7/2010


(Nabanita Dutta)
Department of Physics
Tezpur University
Tezpur-784028(Assam)

CERTIFICATE

This is to certify that the thesis entitled 'Optical Properties of Semiconductor Quantum dots, Interacting Quantum dots and Nano material filled SHI induced Ion tracks' submitted to the Tezpur University in the Department of Physics, under the School of Science and Technology, in partial fulfilment for the award of the degree of Doctor of Philosophy (Ph. D.) in Physics is a record of research work carried out by Miss Nabanita Dutta under our supervision and guidance.

All helps received by her from various sources have been duly acknowledged.

No part of this thesis has been reproduced elsewhere for award of any other degree.



Dr. Dambarudhar Mohanta
(Assistant Professor)
School of Science & Technology
Department of Physics



Prof. Amarjyoti Choudhury
(Professor)
School of Science & Technology
Department of Physics

Date: 30/7/2010

Place: TEZPUR

Date: 30/7/2010

Place: TEZPUR

CONTENTS

<i>Abstract</i>	<i>i</i>
<i>Declaration</i>	<i>v</i>
<i>Certificate</i>	<i>vi</i>
<i>Contents</i>	<i>vii</i>
<i>List of Tables</i>	<i>xii</i>
<i>List of Figures</i>	<i>xiii</i>
<i>Acknowledgement</i>	<i>xvii</i>

CHAPTER 1	1-30
-----------	------

Introduction

1.1	Evolution of nanotechnology	1
1.2	Different kinds of nanomaterials	3
1.3	Properties of nanomaterials	4
1.3.1	High surface to volume ratio(S/V)	4
1.3.2	Quantum confinement effect and excitons	5
1.3.3	Enhancement of band gap and Blue shift	6
1.3.4	Large oscillator strength	8
1.4	Types of nanostructures and density of states	9
1.5	Coupled quantum dot	13
1.6	The approaches used in nanotechnology	14
1.7	Overview of the work on semiconductor quantum dot	17
1.8	Lead sulphide system	21
1.9	Motivation of the present work	23
1.10	Thesis plan	24
	References	26

Theoretical treatments on the Size Dependent Attributes of Nanocrystals based the Kronig-Penney, Free Electron and LCAO Models

2.1	Ideas of the Kronig–Penney model applied to nanocrystals	31
2.2	Free Electron model	37
2.3	Calculation of total number of electrons in PbS nanocrystals	42
2.4	LCAO method	44
	References	61

Synthesis Protocol: Materials and Methods

3.1	Properties of Polyvinyl Alcohol (PVOH) Matrix	62
3.2	Properties of carboxylated styrene butadiene (SBR) rubber latex	64
3.3	Properties of Polyvinyl pyrrolidone(PVP)	65
3.4	Physical properties of PbS	66
3.5.1	Synthesis of PbS quantum dots in PVOH matrix	66
3.5.2	Fabrication of PVP coated PbS quantum dots	68
3.5.3	Fabrication of PbS quantum dots in SBR matrix	69
3.5.4	Fabrication of PbS coupled quantum dots in SBR matrix	70
3.6	Fabrication of PbS/TiO ₂ coupled quantum dot system	72
3.7	Synthesis of nanomaterial filled swift heavy ion induced ion tracks	75
3.8	Preparation of PbS quantum dots with micro emulsion (Reverse micelle) technique	79
	References	82

Characterizations of synthesized quantum dots

4.1 Electron microscopy analysis	84
4.1.1 Scanning electron microscopy (SEM)	
4.1.1.1 SEM analysis of SHI induced etched ion tracks	84
4.1.1.2 SEM analysis of TiO ₂ and PbS/TiO ₂	86
4.1.2 Energy dispersive X-ray analysis (EDS)	87
4.1.2.1 EDS of TiO ₂ and PbS/ TiO ₂	88
4.1.2.2 EDS analysis of PbS prepared through micro emulsion route	89
4.1.3 Atomic force microscopy analysis (AFM)	89
4.1.3.1 Surface morphology analysis of TiO ₂ and PbS/ TiO ₂	90
4.1.3.2 Surface morphology analysis of PbS quantum dots and PbS coupled quantum dots in SBR latex	92
4.1.4 Transmission electron microscopy (TEM)	93
4.1.4.1 TEM analysis of PbS quantum dots in PVOH matrix	93
4.1.4.2 TEM analysis of PbS quantum dots in PVOH matrix with acetonitrile surface passivation	94
4.1.4.3: TEM analysis of PbS quantum dots with Mn ²⁺ incorporation in PVOH matrix	96
4.1.4.4 TEM analysis of PbS quantum dots coated with polyvinyl pyrrolidone (PVP)	97
4.1.4.5 TEM analysis of PbS quantum dots in SBR (styrene butadiene rubber) latex	98
4.1.4.6 TEM analysis of PbS coupled quantum dots in SBR (styrene butadiene rubber) latex	98
4.1.4.7 TEM study of PbS/TiO ₂ coupled quantum dot system	100
4.1.4.8 TEM study of PbS quantum dots prepared through micro emulsion route	102
4.1.4.9 TEM study of nano material filled swift heavy ion induced ion tracks	104

4.2 X-ray diffraction (XRD) analysis of synthesized quantum dots	105
4.2.1 XRD of PbS quantum dots in PVOH matrix	106
4.2.2 XRD analysis of PbS quantum dots with effective acetonitrile surface passivation	106
4.2.3 XRD analysis of PbS quantum dots with Mn incorporation	107
4.2.4 XRD analysis of PbS quantum dots coated with PVP	108
4.2.5 XRD analysis of PbS quantum dots by filling etched ion track	108
4.2.6 XRD analysis of PbS quantum prepared through micro emulsion route	109
4.2.7 XRD analysis of PbS quantum dots in SBR matrix	110
4.2.8 XRD analysis of PbS coupled quantum dots in SBR latex	111
4.2.9 XRD analysis of TiO ₂ and PbS/ TiO ₂	112
4.3 Photoluminescence (PL) study	116
4.3.1 PL analysis of PbS quantum dots in PVOH matrix	120
4.3.2 PL analysis of PbS quantum dots with effective acetonitrile surface passivation	123
4.3.3 Photoluminescence of PbS quantum dots with Mn ²⁺ incorporation	125
4.3.4 PL analysis of PVP coated PbS quantum dots	126
4.3.5 PL analysis of PbS quantum dots prepared through microemulsion route	128
4.3.6 PL analysis of PbS quantum dots in SBR latex	129
4.3.7 PL analysis of PbS coupled quantum dots in SBR latex	132
4.3.8 PL analysis of PbS filled SHI induced ion tracks	133
References	137

CHAPTER 5

139-160

Study of surface-interface phenomena of PbS/TiO₂ coupled quantum dot system

5.1 Nitrogen Adsorption Studies	140
5.2 Optical probing of interfacial charge transfer	150
5.3 Electrical properties of TiO ₂ /PbS	155
References	159

Investigation of nonlinear properties of PbS nanocrystalites through two photon excitation fluorescence (TPEF) and second harmonic generation (SHG) studies

6.1.1	Two photon absorption	163
6.1.2	Second harmonic generation (SHG)	166
6.1.3	Confocal microscopy	168
6.1.4	Set up based on laser scanning microscope	
	laser scanning microscope	168
6.2	Two photon excitation fluorescence spectra and imaging of PbS quantum dots	170
	References	181

Thesis Conclusion and Future directions

7.1	Thesis Conclusion	183
7.2	Future directions	185
7.3	Areas of applications of synthesized quantum dots	187
	References	188
	Appendix	189
	List of Publications	190

List of Tables

Table Caption

Table No.	Page No.
1.1 Energy levels of a semiconductor quantum dot	12
2.1 ΔE s of bulk as well as nano for Au, Ag and Cu	41
2.2 Total number of electrons in 10 a size PbS lattice at different temperatures($E_g=0.41\text{eV}$)	43
2.3 Total number of electrons in 10 a size PbS lattice at different temperatures($E_g=0.37\text{eV}$)	44
2.4 Calculated γ_j	49
2.5 Potential energies of conduction electrons at various lattice sites	52
2.6 $V'(\vec{r} - \vec{R}_j)$ values corresponding potentials due to lattice site no. 1, 2, 3.....etc.	54
3.1 Physical properties of PVOH	63
3.2 Physical properties of SBR latex	64
3.3 Physical properties of PVP	
3.4 Physical properties of PbS	65
3.5 Physicochemical properties of SBR latex used in this synthesis	69
3.5 Physical properties of TiO_2	73

List of Figures

Fig. No.	Page No.
1.1 (a-d) Illustrations representing system dimensionality (a) Bulk semiconductor, 3D (b) Thin films, and quantum well, 2D; (c) Linear chain structures 1D (d) Quantum dots, 0D	9
1.2 (a-d) Density of states of 3D bulk and reduced dimensional systems	10
1.3 Room temperature optical absorption spectra of CdSe nanocrystallites dispersed in hexane and ranging in size from $\sim 12 \text{ \AA}$ to $\sim 115 \text{ \AA}$	20
1.4 Rock salt crystal structure of PbS	22
1.5 Calculated band structure of PbS along the high symmetry directions. The zero of energy is the valence band maximum	22
2.1 Kronig-Penney model of a lattice periodic potential	31
2.2 Plot of $f(\alpha a)$ as a function of (αa)	35
2.3(A) Energy bands in extended reduced zone scheme (B) right half of the energy bands are shown only	36 37
2.4 Energy level diagram of gold bulk crystal of size 1m where $(E_F - E_{F-1} = 4.6 \times 10^{-28} \text{ J})$	39
2.5 Energy level diagram of gold nanocrystal of size 10nm where $(E_F - E_{F-1} = 8.03 \times 10^{-20} \text{ J})$	40
2.6 Size dependence in a Cu nanocrystal	50
2.7 A schematic diagram of a PbS 10a size linear lattice [$a = 0.593 \text{ nm}$]	51
2.8 Size dependence in PbS nanocrystal	55
3.1 Structural representation of PVOH	63
3.2 Structural representation of SBR	64
3.3 Structural representation of PVP	65
3.4 Scheme of acetonitrile treated PbS nanoparticle	67
3.5 Typical example of SBR chain sites for accommodating Pb^{++}	71
3.6 Upon sulfide gas uptake, formation of PbS quantum dots and mutual interaction	71
3.7 Schematic representation of track formation	76

3.8 Schematic representation of the micelle and two ends of surfactant molecule	80
4.1 SEM image of etched track	85
4.2(A) SEM of as- prepared TiO ₂	86
4.2(B, C) SEM image of anatase TiO ₂	86
4.2(D) SEM of PbS / anatase TiO ₂	87
4.3(A) EDS of TiO ₂	88
4.3(B) EDS of PbS/TiO ₂	88
4.4 EDS of PbS quantum dots in microemulsion medium of AOT and n-heptane	89
4.5 (A) AFM image of TiO ₂	91
4.5 (B) AFM image of PbS /TiO ₂	91
4.6 (A) AFM images of PbS quantum dots	92
4.6 (B) AFM images of PbS coupled quantum dots	92
4.7(A) <i>TEM image of PbS quantum dots in PVOH and Size distribution</i>	94
4.7(B) TEM image of PbS quantum dots in PVOH and size distribution(after aging)	94
4.8 TEM image of PbS nanoparticles dispersed in the polymer host with acetonitrile treatment	95
4.9 (A) TEM image of PbS nanoparticles with Mn ²⁺ incorporation dispersed in the polymer host	96
4.9 (B) TEM image of PbS nanoparticles with Mn ²⁺ incorporation dispersed in the polymer host after the aging of one year and size distribution	96
4.10 (A) TEM image of PbS quantum dots in PVOH matrix with effective PVP coating (B) TEM image of PbS dots in PVOH matrix with effective PVP coating after aging of one year	97
4.11 TEM micrograph of PbS quantum dots with size distribution in SBR	98
4.12 TEM image of coupled quantum dots grown in SBR	99
4.13 (A) TEM of as-received TiO ₂	101

4.13 (B) TEM of anatase TiO ₂	101
4.14 (A) TEM of as anatase TiO ₂ after aging	102
4.14 (B) TEM of as anatase PbS/TiO ₂ after aging	102
4.14(C) TEM of as PbS quantum dots in anatase TiO ₂	102
4.15(A) TEM image of PbS quantum dots in microemulsion	103
4.15(B) TEM image of PbS quantum dots in microemulsion after aging for one year	103
4.16 TEM image of PbS filled etched ion track	104
4.17 (A) XRD of PVOH matrix	106
4.17 (B) XRD of PbS quantum dots in PVOH matrix	106
4.18 XRD of PbS in PVOH matrix with effective acetonitrile surface passivation	107
4.19 XRD of PbS quantum dots with Mn ²⁺ incorporation in PVOH matrix	107
4.20 XRD of PbS quantum dots with PVP coating dispersed in PVOH matrix	108
4.21 XRD of PbS filled etched ion track	109
4.22 XRD of PbS quantum dots in a microemulsion of AOT and n-heptane dispersed in PVOH	110
4.23 XRD pattern of SBR latex XRD of PbS quantum dots in SBR latex	111
4.24 XRD of PbS coupled quantum dots in SBR latex	111
4.25(A) XRD of as-synthesized TiO ₂	112
4.25(B) XRD of PbS/ as synthesized TiO ₂	112
4.26 (A) XRD of anatase TiO ₂	113
4.26 (B) <i>Williamson-Hall plot of anatase TiO₂</i>	113
4.27(A) XRD of PbS/ anatase TiO ₂	113
4.27(B) <i>Williamson-Hall plot of anatase PbS /TiO₂</i>	113
4.27 (C) XRD of anatase TiO ₂ (2 nd type)	114
4.27 (D) XRD of anatase TiO ₂ with aging	115
4.28 (A) Combined XRD of anataseTiO ₂ and PbS/TiO ₂	115
4.28 (B) <i>Williamson-Hall plot of TiO₂</i>	115
4.28 (C) <i>Williamson-Hall plot of PbS/TiO₂</i>	115
4.29 Schematic diagram photoluminescence	119

4.30 (A) PL spectra of PbS quantum dots in PVOH matrix	121
4.30 (B) PL spectra of PbS quantum dots in PVOH matrix after aging	121
4.31 (A) PL of PbS quantum dots with effective surface passivation	124
4.31 (B) PL of PbS quantum dots with effective surface passivation after aging of one year	124
4.32 (A) PL spectra of PbS quantum dots with Mn ⁺⁺ incorporation	125
4.32 (B) PL spectra of PbS quantum dots marix with Mn ⁺⁺ incorporation after aging	125
4.33 (A) PL spectra of PVP coated PbS quantum dots	127
4.33 (B) PL spectra of PbS quantum dots after the effect of aging	127
4.34 (A) PL spectra of PbS quantum dots in microemulsion	129
4.34 (B) PL spectra of PbS quantum dots in microemulsion after aging	129
4.35 (A) PL spectra of PbS quantum dots in SBR latex	131
4.35 (B) PL spectra of PbS quantum dots in SBR latex after aging of one year	131
4 36 (A) PL spectra of PbS coupled quantum dots in SBR latex	133
4.36 (B) PL spectra of PbS coupled quantum dots in SBR latex after aging	133
4.37 (A) PL spectra of PbS filled SHI induced ion track	135
4.37 (B) PL spectra of PbS filled SHI induced ion track after aging	135
5.1 (A) Analogy of pore geometry of TiO ₂	144
5.1 (B) Analogy of pore geometry of PbS/TiO ₂	144
5.1(C). Surface area analogy of TiO ₂	146
5.1(D) Surface area analogy of PbS/TiO ₂	146
5.1(E) N ₂ adsorption isotherm of TiO ₂	148
5.1(F) N ₂ adsorption isotherm of PbS/TiO ₂	148
5.2 PL of TiO ₂ and PbS/TiO ₂	151
5.3 (A) Schematic representation of TiO ₂	152
5.3 (B) Schematic representation of PbS	152
5.4: Scheme of interfacial charge transfer	153
5.5 (A) Effect of PbS on PL of PbS/TiO ₂ (Type I)	154
5 5 (B) Effect of PbS on PL of PbS/TiO ₂ (Type II)	154

5.6: Schematic diagram of the source meter used for I-V measurements	156
5.7 (A) I-V plot for PbS/TiO ₂ for gap type connection	157
5.7 (B): Evaluation of nature of I-V plot	157
5.8 (A): I-V plot for PbS/TiO ₂ for sandwich type connection	158
5.8 (B): Evaluation of nature of I-V plot	158
6.1 Schematic representation of TPEF	164
6.2 Schematic representation of SHG	167
6.3 Schematic representation of confocal microscope	169
6.4 TPEF spectra of PbS quantum dots	170
6.5 Graphical representation of TPEF	172
6.6(a-n) Fluorescence images of a specific region (1×1 mm ²) obtained as a result of TPEF process corresponding to different wavelengths	172
6.7 SHG image of the region under investigation	177
6.8 Matlab image of TPEF & SHG	178

Acknowledgement

The main inspiration behind the task of the preparing the thesis is the sincere and sympathetic guidance, constant supervision, creative criticism and intense interest of my supervisors Prof. Amarjyoti Choudhury and Dr. Damdarudhar Mohanta. Therefore it is my duty to express my deep sense of gratitude and heartfull thanks to them.

My special thanks are due for Prof. H. L. Das for the stimulating discussions that I had with him on various theoretical and experimental issues.

I acknowledge DST for providing the financial support received through the project SR/S5/NM33/2005 without which it would have difficult for me to complete the work. I also sincerely thank DST again and Ministry of Education and Research, Government of Romania for sanctioning the project INT/ROMANIA/R-05/07 through which I received an opportunity to perform one major part of my experimental work in Center for Microscopy-Microanalysis and Information Processing, University "Politehnica" of Bucharest. I would like to appreciate Dr. Gazi Ahmed for his positive attitudes towards this work and valuable discussions. I also extend my sincere thanks to Prof. G. A. Stanciu, R. Hristu and S.G. Stanciu. I am also indebted to Dr. P. Deb and Prof. S. K. Dolui for various useful discussions.

I am grateful to IUSC, New Delhi for giving me the opportunity of performing ion irradiation experiment. In this regard I sincerely acknowledge Dr. A. M. P. Hussain. I am also grateful to S. V. Govindraju and Apotex Ltd (India) for providing me SBR latex. I am indebted to Dr. Dipak Dutta, Bibak Borah and NEIST(Jorhat) for giving me the opportunity to carry out one of my experiment.

I also express my sincere thanks to Tezpur University, IIT Guwahati, NEHU(Shillong) and technical persons involved directly or indirectly to this work. Finally, I express my gratitude for all whose blessings and support helped me to complete this work.

CHAPTER I

INTRODUCTION

1.1 Evolution of nanotechnology

Each constituent of this universe, starting from amoeba to stars is composed of matter: what is matter? It is nothing but composition of atoms / molecules organised in a particular fashion. Amoeba is unicellular and small because it consists of small number of molecules on the other hand stars are big because they consist of a vast number of molecules and molecular assemblies. These molecules are CH_4 , H_2O etc. Two or more molecules can come closer to combine to form bigger or smaller cluster called bulk material. This phenomenon mainly follows the fundamental laws of thermodynamics and mechanics and a creation procedure may be termed as chemistry. Materials show different physical as well as chemical properties for example; the properties of Sodium chloride and Iron oxide are different because such properties depend upon the composition i.e. its constituent atoms as well as their arrangements.

Molecules follow quantum mechanics but bulk materials follow classical laws [1]. Evolution of bulk materials from molecules must undergo by an intermediate phase of chemical reaction and it must obey the rules of chemical potential, internal energy and hence governed by thermodynamics [2]. Now materials are divided into different parts as crystalline and amorphous. But why does this variation come? This is because the properties of these materials depend not only on its composition but also its stoichiometry. The property of materials is mainly governed by electron transport and electron transition between allowed the energy states. Their energy states have got more effective role in the physical and chemical properties of the materials. Certain energy of interaction takes place according to the molecular orbital theory. But when molecules come up to bulk state they develop mutual interaction while arranging themselves to arrange themselves to reside together. Depending on atomic ordering and arrangements one obtains crystalline and amorphous compounds. Again single crystal materials are those where exactly identical environment of atoms i.e. arrangement is observed. Here orientation of atoms remains same throughout the distribution. More than one kind of arrangement of atoms is observed in polycrystalline materials. It is made of smaller crystallite with varying direction. The variation in direction can be

random or directed as per growth processing condition. All the materials grow following a process called nucleation state. Nucleation starts from chemical bonding itself. One kind of arrangement follows periodicity which is termed as crystalline type. The other which loses periodicity during their growth is called amorphous material and they have short-range ordering. Generally a particular set of atoms organise in a definite way. All the materials follow this evaluation process of growth. Through this evaluation process, molecules agglomerate resulting bulk state. The order of crystallinity varies from material to material. The stability of the material increases with the increase of crystallinity. In contrast, amorphous materials also show certain stability known as local stability. The crystalline material may undergo some defect states and these defect states include *point defect* (absence of atom from respective position) *stacking fault* (deviation from respective arrangements of atoms) *dislocation* etc. Moreover, materials are affected by grain boundaries. Grains are certain portion of polycrystalline material where uniform arrangement of atoms is observed. Orientations of atoms also remain same within same grain. Breaking down of materials at grain boundaries is known as *corrosion*. Mainly polymers are very corrosive. The strength of grain boundaries is given by *Hall Petch relation* [3]. Grain boundary migration plays an important role in dislocation which is another irregularity in crystal structure.

Further more; there exist another class of material known as low dimensional solids or so called nanomaterial which is intermediate state between molecular state and bulk state. This is the so called class of nanomaterial. Here growth is restricted after achieving a certain dimension in the range of the several orders of nanometers. Their growth is not complete. Now, here every atom tries to go to the surface to reduce its chemical potential and most of the atoms remain on the surface owing to extremely large surface to volume ratio. Because of its small dimension grain boundaries also play an important role. Here grain boundaries are dominating over grain size.

Depending on electronic transport capacity materials can be divided into conductor, semiconductors, and insulators. Considering Bloch functions in to account band theory evolves to explain these characteristic properties to a great extent. Here energy equation of particles is solved using Schrödinger equations. Again depending upon the magnetic response, the materials can be classified into magnetic material (*Para, Ferro, Antiferro*) and non magnetic material (*Dia*). Magnetism evolves from motion of circulating electrons in individual atoms. All magnetic materials consist of magnetic dipoles. A

certain area in a magnetic material with same orientation of magnetic dipoles is called as *magnetic domains*.

Technology always looks for materials having novel properties. Note that physical properties generally diverge with structure and composition. For example, optical and mechanical properties of piece of copper and a copper thin film are drastically different. The strategy of achieving high throughput, integrating and user-friendly application has evolved as '*Nanotechnology*' analysing varieties of choice properties.

The importance of nanotechnology is an outcome of ongoing demand for miniaturization of device with high performance, high efficiency, and taming of a substance according to a particular requirement [4, 5]. Gordon Moore (cofounder of the *Intel Corporation*) predicted that the number of transistors on a microprocessor would double periodically (approximately every 18 months). In this process for a certain size regime quantum mechanics begins to influence the physical properties, replacing conventional "bulk" physics. It was realized that lithographically defined structures below a certain size may be regarded as '*artificial atoms*'. This term is in practice as such structures exhibit properties similar to those of natural atoms [6]. The energy-level spectrum depends on the chemical composition and crystal structure of the nanocrystals and on their size and shape.

At the nanoscale, physics, chemistry, biology, materials science, and engineering converge toward the same goal [7, 8]. As a result, progress in nanotechnology will have very far-reaching impact. Nanotechnology's relevance is underlined by the importance of controlling matter at the nanoscale for healthcare, environment, energy sustainability, and almost every aspect of modern industry [9, 10].

1.2 Different kinds of nanomaterials:

The nanomaterials are mainly divided in to two classes. One is metallic nanoparticles [11] and other is semiconductor nanoparticles [12]. In case of semiconductor nano materials, the separation of the valance band and conduction band decides the property of the material at that state. This difference between the bands is called the band gap is larger than the bulk counterpart in nanomaterial.

There is no band gap in case of metals, so tunability of band gap with size is not possible but the band dispersions show the curvature of the bands at the edges is high compared to curvature at the centre of the band in this case[13].

As against the bulk state is characterized by semi continuous energy spectrum, one observes discrete energy levels in nanoscale of a material. This was established by solving the Schrödinger wave equations for these complicated structures. To give theoretical explanation '*Molecular dynamics*' is used in the beginning where molecules are allowed to interact for a period of time by suitable approximations of known physics, giving a view of the motion of the particles generating a static external potential V [14]. On the other hand, density functional theory (*DFT*) has become most popular and versatile method in this field where the properties of a many-electron system can be determined by using functional, i.e. functions of another function, which in this case is the spatially dependent electron density[15]. In case of magnetic nanomaterials the size of the nanoparticles become comparable to the size of the magnetic domains. Such structures exhibit '*superparamagnetism*' behaviour [16].

1.3 Properties of Nanomaterials: The novel properties of nanoscale material are as follows.

1.3.1 High surface to volume ratio(S/V)

One of the most important properties of nanomaterials is high surface to volume ratio. Here the number of atoms present in a certain volume becomes comparable to the number of atoms present on the surface [17]. Physical and chemical properties of a certain material strongly depend on the arrangement of the atoms on the surface. In case of nanomaterials, therefore reactivity is greatly enhanced as most of the atoms lie on the surface [18]. For example, melting point, boiling points are largely influenced by high s/v . Significant difference in these properties compared to the bulk system is seen in case of nanomaterials. Presence of maximum percentage of the total atoms on the surface results in some surface defects. These defect states analogous to some definite energy state referred as surface states responsible for overall changes in other energies corresponding new energy states. [19].

These surface states also act as an electron trap centres as they take part in different electronic transitions [20]. Their role can be observed in luminescence, photo catalytic activity and single electron tunnelling phenomena [21].

1.3.2 Quantum confinement effect and excitons

Quantum confinement is a typical *size effect* observed in semiconductor nanocrystals [22]. The optoelectronic properties change as solids transform from the bulk phase to nanoscale phase [23]. The nature of transition is determined by an intrinsic property of the system known as '*Bohr excitonic radius*' [24]. In a direct band gap semiconductor, with energy gap E_g centred at $K=0$ in the Brillion zone, and with non-degenerate parabolic valence and conduction bands, the bound electron-hole pairs are known as excitons (of energy $E_{n,K}$) created by absorption of photons of appropriate wavelength. When the size of the semiconductor becomes comparable to the exciton Bohr diameter, the electronic properties start changing from that of its corresponding bulk state [25]. The general expression for the set of energy levels of excitons can be given by the simple hydrogenic model:

$$E_{n,K} = E_g - \frac{\mu e^4}{2n^2 \hbar^2 \epsilon_2^2} + \frac{\hbar^2 K^2}{2(m_e^* + m_h^*)} \text{ (c.g.s)} \quad (1.1)$$

$$= E_g - \frac{\mu e^4}{32\pi^2 n^2 \hbar^2 \epsilon_2^2 \epsilon_0^2} + \frac{\hbar^2 K^2}{2(m_e^* + m_h^*)} \text{ (SI)} \quad (1.2)$$

Here, m_e^* and m_h^* being the effective masses of the electron and hole respectively, ϵ_0 is static and ϵ_2 is background dielectric constant of the semiconductor material, K is the wave vector of exciton such that $K=k_e+k_h$, μ is the reduced exciton mass and given by $\frac{1}{\mu} = \frac{1}{m_e^*} + \frac{1}{m_h^*}$, E_g is the bulk energy band gap, n being the principal quantum number [26^{a,b}].

The confinement could be divided into three regimes according to the relationship between microcrystallite radius (R), and the Bohr exciton radius (a_B) of bulk semiconductor where, $a_B = a_e + a_h$. If $R \gg a_B$ then this regime is called weak confinement. The shift ΔE , in energy of the ground state exciton can be approximated by:

$$\Delta E \approx \frac{\hbar^2 \pi^2}{2MR^2}, \quad (1.3)$$

where, M is the net mass of the exciton is given by $M = m_e^* + m_h^*$.

If $R \ll a_h$ and $R \ll a_e$ and this regime is called strong confinement. The shift ΔE in energy of the ground state carriers can be expressed by,

$$\Delta E \approx \frac{\hbar^2 \pi^2}{2\mu R^2} \quad (1.4)$$

In which the exciton mass M is replaced by reduced exciton mass μ .

There is another type of typical confinement regime observed in very small micro crystallites. Here $R \ll a_e$ but $R \gg a_h$. This regime is known as medium confinement regime [26].

1.3.3 Enhancement of band gap and Blueshift:

A microscopic system is defined by its energy sketch and subjected to quantum mechanical law. The quantum size effect can be explained qualitatively by considering a particle-in-a box like situation where the energy spacing between the levels increases as the dimensions of the box are reduced. Consequently, enhancement of band gap with decrease in particle size is observed. This relationship can be rather termed as inverse size dependence. There exist some theoretical models to figure out energy levels of the nanocrystals. An effort is made [chapter2] to understanding on the inverse size dependence of the energy band gaps in nanocrystals. As band gap can be tuned over broad range of energy in case of nanomaterials depending on its size, it is the most fundamental property of the semiconductor nanocrystals.

Therefore by tuning the bandgap property of semiconductor nanocrystals can be dramatically altered.

The effect of enhancement of band gap as observed in *blueshift* in the absorption spectra [27]. The absorption band shifts towards blue region in case of nanomaterials. (Effective Mass Approximation) EMA a theoretical understanding of band gaps as well as blue shift in semiconductor nanomaterials. The model which gives theoretical understanding of the band-gaps as well as blue shift will be described in subsequent sections.

Effective-mass approximation (EMA): The pioneers of this model are Efros and Efros.

They considered parabolic bands for calculating the Hamiltonian of such nanocrystal which was further extended by Kayanuma for various kinds of semiconducting system [28]. Later Borrelli (1987) used envelope functions for electrons and holes in EMA and had set down for the more general case as different types of confinements.

An electrically neutral excited state of an insulator or semiconductor is regarded as a bound state of an electron and a hole which is also known as excitons. Evidence of quantum size effects of excitons confined in all three dimensions was found by Ekimov and Onushchenko in 1981[29]. Efros and Efros gave a theoretical explanation of this phenomenon.

They applied the effective mass approximation (EMA) and assumed parabolic energy bands. The main energy terms are the electron-hole interaction energy, Coulomb term, and secondly, the confinement energy of the electron and hole, and kinetic energy term. It is solved by taking various choices for electron and hole wave functions and solving the effective mass equation variationally.

The energy expression in EMA proposed by Brus[30] is

$$E(R) = E_g + \frac{\hbar^2}{2} \left(\frac{1}{m_e^*} + \frac{1}{m_h^*} \right) \frac{\pi^2}{R^2} - 1.786 \frac{e^2}{\epsilon R} - 0.248 E_{Ry}^* \quad (1.5)$$

where E_g is the bulk band gap. The second term is the kinetic energy term containing the effective masses m_e^* and m_h^* of the electron and hole, respectively. The third term arises due to the spatial correlation between the electron and hole which is generally small compared to first two terms.

Hyperbolic band model: The effective mass approximation is not valid for all types of small clusters such as PbS where strong confinement regime is observed. Instead of parabolic band a hyperbolic band is considered here. The hyperbolic band model provides [31]

$$E_g^2(r) = \frac{E_g^2 + 2\hbar^2 E_g \left(\frac{\pi}{r} \right)^2}{m_e^*} \quad , \quad (1.6)$$

where E_g is the band gap of bulk semiconductor, r is the particle radius m_e^* is the effective electron mass.

The tight binding model is also used in calculation of band gap of nanocrystal where the wavefunctions of crystallites are constructed as linear combinations of orbital on each site of the crystallites [32]. For an fcc lattice, without spin lattice interaction included VBM (Valence Band Model) the tight binding Hamiltonian is given by

$$\langle R_\alpha | H | R' \alpha' \rangle = E_p \delta_{R,R'} \delta_{\alpha\alpha'} + \sum_{\tau} \delta_{R-R',\tau} \{ E_{xy} \tau_x \tau_y (1 - \delta_{\alpha\alpha'}) + [E_{xx} \tau_x^2 + E_{zz} (1 - \tau_x^2)] \delta_{\alpha\alpha'} \}, \quad (1.7)$$

where $\alpha=x,y,z$, $|R\alpha\rangle$ denotes an orbital located at the site R and τ stands for the nearest neighbour displacement vector with $\tau = (a/2(\tau_x \tau_y \tau_z))$ a being the lattice constant.

Theories have been developed like four-band envelope function approximation used for calculation of band gap of semiconductor quantum dots [33]. Kane et. al. used this formulation for calculating energy wavefunction of PbS and PbSe quantum dots. The calculation is based on a realistic model of the nonparabolic and the anisotropic band structures of these materials.

1.3.4 Large oscillator strength

Oscillator strength is related to the strength of transitions between the energy levels rather it can be said frequency of transition [34]. The general expression for oscillator strength is given by

$$f \approx \frac{2m}{\hbar^2} \Delta E |\mu|^2 |U(0)|^2 \quad (1.8)$$

where m is the electron mass, ΔE is the transition energy, μ is the transition dipole

moment, and $|U(0)|^2$ represents the probability of finding the electron and hole on the same site (the overlap factor) by confining the electron and hole in a small cluster. Oscillator strength increases due to the enhanced spatial overlapping between the electron and hole wave functions as well as due to the coherent motion of the exciton. The oscillator strength per unit volume determines the absorption coefficient.

1.4: Types of nanostructures and density of states

Nanomaterials can be divided into following classes according to the size confinement effects.

Quantum well: If movement of the electrons are restricted in one dimension then this type of structure is called quantum well [35]. In such system at least one of its three dimensions ranges in order of the size of Bohr excitonic radius.

Nanorod: If movement of the electrons are restricted in two dimensions then this type of structure is called nanorod [36]. In such system two of its three dimensions range in order of the size of Bohr excitonic radius.

Quantum dot: If movement of electrons are restricted in all three dimensions then this type of structure is called quantum dot. In such system all three of its three dimensions range in order of the size of Bohr excitonic radius. Single quantum dots are regarded as artificial atoms [37^a].

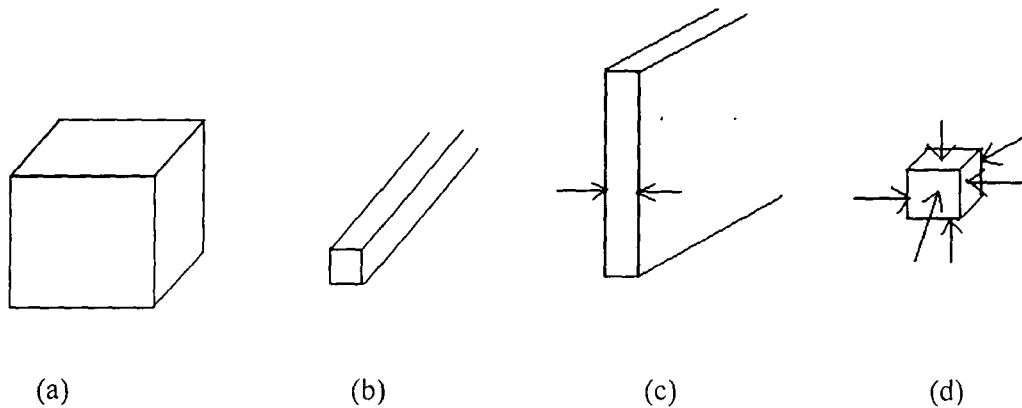


Fig1.1 (a-d): Illustrations representing system dimensionality (a) Bulk semiconductor, 3D; (b) Thin films, quantum well, 2D; (c) Linear chain structures 1D (d) Quantum dots, 0D

The variation of density of states (DOS) from a 3D bulk to quasi zero dimensional semiconductor quantum dot can be found in the literature [37^b].

DOS for a bulk semiconductor,

$$\frac{dN}{dE} \propto \frac{dE^{3/2}}{dE} = E^{1/2}$$

DOS for a two-dimensional system (quantum well) is a step function,

$$\frac{dN}{dE} \propto \frac{d}{dE} \sum_{\epsilon_i < E} (E - \epsilon_i) = \sum_{\epsilon_i < E} 1$$

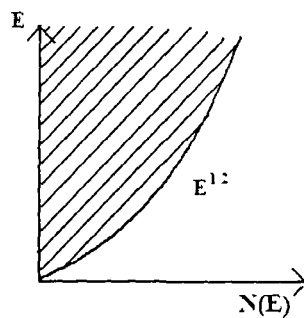
DOS for a one dimensional system (quantum wire)

$$\frac{dN}{dE} \propto \frac{d}{dE} \sum_{\epsilon_i < E} (E - \epsilon_i)^{1/2} = \sum_{\epsilon_i < E} (E - \epsilon_i)^{-1/2}$$

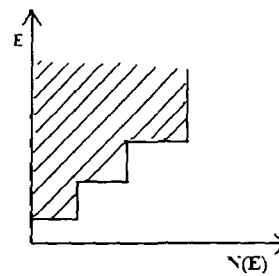
DOS for a zero-dimensional system (quantum dot) has the shape of δ - peaks

$$\frac{dN}{dE} \propto \frac{d}{dE} \sum_{\epsilon_i < E} \Theta(E - \epsilon_i) = \sum_{\epsilon_i} \delta(E - \epsilon_i)$$

Where ϵ_i are discrete energy levels, Θ is the Heaviside step function, and δ is the Dirac function [38]. The variation of density of states (from continuous to discrete) with reducing dimensionality is shown in Fig.2



(a) 3D bulk



(b) 2D Quantum Well

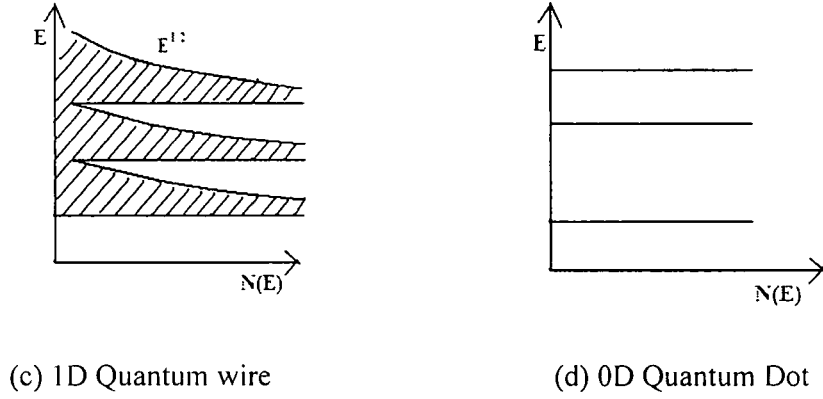


Fig1.2(a-d): Density of states of 3D bulk and reduced dimensional systems

Y.V.G.S. Murti et al[39] made an effort to calculate the energy levels of a spherical quantum dot adopting this formulation.

The exciton hamiltonian is the sum of the kinetic energies of the electron and hole, the Coulomb interaction energy (V_c) of the electron hole pair, the potentials $V_e(r_e)$ and $V_h(r_h)$ experienced by the electron and hole respectively due to the barrier. Thus

$$H = -\frac{\hbar^2}{8\pi^2 m^2} \nabla_e^2 - \frac{\hbar^2}{8\pi^2 m_h} \nabla_h^2 + V_c + V_e(r_e) + V_h(r_h), \quad (1.9)$$

where,

$$V_i(r_i) = 0, \quad \text{for } r_i < R, \quad (i=e, h)$$

$$V_i(r_i) = 0, \quad \text{for } r_i > R, \quad (i=e, h)$$

The exciton wave function is then represented as product of the individual particle wave functions $\varphi_h(r)$ for the hole and $\varphi_e(r)$ for the electron.

$$\Psi(r_e, r_h) = \varphi_e(r_e) \cdot \varphi_h(r_h)$$

These individual wavefunctions of the electron and hole ($i=e$ for electrons and $i=h$) for holes are given by

$$\phi_{nml}(r) = \left(\frac{2}{R^3}\right)^{1/2} \frac{J_l(\alpha_{nl}([r/R])}{J_{l+1}(\alpha_{nl})} Y_{lm}$$

The quantum numbers m , l and n are restricted $l \leq m \leq l; n = 1, 2, 3, \dots$. Here the Bessel functions of the order l and Y_{lm} are spherical harmonics $J_l(x)$, are related to the Bessel functions of the first kind

$$J_l(x) = \left(\frac{\pi}{2x}\right)^{1/2} J_{l+1/2}(x)$$

l	State	α_{nl}	E_h	E_e
0	1s	3.1416	$-\frac{(3.1416)^2 h^2}{m_h 8\pi^2 R^2}$	$-\frac{(3.1416)^2 h^2}{m_e 8\pi^2 R^2} + E_g$
1	1p	4.4934	$-\frac{(4.4934)^2 h^2}{m_h 8\pi^2 R^2}$	$-\frac{(4.4934)^2 h^2}{m_e 8\pi^2 R^2} + E_g$
2	1d	5.7635	$-\frac{(5.7635)^2 h^2}{m_h 8\pi^2 R^2}$	$-\frac{(5.7635)^2 h^2}{m_e 8\pi^2 R^2} + E_g$
0	2s	6.2832	$-\frac{(6.2832)^2 h^2}{m_h 8\pi^2 R^2}$	$-\frac{(6.2832)^2 h^2}{m_e 8\pi^2 R^2} + E_g$
1	2p	7.7253	$-\frac{(7.7253)^2 h^2}{m_h 8\pi^2 R^2}$	$-\frac{(7.7253)^2 h^2}{m_e 8\pi^2 R^2} + E_g$
2	2d	9.0950	$-\frac{(9.0950)^2 h^2}{m_h 8\pi^2 R^2}$	$-\frac{(9.0950)^2 h^2}{m_e 8\pi^2 R^2} + E_g$

Table 1 Energy levels of a semiconductor quantum dot

This intrinsic electronic structure of semiconductor quantum dots affects photo absorption and photoluminescence in these materials. Further, the nature of doping could also affect the photoabsorption and photoluminescence responses.

1.5 Coupled quantum dots

If two quantum dots are separated by a distance of a few angstroms only then an electrical or chemical interaction can take place between them. This type of a pair of interacting quantum dots is called coupled quantum dots. The coupled quantum dots can be considered as an artificial molecular system. The coupled quantum dot can behave as a weak-tunnel-coupling or covalent like coupling depending on the strength of the inter dot coupling. The bonding state of a strongly coupled artificial molecule has a lower energy than the energies of the original states of the individual dots. This amount of energy forms the binding force between the two dots [40].

In this context, researchers have worked on various aspects of coupled quantum dot systems, for instance, the GaAs/AlGaAs system. The effective Hamiltonian of GaAs/AlGaAs system fabricated by embedding GaAs quantum dots in AlGaAs matrix can be represented by:

$$H = -\frac{\hbar^2}{2m_e^*} \nabla_e^2 - \frac{\hbar^2}{2m_h^*} \nabla_h^2 - \frac{e^2}{k|\vec{r}_e - \vec{r}_h|} + V_e(\vec{r}_e) + V_h(\vec{r}_h) \quad (1.10)$$

where, m_e^* and m_h^* are the respective effective masses of electrons and holes, k is the dielectric constant and \vec{r}_e and \vec{r}_h are the position vectors of the electron and the hole. $V_e(\vec{r}_e)$ and $V_h(\vec{r}_h)$ are the confining potentials for the electron and hole. The variational method is used to obtain the exciton ground state energy using the following trial wavefunction,

$$\psi(\rho_e, \rho_h, \rho_{eh}, z_e, z_h) = \psi_e(\rho_e) \psi_h(\rho_h) \phi_e(z_e) \phi_h(z_h) e^{-\alpha \rho_e} e^{\beta(z_e - z_h)^2}$$

where, $\psi_i(\rho_i)$ and $\phi_i(\rho_i)$ describe the motions of the noninteracting electron and hole ($i=e,h$) in the directions perpendicular and along the z -axis respectively and $e^{-\alpha \rho_i}$ and $e^{-\beta(z_e - z_h)^2}$ describe the spatial extensions of excitons in the respective directions.

The exciton ground-state wavefunction and energy in the coupled quantum dots are then determine by minimizing the total energy

$$E_{ex}(\alpha, \beta) = \frac{\langle \psi | H | \psi \rangle}{\langle \psi | \psi \rangle}$$

CENTRAL LIBRARY, T. U.
ACC. NO. 49656

CENTRAL LIBRARY, T. U.
ACC. NO. 1146

The binding energy of the exciton was calculated by adjusting the parameters α and β and is found to be

$$E_b = E_e + E_h - E_{ex}, \quad (1.11)$$

where E_{ex} is the exciton energy and E_e , E_h are electron and hole subband energies. The shift of fundamental optical transition energy due to quantum confinement is given by the following equation,

$$\Delta E = E_g + E_e + E_h - E_b - \Delta E_0$$

Here, E_g is the energy gap of bulk GaAs and ΔE_0 is the fundamental optical transition energy in bulk GaAs [41].

1.6 The approaches used in nanotechnology

Bottom up process: In bottom up approach nanostructures are produced and nano devices are built from assembling molecular components. Here, construction is assured by controlling at atomic scale [42].

Top down process: In top down process, nanostructures are manufactured from larger entities. Here atomic level control is not taken into account rather trimming of bulky system into tiny particles is considered [43].

Fascinating nanostructured materials are becoming major contributors of current technology. Their production and use is rapidly growing in to a powerful industry [44]. The microstructure and properties of nanostructured materials depend largely on the synthesis protocols as well as on the processing parameters [45]. Therefore, it is of utmost importance to select the most appropriate technique for preparation of nanomaterials with desired properties.

Physico-chemical method: In these methods, nanoparticles are synthesized exploiting some chemical reactions. This method includes colloidal dispersion [46], solgel method [47], microemulsion, and electrochemical deposition [48], encapsulation with different matrix [49]. In solgel method, gels are synthesized by hydrolysis of a complex solution. These gels are given various heat treatments to achieve required form. Micro emulsion

is stable thermo dynamical process where two liquid phases are mixed together with the help of surfactant and co-surfactant and nanoparticles are produced in micelles [50]. For the purpose of encapsulation different matrices have been selected to produce nanoparticles having different properties. Generally, the matrix includes various inorganic types such as glass, zeolite etc. and organic matrix mainly comprise of polymers.

Advantages: The main advantages of this route is

- * Simplicity of production
- * Cost effective
- * Possibility of large scale production

Limitations: The limitations of the chemical route are

- * Comparatively less purity
- * Difficulty in mono dispersity
- * Inhomogeneous particle growth

Choice of host matrix

Fabrication of nanoparticles has been tried in different matrices to investigate if it leads to changing physical, optical, electrical and magnetic properties. For this purpose different matrices have been selected to encapsulate the nanoparticles. Generally, the matrix includes various inorganic matrix such as glass matrix, zeolite etc. and of polymers as organic hosts. The porous matrices are more useful for embedding quantum dots. The entire matrix is known to have different properties for example, the pore size is more or less uniform in zeolite [51]. Mostly used polymer matrix to be listed out are PVOH, Nafion etc.

Physical methods of synthesis

Different physical methods includes Molecular beam epitaxy (MBE)(52), Metal organic chemical vapour deposition (MOCVD), sputtering, laser ablation method(53), ball milling(54), mechanical grinding(55) etc. MBE has produced a wide range of very high-purity semiconductor nanostructures with excellent optical and electrical properties. MOCVD is a versatile technique and has been used to deposit materials that are difficult to grow using MBE, such as phosphides and nitrides. Different frequency and different substrates are used for development of different nanoparticles in sputtering techniques (56). High energy ball milling of metal or semiconductor leads to particles with diameters down to 5nm.

Advantages:

- * High purity
- * Effective mono dispersity
- * Uniform size distribution

Limitations:

- * Highly Expensive
- * Limited scope of large scale production
- * Difficulties in forming composites

Biological synthesis:

Biological route has become popular now a days. By adopting biological approach, one needs to use biological species such as microorganisms. Different plant (such as Alfalfa) [57], algas(such as diatoms)[58] are used to produce various nanostructured materials for example (metallic nanoparticles, silica composites etc). On the other hand, some bacteria are also being used to develop nanoparticles from a bulk system [59].

Swift heavy ion induced technology: SHI technology is also used to produce nano structured material. Templates of track etched membranes facilitate the growth of other nanoparticles. In this process, with interest to develop ion tracks in various films such as alumina or silicon etc. polymer films like pristine polycarbonate and polyvinylidene fluoride polymer films of thickness 10-40 μ m are irradiated using swift heavy ion beam of Ni, Cl and Ag etc.

After formation of latent tracks in these films [60], the amorphized tracks are etched out to obtain voids with diameter in the range of nano to micrometer scale. Next, these nanopores are filled with metals, semiconductor nanoparticles or by conducting polymers. Different techniques are applied to fill up these pores namely dip-coating, electrodeposition etc. Finally, these filled membranes become useful to fabricate various kinds of nanodevices (e.g. nanofilters, photocells and other passive elements).

1.7 Overview of the work on semiconductor quantum dots:

Semiconductor quantum dots are first demonstrated simultaneously by L. E. Brus of USA and A. I. Ekimov of former Soviet Union while trying to explore the advantages given by high surface to volume ratio in semiconductor nanocrystal [61]. Their observation got hold of the concept quantum confinement achieved by decreasing the size of in semiconductor quantum dot. The most important aspect of semiconductor quantum dot is reorganization of energy levels and accordingly density of states.

The dependence of optical properties in semiconductor quantum dots was first realized in semiconductor doped glasses by Ekimov et al and at the same time in colloidal solutions by Henglein [62]. Many of the exciting experiments are being performed in the field of optics which includes luminescence, non linear optics and solar energy conversion. Alongwith this advances in the processing routes, applications in the area of electronics, optoelectronics, catalysis, and biotechnology have caught the attention of researchers/technologists.

The work on quantum dots began with its synthesis. The two main strategies exploited to make semiconductor nanocrystallites are: controlled, arrested precipitation in solution and the precipitation in specially restricted reaction voids of porous host materials [63]. The size quantized properties of semiconductor nanoclusters was first observed in colloidal dispersion where nanoparticles remain suspended in the solution. In 1984 Rossetti et al. developed controlled formation of CdS nano particles in aqueous solution.

Major problems with colloidal solutions are the irreproducibility in preparation, their stability, and the difficulty in establishing the definitive identity of the semiconductors [64]. They observed the electronic properties of these small nano particles in their excited state. Moreover they tried to model the correlation between photochemical redox potential with size.

The use of matrix has resolved this problem to some extent. Ligand environment not only prevents aggregation but also assist luminescence by reducing surface defects. Wang et al in 1987 prepared PbS nanocrystallites using ethylene-15% methacrylic acid copolymer [E-MAA]. They have developed two theoretical models observing blue shift with reduced size of nanocrystallites. The theoretical prediction of spatial distribution of nanoparticles in a polymer matrix depends on the surrounding environment along with ligand periphery.

Since nanocrystallites contain mostly dangling or unsaturated bonds on the surfaces therefore researchers also have developed methods where controlled passivation of surfaces could be done. These surface passivating agents are amines, hydroxide ions, ammonia etc. various capping agents had been tried to prevent agglomeration of nanocrystallites [65].

Further, path of chemical synthesis followed by sol-gel, micellar micro emulsion etc and physical synthesis followed by MBE, sputtering etc. In 1992, A.V. Prasadarao et al prepared lanthanum and neodymium titanate by a sol-gel route [66]. Moullick et al synthesised PbS nanocrystal using micellar medium. The effect of size variation with temperature on ZnO quantum dots was observed by J-Y Zhuang et al. [67], Mahamuni et al obtained ZnO quantum dots using polyvinyl pyrrolidane as a capping agent. Nayoki Veda et al obtained CdO nanostructures by *rf* sputtering method. Passler et al prepared thin films of ZnS, ZnSe, and ZnTe nanoparticles on GaAs substrate using MBE technique. Bera et al. prepared Silicon nanocrystals using the method of dc magnetron sputtering [68]. Lieber et al. synthesized Silicon and Germanium nanocrystal with the help of Laser ablation method. Synthesis process has continued further in this way.

Different theories were proposed to explain the scheme that supports formation of quantum dots. These theories are mean field theory which deals with transformation of atoms during island growth [69]. Kelvin's theory explains how nano particles of a particular size take place at the expense of evaporation of other nanoparticles [70]. Since the effect of size on the surface energy is important when the size is comparable with that of few atom therefore many approaches have been put forward to evaluate

surface energy of nanoparticles. Larger values of surface energy as compared to the bulk materials have been reported for nanoparticles from the size-dependent lattice parameter (SDLP) [71]

From the application point of view, large scale production along with preservation is highly desirable. Worthwhile progress has been achieved in the areas of synthesis, structural characterization, electrical and optical properties of quantum dots [72]. These fundamental properties of nanoscale semiconductor structures are strongly influenced by their size and dimensionality [73]. Such dependence offers the possibility to manipulate their properties by size and shape control. Controlled variation of nanocrystallites size results in remarkable changes in properties from molecular to bulk [74]. Basically optical properties were studied in detail at the beginning. The main tools for optical study were optical absorption spectroscopy and photoluminescence spectroscopy. Optical absorption study is used so identify the basic excitonic response of the synthesized quantum dots. Murray et. al have obtained the evolution of the optical absorption spectrum with size for a series of CdSe crystallites ranging from $\sim 12 \text{ \AA}$ to $\sim 115 \text{ \AA}$ at room temperature. The series of sizes ranges from nearly molecular species containing fewer than 100 atoms to fragments of the bulk lattice containing more than 30000 atoms. [Fig.1.3]. It clearly shows the effect of quantum confinement.

Photoluminescence studies also exhibits interesting features of quantum dots. Mahamuni et. al. studied in detail the photoluminescence spectra of ZnO quantum dots and emphasised about the origin of different emission parameters. These origins are electron-phonon coupling, lattice distortions, localization of charge carriers due to interface effects, and point defects. Tomasolu et. al. have reported about the pH sensitive photoluminescence of CdSe-ZnS core shell quantum dots. They described how intensity of luminescence changes with pH [75]. The luminescence of quantum dots was tried to increase using doping and the concept of DMS came. Bangal et. al reported the effect of Mn doping on hyperfine interactions in case of CdS nanoparticles [76]. Conducting polymer MEH-PPV also used to enhance the luminescence efficiency of quantum dots [77].

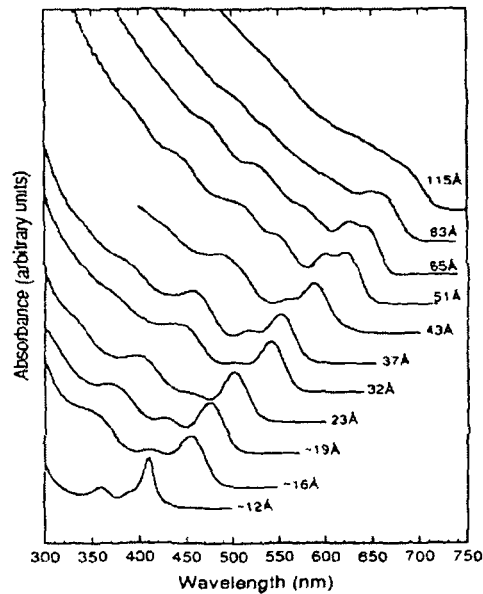


Fig1.3. Room temperature optical absorption spectra of CdSe nanocrystallites dispersed in hexane and ranging in size from $\sim 12 \text{ \AA}$ to $\sim 1.15 \text{ \AA}$ [78]

Nonlinear phenomena were also studied in semiconductor quantum dots. Large nonlinear optical response is expected in these systems which is a consequence of huge enhancement of transition probabilities resulting from the quantum confinement. Vibrational features are also prominent in nanoparticle systems therefore different methods like Raman spectroscopy [79], IR spectroscopy are being used [80]. Stokes shift in luminescence was used to study various effects of quantum dots [81]. In this regard, it is quite rational to emphasize that photoluminescence upconversion or anti-Stokes photoluminescence can be observed in some semiconductor quantum dots where emission energy is higher than the excitation energy [82].

The information regarding charge carrier dynamics in semiconductor quantum dots is most important for optoelectronic applications. Optical techniques could not provide this information adequately therefore, charge carrier dynamics is characterized through electrical measurements. This has been studied in detail in both embedded system [83] as well in nanostructured thin films [84].

Special kind of compound nanoscale systems like BaTiO_3 has also emerged as strong technologically important material. BaTiO_3 nanoparticles were used to induce desired Ferroelectricity [85]. Hybrid quantum dots were also grown. Here, a fluorescent nanoparticle attached with a magnetic nanoparticle can be used for bio-medical

applications [86]. Porous semiconductors, such as porous alumina, ZnO, TiO₂, SiO₂ also became popular. Sensitization of a narrow band gap semiconductor in the pores of wide band gap semiconductor also worked out. These have a number of potential application like solar cell, catalytic activity, sensing elements etc.

Coupled quantum dots also have gained importance due to their unique properties. Various phenomena such as Coulomb blockade, single-electron transport, and individual electronic states shown by coupled quantum dots are mainly prepared through physical methods [87].

Coupled quantum dots or quantum dot pairing are suitable nanostructured schemes to understand the kinetics of interfacial charge transfer, single electron characteristics and efficient biomolecular labelling. Basically, these nanostructures are heterogeneous systems e.g. CdS/TiO₂, CdS/ZnS, CdSe/ZnS, and PbS/TiO₂ etc. Homogeneous coupled system such as PbS/PbS has been rarely witnessed. Attempts have been made worldwide to connect two nearby dots and use them as qubit devices. The optically generated excitons can be dissociated and stored as separate $e-h$ pairs in coupled quantum dot pairs. Also, coupled quantum dots have been reported to work as quantum logic gates[88]. Similarly, double quantum dots can be formed in a gated heterostructure with negligible interdot coupling. Coupled quantum dots have been tested for single electron switching recently [89].

1.8 Lead sulphide system

Lead sulphide (PbS) is also known as *Galena* and is the chief ore of lead. Pliny has mentioned this name. It is found in cubic rock salt structure. A formula unit of PbS corresponds to lead 86.6 and sulphur 13.4%. The colour of the mineral is dark grey, it is hard and opaque. The specific gravity of PbS is found to be equal to 7.5 [90]. Bulk PbS is a narrow band gap semiconductor. It shows two types of band gaps namely, direct band gap (0.41eV) and indirect band gap (0.37eV) at room temperature [91].

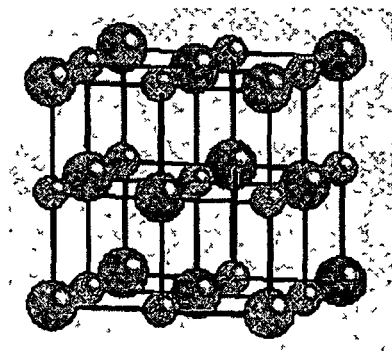


Fig1 4 Rock salt cvstal structure of PbS

Fig1.4 shows the estimated band structure of lead sulphide. Considering the fact that the energy gap increases with decreasing crystallite size, nanoscale PbS could provide maximum tunable energy gap (about 10 fold value) compared to its bulk counter part. [92]

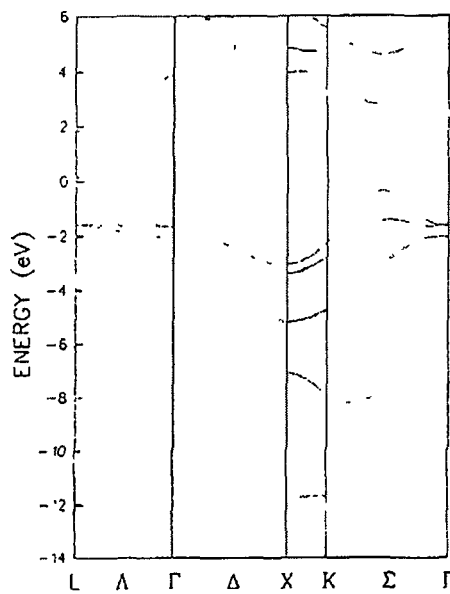


Figure1 5 Calculated band structure of PbS along the high symmetry directions The zero of energy is the valence band maximum[93]

Lead sulphide (PbS) quantum dots are considered important because of well known strong confinement effects. PbS has got relatively large exciton Bohr radius of 18nm due to its small carrier effective masses ($m^* = 0.22m_e$) and large optical dielectric constant ($\epsilon = 17$) [94]. The large Bohr radius allows it to retain this quantum confinement effect for a little larger size PbS nanoparticles. Lead sulphide being a narrow band gap material it offers possibility of large tunability. Thus, band gap of PbS can be varied over a wide range, from its bulk value of 0.41eV to 2.0eV, by changing the mean cluster size of the nanoclusters [95]. The surface energy of bulk PbS delivers two different values as 0.383 J/m² and [96] 1.4 J/m² [97]. Being an ionic semiconductor, it must maintain the decorum of surface energy of the order 1J/m². On the other hand surface energy of PbS nanoparticles has been found out to be equal to 2.45 J/m² [98]. PbS displays a broad emission response near the telecommunication wavelength ($\sim 1.56\mu\text{m}$). This emission response endows it with immense technological importance for application in fibre optical communication devices [99]. It has been predicted that the PbS nanoparticles can be used in the fabrication of infra-red sensors and detectors. Previously, it was reported that the PbS quantum dot doped glasses could be used as saturable absorbers for solid state lasers. Since PbS nanoparticles show strong confinement therefore, they could display resonantly enhanced optical nonlinearities. It was predicted that the third-order nonlinearities of PbS nanoparticles are ~ 30 times as large as those of GaAs, and even three orders of magnitude larger than those of CdS. Guo Lin et al investigated the sub-picosecond optical non-linearities of PbS nanoparticles by femtosecond optical Kerr effect (OKE) experiment [100]. Such nonlinear optical properties can be used to create optical devices with functionalities that have not been possible previously.

1.9 Motivation of the present work

In recent years size dependent physical and chemical properties of semiconductor nanoparticles have received a significant importance in the field of Nanotechnology. It is worthwhile to identify an appropriate and efficient route for fabrication of nano scale particles that exhibit novel physicochemical properties. In this regard size control and uniform dispersion of PbS nanoparticles are attempted via selected routes: sol gel

method and by filling of etched track in polyvinyl alcohol created by swift heavy ion irradiation. PbS coupled quantum dots are also obtained through user-friendly physicochemical process. The optical properties of PbS nanoparticles are explored for their possible application in optoelectronic devices. Photoluminescence study of the synthesized nanoparticles is taken as initial step of investigation. The type of emission and intensity has provided the information that helped in exploring efficient luminescent data for use in lasing, light emitting and sensing devices.

The surface photochemistry alongwith environmental stability of anatase TiO_2 also attracts attention as it can be efficiently sensitized by a narrow band gap semiconductor such as PbS. The strategy behind the formation of coupled quantum dot system of PbS/ TiO_2 is investigated. The electrical and optical properties of such heterostructure system is greatly influenced by their surface/interface kinetics, the study of surface/interface kinetics is also given attention in this work. This heterostructure system is an ideal coupled quantum dot system to understand interfacial charge leakage phenomena that can be applied to nanoelectronic components, junctions and also has potential in dye sensitized photovoltaic cells. PbS is also promising for nonlinear optical studies. The nonlinear optical properties of PbS quantum dots is investigated by two photon excitation fluorescence (TPEF), Second harmonic generation (SHG) and TPEF imaging.

1.10 Thesis Plan

In *Introduction* part (*chapter1*) of the thesis, we shall describe the background and importance of our research work. The *chapter2* will comprise of theoretical aspects on band-gap enhancement mechanism in nanocrystallites with a special reference to PbS system. In *chapter3*, we shall discuss fabrication and synthesis protocols of various nanostructured systems. These synthesis protocols include nanostructured material embedded in organic as well as inorganic, rigid flexible host matrices. Synthesis of coupled quantum dot systems is also included in this chapter. The characterizations of as synthesized and modified semiconductor nanostructures will be presented in *chapter4*. The characterizations techniques such as Transmission electron microscopy (TEM), Scanning electron microscopy (SEM), Atomic force microscopy (AFM) and X-Ray diffraction (XRD) and Energy dispersive X-Ray analysis (EDS) were taken into

account after structure morphological, composition analysis and also the ageing effect being studied in this chapter. In *chapter5* we discuss studies with regard to surface and interface kinetics of heterogeneous nanostructured systems. Optical probing of interface charge transfer, electrical properties of PbS/TiO₂ will also be included in the study. The nitrogen adsorption study on this heterogeneous system is greatly emphasized in this chapter to bring new insight of interface kinetics. Further, on verification related to nonlinear optical properties (two photo absorption, SHG etc.) will be elaborated in *chapter6*. The unusual signatures of second harmonic generation in PbS is detailed in this chapter. In the concluding remarks (*chapter7*), prospective applications of our results are highlighted.

References

- [1] A. K. Ghatak , S. Lokanathan, *Quantum Mechanics*, Macmillan India Ltd. (1984)
- [2] Brij Lal, N. Subrahmanyam, *Heat and Thermodynamics*, S. Chand and Company Ltd, 1998
- [3] K. Sülleiová, M. Besterici, T. Kvackaj, *Metal*, **5** (2009) 19
- [4] G. Cao, *Nanostructures & Nanomaterials*, Imperial College Press (2004)
- [5] M. Bangal, S. Ashtaputre, S. Marathe, A. Ethiraj, N. Hebalkar, S. W. Gosavi, J. Urban, S. K. Kulkarni *Hyperfine Interactions* **94** (2005) 81
- [6] S. K. Kulkarni, H. S. Nalwa (ed.), *Encyclopedia of Nanoscience and Nanotechnology*, Vol. X, Ame. Sci. Pub. , USA.
- [7] R. Bratschitsch , A. Leitenstorfer , *Nature Materials*, **5** (2006) 855
- [8] J. M. Martínez-Duart, R. J. Martín-Palma, F. Agulló-Rueda, *Nanotechnology for Microelectronics and Optoelectronics*, Elsevier, 2006
- [9] M. Wilson , *Nanotechnology: basic science and emerging technologies*, CRC Press (2002)
- [10] I. Malsch, *Nanotechnology and Human Health*, CRC Press (2010)
- [11] J. Blackman, *Metellic Nanoparticles* Elsevier (2008)
- [12] H. Bonnemann, R. M. Richards, *Eur. J. Inorg. Chem.* **10** (2001) 2455
- [13] K. E. Drexler , *Engines of Creation*, Knopf Doubleday Publishing Group (1987)
- [14] M. Luo, L. L. Dai, *J. Phys.: Condens. Matter* **19** (2007) 375109
- [15] N.S. Phala, E.V. Steen, *Gold Bulletin* **40** (2007) 150
- [16] N. del Fatti, F. Valee, C. Flytzanis, Y. Hamanaka, A. Nakamura, *Chemical Physics*, **251** (2000) 215
- [17] T. I. Mizan, P. E. Savage, R. M. Ziff, *J. Phys. Chem.* **98** (1994) 13067
- [18] D. Nguyen-Manh, M. Yu. Lavrentiev, S. L. Dudarev, *Chemistry and Material Science* **14** (2008)149
- [19] Y. Lu, Y. Yin, B. T. Mayers, Y. Xia, *Nano Letters*, **2** (2002) 183
- [20] J. H. Davis, *Physics of Low Dimensional Structures*, Cambridge (1998)
- [21] L. M. Liz-Marzan, *Mater. Today* **7** (2004)26
- [22] K. K. Nanda, F. E. Kruis, H. Fisan, *Nano Lletters*, **1** (2001) 605
- [23] S. Zhang, E. R. Hemesath, D. E. Perea, E. Wijaya, J. L. Lensch-Falk L. J. Lauhon, *Nano Lett.*, **9** (2009) 3268
- [24] M.Y. Jiang, G. Pajer, E. Burstein, *Surface Science*, **242**(1991) 306

- [25] X. Chen, S. S. Mao *Chem. Rev.*, **107**(2007) 2891
- [26^a] R. J. Elliot, *Phys. Rev.* **108** (1957) 1384
- [26^b] G. Dresselhaus, *J. Phys. Chem. Solids*, **1**(1956)15
- [27] A. D. Yoffe, *Advances in Physics*, **42** (993)173
- [28] Y. Wang, N. Herron, *The Journal of Physical Chemistry*, **95** (1991)525
- [29] Y. Kaynuma, *Phys. Rev.B*, **38**, (1998) 9797,
- [30] A. I. Ekimov, A. A. Onushchenko, *JETP Lett.* **34** (1981)345
- [31] L. E. Brus, *J. Chem. Phys.*, **80** (1984) 4403
- [32] Y. Wang, A. Suna, W. Mahler, R. Kasowski, *J. Chem Phys*, **87** (1987)7315
- [33] C. S. Lent., M. A. Bowen, J. D Dow, R. S Allgaier., O.F Sankey, E. S. Ho,
Superlattices Microstruct., **2**(1986)491
- [34] R. S. Kane, R. E. Cohen, R. Silbey, *J. Phys. Chem.*, **100**(1996)7928
- [35] R. C. Hilborn, *Am. J. Physics*, **50** (1982) 982
- [36] D. Tang, H. Zhang, L. Zhao, X Wu, *Physical review Letters*, **34** (2008)153904
- [37^a] S. Ramanathan, S. Patibandala, S. Bandyopadhyay, J. D. Edwards, J. Anderson,
J. Mater. Sci, **17**(2006) 651
- [37^b] U. Woggon, *Optical Properties of Semiconductor Quantum dots*, Springer (1996)
- [38] R. Bratschithch, A. Leitenstorfer, *Nature Materials*, **5** (2006)855
- [39] L. Jacak, P. Hawrylak, A. Wojs, *Quantum Dots*, Springer, Berlin (1998)
- [40] Y. G. V. S. Murti, P Nandankumar, C Vijayan, *Phys Edn* 99.
- [41] G. Ortner, I. Yugova, A. Larionov, G. Baldassarri H.v.H., M. Bayera,
P. Hawrylakb, S. Fafardb, Z. Wasilewski, *Physica E*, **26** (2005) 281
- [42] Xin Xu, Y. P. Feng, *Journal of Physics and Chemistry of Solids* **64**(2003) 2301
- [43] V. Balzani, Al. Credi, M. Venturi, *Pure Appl. Chem.* **75**(2003)541
- [44] T. Kraus, L. Malquin, H. Schmid, W. Riess N. D. Spencer, H. Wolf,
Nature Nanochnology, **2**(2007) 570
- [45] D. Miloni, *Nanotechnology application to telecommunication and networking*,
A Jhon and Wiely Sons, Interscience Publication. (2006)
- [46] R. S. Choughule, R. V. Ramanujan, *Nanoparticle: synthesis, Characterization
and application*, American scientific publisher (2010)
- [47] Y. Yin, P. Alvisatos, *Nature*, **437**(2004) 664
- [48] L. L. Hench, J. K. West, *Chem. Rev.* **9** (1990) 33

- [49] M. J. Zheng, L. D. Zhang, G. H. Li, W. Z. Shen, *Chem. Phys. Letters*, **363** (2002) 123
- [50] S. Mahamuni, A. S. Brenndre, J. Iepert, C. A. Smith, D. Cook, S. H. Risfud , H. W. H. Lee, *Nanostructured Material*, **7** (1996) 6
- [51] M. P. Pileni, *Pure and Appld. Chem.*, **72**(2000) 53
- [52] B. F Chmelka , *Nature material*, **5** (2006) 681
- [53] E. Leobandung, L. Guo, Y. Wang, S. Y. Chou, *App. Phys. Lett.* **67**(1995) 938
- [54] J. Perrière, C. Boulmer-Leborgne , R. Benzerga , S. Tricot, *Journal of Physics D: Applied Physics* , **40**(2007) 7069
- [55] J. Dutkiewicz , L. Lityńska . W. Maziarz , K. Haberko . W. Pyda , A. Kanciruk , *Crystal Research and Technology*, **44**(2009) 1163
- [56] T. Fukui, S. Ando, Y. Tokura, T. Toriyama, *Appl. Phys. Lett.* **58** (1991) 2018
- [57] F.H. Kaatz, G.M. Chow, A.S. Edelstein, *J Mater Res.* **8** (1993)1995
- [58] J. L. Gardea-Torresdey. J. G. Parsons. E. Gomez. J. Peralta-Videa. H. E. Troiani. P. Santiago, M. Jose Yacaman, *Nano Letters*, **2** (2002) 397
- [59] J. Toster. K. S. Iyer, R. Burtovvy. S. S. O. Burgess, I. A. Luzinov, C. L. Raston. *J. Am. Chem. Soc.*, **131**(2009) 8356
- [60] H. Bai, Z. Zhang, Yu Guo , W. Jia , *Nanoscale Research letters*, **7**(2009) 1931
- [61] I. Enculescu, *Digest Journal of Nanomaterials and Biostructures*, **1** (2006) 15
- [62] Al. L. Efros, A. L. Efros, *Sov. Phys. Semicond.*, **16** (1982) 772
- [63] A. Henglein, *Top. Curr. Chem.* **143** (1988) 113
- [64] P. V. Kamat, D Meisel, *Semiconductor Nanoclusters-Physical Chemical and catalytic aspects*, Elsevier science B. V., (1997)
- [65] R. Rossetti, J. L. Elision, J. M. Gibson, L.E. Brus, *J. Chem Phys.* **80**(1984) 4464
- [66] K.D. Nisha, M. Navaneethan, S. Ponnusamy, Muthamizhchelvan, *Journal of Alloys and Compounds*, **486** (2009) 844
- [67] A.V. Prasadarao, U. Selvaraj, S. Komarneni, A.S. Bhalla, *Ferroelectric Lett.*, **14**(1992) 65
- [68] J-Y Zhuang, L. Li, X-S Zhang, J-P Xu , Jun Wei , *Optoelectronics Letters*, **5**(2009)1
- [69] S. K Bera, S. Chaudhuri , A. K. Bandyopadhyay , B. R. Chakraborty , A. K. Pal, *Journal of Physics D: Applied Physics*, **34** (2001) 273
- [70] T. Harvey Dobbs, D. Dimitri , Vvedensky, A. Zangwill, J. Johansson, N. Carlsson, S. Werner, *Phys. Rev. letters*, **79**, (1997) 897

- [71] W. Thomson (Kelvin) , *Philos. Mag.* **42** (1871) 448
- [72] C. R. Berry, *Phys. Rev.* **88** (1952) 596
- [73] R. Rosseti, S. Nakahara, L.E. Brus *J. Chem. Phys.* **79**, (1983), 1086
- [74] G. Z. Jaeckel, *Tech. Phys.*, **6**(1926) 301
- [75] A. I. Ekimov, A. A. Onushchenko, *Semiconductors*, **16** (1982) 1215
- [76] M. Tomasulo, I. Yildiz, F. M. Raymo , *J. Phys. Chem. B*, **110** (2006), 3853
- [77] M. Bangal, S. Ashtaputre, S. Marathe, A. Ethiraj, N. Hebalkar,
S. W. Gosavi, J. Urban, S. K. Kulkarni , *Hyperfine Interaction* ,**160**(2005) 81
- [78] M. S. Kim, D. H. Park, E. H. Cho, K. H. Kim, Q-H Park, H. Song, D-C Kim,
J. Kim. J. Joo, *ACS Nano*, **3**(2009) 1329
- [79] C. A. Leatherdale, W-K. Woo, F. V. Mikulec, M. G. Bawendi,
J. Phys. Chem. B **106** (2002) 7619
- [80] D. A. Tenne, A. K. Bakarov I. Toropov D. R. T. Zahn,
Physica E: Low-dimensional Systems and Nanostructures **21**(2004) 241
- [81] D. A. Tenne. K. Bakarov. I. Toropov, D. R. T. Zahn
Physica E: Low-dimensional Systems and Nanostructures **13**(2002) 139
- [82] A. Bagga, P. K. Chattopadhyay, S. Ghosh , *Phys. Rev. B* **74** (2006) 035341
- [83] A. Satake, Y. Masumoto , *Phys. Rev. B*, **61** (2006) 12654
- [84] V. V. Matyilitsky, A. Shavel, N. Gaponik, A. Eychmüller, J. Wachtveitl, *J. Phys. Chem. C*, **112** (2008)2703
- [85] C. Bauer, G. Boschloo, E. Mukhtar , A. Hagfeldt, *Chemical Physics Letters*,
387(2004)176
- [86] R. S. Devan. S. B. Deshpande. B. K. Chougule , *J. Phys. D: Appl. Phys.*
40 (2007) 1864
- [87] S. Coe-Sullivan, W-K Wo , J. S. Steckel M. Bawendi , V. Bulovi ,
Organic Electronics **4** (2003) 123
- [88] D. G. Deppea, Q. Deng, *Applied Phys. Letters* **73**(1998) 3536
- [89] G. Burkard D. Loss *Phys. Rev. B* ,**59**(1991) 2070
- [90] I. H. Chan , P. Fallahi, R.M Westervelt, K.D Maranowski , A.C. Gossard ,
Physica E: Low-dimensional Systems and Nanostructures **17**(2003) 984
- [91] Amethyst Galleries' Mineral Gallery (MINERALS)
- [92] Li Wei , C. Jun-fang, W. Teng , *Physica B: Condensed Matter* **405**(2010) 5

- [93] A. Lipovskii, E. Kolobkova, V. Petrikov, I. Kang, A. Olkhovets, T. Krauss, M. Thomas, J. Silcox, F. Wise, Q. Shen and S. Kycia, *Appl. Phys. Lett.* **71**(1997) 3406
- [94] A. Santoni, G. Paolucci, G. Santorost, K. C Prince , N. E. Christensen , *J. Phys.: Condens. Matter* **4** (1992) 675
- [95] A. Lipovskii, E. Kolobkova, and V. Petrikov , I. Kang, A. Olkhovets, T. Krauss, M. Thomas, J. Silcox, and F. Wise, Q. Shen and S. Kycia , *Appl. Phys. Lett.* **71**(1997)3406
- [96] K. K. Nanda, F. E. Kruis, H. Fissan, *Journal of Applied physics*, **91**(2002) 2315
- [97] B. Janczuk, et al, *Mater Chem. Phys.* **37**(1994) 64
- [98] K. K. Nanda, S. N. Behera, *Phys. Rev. A* **66** (2002) 13208
- [99] K. K. Nanda, S. N. Behera, *Phys. Rev. Lett.* **89** (2002)256103
- [100] J. Heo, C. Liu, *Journal of Materials Science: Materials in Electronics*,**18**(2007)35
- [101] X. Ai, J. Rong, J. J. Wang, Z. Xia, Y. Zuo, L. Guo, Q. Li, H. Zhu , *Chin. Phys. Lett.*, **55**(1992) 198

CHAPTER 2

Theoretical treatments on the Size Dependent Features of Nanocrystals based on the Kronig-Penney, Free Electron and LCAO Models

Introduction:

It is thought it worthwhile to apply some synthesis of the concepts of the Kronig-Penney[1], Free Electron [2] and LCAO[3] [Linear Combination of Atomic Orbital] models to explore theoretically on the nature of the size dependent attributes of nanocrystals in general and PbS nanocrystal in particular. With this objective in mind we proceed as follows.

2.1: Ideas of the Kronig-Penney model applied to nanocrystals

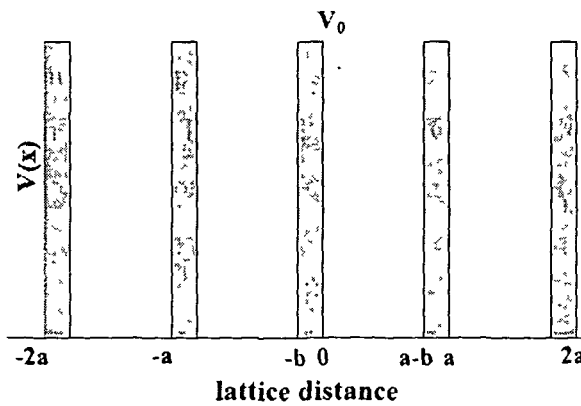


Fig.2 1: Kronig-Penney model of a lattice periodic potential

In a periodic potential the Schrodinger equation becomes

$$\frac{d^2\psi}{dx^2} + \frac{2m}{\hbar^2}[E - V(x)]\psi = 0 \quad (2.1)$$

According to this model, periodic potential $V(x)$ is supposed to have the following attributes,

$$V = V_0, -b \leq x \leq 0,$$

$$V = 0, 0 \leq x \leq a - b \quad (\text{See Fig.1.1}) \quad (2.2)$$

$V(x+a) = V(x)$, i.e. a periodic potential

The appropriate wave function is a Bloch function given by

$\psi(x) = u_k(x)e^{ikx}$, where $u_k(x)$ is a periodic function with the periodicity of the lattice, i.e.

$$u_k(x) = u_k(x \pm na)$$

In this case it can be noted that the general solution of Schrodinger Eqn.(1.1) are

$$(1) \quad \psi_1 = Ae^{i\alpha x} + B^{-i\alpha x} \quad \text{for } V=0 \quad \text{with } \alpha = \frac{\sqrt{2mE}}{\hbar} \quad (2.3)$$

and

$$(2) \quad \psi_2 = Ce^{\beta x} + De^{-\beta x} \quad \text{for } V=V_0 \quad \text{with } \beta = \frac{\sqrt{2m(V_0 - E)}}{\hbar} \quad (2.4)$$

Periodicity condition guarantees,

$\psi_2(-b) = e^{-ika} \psi_1(a-b)$ [A Bloch function transforms under any lattice translation as $\psi_2(x+a) = e^{\pm ika} \psi_1(x)$]

$$\frac{\partial \psi_2(-b)}{\partial x} = e^{-ika} \frac{\partial \psi_1(a-b)}{\partial x} \quad (2.5)$$

Continuity of the wave function requires (at $x=0$ say)

$$\begin{aligned} \psi_2(0) &= \psi_1(0) \\ \frac{\partial \psi_2(0)}{\partial x} &= \frac{\partial \psi_1(0)}{\partial x} \end{aligned} \quad (2.6)$$

Substituting (1) and (2) in equation (5) and (6) we get four homogeneous linear equations in A, B, C and D given by

$$\begin{aligned} C + D &= A + B \\ \beta C - \beta D &= i\alpha A - i\alpha B \end{aligned}$$

$$\begin{aligned} e^{-\beta b} C + e^{\beta b} D &= A e^{-ika + i\alpha(a-b)} + B e^{-ika - i\alpha(a-b)} \\ e^{-\beta b} \beta C - \beta e^{\beta b} D &= i\alpha A e^{-ika + i\alpha(a-b)} - i\alpha B e^{-ika - i\alpha(a-b)} \end{aligned}$$

The condition for the determinantal compatibility is

$$\begin{vmatrix} 1 & 1 & -1 & -1 \\ \beta & -\beta & -i\alpha & i\alpha \\ e^{-\beta b} & e^{\beta b} & -e^{-ika+i\alpha(a-b)} & -e^{ika-i\alpha(a-b)} \\ \beta e^{-\beta b} & -\beta e^{\beta b} & -i\alpha e^{-ika+i\alpha(a-b)} & i\alpha e^{-ika-i\alpha(a-b)} \end{vmatrix} = 0$$

On a simplification, we obtain

$$\cos ka = \frac{\beta^2 - \alpha^2}{2\alpha\beta} \sin \alpha(a-b) \sinh \beta b + \cos \alpha(a-b) \cosh \beta b$$

Following Kronig-Penney, let us now introduce a simplifying condition that as $b \rightarrow 0$

$V_0 \rightarrow \infty$ (Infinity) in such a manner that the quantity $\frac{mV_0}{\hbar^2} b(a-b)$ remains a

constant equal to c (say). The restriction assures us that the “potential area” remains finite. With this condition the quantity βb becomes equal to

$$\beta b = \frac{\sqrt{2m(V_0 - E)b^2}}{\hbar} = \sqrt{\frac{2m(V_0 - E)b^2(a-b)}{(a-b)\hbar^2}} = \sqrt{\frac{2cb}{a-b}}$$

so,

$$\cos ka \cong \frac{c}{\alpha a} \sin \alpha a + \cos \alpha a, \quad \text{in the limit as } b \rightarrow 0 \quad (2.7)$$

This equation is represented in the Fig.2.2 on a numerical basis

$$f(\alpha a) = \frac{c}{\alpha a} \sin(\alpha a) + \cos(\alpha a)$$

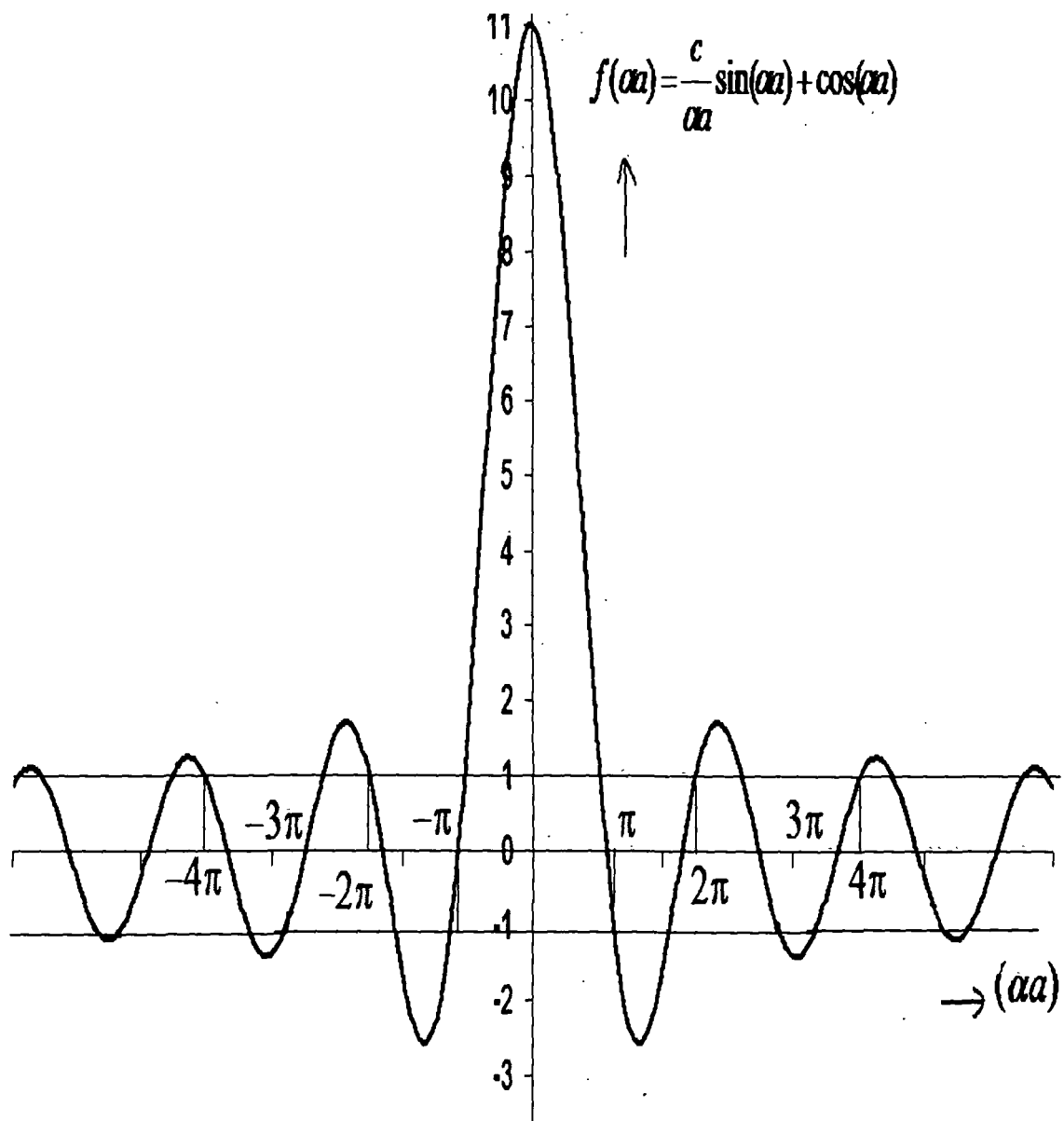


Fig.2.2: Plot of $f(\alpha\alpha)$ as a function of $(\alpha\alpha)$

From the $f(\alpha a)$ vs (αa) plot based on the Kronig-Penney model it is clear that at low energies the width of the forbidden energy bands are larger than those at higher energies.

In low dimensional system, particularly in nanocrystals, the number of charge carriers (electrons and holes) is small. Therefore only a few numbers of energy levels in the lowest energy bands are occupied by the charge carriers. Consequently in such low energy regions they come across wider forbidden energy gaps. This is a qualitative manner, on the basis of Kronig-Penney model, one therefore expects enhancement of energy band gaps. These ideas concerning size dependence of energy band gaps in nanocrystals can be expressed on exact numerical basis by suitable computational method.

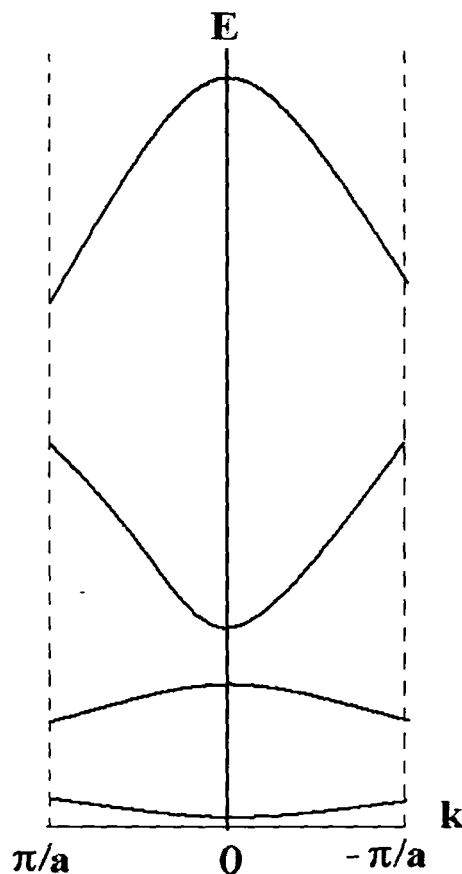


Fig.2.3: (A)

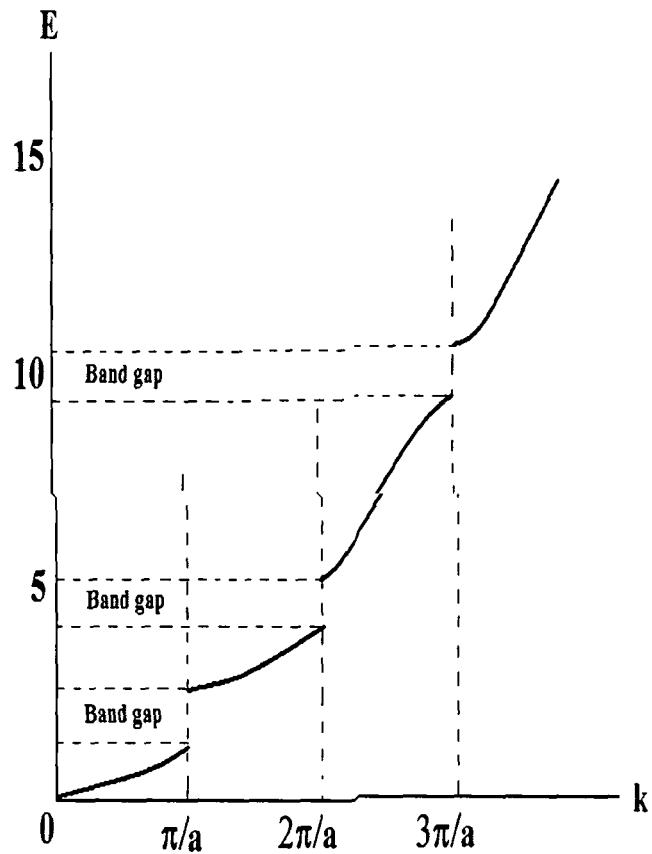


Fig2.3: (A), (B): Energy bands in extended reduced zone scheme in Fig.2.3: (B) right half of the energy bands are shown only.

2.2: Free Electron model:

Let us consider, a free electron confined in one dimensional potential box of dimension L.

The potential inside the box $V(x)$ is given by

$$V(x) = 0 \text{ within } 0 \leq x \leq L$$

The corresponding Schrödinger equation is

$$\frac{d^2\psi}{dx^2} + \frac{2m}{\hbar^2} E\psi = 0 \quad (2.8)$$

The energy eigen values of a free electron inside this potential well are given by

$$E_n = \frac{\hbar^2 K_n^2}{2m} = \frac{\hbar^2 \pi^2}{2mL^2} n^2 \quad (2.9)$$

For a bulk crystal let L be equal to 1m. In this case from equation (2.9)

$$E_n = \frac{\hbar^2 \pi^2}{2m} n^2$$

$$E_{n-1} = \frac{\hbar^2 \pi^2}{2m} (n-1)^2$$

$$E_n - E_{n-1} = \frac{\hbar^2 \pi^2}{2m} (2n-1)$$

For a gold [Au] bulk crystal of 1m, the number of free electrons are equal to $5.9 \times 10^{28} \text{m}^{-3}$ [4]. Therefore 1D gold crystal of length 1m, the number density of free electron is $3.89 \times 10^9 \text{m}^{-1}$. Since the electrons are fermions the highest energy occupied by 3.89×10^9 electron is the $(3.89 \times 10^9)^{\text{th}}$ energy level, which is the Fermi level E_F . The next energy level occupied below E_{F-1} is the $(3.89 \times 10^9 - 1)^{\text{th}}$ energy level. The difference between these two energy levels is,

$$\Delta E = E_F - E_{F-1}$$

$$\frac{\hbar^2 \pi^2}{2m} [2 \times 3.89 \times 10^9 - 1]$$

$$m = 9.1 \times 10^{-31} \text{ Kg}$$

$$\hbar = 1.05 \times 10^{-34} \text{ JS}$$

$$\pi = 3.14$$

$$= 4.6 \times 10^{-28} \text{ J}$$

The difference between the highest two occupied energy levels, ΔE in an 1D bulk gold crystal of length 1m is equal to $(E_F - E_{F-1}) = 4.6 \times 10^{-28} \text{ J}$

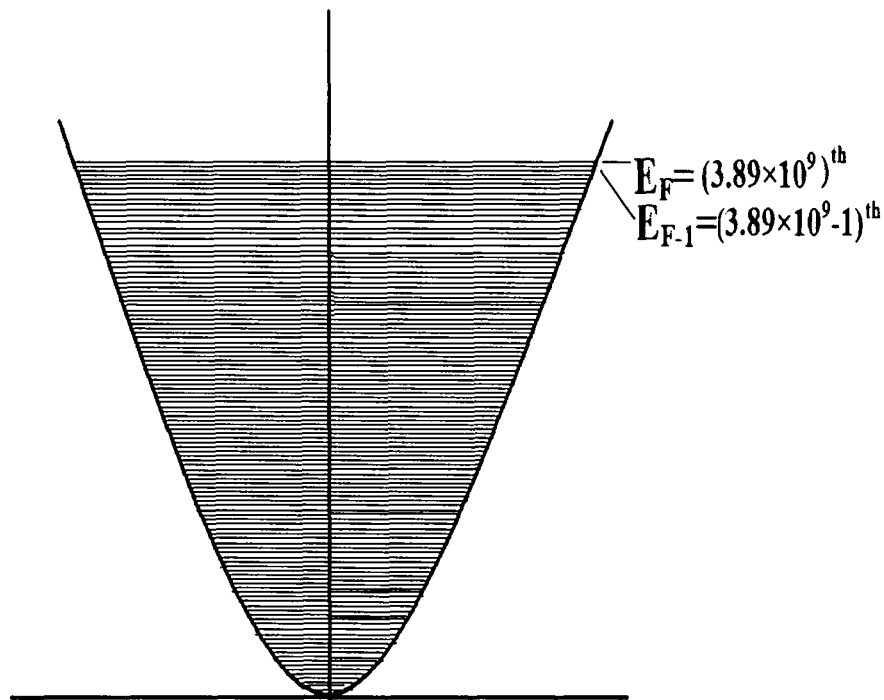


Fig.2.4: Energy level diagram of gold bulk crystal of size 1m where $(E_F - E_{F-1} = 4.6 \times 10^{-28} \text{ J})$

Let us consider now a gold nanocrystal of size 10nm.

$$10 \times 10^{-9} = 10^{-8} \text{ m}$$

For Gold $a_{fcc} = 4.07 \times 10^{-10} \text{ m}$ [5]

The number of unit cell in 10^{-8} m is equal to $\frac{L}{a} = \frac{10^{-8}}{4.07 \times 10^{-10}} = 0.24 \times 10^2 = 24$

Gold nanocrystal of dimension of length 10^{-8} m contains 24 unit cells. So in free electron gas there are 24 electrons. Hence the Fermi energy of 24th energy level. The next energy below the Fermi level is the 23rd energy level.

The difference between these two energy levels is

$$\frac{\hbar^2 \pi^2}{2m \times 10^{-16}} [24^2 - 23^2] = 67 \frac{\hbar^2 \pi^2}{2m \times 10^{-16}} = 8.03 \times 10^{-20} \text{ J}$$

the difference between the highest two occupied energy levels, ΔE of a Gold nanocrystal of length 10nm is equal to $(E_F - E_{F-1}) = 8.03 \times 10^{-20} \text{ J}$

$$\frac{(E_F - E_{F-1})_{nano}}{(E_F - E_{F-1})_{bulk}} = \frac{8.03 \times 10^{-20} \text{ J}}{4.6 \times 10^{-28} \text{ J}} = 1.7 \times 10^8$$

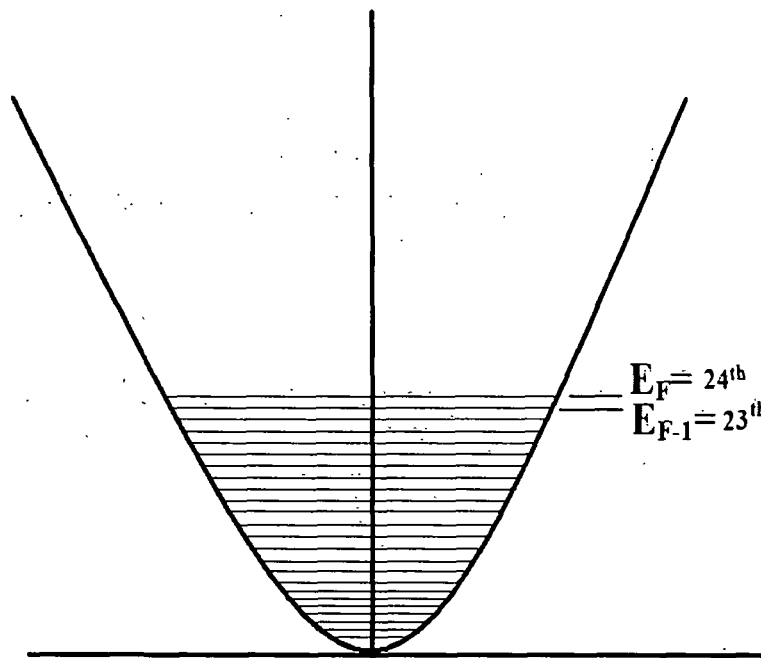


Fig.2.5: Energy level diagram of gold nanocrystal of size 10nm where $(E_F - E_{F-1}) = 8.03 \times 10^{-20} \text{ J}$

In this simple example it is clearly seen that the difference in energy in the top two occupied energy levels $[E_F - E_{F-1}]$ in $L=1.0\text{nm}$ size linear gold bulk crystal and the

corresponding energy difference between the top two occupied energy levels i.e. $[E^{24\text{th}} - E^{23\text{rd}}]$ in $L=10 \times 10^{-9}$ m gold nanocrystal is very large. The ratio of the difference between the nanos and that of the bulk is 1.7×10^8 . This clearly indicates that the band width in nanocrystals become higher compared to that of bulk. The energy band widths in nanocrystals are strongly size dependent (inversely dependent in the size). This picture also agrees well with the qualitative picture obtained in the Kronig-Penny model.

Along with gold[Au] the ΔE s of bulk as well as nano for Ag and Cu are also presented in Table2.1:

Crystal Material	$\Delta E = E_F - E_{F-1}$	
	$\Delta E_B (\text{in } 10^{-28} \text{J})$	$\Delta E_N (\text{in } 10^{-20} \text{J})$
Au	4.32	8.3
Ag	4.29	5.8
Cu	5.23	6.3

Table2.1: ΔE s of bulk as well as nano for Au, Ag and Cu

It is however not immediately clear how the corresponding attributes in semi conductor lead sulphide (PbS) nanocrystal can be accommodated in light of these two approaches. For this purpose we need to go a little further by bringing in the concepts of the LCAO method.

Since the present work concerns PbS nanocrystal , it seems pertinent to point out some relevant data of both direct and indirect band gaps of PbS nanocrystals. A few theoretically calculated features of 10a and 100a sized lattice of PbS nanocrystal (where $a=5.92 \times 10^{-10}$ m) [6] are discussed in the section2.3 . The relatively low number of electrons occupy only a few energy levels. Therefore as per the Kronig Penny Model, the bandgap of the PbS nanocrystal should be relatively large.

2.3 Calculation of total number of electrons in PbS nanocrystals:

The number density of electrons is given by [7],

$$n = 2 \left[\frac{2\pi k}{h^2} \right]^{3/2} T^{3/2} (m_e^* m_h^*)^{3/4} e^{-\frac{E_g}{2kT}} \quad (2.10)$$

where k is the Boltzmann's constant [$k=1.38 \times 10^{-23} \text{J}$],

m_e^* and m_h^* are the effective masses of electrons and holes respectively in PbS nanocrystals,

where, $m_e^* = 0.22m_e$ and $m_h^* = 0.29m_h$

$E_g = 0.41 \text{eV}$ (For direct band gap), $E_g = 0.37 \text{eV}$ (For indirect band gap) semiconductor PbS

Let us consider the total number of electrons present in a PbS nanocrystal of size $10a$ and $100a$, where, $a = 5.92 \times 10^{-10} \text{m}$ for PbS. The calculated electron density along with total number of electrons is presented in Table 2.2 and Table 2.3 respectively. For direct band gap, Band gap = 0.41eV , at different temperatures in bulk PbS crystal, the electron density and total number of electrons calculated with the help of eqⁿ(2.10) are given in the Table 2.2

Temperature (K)	Electron density (n/m ³)	Total number of electrons in a 10a size lattice	Total number of electrons in a 100a size lattice
300	5.44×10^{26}	112.86	1128.63
350	2.12×10^{27}	439.83	439836.4
400	6.07×10^{27}	1259.34	1259342.9
450	1.40×10^{28}	2904.58	2904580
500	2.18×10^{28}	5767.66	5767666

Table: 2 2 Total number of electrons in 10 a size PbS lattice at different temperatures($E_g=0.41\text{eV}$)

For indirect band gap, band gap= 0.37eV , at different temperatures in bulk PbS crystal, the electron density and total number of electrons calculated with the help of eqⁿ(2.10) are given in the Table2.3

Temperature (K)	Electron density (n/m ³)	Total number of electrons in a 10a size lattice	Total number of electrons in a 100a size lattice
300	1.18×10^{27}	224.81	244814.6
350	4.10×10^{27}	850.62	8,50,627
400	1.08×10^{28}	2240.67	22,40,676
450	2.35×10^{28}	4875.54	48,75,545
500	4.43×10^{28}	9190.92	91,90,921

Table 2.3. Total number of electrons in 10 a size PbS lattice at different temperatures($E_g=0.37\text{eV}$)

2.4 The LCAO method:

On the basis of LCAO method, the energy band width of conduction electrons in a one dimensional crystal is found to be 4γ . The quantity γ is a measure of overlapping interactions among the atomic orbital of a conduction electron in a crystalline solid[8]. In the present work, with a purpose to see the nature of dependence of γ on size of a copper nanocrystal, the LCAO method is applied. The result reveals that γ bears an inverse dependence on the size of nanocrystals. This observation agrees well with the already published findings. It has been found on a numerical fit basis that γ decreases exponentially with the nanocrystal size.

On extension of this method of analysis to lead sulphide[PbS] crystals which is a semiconductor having rock salt type crystal structure, it is seen that the overlapping interaction potentials experienced by a conduction electron in PbS is also an inverse function of size of the crystal, particularly in the nano size region. For a comparative assessment of size dependence of the overlapping potential, $V'(\vec{r} - \vec{R}_j)$ [9] in metallic and semi conducting nanocrystals some relevant analysis done on 10a size lead sulphide (PbS) nanocrystals is presented in this work.

Molecular orbital method has been applied to study the size dependence of band structure in some covalent bond semiconductor nanocrystals [10]. Metal nano crystals, on the other hand, are formed by metallic bond. It is worthwhile to make some assessment of the size dependence of band structure attributes by applying the LCAO method in metals as well as semiconductor nanocrystals. With this objective in mind, some results are obtained in this work by the application of the LCAO method in a 10a sized copper and lead sulphide nanocrystal.

By applying the LCAO method, one obtains the energy eigen values of a conduction electron in a crystalline solid

$$E(\vec{k}) = E_0 - \alpha_j - \gamma_j \sum_m e^{i\vec{k} \cdot (\vec{R}_j - \vec{R}_m)} \quad (2.11)$$

Where E_0 is the atomic energy α_j and γ_j are two positive quantities defined by

$$\alpha_j = - \int \phi^*(\vec{r} - \vec{R}_j) V'(\vec{r} - \vec{R}_j) \phi(\vec{r} - \vec{R}_j) d\tau \quad (2.12)$$

$$\gamma_j = - \int \phi^*(\vec{r} - \vec{R}_m) V'(\vec{r} - \vec{R}_m) V'(\vec{r} - \vec{R}_j) d\tau, \quad (2.13)$$

Where the other symbols have their usual significance and

$$V'(\vec{r} - \vec{R}_j) \equiv V(\vec{r}) - V_a(\vec{r} - \vec{R}_j) \quad (2.14)$$

In Eq.(2.14) $V(\vec{r})$ is the lattice potential energy and $V_a(\vec{r} - \vec{R}_j)$ is the potential energy experienced by a conduction electron at a position \vec{r} in the vicinity of the j^{th} lattice site. $V'(\vec{r} - \vec{R}_j)$ is a measure of overlapping interactions amongst the atomic orbital.

In a one dimensional (fcc) crystal the top and bottom energy levels of an energy band are given by

$$E_{\text{top}} = E_0 - \alpha + 2\gamma$$

$$E_{\text{bottom}} = E_0 - \alpha - 2\gamma$$

Hence width of an energy band is

$$E_{\text{top}} - E_{\text{bottom}} = 4\gamma \quad (2.15)$$

Therefore, according to this model, the energy band width increases when γ increases. In the present work, γ for a 10a sized one dimensional copper as well as lead sulphide nano crystal (a, lattice constant) have been evaluated.

The maximum lattice potential energy of a 10a sized copper lattice is (Cu, fcc, monovalent)

$$V(\vec{r}) = \frac{1}{4\pi\epsilon} \frac{eq^{+1}}{a} \sum_{n=1}^{10} \frac{1}{n} = -11.39eV \quad (2.16)$$

The potential energies are measured with respect to the bottom of the overall potential energy well for conduction electrons in the metal. It can be seen that when a conduction electron approaches a positively ionized copper lattice site to a distance

$\frac{a}{2.997}, V'(\vec{r} - \vec{R}_j)$ becomes equal to zero. From distances of approach $\frac{a}{4}$ and nearer, $V'(\vec{r} - \vec{R}_j)$ becomes repulsive. It is pertinent to consider the atomic orbital in their ground state. The atomic orbital corresponding to singly ionize copper atom is similar to hydrogen atom orbital. These are given by [11]

$$\phi(\vec{r}) = e^{-\frac{\bar{r}}{2}} \bar{r}^l L_{n+l}^{2l+1}(\vec{r}),$$

Where different symbols have their usual significance,

Hence,

$$\gamma_j = - \int [\{e^{-\frac{1}{2}\bar{r}'} L_{n+l}^{2l+1}(\vec{r}')\}^* V'(\vec{r} - \vec{R}_j) \{e^{-\frac{1}{2}\bar{r}'} L_{n+l}^{2l+1}(\vec{r}')\}] d\tau$$

If we include the effect of overlapping interactions in $V'(\vec{r} - \vec{R}_j)$ only, the normalization integral in γ_j can be evaluated separately. Thus one obtains from the normalization integral

$$\int_0^{\infty} e^{-\bar{r}2l} [L_{n+l}^{2l+1}(\vec{r})]^2 \bar{r}^2 d\vec{r} = \frac{2n[(n+l)!]^3}{(n-l-1)!}$$

For an s orbital,

$$\frac{2n[(n+l)!]^3}{(n-l-1)!} = 2$$

Hence,

$$\gamma_i = - 2V'(\vec{r} - \vec{R}_j) \quad (2.17)$$

In the Table2.4, the calculated values of γ_j for different nanocrystal sizes are listed. It is evident that the energy band width bears an inverse dependence on the size of a nanocrystal. This observation is in agreement with already published results [11]. In Fig2.6 is shown the numerical fit of the γ_j versus nanocryatal size data. The numerical fit equation is

$$\gamma_j = A_1 \exp(-x/t_1) + A_2 \exp(-x/t_2) + y(0) \quad (2.18)$$

$$A_1=7.70098, \quad t_1= 7.88617, \quad A_2=39.47593, \quad t_2= 1.22408 \text{ and}$$

$$Y(0)=-23.08099.$$

Electron at the vicinity (a=0.361)	$\gamma_j(\text{eV})$
a/2	-7.94
3/4a	-13.248
7/8a	-14.765
15/16a	-15.37
a	-16.64
3/2a	-18.554
7/4a	-19.312
2a	-21.208
3a	-21.87
4a	-22.268
5a	-22.532
6a	-22.724
7a	-22.866
8a	-22.976
9a	-22.976
10a	-23.064

Table2.4: Calculated γ_j

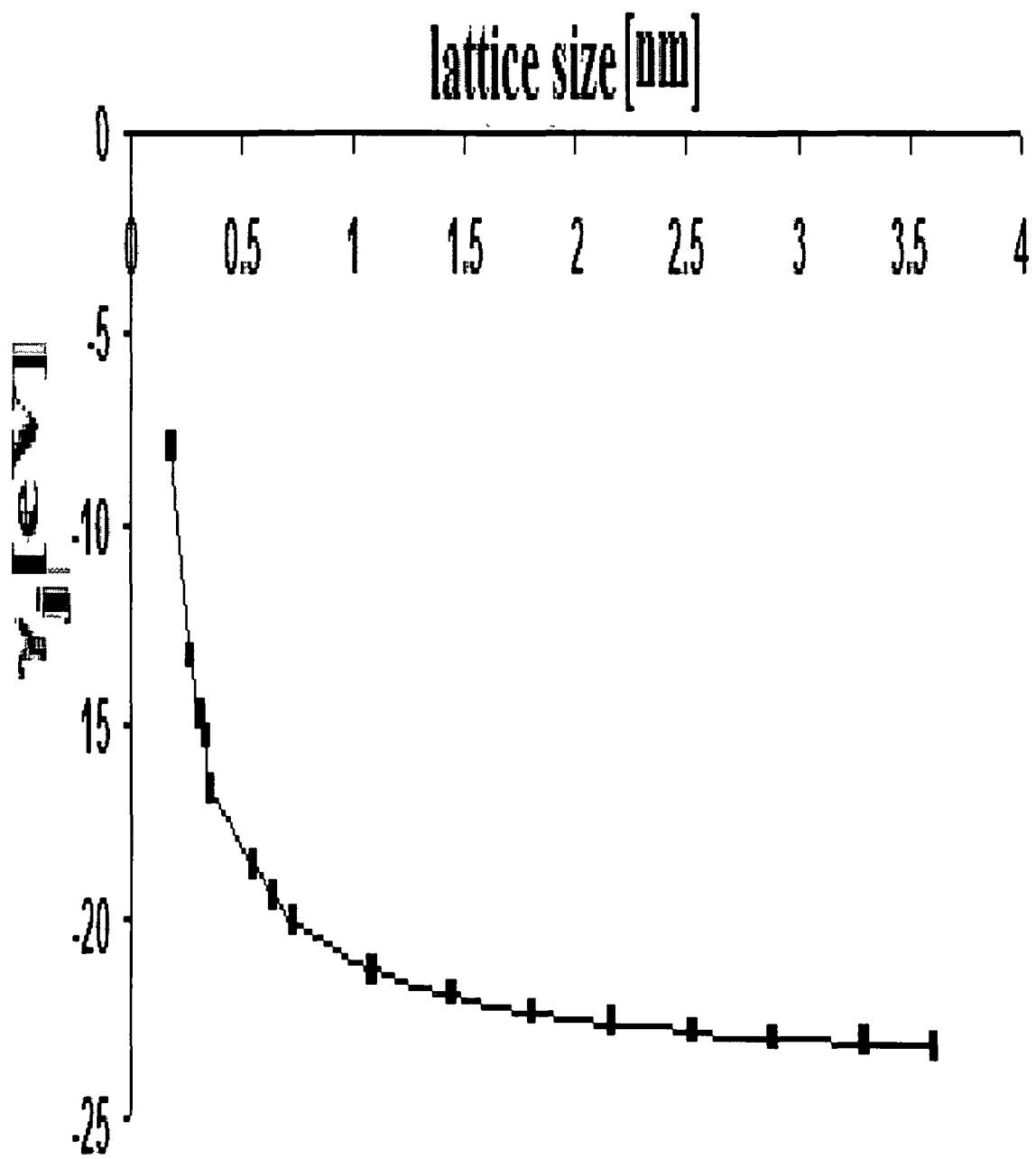


Fig 2.6. Size dependence in a Cu nanocrystal

Now let us consider 1D PbS nano crystal of length of $10a$ i.e. 5.93nm . It may be noted that Pb^{++} and S^{--} ions are situated at alternate lattice sites. A PbS crystal is characterized by fcc lattice[13]. Hence the distance between successive Pb^{++} and S^{--} lattice sites is $\frac{a}{2}=0.296\text{nm}$. The total lattice potential experienced by a conduction electron in this PbS 1D nano crystal is given by

$$\begin{aligned}
 V(r) &= \\
 &\frac{(2e)(2e)}{4\pi\epsilon_0 a}[-2+1-2/3+1/2-2/5+1/3-2/7+1/4-2/9+1/5-2/11+1/6-2/13+1/7-2/15+1/8-2/17+1/9-2/19+1/10] \\
 &= 9.71 \times (-0.665)\text{eV} \\
 &= -6.457\text{eV} \tag{2.19}
 \end{aligned}$$

The negative sign appearing in Eqⁿ.(2.19) indicates that the total lattice potential is an attractive one, which is essential for cohesion of PbS crystal.

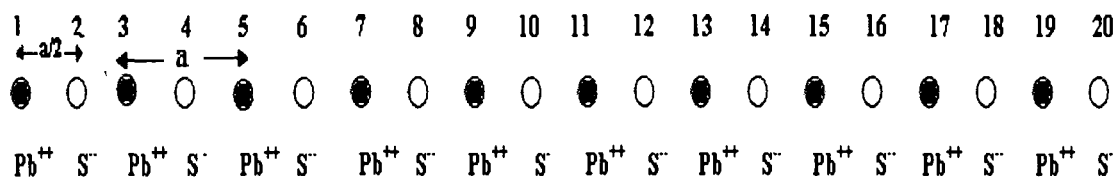


Fig2.7: A schematic diagram of a PbS $10a$ size linear lattice [$a=0.593\text{nm}$]

In this 1D nano crystal Pb^{++} ions are situated at lattice site positions 1, 3, 5.....17....and 19. These equal to 10Pb^{++} ions. S^{--} ions are situated at lattice site position 2, 4, 6,.....18 and 20. This is equal to 10S^{--} ions. Starting from Pb^{++} ion situated at lattice site (1), the Coulomb interaction between this lattice site and its nearest neighbour lattice site no2 occupied by a S^{--} ion is attractive and Coulomb interaction

between this lattice site and its next nearest neighbour lattice site no3 occupied by a ion Pb^{++} ion is negative. The various potential energies $V(\vec{r} - \vec{R}_j)$ experienced by a conduction electron in the vicinity of different lattice sites no = 1,2,3,4,5,5,6 etc. are given in Table 2.5

Potential energy $V(\vec{r} - \vec{R}_j)$ of a conduction electron in the vicinity of various lattice sites,

Lattice site no.	Lattice distance in units of 'a'	$V(\vec{r} - \vec{R}_j)$ (eV)
1	1/2	-19.42
2	1	9.71
3	3/2	-6.47
4	2	4.86
5	5/2	-3.88
6	3	3.24
7	7/2	-2.77
8	4	2.43
9	9/2	-2.16
10	5	1.94
11	11/2	-1.76
12	6	1.62
13	13/2	-1.49
14	7	1.38
15	15/2	-1.29
16	8	1.21
17	17/2	-1.14
18	9	1.08
19	18/2	-1.02
20	10	0.97

Table: 2.5 Potential energies of conduction electrons at various lattice sites

We note that,

$$V'(\vec{r} - \vec{R}_j) = V(\vec{r}) - V(\vec{r} - \vec{R}_j) \quad (2.20)$$

Eqn.(2.20) defines the overlapping interaction potential.

In Table2.6 $V'(\vec{r} - \vec{R}_j)$ values corresponding potentials due to lattice site no. 1, 2, 3.....etc. are shown.

Lattice site	Potential corresponding to different lattice sites $V'(\vec{r} - \vec{R}_j)$ eV	$V'(\vec{r} - \vec{R}_j)$ eV= $V(\vec{r}) - V(\vec{r} - \vec{R}_j)$ eV
1	V'_{01}	12.96
2	V'_{02}	-16.17
3	V'_{03}	0.01
4	V'_{04}	-11.30
5	V'_{05}	-2.58
6	V'_{06}	-9.70
7	V'_{07}	-3.69
8	V'_{08}	-9.09
9	V'_{09}	-4.30
10	V'_{10}	-8.40
11	V'_{11}	-4.70
12	V'_{12}	-8.08
13	V'_{13}	-4.84
14	V'_{14}	-8.08
15	V'_{15}	-5.17
16	V'_{16}	-7.67
17	V'_{17}	-5.32
18	V'_{18}	-7.54
19	V'_{19}	-5.44
20	V'_{20}	-7.43

Table: 2.6 : $V'(\vec{r} - \vec{R}_j)$ values corresponding potentials due to lattice site no. 1, 2, 3.....etc.

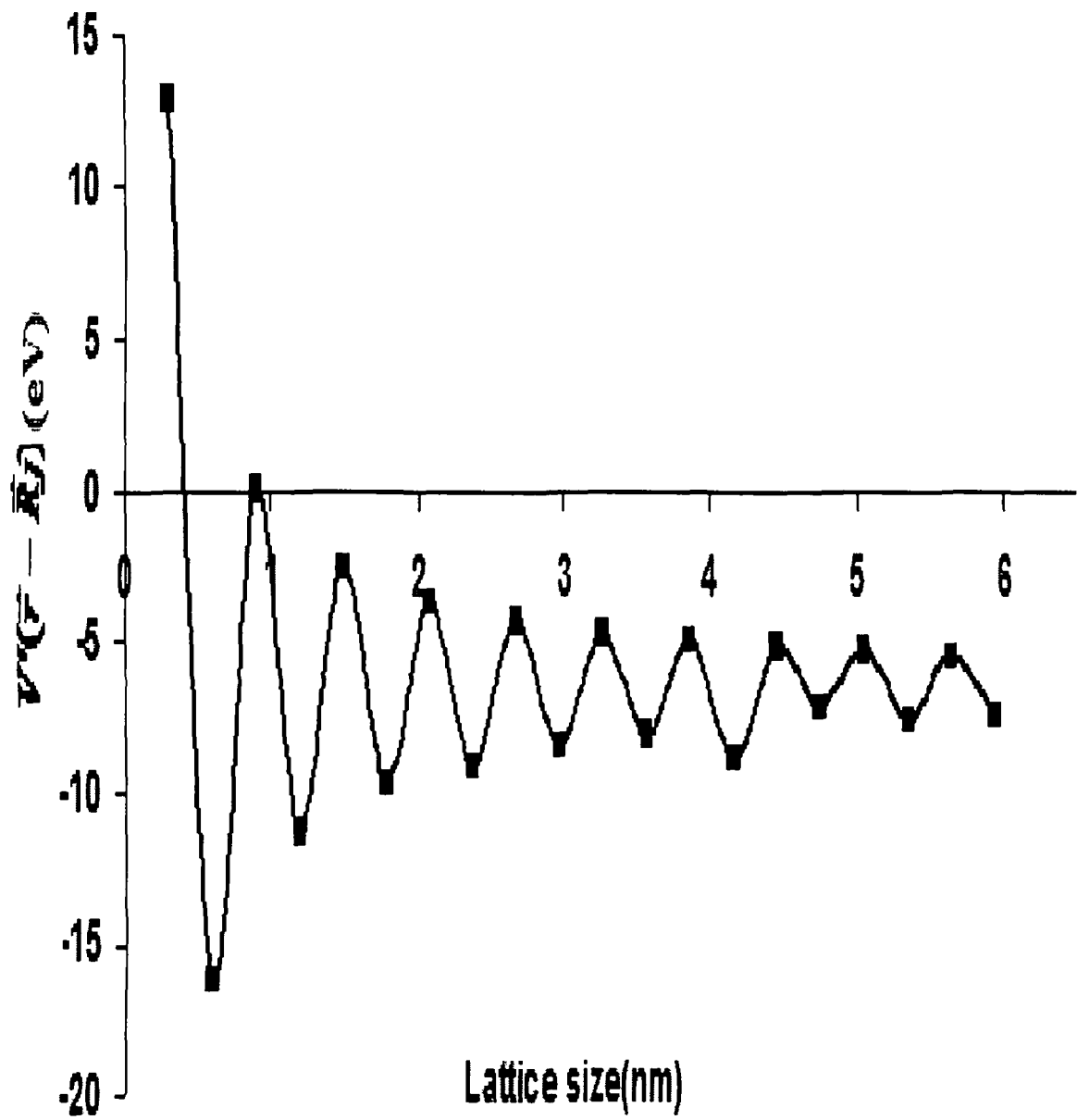


Fig.2.8: Size dependence in PbS nanocrystal

We see from equation(2.17) that the overlapping interaction potential $V'(\vec{r} - \vec{R}_j)$ is proportional to γ_j . In the 1D PbS nano crystal considered in this work the size dependence of $V'(\vec{r} - \vec{R}_j)$ is studied instead of γ_j 's. The numerically evaluated dependence of $V'(\vec{r} - \vec{R}_j)$'s on nanocrystal size is shown in Fig2.8. The values of other relevant parameters are shown in the Table2.4 and Table2.6.

It can be noted that the total lattice potential of 10a size 1D PbS nano crystal $V(r)$, is found to be equal to -6.46eV. It is significant to observe that $V(r)$ is of attractive nature. This implies that the present example of 10a 1D PbS crystal is a result a net attractive cohesive lattice binding force. In other words from binding energy consideration point of view such a crystal is stable one.

The periodic oscillations present in the $V'(\vec{r} - \vec{R}_j)$ versus lattice size curve i.e. Fig2.3 is a result of periodic arrangement of doubly positively ionised Pb^{++} ions and doubly negatively ionised S^{2-} ions situated at the alternate lattice sites[See Fig2.8]. The most important attribute discernable in the nature of the graph of Fig8 is that the average values of $V'(\vec{r} - \vec{R}_j)$ bear some strong inverse dependence on the size of nano crystal.

It can be observed that $V'(\vec{r} - \vec{R}_j)$ exhibits a composite nature having a damped harmonic oscillation characterized by a systematic lowering of the mean value, as if a decay curve is amplitude modulated by a damped harmonic oscillation. The period of this oscillation is $(a + \frac{a}{2} = 0.89nm)$. On a numerical fit of this composite variation of

$V'(\vec{r} - \vec{R}_j)$ with the size of the nano crystal, it is obtained that the best numerical fit is given by

$$Y = Ae^{-\beta x} \sin kx + B$$

where $A=30$, $B=-5$, $\beta=1.629$ (damping constant) and $k=0.89$

We note that relation (4), $V'(\vec{r} - R_j) = V(\vec{r}) - V_a(\vec{r} - \vec{R}_j)$, defines the potential due to overlapping interactions between the atomic orbitals.

This chapter mainly describes size dependent evolution of band gaps for both direct and indirect band gap type PbS structures.

Bulk PbS is characterized by both types of band gaps; direct band gap of 0.41eV and indirect band gap of 0.37eV at room temperature. Direct band gaps correspond to the direct electronic transitions whereas indirect band gaps correspond to indirect electronic transition (phonon assisted electronic transition). The size of the band gap changes as one makes a transition from the bulk to nanoscale regime. The nano scale PbS is also characterized by direct and indirect band gaps. But probability of direct/indirect transitions is not equivalent. In case of bulk PbS, the optical transitions are characterized by direct transition and rest of the transitions are indirect transitions. This is also evident in the lattice vibrational mode of phonon spectrum.

Let us consider a diatomic lattice in one dimension where the vibrational frequency is given by

$$\omega^2 = f\left(\frac{1}{m} + \frac{1}{M}\right) \pm f\left[\left(\frac{1}{m} + \frac{1}{M}\right)^2 - \frac{4 \sin^2 qa}{Mm}\right]^{1/2}$$

where ω is the frequency of vibration m , M are the masses of the particles and a is lattice constant and q is the wave vector [14].

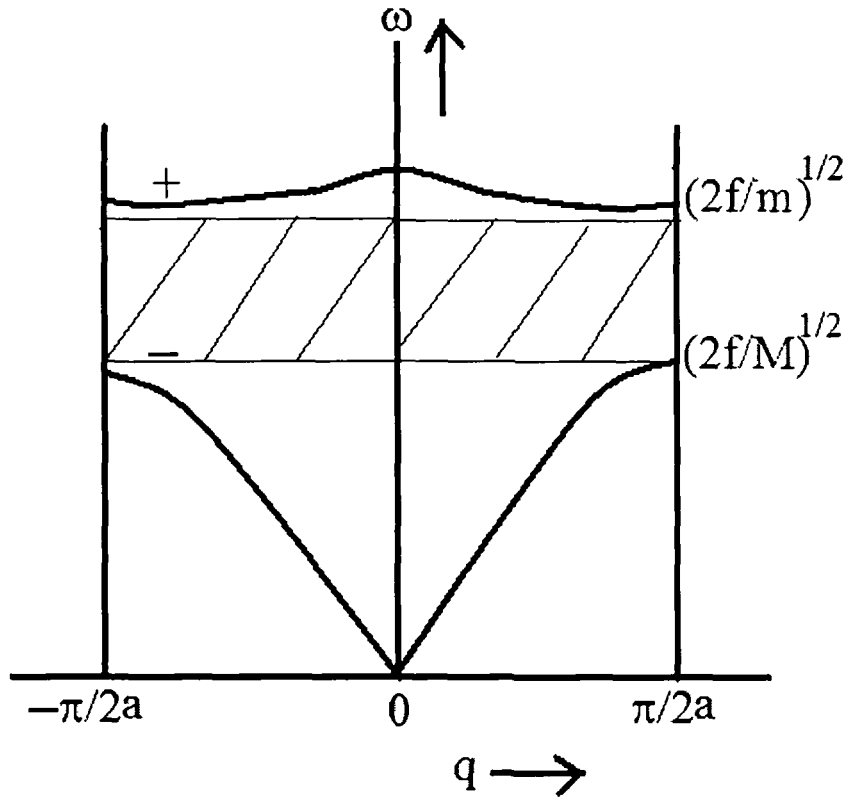


Fig2 9 Vibrational Mode

The two frequencies are described as optical branch and acoustic branch. In this aspect one can remark upon interlinking the absorption of electromagnetic radiation with the dispersion relation exhibited by such diatomic ionic crystal. These crystals absorb strongly in infra-red (IR) region of the spectrum corresponding to the frequency ($\nu \approx 10^{13}$ Hz). It is clear that IR radiation is absorbed near the center of the Brillouin zone that corresponds to the optical branch at $q \approx 0$. The IR absorption corresponds to a vibration of the positive ion lattice relative to the negative ion lattice in a way such that the center of gravity in each of the unit cell remains at rest. The IR absorption substantiates direct transition. The corresponding time period of the transition is $\tau_{bulk} \approx 10^{-13}$ s.

Conversely, in PbS nanocrystals, the time scale $\tau_{nano} \approx 10^{-12}$ s as observed experimentally [15]. This infers that the application of the Frank-Condon principle will be limited. This is illustrated in Fig2.10

According to the Franck-Condon principle, all optical transitions are direct transitions which correspond to the direct band gap and indirect band gap corresponds to all those

transitions which are non optical. The invalidity of the Franck Condon principle in case of nanocrystal is known as Nonadiabaticity [16]. Obeying of the Franck-Condon principle of optical transition is an adiabatic process where phonon should not take part in transition.

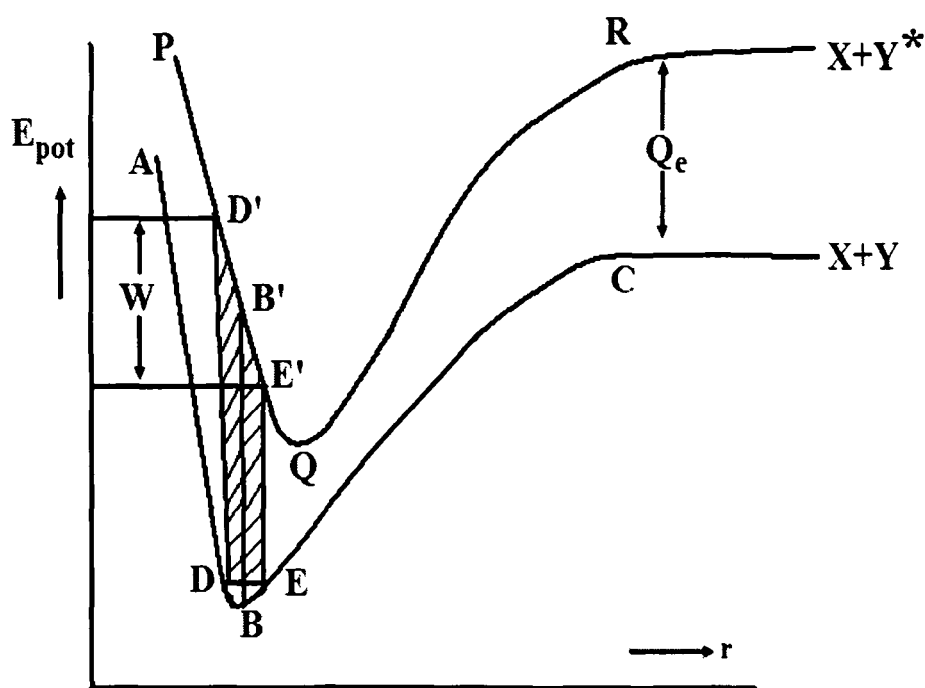


Fig 2 10 Illustration of franck-Condon Principle

But phonon assisted transition takes place in case of nanocrystal where, low energy phonons contribute in optical transition occurring through scattering events. Since Franck-Condon principle is not applicable in case of nanocrystal therefore simultaneous validity of IR absorption of frequency of 10^{13} Hz and subsequent time period of the order of 10^{-12} s is also feasible in case of PbS.

2.4. Conclusion

The results obtained for a 10a sized monovalent copper and divalent PbS nanocrystals are that the energy bandwidths bear an inverse dependence on the nanocrystal size. The numerical fits show clearly that the energy bandwidth decreases exponentially with the increase of nanocrystal size.

Thus, it is seen that the enhancement of band width in nanocrystals in general and PbS in particular can be well accommodated on the concepts of the Kronig-Penney, Free Electron and the LCAO models. Along with this the novel band gap nature of PbS is also understood to some extent.

References

- [1] R. de. L. Kronig, W. G. Penney, *Proc. Roy. Soc. (London)*, **499**(1930)499
- [2] H. M. Rosenberg, *Low temperature solid state physics*, Oxford, (1963)
- [3] N. F. Mott H. Jones, *The Theory of the properties of Metals and Alloys*,
Dover: oxford University Press (1958) 65
- [4] wikipedia.org/wiki/Gold
- [5] www.infoplease.com/periodictable
- [6] S. Kaci, A. Keffous, M. Trairi, O. Fellahi, H. Menari, A. Manseri,
L. Guerbous, *Journal of Luminescence*, **130**(2010) 1849
- [7] C. Kittel, *Introduction to Solid State Physics*, Wiley, Eastern University
Edition (1989)
- [8] J. C. Slater, *Phys. Rev.* **45**(1934) 794
- [9] A. J. Dekker, *Solid State Physics*, Macmillan(2006)
- [10] A. J. Nozik, F. Williams , *J. Phys. Chem.* **89** (1985) 397
- [11] L. I. Sciff , *Quantum Mechanics* (New York: Mc Graw- Hill) (1955)85
- [12] S. V. Nair, L. M. Ramaniah, K. C. Rustagi, *Phys. Rev. B.* **45**(1992)5969
- [13] [http://en.wikipedia.org/wiki/Lead\(II\)_sulfide](http://en.wikipedia.org/wiki/Lead(II)_sulfide)
- [14] <http://en.wikipedia.org/wiki/Phonon>
- [15] R. J. Ellingson, M. C. Beard, J. C. Johnson, P. Yu, O. I. Micic, A. J. Noizk,
A. Shabaev, A. L. Efros, *Nano letters*, **5**(2005)865
- [16] M. Bissiri, M. Capizzi, V. M. Fomin, V. N. Gladilin, J. T. Devreese,
Phys. Stat. Sol. (b) **224** (2001) 639

CHAPTER 3

Synthesis Protocol: Materials and Methods

In this chapter, various synthesis protocols and fabrication techniques of PbS quantum dots, PbS homogeneous coupled quantum dots, heterogeneous PbS/TiO₂ coupled quantum dots, and nanomaterial filled swift heavy ion (SHI) induced ion tracks have been discussed.

The selection of a matrix in nanocrystal growth is imperative in the way of process of synthesis of semiconductor quantum dots [1]. Its cage like structure and thermal stability furnishing the ability to assemble in ordered structure and provides an optimal environment for nanocrystal growth. Generally, the matrix includes various inorganic matrix such as glass matrix, zeolite etc. and organic matrix mainly of polymers. The size-dependent absorption in quantum dots is well understood, but very little is known concerning the equally important surface effects which control the electron-hole recombination in these semiconductor nanocrystallites for which surface states can be meaningfully defined. However, since many interesting effects occur at non ideal surfaces, it is important to understand the processes occurring at these interfaces. It is to be noted that the surface chemistry changes with the effect of surface capping, surface coating and surface passivation.

Polymer matrix: Polymers are made of organization of chain like structures which offers a porous configuration. The pore size and distribution is controlled during its synthesis process namely *polymerization* [2]. In general, there are two types of polymers as per the nature of its constituent chains that is predominantly responsible for exhibiting rigidity. The arrangement of branched chain is flexible and rest of all are rigid. PbS quantum dots are prepared using both rigid polymer such as polyvinyl alcohol (PVOH) and flexible matrix such as styrene butadiene rubber (SBR) latex.

3.1 Properties of Polyvinyl Alcohol Matrix (PVOH):

Polyvinyl Alcohol (PVOH) is a water soluble polymer [3]. It is produced by hydrolysis of polyvinylacetate. Polymerization of vinyl acetate monomer provides polyvinylacetate. PVOH shows crystalline nature. PVOH is widely used as adhesive,

ceramic binder and as stabilizer in emulsion. It has also got some uses in cosmetics, textile wrap sizing, paper sizing agent, civil engineering, pharmaceutical and electronic industries. Polyvinyl alcohol was also used previously as phosphorylated-polyvinyl alcohol (PPVA) which is a mechanically stable matrix [4]. PVOH films are also used for incorporation of gold nanorods with well defined aspect ratio [5]. On the other hand, PVOH films were doped with PbSe/PbS core-shell structures in another similar process. CdS nanoparticles embedded in PVOH matrix is also used as a nanocomposite. Also, PVOH was used as a capping agent in the synthesis of TiO₂ matrix.

Some of the physical parameters of PVOH are listed in the table3.1.

Physical properties	
Glass transition temperature (° K)	343
Melting temperature (° K)	483
Refractive index	1.55
Specific heat (J/gm K)	1.66
Thermal conductivity (W m ⁻¹ K ⁻¹)	2.0
Molar mass of single structure unit(g)	58.2
Dielectric constant	2.0
Specific gravity(gmcm ⁻³)	1.30

Table3.1 physical properties of PVOH

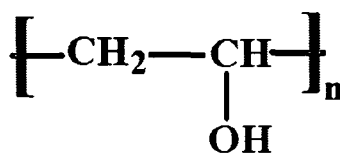


Fig 3.1: Structural representation of PVOH

3.2 Properties of carboxylated styrene butadiene (SBR) rubber latex

SBR is a synthetic rubber and it is a co-polymer of butadiene and styrene. They are made by the free radical polymerization in an emulsion system using redox initiators such as hydrogen peroxide and ferrous sulphate. The resultant copolymers usually contain 80% of 1,3 (cis and trans) and 20% of 1,2 and 3,4 repeat units [6]. Some physical properties of SBR latex is listed in the table3.2. CdS quantum dots were fabricated in SBR latex previously [7]. The grain growth in this after ion irradiation is also examined by our group previously.

Physical properties SBR	
Glass transition temperature ($^{\circ}$ K)	211
Melting temperature ($^{\circ}$ K)	273
Refractive index	1.53
Specific heat (J/gm K)	1.89
Thermal conductivity ($W m^{-1}K^{-1}$)	1.34
Molar mass of single structure unit(g)	221.6
Dielectric constant	3.1
Specific gravity	1.30

Table3.2: Physical properties of SBR latex

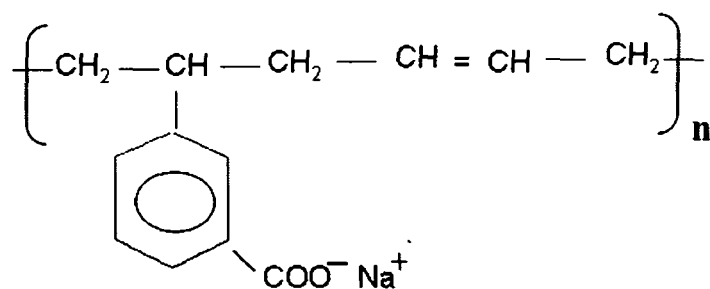


Fig.3.2 Structural representation of SBR

3.3 Properties of Polyvinyl pyrrolidone (PVP)

PVP is a water soluble functional co-polymer made from the monomer of N-vinylpyrrolidone. It is used as a binder in many pharmaceutical tablets. It is also used as a coating in inkjet printers and as coating in inkjet paper to enhance the photo quality. PVP is also used in shampoos and toothpastes. It has got some other use in contact lens solution and steel quenching solution. In the synthesis method PVP of average molecular weight 36,000 is used. It is classified in the class of conducting polymer and shows conducting behaviour [8]. Previously PVP capped CdS quantum dots dispersed in PVOH matrix was explored [9]. Enhanced optical properties were also observed in PVP surface modified ZnO quantum dots [10]. Certain regulation in electron dynamics was also observed quantum well heterostructures having surface modification with PVP [11].

Physical properties	
Glass transition temperature ($^{\circ}$ K)	106-175
Melting temperature ($^{\circ}$ K)	110-180
Specific heat (J/gm K)	1.66
Specific gravity(gmcm^{-3})	1.20

Table3 3 Physical properties of PVP

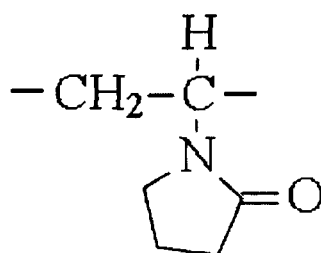


Fig3.3: Structural representation of PVP

3.4 Physical properties of PbS

PbS is an ionic crystal. It has got an acute tendency to get oxidised. Lead sulphide is insoluble in water. Though lead compounds are hazardous lead sulphide is considered relatively less toxic among of them.

Physical properties	
Melting temperature ($^{\circ}$ K)	1392
Refractive index	3.91
Specific heat (J/gm K)	1.89
Thermal conductivity ($\text{W m}^{-1}\text{K}^{-1}$)	2.76
Molecular weight	239.28
Dielectric constant	17.3
Specific gravity	7.6

Table3 4 Physical properties of PbS

3.5.1 Synthesis of PbS quantum dots in PVOH matrix

Preparation of PVOH matrix: 5% PVOH solution is used as a matrix to encapsulate PbS quantum dots. For this 5 gm of polyvinyl alcohol (Loba Mol. Wt. 80,000) is added to 100 ml of doubled distilled water and allowed to stir for 2 hours with the help of a magnetic stirrer while maintaining a temperature of 70°C until the solution becomes transparent.

* At first 0.01M PbCl_2 solution is prepared in distilled water. Then this solution is added to PVOH matrix in the ratio 1:2 and kept under stirring condition in a hot water bath of 80°C and at a stirring rate $\sim 200\text{rpm}$. Meanwhile, 0.01M Na_2S (sodium sulphide) solution is freshly prepared for sulphur treatment. After an hour the previous solution is acidified by addition of few drops of normally dilute nitric acid (HNO_3) to it and Na_2S solution is injected drop wise with the help of a syringe till the solutions turns dark brown keeping the stirring rate and temperature constant.

The quality of synthesized quantum dots was optimised by changing the pH of the medium from acidic, neutral to basic. Na_2S solution of different concentration was used if it led to some changes in the nature of PbS quantum dots. Best quality quantum dots were found in case of Na_2S where its concentration was kept equal with concentration of PbCl_2 used. The amount of Na_2S also affects the property of the PbS quantum dots. Use of very small amount of Na_2S manifest small size of quantum dots but they are less stable because those quantum dots are more easily get oxidised in a small interval of time. Although abundant use of Na_2S produces slightly bigger size of quantum dots yet these are found to be quite stable against the surrounding environment.

Preparation of acetonitrile surface passivated quantum dots

Acetonitrile is an organic solvent having a lone pair of electrons which forms a dative bond to the lead ions at the nanoparticle surface [12]. The effect of the bond strength to the nano particle surface can be ascertained by comparing the properties of the sulphur and nitrogen-bonded samples. In a dark atmosphere 0.1M PbCl_2 solution was added to a PVOH matrix in a matrix-to-aqueous PbCl_2 volume ratio of 2:1, followed by vigorous stirring (~200 rpm) for 2 hours. Then drop wise injection of Na_2S in acidic medium was allowed till the precursor turned faint brown.

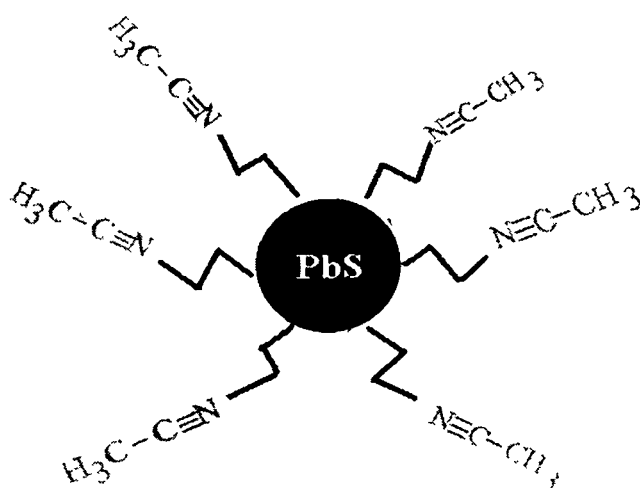


Fig3.4: Scheme of acetonitrile treated PbS nanoparticle

During the reaction, GR-grade acetonitrile was added to the above solution simultaneously. The molar ratio of Na₂S and acetonitrile is kept equal. It is stirred for another 3 hours at a moderate temperature. It is basic the strategy of nanoparticle synthesis where a large number of nucleation centres can be created. In this way, the PbS nanocrystals were encapsulated in a water soluble dielectric media (PVOH) while effective surface passivation was achieved by treatment with acetonitrile.

Fabrication of Mn²⁺ incorporated PbS quantum dots in PVOH matrix

The Mn²⁺ incorporation is also attempted to reduce the dangling bonds because Mn²⁺ accumulation at the surface produces MnO₂ layer which acts as surface passivating agent. For Mn²⁺ incorporation MnCl₂ solution is prepared in a concentration ratio (1:500, Mn²⁺:Pb²⁺). Next, 0.1M PbCl₂ solution was added to as prepared PVOH matrix in a matrix-to- aqueous PbCl₂ volume ratio of 1:1, followed by vigorous stirring (~200 rpm) for 2 hours. Then drop wise injection of Na₂S in acidic medium was allowed till the precursor turned faint brown. The quenching method is employed to incorporate Mn²⁺. For this purpose the solution is kept in an ice cold environment and 1M MnCl₂ solution is injected slowly with the help of a syringe. PbS quantum dots are obtained in PVOH dispersion which is kept overnight in an dark chamber for stabilization.

3.5.2 Fabrication of PVP coated PbS quantum dots

0.1M PbCl₂ solution is prepared in distilled water. 10% PVP solution is prepared by dissolving 10gm of PVP in methanol and kept on stirring condition for 10 minutes. PbCl₂ solution is added in a ratio 1:1 to PVP solution under stirring for another 1 hour at a temperature of 60⁰C. 0.1M aqueous Na₂S was injected drop wise followed by heating to dry at a temperature of 120⁰C. PVOH solution (2% w/v) is prepared and as prepared PbS quantum dots are added to the solution. In this way, PbS quantum dots coated with PVP dispersed in PVOH matrix is obtained.

The films of PbS quantum dots dispersed in PVOH matrix were casted on glass substrate. Glass substrates were cleaned at first with chromic acid then with

ethanol/acetone. The solid films of different thickness were received. Thick films were made by drowning one coat of PbS quantum dots over glass substrates and also with dip coating method. Thin films were received through spin coating at medium rpm. The thickness of the films was ranges from 30µm to 200µm.

3.5.3 Fabrication of PbS quantum dots in SBR matrix

The carboxylated SBR latex (99% pure, Synthomer, Germany) was selected as matrix to encapsulate the PbS quantum dots. We have also tried another brand of SBR latex which is a product of (Apcotex Ltd). Typical characteristics of latex are given in Table3.5. We have decided to specifically work in this medium as it provides a flexible polymer system which could accommodate nanoparticles and help in establishing better size dispersity.

Appearance	Milky white pour able liquid
Emulsifying system	Synthetic anionic
Percentage of total solids	50.0 ± 1.0
pH at 25°C	8.5 ± 0.5
Brookfield viscosity Lvf (CPS) SP.1, 12 rpm at 25°C	50 Max
Surface Tension (Dynes/cm) at 25°C	45.0 ± 3.0
Film characteristics	Hazy and slightly tacky
Compatibility	Good compatibility with pigments, co-Binders.
Particle Size (micron)	0.18

Table3 5 Physicochemical properties of SBR latex used in this synthesis

One coat of SBR latex was drawn over a laboratory glass substrate and left for drying up to 24 hours. Next, as received SBR thick films were washed in double distilled water and dipped into 0.1M PbCl₂ solution up to 1 hour. Finally, the films containing Pb⁺⁺

were treated with H₂S (prepared by Na₂S solution in an acidic medium). Thus, PbS quantum dots are grown in flexible SBR latex matrix.

3.5.4 Fabrication of PbS coupled quantum dots in SBR matrix

0.05 M PbCl₂ solution was prepared in an ice cold dark chamber. As received SBR was diluted up to 70% by volume (in a ratio 1:10) and correspondingly an aqueous solution containing Pb⁺⁺ was injected in a drop wise manner. These precursors were kept for 16 hours at moderate stirring (~250rpm) in a sealed container followed by sulphide gas diffusion. Diffusion gas uptake has direct control on the dimension of quality PbS quantum dot pairs. An ice cold temperature and a neutral medium (pH = 7.0) is maintained throughout the process. Note that as Pb⁺⁺ ions have been incorporated into selective amounts of carboxylated SBR in a neutral medium under magnetically stirring environment, Pb⁺⁺ ions would interact with the energetic carbon chains of SBR latex. Since carboxylated SBR contains –COONa functional groups in each of its structural units, the divalent Pb⁺⁺ ions can easily displace two Na⁺ ions. This is, in fact, energetically favourable and therefore, increases the chances of Pb⁺⁺ to attach with the two ligands of the same or different carbon chains (Fig3.5, Fig3.6). In this situation, Pb⁺⁺ gets attached to both the ligands with a weak bonding similar to van der Waal type.

Under ambient conditions, when the sulfide gas was diffused (in N₂ atmosphere), the weak van der Waal bonds break and Pb⁺⁺ ions would capture incoming S²⁻ ions, forming PbS quantum dots. The formation of PbS quantum dots was instantaneous and is governed by the destruction of the weak coordination with –COO....., which in turn forms –COO(H) as a result of H⁺ ion uptake from the sulphide gas. In other words, formation of PbS quantum dots is accompanied by participation of two carboxyl groups of SBR.

As far as two body systems is concerned, coupling is possible due to one or more mechanisms: (i) two bodies must be oppositely charged or polarized by external fields (ii) carrier (electron) transport occurs between the two entities and (iii) electron-electron attraction via virtual phonon exchange. Normally, the first case is applicable in electrostatics, where as the third condition is relevant for Bardeen-Cooper-Schrieffer type of superconductors. In our case, we speculate the second mechanism is

energetically favourable resulting *D*(donor)-*A*(acceptor) combination. Polymers have serpent like cage structures and can be moulded while subjected to thermal, pressure and electric fields. In our case, SBR polymer which exists in *cis-trans* geometric isomers is capable of accommodating PbS quantum dots in an efficient way.

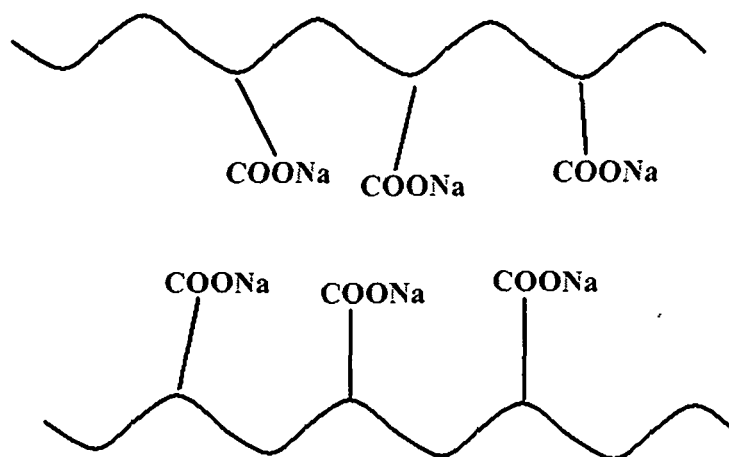


Fig.3.5: Typical example of SBR chain sites for accommodating Pb²⁺

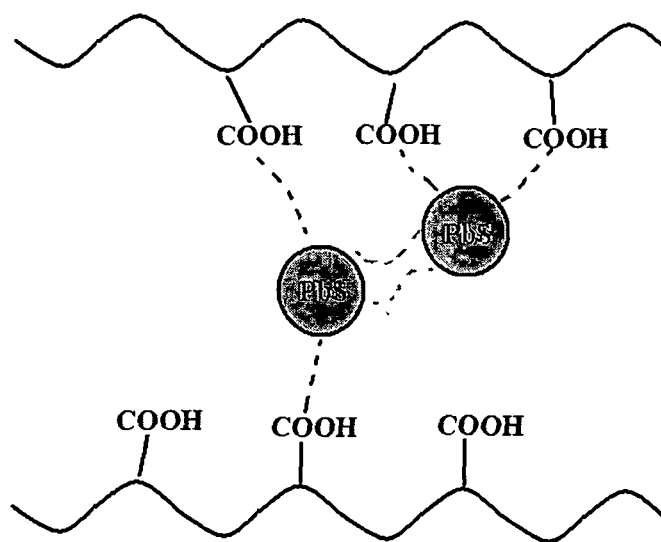


Fig3 6: Upon sulfide gas uptake, formation of PbS quantum dots and mutual interaction

3.6 Fabrication of PbS/TiO₂ coupled quantum dot system

Sol-gel technique

It is a wet chemical process where an integrated network of typically metal oxides is fabricated through hydrolysis and condensation reaction of metal alkoxide and metal chloride precursors in alcohol medium. First sols of metal oxide are obtained initially as a sol and it can be further converted to gel if required. (Battisha et al 2002 ;) used this solgel technique to synthesis SiO₂ nanoclustets. This fabrication technique is quite popular in the synthesis nanoporous TiO₂ and the nano particles received are always in the form of aggregates. In this form metal oxides are generally amorphous and necessary heat treatments such as sintering is employed to obtain it in crystalline form. Occasionally, the synthesized metal oxides are also found in crystalline forms.

Titanium dioxide (TiO₂)

TiO₂ is a wide band gap semiconductor having a direct band gap of 3.2eV [13]. It is found in three forms: anatase, rutile and brookite [14]. These three forms of TiO₂ can be obtained by varying synthesis condition of the same sol gel fabrication technique. TiO₂ has a porous structure and the porosity changes with its change in different factors and due to the porous structure it has got large specific surface area that can be suitably controlled during synthesis process [15]. The large specific area of nanostructured TiO₂ can have direct relevance in photocatalytic activity, sensitized solar cell etc. [16]. Its pores can also be used in controlled growth of other nanoparticles [17]. The mesoporous TiO₂ is not only suitable for controlled growth of other materials but also useful for understanding several interfacial properties including growth kinetics and charge leakage events. Such phenomena are particularly important when a narrow band gap material is grown into the pores of a wide band gap system. In fact, a large number of oxygen vacancies are expected in TiO₂ network leading to creation of many surface states [18]. The surface states of TiO₂ act as trapping and recombination sites which could influence directly on its electrical and optical properties [19]. Physical properties of TiO₂ are tabled in Table 3.5.

Physical properties of TiO ₂	
Melting temperature (° K)	1843
Refractive index	2.488(anatase)
	2.609(rutile)
Specific heat (J/gm K)	13-15
Thermal conductivity (W m ⁻¹ K ⁻¹)	11.7
Molecular weight	79.9
Dielectric constant	85
Specific gravity	3.84(anatase)
	4.26(rutile)

Table3.6: Physical properties of TiO₂

Fabrication of nanoporous TiO₂

Considering a method reported by William et al. [20], stable titania nanopowders were synthesized via hydrolysis of commercially available titanium isopropoxide [Ti{OCH(CH₃)₂}₄] without further purification in alcohol medium followed by rapid condensation. The hydrolysis was carried out by transferring 6ml of titanium isopropoxide into 15ml of propanol-2 in a ratio (1: 3) kept in a conical flask. Keeping the mixture on a water bath at moderate temperature (~70 °C), this mixture was magnetically stirred (~250 rpm) for 12 hours with the drop wise injection of D/D water with the help of a micro syringe in a interval of 5 minutes. It is to be noted that the amount of water should not be more than 5ml. Finally, TiO₂ was received and it was kept in a dark chamber overnight for stable growth of TiO₂ nanocolloids. As prepared TiO₂ sols were washed with ethanol by employing sonication three times, to remove remaining unreacted species. Next, Nanostructured TiO₂ films were casted by dip coating as well as by spin coating. These sols are amorphous in nature. Crystalline phase can be achieved employing different procedures. In another method, as-received sol was drawn on 1x1cm² laboratory glass substrates followed by natural drying. In spin coating method, a very small rpm of 200 is optimised for best quality film. Abrupt heat treatment (~200°C) was carried out on these films to remove unwanted species and to

achieve perfect anatase crystalline phase. The crystalline phase can also be obtained after for a period of two months of the as-prepared amorphous sol. Although in the chemical synthesis of TiO₂ using surfactant is a widespread process [21] because of the assurance of effective size control and prevention of agglomeration but this trendy process has several shortcomings. Removal of surfactant from outer surface of TiO₂ nano particles is a prolonged practice but in this synthesis stable TiO₂ nanostructure network with effective size control is achieved avoiding use of surfactant.

TiO₂ gels were also obtained by changing the synthesis procedure slightly. In this case nanoporous TiO₂ network was developed from colloidal TiO₂ as follows: 15 ml of titanium isopropoxide[Ti{OCH(CH₃)₂}₄] was taken in a conical flask containing 25 ml of propanol-2. By adding drop wise injection of dilute nitric acid the *pH* was reduced to 1. The mixture was stirred with the help of a magnetic stirrer for 6 to 8 hours at a temperature of 60⁰C and medium stirring rate until colloid phase was achieved. On receiving the colloid phase the temperature was increased along with changing the stirring rate to a higher side. Viscous gel of TiO₂ was formed and it was drawn over laboratory glass slides to make solid films. The films were subjected to different heat treatments for drying. Few films were dried at room temperature and then subsequently annealed and few of them were dried at a higher temperature by maintaining at temperature of 400⁰C.

Incorporation of PbS in nanoporous TiO₂

Concentrated Pb⁺⁺ solution was prepared using PbCl₂ precursor of concentration 1M, by dissolving it in doubled distilled water. TiO₂ films were dipped in this solution for 5 to 10 minutes. Pb⁺⁺ ions were supposed to enter into the pores of TiO₂ and get attached to the surfaces of TiO₂. PbS quantum dots were obtained by S²⁻ treatment. For this 0.01M Na₂S solution was prepared using distilled water as a solvent. TiO₂ films containing Pb⁺⁺ ions were again dipped into the freshly prepared Na₂S solution. Thus PbS quantum dots developed after reduction of Pb⁺⁺ by active S²⁻ ions in the pores having diameter in the nanoscale regime. The concentration of PbCl₂ was varied to receive optimal Pb⁺⁺ ion uptake. In a different way, nanoporous TiO₂ films were dipped in 0.01M PbCl₂ solution for 12 hours and then H₂S treatment was done in an acidic medium. PbS/TiO₂ coupled quantum dot systems were obtained through these approaches.

3.7 Synthesis of nanomaterial filled swift heavy ion induced ion tracks:

In recent years, there has been growing interest in swift heavy ion track technology for novel applications, e.g. building nanoscale electronic devices. Track-etched membranes offer distinct advantages over conventional membranes due to the flexibility of designing precisely defined structures. Their pore size, shape and density can be varied in controlled manner so that a membrane with the required transport and retention characteristics can be reproduced. In this work PVOH films are chosen for suitable pore creation and filling with nanomaterial. Ion irradiation in polymers facilitates significant microscopic changes in the irradiated layer. This is associated with the change in density correlated to polymers where free volume could led to transformation of physical and chemical properties. Two basic changes in surface properties occur due to chain scission and cross linking which affect mechanical strength and hardness of the polymers [22].

In an ion radiation process, certain material is bombarded with energetic swift heavy ions. The interaction between SHI and bulk materials leads to specific effects due to huge amounts of energy being deposited on the target electrons by incident ions. The stopping power $(dE/dx)_e$ gives the energy transfer per path length of a particle along its trajectory. This energy loss of the energetic ions during the passage through a material is quantitatively governed by the ion mass and energy. It can lose energy either by elastic collisions (due to nuclear stopping) or by in-elastic collisions (due to electronic stopping). It also depends upon the fluence (no. of ions per unit area) used and type of ion species. The total stopping power is the sum of both components. Its reciprocal integral defines the projectile's total range and projectile range of energetic ions is calculated with help of SRIM (Stopping and range of Ions in Matter), which is a Monte Carlo simulation programme [23]. Chain scissioning occurs along the trajectory as a result of amorphized zone is created which is called latent track. It has got a special importance because chain scissioning enhances the etchability of the polymers. When these damaged zones of such polymers are treated with an etchant then irradiated polymer foil leads to the formation of ultra small micropores called "etched tracks". The latent track formation in polymers can be explained with the help of two models '*Thermal Spike*' [24] and the other is '*Coulomb Explosion*' model [25].

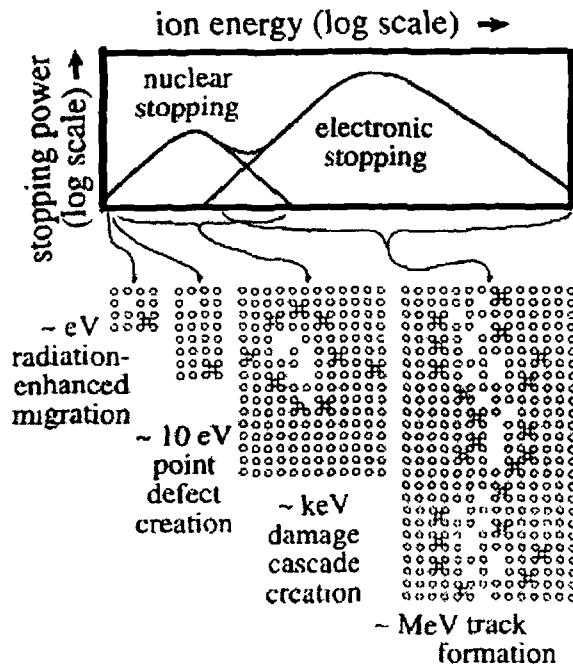


Fig.3.7: Schematic representation of track formation

According to *Thermal spike* model, during the passage of energetic ions, the electrons of the solid are ejected due to inelastic collision induced electronic excitation. In this way, induced excitation is transmitted to the lattice via electron-phonon interaction. Hence the temperature of the local lattice increases enough and this is sufficient to attain the melting point of the material. Because of the unique path of the ion trajectory this heating effect occurs in controlled manner. This interaction persists for an infinitesimal fraction of time which is followed by rapid lowering of temperature (10^3-10^4 K/s). This quenching effect results in an amorphous linear zone namely latent track along the ion trajectory.

While swift heavy ion passes through the material, the electrons belong to the host material also try to follow its path. As a consequence nearby positive target ions are produced resulting induced ionization. These positive ions are mutually repulsive. Subsequently a displacement occurs from their original position as a result of creation of an electrostatically unstable array of adjacent ions which eject one another from their normal sites to interstitial positions. Though it is followed by relaxation due to elastic strain but time interval is larger than the response time of the conduction electrons. The

Coulomb repulsive force within the ionized region is sufficient to overcome the lattice bonding forces. Therefore during the passage of the energetic ion a long cylinder containing charged ions is produced. This cylinder containing the charged ions explodes radially as result of conversion of electrostatic energy to coherent radial atomic movements under Coulomb forces. This explosion remains until ions are screened by conduction electrons. This radial Coulomb explosion results a cylindrical shock wave along the trajectory of the swift ion and due to which a comparatively unstable cylindrical structure is produced known as latent tracks. Since the response of the conduction electron is very quick in case of conductors and relatively slow in insulators therefore tracks are observed only in case of insulators and never in conductors.

Each ion passing through the material is capable of producing an ion track of several dia. This has got importance because by choosing the appropriate ion fluences one can select the number of tracks desired for the porous membrane that can act as a template. Pore creation from the latent tracks is usually done with the help of chemical etching. In this case the chemical composition of the etchant and temperature of the etching bath is chosen carefully. There are two parameters which determine the shape and size of the pore: v_b the bulk etch rate (etching rate for non-irradiated material) and v_t the track etch rate (the etching rate along the ion track) [26]. In case of selective etching conditions $v_t \gg v_b$ i.e. the shape of the pores can be approximated to a cylinder. Typically, a composition of NaOH and methanol is generally used as a good quality etchant. Here, NaOH plays the role of main etchant where as methanol in the etching solution improves the qualities (smoothness of the pore wall) by the way of enhancing bulk etch rates.

In this experiment PVOH films are chosen for fabricating template embedding PbS quantum dots. Ion irradiation experiment was carried out in IUAC, New Delhi. Silicon ion of energy 100 MeV was selected for the irradiation of the samples. The electronic energy loss of the projectile ion should be high with respect to the thickness of the film in this energy range. Since, the thickness of the polymer films are $30\mu\text{m}$ therefore the projected range of the ions was ensured to cross it. A very low fluence was explored to obtain minimum number of ion tracks. This low fluence is controlled with help of gold foil scattering experiment. In this experiment eight sets of fluences such as $(1 \times 10^5,$

2.5×10^5 , 5×10^5 , 7.5×10^5 , 1×10^6 , 2.5×10^6 , 5×10^6 , and 7.5×10^6 ions/cm²) to optimise the appropriate number of latent tracks.

Irradiated PVOH films were then prepared for etching. The concentration of NaOH was employed as *1N* and *2N* respectively along with that addition of a small amount of methanol. The time interval for etching and temperature variation was also investigated during the experiment. The temperatures were chosen as 50°C and room temperature. For this purpose irradiated films were dipped in a solution of NaOH and methanol for two minutes and five minutes respectively. There is no pore observed in case of etchant concentration of *1N* and time interval of two minutes. Pores were apparently visible only after the etching time has increased to five minutes. In case of using etchant concentration of *2N*; the pores were also created for an etching time interval of two minutes. The better pore quality in terms of smoothness can be obtained in case low etching rate only and also it was realized in this fabrication procedure. PVOH films were washed properly with doubled distilled water immediately after the etching and, creation of the pores of in the nanoscale regime has also been accomplished. As received etched PVOH films were then employed for filling with nanomaterials.

0.01M PbCl₂ solution was prepared and etched films were dipped in this solution for eight hours for complete uptake of Pb⁺⁺. This was followed by subsequent washing for removal of extra Pb⁺⁺ ions which were attached to the surfaces of PVOH films. Aqueous Na₂S solution (concentration 0.01M) was prepared and then acidified with addition of few drops of nitric acid and PVOH films containing Pb⁺⁺ ions were dipped in this solution for one hour. Etched pores were expected to get by filled with PbS molecular adsorption.

Pore filling phenomena in these very small pores occurs as a result of capillary condensation and along with chemical adsorption and diffusion of Pb⁺⁺ and S²⁻ ions. The etched track structures possess unique capillary characteristics [27]. Capillary forces furnish significant forces in the liquid film which led to the spreading of Pb⁺⁺ solution over the surface of etched tracks. The surface of PVOH is also energetic enough to capture the Pb⁺⁺ ions. Again, evaporation of water takes place due to relative pressure gradient but Pb⁺⁺ remained attached to the surface of PVOH. Next, while these films

containing Pb^{++} experiences H_2S treatment S^{2-} diffuses through the pores naturally and react with Pb^{++} and to form PbS molecular structures .

3.8 Preparation of PbS quantum dots with micro emulsion (Reverse micelle) technique

Micro emulsion is a stable mixture of oil, water and surfactant where two immiscible phases (water and 'oil') exists in such a way that the surfactant molecules may form a monolayer at the interface between oil and water, with the hydrophobic tails of the surfactant molecules dissolved in the oil phase and the hydrophilic head groups in the aqueous phase. Micelles are aggregates of surfactant molecule surrounded by hydrophilic head region of the solvent medium. On the other hand reverse micelles are discrete nanoscale region of water core surrounded by the surfactants. Micelles or reverse micelles form only when the concentration of surfactant is greater than the critical micelle concentration (CMC), and the temperature of the system is greater than the critical micelle temperature, or *Krafft* temperature [28]. The amount of water can be manipulated to directly affect the size of the water pool and it depends on the molar ratio of water to surfactant ratio w . Generally, w is preferred in the range of 1 to 10 [29].

In this synthesis process, reverse micelles are used as templates to disperse PbS quantum dots. Reverse micelles are dynamic and which results some sort of attractive interactions between droplets. These attractive interactions led to the higher inter miceller potential and whole system becomes unstable. The stability of the system could be retained either by decreasing the number of carbon atoms of the bulk solvent or by increasing the number of droplets.

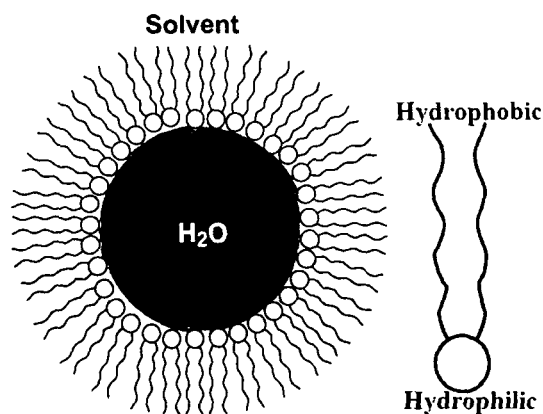


Fig 3 8 Schematic representation of the micelle and two ends of surfactant molecule

Particular types of depletion forces exist substantially between two micelles and accordingly solvent molecules show discrete nature. Water droplets exchange their water contents while they are in contact forming a dimer. This exchange process is associated with the interface rigidity, which corresponds to the bending elastic modulus of the interface. Hence, in collisions the droplets exchange water contents by driving off their solvent and they again form two independent droplets. This strategy is employed to produce water droplets holding PbS quantum dots through arrested precipitation.

One 20ml reverse micellar micro emulsion was prepared using sodium dioctyl sulfosuccinate (AOT; Molecular weight 444.45gm, Sigma Alrich) as a surfactant n-heptane(Merk Chemical) as a solvent. The concentration of AOT was taken as 0.2M ensuring CMC limit. The amount of water can be added for $w = 10$ using the modified formulae $w = v(H_2O) \times d(H_2O) / M(H_2O) / W(AOT) / M(AOT)$, where v is the volume of water, d is the density of water, M refers to molecular weights of AOT and water W is weight of AOT used in this microemulsion and the total volume of the precursor was found out to be equal to 0.07ml[30]. The micro emulsion of AOT and n-heptane was divided into two parts of amount 10 ml. 0.01M PbCl₂ and 0.01M Na₂S solutions were prepared in distilled water separately. Note that, the total amount of water content should not exceed 0.07ml therefore 0.035ml of PbCl₂ and 0.035ml of Na₂S solution was added to each 10 ml microemulsion of AOT and n-heptane with the help of a micro pipette. After that the two microemulsions were added and kept under stirring condition for one hour. The water droplets are in a state of continuous motion favouring mass

transport for growth PbS by exchanging the water content, where microemulsion containing Pb^{++} and S^{2-} got interchanged and meanwhile Pb^{++} reacts with S^{2-} to form PbS quantum dots. As received PbS quantum dots remain inside these micelles.

PbS quantum dots have been synthesized by adopting various fabrication protocols. Various parameters affecting the quality such as temperature, impurities of the surrounding environment were also given attention in the best possible way. The PbS quantum dots prepared in PVOH matrix offer many opportunities to arrive at varied range of properties like wide range of emission spectrum, chain like organization, incorporation of new element etc. PbS quantum dots prepared in SBR matrix are more stable against agglomeration and oxidation as compared to those prepared in PVOH. Moreover, it provides an ambient atmosphere for coupling of PbS quantum dots. TiO_2 is also a stable matrix but incorporation of PbS inside the mesopores appear tricky. The PbS/ TiO_2 however, offers some additional advantages (better performance in electron transport) over individual performances of PbS or TiO_2 while exploring the electrical properties of semiconductor quantum dots. The PbS quantum dots prepared through microemulsion route is not only stable but offers a better size control. PbS quantum dots prepared through filling the ion tracks produced by SHI irradiation is very much stable but the size of these quantum dots are comparatively larger than the PbS quantum dots fabricated through other processes.

In this chapter, various synthesis protocols of semiconductor quantum dots and semiconductor coupled quantum dots are presented. The explored methodology has been shown that the quality semiconductor quantum dots and coupled quantum dots could be efficiently grown through these simple and less expensive procedures.

References

- [1] S. Wo, L-H Han, S. Chen, *Nanotechnology*, **20** (2009) 285392
- [2] R. J. Young, *Introduction to Polymers*, Chapman & Hall (1987)
- [3] C. Bastioli , ISmithers Rapra Publishing(2005)
- [4] A. Ying, U. Toshiyuki, S. Masahiro, K. Toshiki, H. Kenji, S. Hirofusa ,
Polymer, **37**(1996) 3097
- [5] F. Ratto , P. Matteini, F. Rossi, R. Peni Proc. SPIE, **7**(2010) 7577
- [6] D. Mohanta, *Ph D. Thesis*, Tezpur University, 2004
- [7] D. Mohanta, N. C. Mishra, A. Choudhury *Optical Materials* **58** (2004) 3694
- [8] F. F. Hatta, M. Z. A. Yahya, A. M. M. Ali, R. H. Y. Subban, M. K. Harun,
A. A. Mohamad , *Ionics* , **11**(2005) 418
- [9] M. Pattbai, B. Saraswathi Amma, K. Manzoor, *Materials Research Bulletin*,
42 (2007) 828
- [10] C. L. Yang, J. N. Wanga, W. K. Ge , L. Guo, S. H. Yang D. Z. Shen,
Journal of Applied Physics **90**(2001) 4489
- [11] A. W. Schill, M. A. El-Sayed, *J. Phys. Chem. B*, **108**(2004)13619
- [12] S. A. Majetich, A. C. Carter, *J. Phys. Chem.*, **97** (1993) 8727
- [13] J. Moser, S. Punchihewa, P. P. Infelta, M. Gratzel, *Langmuir*, **7** (1991)3012
- [14] S. Mahshid, M. Askari, M. S. Ghamsari, *International Journal of Nanotechnology*,
6 (2009) 961
- [15] T. Miki, K. Nishizawa, E. Watanabe, H. Taoda, *Research on Chemical
Intermediates*, **35** (2009) 257
- [16] Y. Wang, S. Zhang, X. Wu, *Nanotechnology*, **15** (2004)1162
- [17] J. Bisquert, A. Zaban, P. Salvador, *J. Phys. Chem. B*, **106**(2002) 8774
- [18] D. Bahnemann, A. Henglein, J. Lilie, L. Spanhel, *J. Phys. Chem.* **88** (1984) 709
- [19] B-R Hyun, Y-W Zhong, A. C. Bartnik. , L. Sun, H. D. Abrun , F. W. Wise,
D. Jason, Goodreau, J. R. Matthews, T. M. Leslie, N. F. Borrelli, *ACS Nano*,
2 (2008) 2206
- [20] W. E. Stallings, H. Henry Lamb, *Langmuir*, **19** (2003) 2989
- [21] X. Guang-jian, Y. Wang, *Journal of Beijing Universtry of Technology*,
30 (2004) 1239
- [22] Y. K. Vijay, *Indian Journal of Physics* **83**(2009)927
- [23] www.srim.org

- [24] S. Dhamodaran, A.P. Pathak, A. Dunlop, G. Jaskierowicz, S. Della Negra
Nuclear Instruments and Methods Physics Research B, **256** (2007)229
- [25] R. L. Fleischer, P. B. Price, R. M. Walker, *Nuclear tracks in Solids. principles
and Applications*, University of California Press (1975)
- [26] I. Enculescu, *Digest Journal of Nanomaterials and Biostructures*. **1** (2006) 15
- [27] M. C. Porter, *Handbook of industrial membrane technology*,
William Andrew Publishing (1990)
- [28] B. K. Parekh, J.D. Miller , *Advances in flotation technology*, SME(1999)
- [29] C. Petit, P. Lixon, M-P Pileni *J. Phys. Chem.*, **97** (1993) 12974
- [30] I. Chakraborty, S. P. Moulik, *Journal of Nanoparticle Research*, **7** (2005) 237

CHAPTER 4

Characterizations of synthesized quantum dots

In this chapter, various characterization techniques and characterization details are discussed elaborately. For characterizing size, structure and composition of synthesized products, we used various analytical techniques such as Transmission electron microscopy (TEM), Scanning electron microscopy (SEM), Atomic force microscopy (AFM), X-Ray diffraction (XRD) and Energy dispersive X-Ray analysis (EDS). Also, *photoluminescence characteristics of synthesized PbS quantum dots are presented towards the end of the chapter.*

4.1 Electron microscopy analysis

4.1.1 Scanning electron microscopy (SEM)

It is a class of electron microscope which images the surface of a particular sample by scanning it with a high-energy electron beam and signals coming out of the sample are patterned through a raster scan[1]. The signals are produced by the interaction of electrons with the surface atoms that contain information about the sample's surface topography, composition and other properties such as electrical conductivity. Scanning electron microscope of model name (JEOL, Model 6390 LV) was used to for necessary investigation.

4.1.1.1: SEM analysis of SHI induced etched ion tracks

Fig4.1 shows the SEM image of the etched ion tracks. The typical development of pores can be evident from the images. Fig4.1 (A) infers enlarged view of such pore which predicts the conical shape of the pores. On the other hand the arrangement of such pores is depicted in Fig4.1. (B) and Fig4.1(C). The size of the pores ranges from 15 to 25nm. The SEM was followed over several times to ensure the optimum etching parameters and to receive smallest pores. We speculate that though pores of size in the range ~ 10 nm are existed, due to limitation of the instrument that could not be visualized.

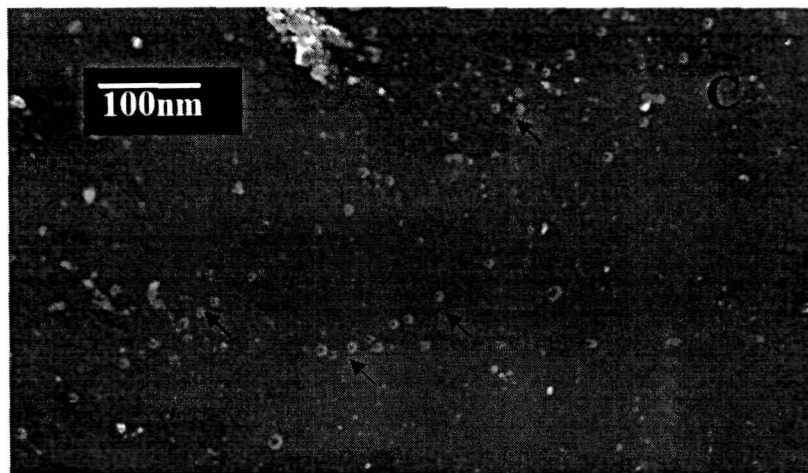
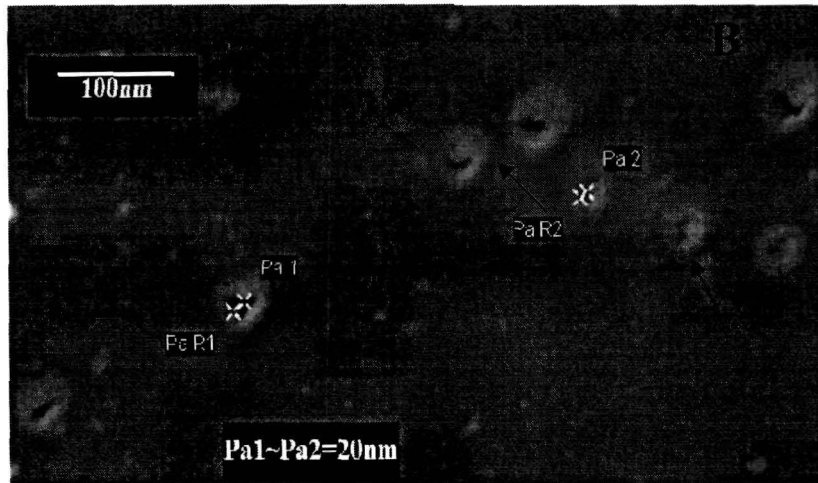
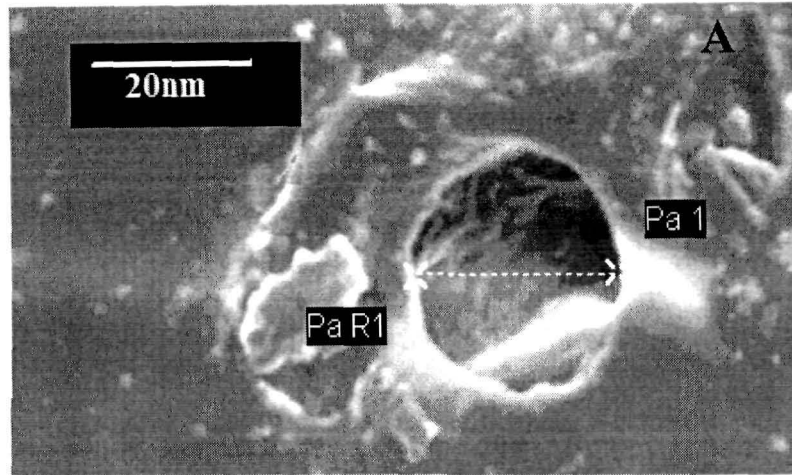


Fig.4.1: SEM image of etched track

4.1.1.2: SEM analysis of TiO₂ and PbS/TiO₂

Fig.4.2 (B) and Fig.4.2 (C) show selective area SEM images of TiO₂ and PbS/TiO₂. As-synthesized TiO₂ is amorphous in nature and contains a few particles therefore; the instrument was unable to resolve the separation of the grains distinctly [Fig.4.2 (A)]. On the other hand, as shown [Fig.4.2 (B, C)], plenty of voids and gaps between TiO₂ nanograins were observable upon heat treatment. The development of clear microstructured grains with heat treatment can be distinguished.



Fig.4.2 (A): SEM of as-prepared TiO₂

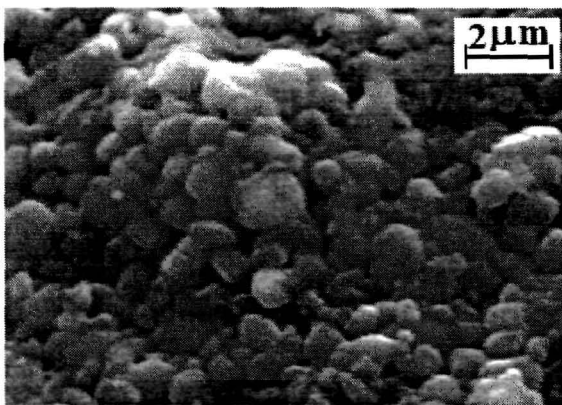


Fig.4.2 (B): SEM image anatase TiO₂

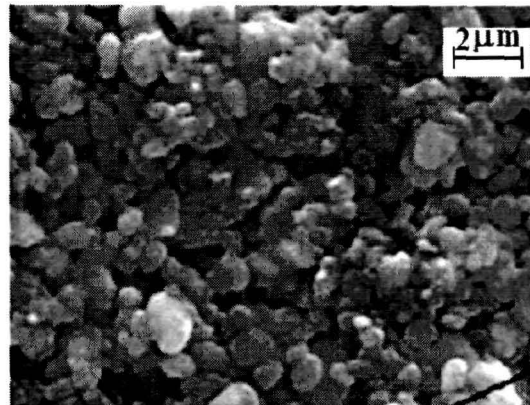


Fig.4.2 (C): SEM image anatase TiO₂

In contrast, relatively compact nanograins are seen in case of PbS adsorbed TiO₂ system [Fig4.2(D)]. The compactness in the later system is expected to have arisen owing to the growth of PbS nanoparticles within the pores as well as along the interfaces separating the TiO₂ grains. Average size of grains varies from a few nanometer to several hundreds of nm. Each of the grains is consisting of many ultra small particles that are not resolved in SEM micrographs.

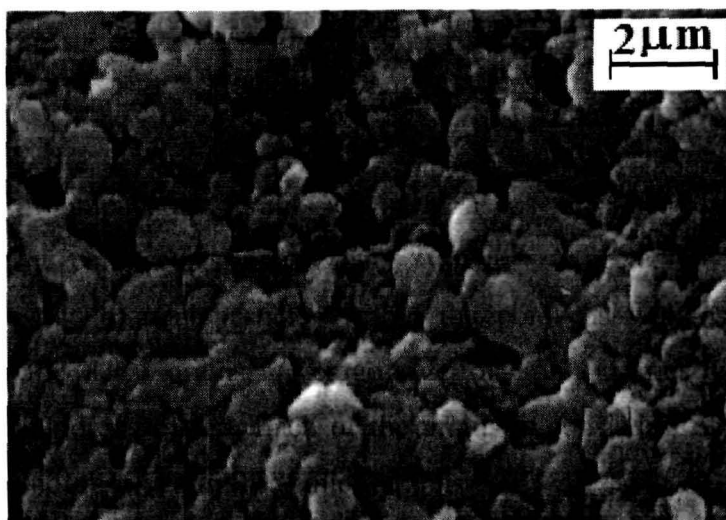


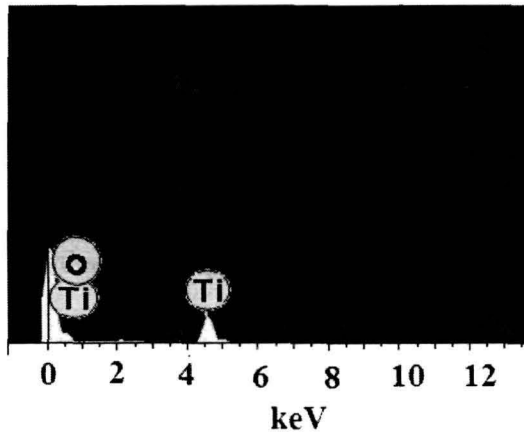
Fig.4.2 (D) SEM image of PbS/anatase TiO₂

4.1.2 Energy dispersive X-ray analysis (EDS)

EDS is a technique used to identify the elemental composition of a sample or small area of interest on the sample. EDS is associated with a scanning electron microscope (SEM) and sample is exposed to an electron beam in this process. These electrons collide with the electrons within the sample, causing some of them to be knocked out of their orbits. The vacated positions are filled by higher energy electrons which emit x-rays in the process. The elemental composition of the concerned sample can be determined by analyzing the emitted x-rays [2].

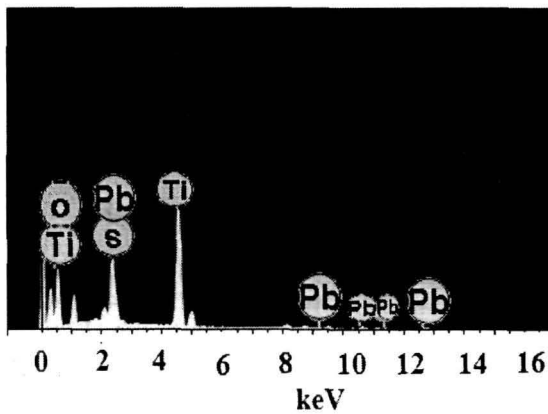
4.1.2.1: EDS of TiO_2 and PbS/TiO_2

In order to verify further, we took energy dispersive x-ray (EDS) measurements which are depicted in Fig.4.3(A) and Fig.4.3(B). EDS spectrum of TiO_2 shows signals emanating from titanium and oxygen atoms present in TiO_2 . Absence of any other peaks corresponding to unwanted species indicates that our TiO_2 nanostructured network is of very high quality.



Element	Atomic%
O K	80.83
Ti K	19.17

Fig 4.3(A) EDS of TiO_2



Element	Atomic%
O K	80.69
S K	1.99
Ti K	14.85
Pb M	2.47

Fig: 4.3(B) EDS of PbS/TiO_2

In contrast, traces of signal due to Pb and S atoms are noticed in case of PbS/TiO_2 system. This validates further, formation of lead sulphide inside the nanopores of TiO_2 .

4.1.2.2: EDS analysis of PbS prepared through micro emulsion route

After observing a prominent interaction of PbS with microemulsion medium EDS analysis was also carried out to know the percentage of each component. The percentage of Na signifies the amount of the AOT since total amount of Pb^{++} and S^{--} is equal to the total amount Na.

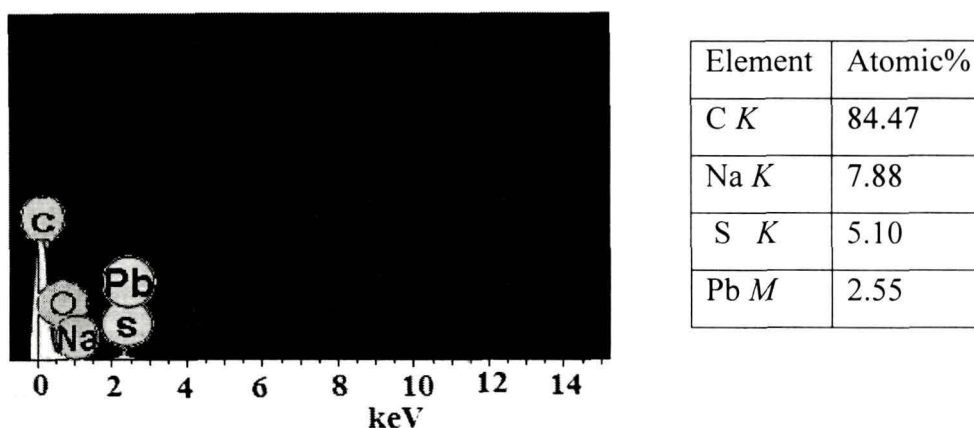


Fig.4.4: EDS of PbS quantum dots in micro emulsion medium of AOT and n-heptane

Hence, it indicates a strong interaction between the signals coming from the different energy state of PbS and AOT undergoes an interference state of affairs while subjected to the exposure of electron beam.

4.1.3 Atomic force microscopy (AFM) analysis

AFM is another very high resolution type of microscopy which can perform better than optical diffraction limit and can image in the nanometer scale. The surface morphology of a sample is obtained by gathering the information by "feeling" the surface with a mechanical probe. Piezoelectric elements that facilitate tiny but accurate and precise movements on (electronic) command enable the very precise scanning. The AFM can be operated in a number of modes, depending on the principle of application. In general,

possible imaging modes are divided into static (also called *contact*) modes and a variety of dynamic (*or non-contact*) modes where the cantilever is vibrated [3]. In the contact mode the static tip deflection is used as a feedback signal. Since measurement of a static signal is prone to noise and drift therefore low stiffness cantilevers are used to boost the deflection signal. The attractive forces can be quite strong close to the surface of the sample causing the tip to 'snap-in' to the surface. In non contact mode, the tip of the cantilever does not contact the sample surface. The van der Waals forces can be strongest from 1 nm to 10 nm just above the surface, or any other long range force which extends above the surface acts to decrease the resonance frequency of the cantilever. To avoid noise, cantilever is allowed to oscillate at a frequency slightly above its resonance frequency where the amplitude of oscillation is typically a few nanometers (<10 nm).

4.1.3.1 Surface morphology of TiO₂ and PbS/ TiO₂

Surface morphology of TiO₂ and PbS/TiO₂ systems are characterized by noncontact AFM measurements and are presented in Fig.4.5 (A) and Fig.4.5(B), respectively. Well organized and uniform structures are noticed for untreated TiO₂ network [Fig.4.5 (A)]. Such distributed structures indicate presence of independent grains in the system. Bigger clusters would correspond to the aggregation of small TiO₂ nanoparticles which is thermodynamically favourable.

In contrary, AFM micrograph as shown in Fig.4.5(B) exhibits relatively uniform surface due to filling up of TiO₂ void spaces by PbS molecules. Note that AFM could provide better contrast in case of independent grains but unable to resolve them if the interfaces are occupied by the surface adsorbed PbS molecules.

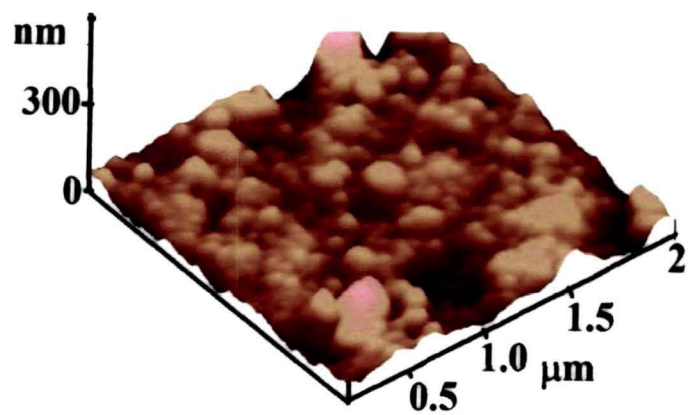


Fig.4.5 (A) AFM image of TiO₂

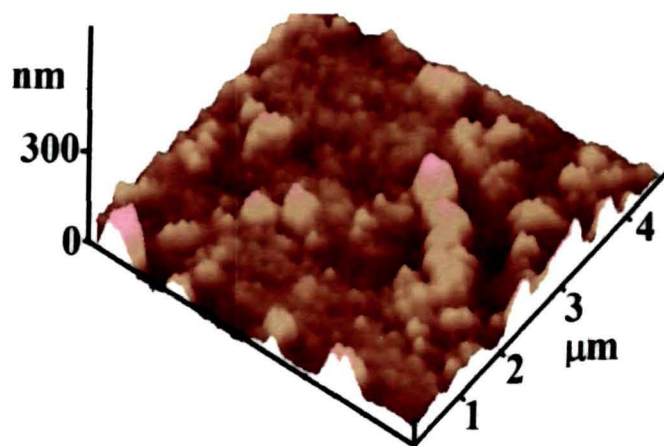


Fig.4.5 (B) AFM image of PbS /TiO₂

4.1.3.2 Surface morphology of PbS quantum dots and PbS coupled quantum dots in SBR latex

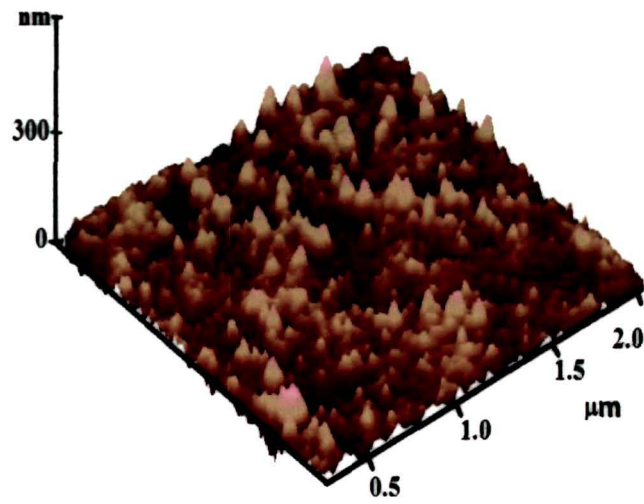


Fig.4.6 (A) AFM images of PbS quantum dots

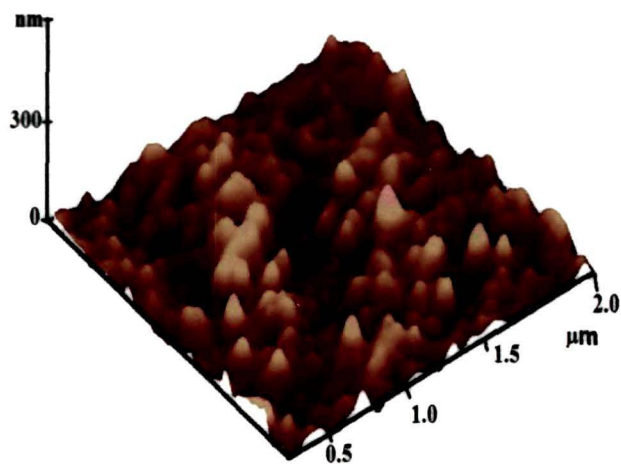


Fig. 4.6(B) AFM images of PbS coupled quantum dots

Fig4.6(A) and Fig4.6(B) show the AFM images of PbS quantum dots and PbS coupled quantum dots in SBR latex, respectively. AFM image of isolated quantum dots exhibits comparatively compact and uniform size distribution representing non-aggregation of individual grains with efficient resolution and is consistent with the TEM micrograph.

On the other hand, AFM image of PbS coupled quantum dots reveal a well organized array. The separation between the interfaces infers the dispersity of the coupled quantum dots being relatively low.

4.1.4 Transmission electron microscopy (TEM) analysis

In this technique a beam of electrons is transmitted through an ultra thin specimen and it is allowed to interact with the specimen as it passes through. An image is received from the interaction of the electrons transmitted through the specimen and the image is magnified and focused onto an imaging device, such as a fluorescent screen, on a layer of photographic film, or to be detected by a sensor such as a CCD camera. It is the chief characterization tool in the nano scale regime [4].

The specimen was first allowed to experience sonication for 20 minutes to 1 hour to get it prepared for TEM measurements. TEM analysis of PbS quantum dots in PVOH matrix: The TEM image of freshly prepared PbS quantum dots dispersed in PVOH matrix are shown in Fig4.7 (A). The average size of the PbS quantum dots is found to be 3-5nm. The PbS quantum dots are almost spherical in shape isolated from one another. The TEM micrographs clearly assert uniform and relatively sparse distribution PbS quantum dots in PVOH matrix.

4.1.4.1: TEM analysis of PbS quantum dots in PVOH matrix

TEM analysis is also explored to study the ageing effect of PbS quantum dots.[Fig.4.7] (B) shows the TEM image of PbS quantum dots dispersed in PVOH matrix after one year. The samples were preserved at (-20⁰C) in deep refrigerator. The sample bottles were wrapped with black paper to avoid exposure of light. It also reflects a good quality image as they retain their stability after such a long period of time. Hence,

PVOH provides efficient encapsulation to overcome agglomeration. Although the dispersion gets dense over this long period which led to an intense distribution of PbS quantum dots in PVOH matrix uniform size distribution persisted. The size of the quantum dots has slightly increased 5-10 nm as result of Ostwald's ripening [5] since there was no additional coating.

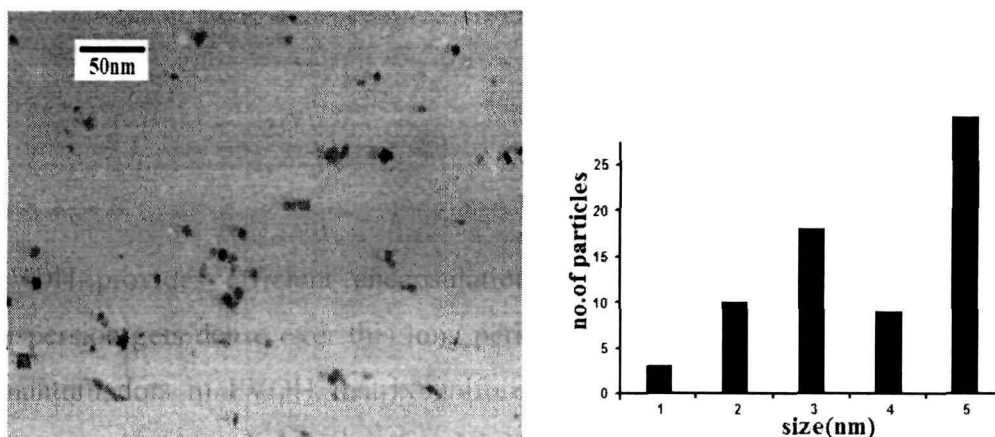


Fig.4.7(A): TEM image of PbS quantum dots in PVOH and Size distribution

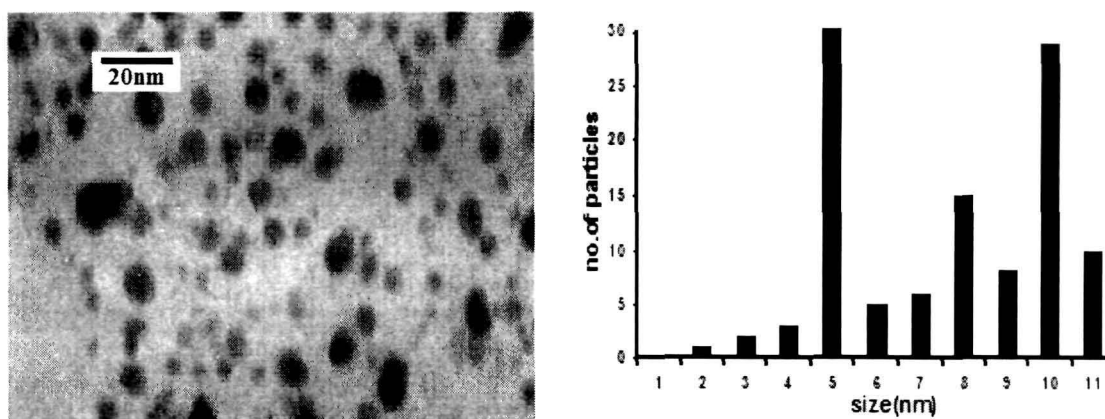


Fig.4.7(B): TEM image of PbS quantum dots in PVOH and size distribution(after aging)

4.1.4.2: TEM analysis of PbS quantum dots with acetonitrile surface passivation

The transmission electron micrograph of synthesized PbS nanoparticles is shown in Fig.4.8. It ensures the formation of quasi-spherical nanoparticles of average size ~ 5

nm, a narrow size distribution and dispersion of $4.3 \times 10^{11}/\text{cm}^2$. The particles are found to be in unclustered form and are in isolation from each other. The faint dark impressions are believed to be image contrast of the nanoparticles spreading on the underneath planes. Occasional instances of chain like arrangements have also been noticed that are shown by arrow marks. Formations of such organized arrays are assigned to the interparticle interaction owing to the unequal charge distribution resulting a strong dipole-dipole interaction for particles of varied sizes [6]. In addition, acetonitrile could have been strongly adsorbed on to the nanoparticle surface through its lone pair electron on the nitrogen which has resulted in dominant surface passivation compared to dissolution [7].

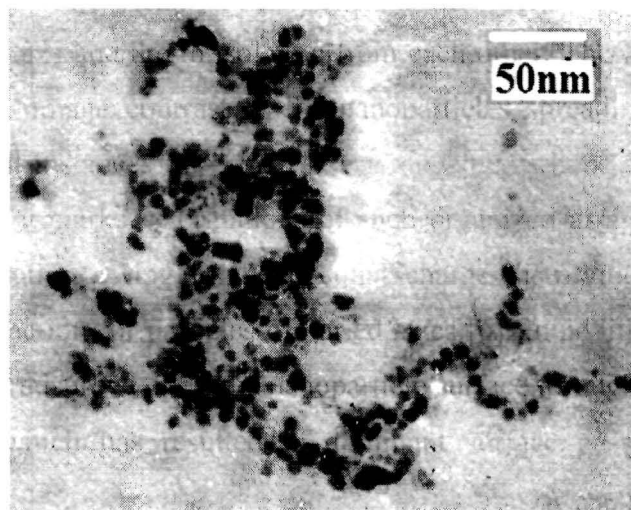


Fig.4.8: TEM image of PbS nanoparticles dispersed in the polymer host with acetonitrile treatment

Note that, we have not observed chain-like patterns in case of nanoparticle synthesis without acetonitrile treatment Fig.4.7 (A). It is known that acetonitrile is a polar, water soluble and weakly reactive compound which is extensively employed as a displaceable ligand [8]. The nanoparticle surface containing dangling or unsaturated bonds can be passivated efficiently in view of the presence of lone pair of electrons located at the N-site of the acetonitrile. PbS quantum dot pairing as a result of charge manifestation events has been reported by our group only recently [9].

4.1.4.3: TEM analysis of PbS quantum dots with Mn²⁺ incorporation

Formation of quasi-spherical PbS quantum dots with size distribution 5-10 nm is revealed from the TEM micrographs as represented in Fig.4.9 and Fig.4.9 (B).

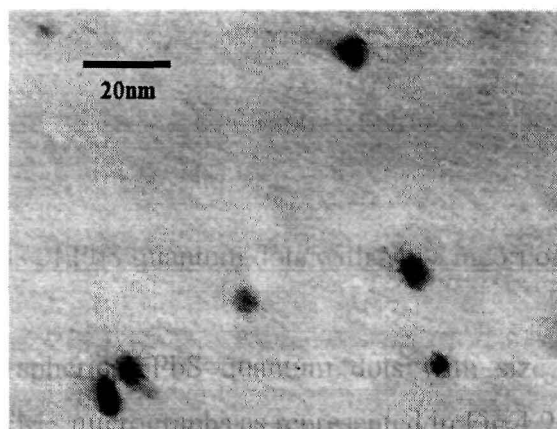


Fig.4.9 (A): TEM image of PbS nanoparticles with Mn²⁺ incorporation dispersed in the polymer host

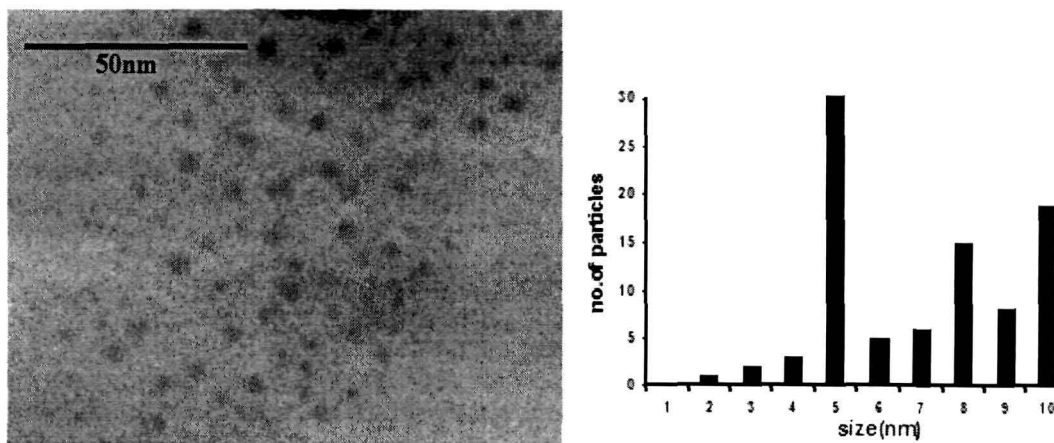


Fig. 4.9 (B): TEM image of PbS nanoparticles with Mn²⁺ incorporation dispersed in the polymer host after the aging of one year and size distribution

A small amount of increase in size is noticed while investigating the aging effect on PbS quantum dots in PVOH after the inclusion Mn²⁺. The facet statistics of rocksalt crystal

structure PbS is not compatible with incorporation of Mn^{2+} inside its lattice [10] Therefore Mn^{2+} incorporation is expected to furnish surface passivation by forming a layer of MnO_2 and protects Ostwald ripening. Therefore, in this case the increase of size is attributed as Kelvin effect. According to this effect, the small nanoparticles get evaporated to form bigger nanoparticle so as to minimize their potential energy [11].

4.1.4.4: TEM analysis of PbS quantum dots coated with polyvinyl pyrrolidone (PVP)

Fig.4.10 (A) refers the TEM image of PbS quantum dots with effective PVP coating dispersed in PVOH matrix. The size distribution ranges 1-3nm. A scanty distribution of PbS quantum dots is observed.

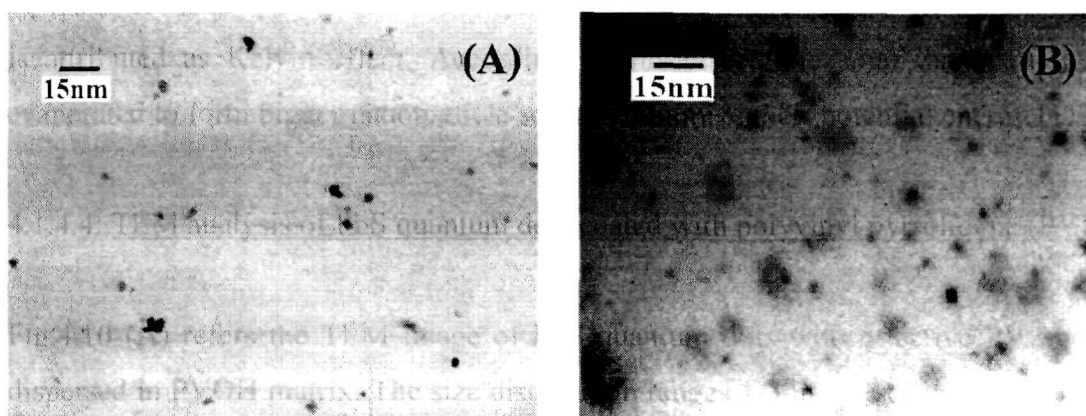


Fig.4.10 (A) TEM image of PbS quantum dots in PVOH matrix with effective PVP coating (B) TEM image of PbS dots in PVOH matrix with effective PVP coating after aging of one year.

Fig.4.10 (B) refers the TEM image of PbS quantum dots with effective PVP coating dispersed in PVOH matrix after the aging of one year. The appealing characteristic of PVP coating is that it prevents Ostwald ripening efficiently. The size of the PbS quantum dots remain almost same even after a year has passed.

4.1.4.5: TEM analysis of PbS quantum dots in SBR (styrene butadiene rubber) latex

The TEM micrographs, shown in Fig.4.11 indicate formation of PbS quantum dots with a size regime of 5-10 nm. They are spherical in size and isolated from each other. The reasonable amount of inhomogeneity seen in the size distribution could be due to nonuniform incorporation of Pb^{++} into SBR coatings. The advantage is unclusteredness thus providing a system to study the individual quantum dots. In case of nanostructured films, grain boundary effect is a serious problem [12].

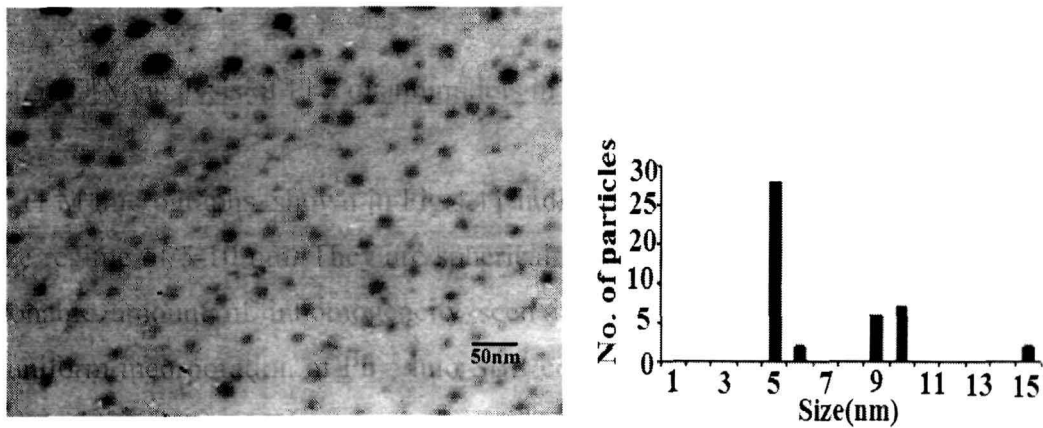


Fig.4.11: TEM micrograph of PbS quantum dots with size distribution in SBR

4.1.4.6: TEM analysis of PbS coupled quantum dots in SBR (styrene butadiene rubber) latex

Fig.4.12 is a TEM image where we notice exactly identical and paired PbS quantum dots distributed over the host SBR matrix. It describes formation of quantum dots which are spherical, perfectly paired and highly oriented with fairly good size distribution ~15 nm (The strategy behind the formation of isolated as well coupled quantum dots in same matrix SBR is discussed in chapter (3) We believe that the development of coupled quantum dots in SBR is based on the principle of formation, pairing and orientation. The surface of the nanoparticles is very energetic. PbS quantum dots get attached to the polymer chain as it encapsulates the nanoparticles. Some sort of interaction similar through chemical adsorption takes place [13]. They interact mainly with carboxylated part of the polymer chain. In this interaction, electrons are supplied from the carbon

chains. Since the carbon chain breaks after vigorous stirring as result of that the smaller and bigger cages result. The number of electrons supplied from the carbon chain depends upon the length of the carbon chain. The nanoparticles which is get attached to the longer carbon chain receives more number of electrons than the nanoparticles which is attached to the smaller chain.

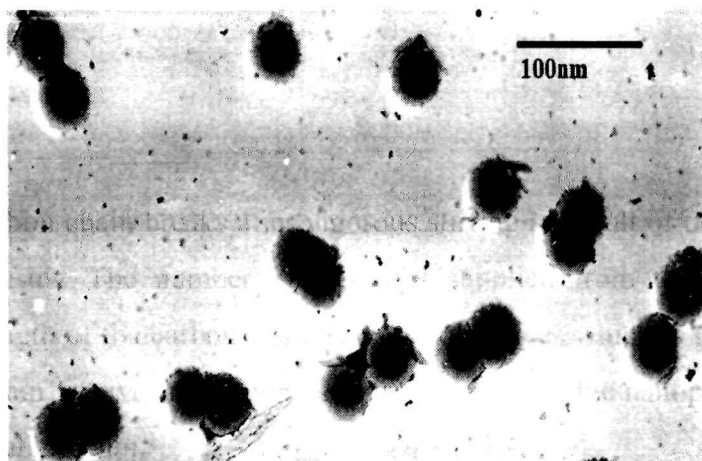


Fig.4.12: TEM image of coupled quantum dots grown in SBR

In fact, the formation of PbS quantum dots depends on the bond length, bond strength and bond angle of the C-C chains and $-\text{COONa}$ ligands. Knowing the typical bond lengths of C-H, C-C as 1.09 \AA and 1.37 \AA , respectively one can say that the region between the two ligands of different chains is more abundant than those of the same chains. Since, quantum dots have abundant trap centres and act as electron reservoir, its strength could be described by its capacitance C (charge holding capacity) which is proportional to its radius R , The number of electrons that can be accommodated would be more for the larger quantum dot than the quantum dots having smaller diameter [14]. In other words, PbS quantum dots with bigger dimension should accommodate more charges (electrons) than smaller ones. An electron density gradient occurs between two nearby PbS quantum dots, now, if the separation between the PbS quantum dots is close to their lattice parameter ($\sim 5.8 \text{ \AA}$) trapped electrons can escape easily from bigger dot to smaller one, through their interface until charge neutrality occurs, making PbS quantum dots absolutely paired. One of the reasons behind the observation of couples in case of PbS is due to relatively larger excitonic Bohr radius. Although the PbS quantum dots

come closer for pairing, clustering effect was not seen because of the established fact that the quantum dots repel each other [15], This repulsive interaction make these quantum dots isolated and unclustered while interfacial charge leakage promotes pairing. This is more effective when two dots experience size smaller than the bulk Bohr exciton size (strong confinement regime) and are separated by a distance close to the lattice parameter of the material. As the separation is tunable in a flexible media like SBR facilitates quantum dot pairing [Schematic diagrams of quantum dot pairing in SBR is shown in chapter3, Fig.3.5 and Fig.3.6]. It offers not only stability to the quantum dots assuming that it behaves as a permeable membrane to provide ambient atmosphere emulating charge leakage between the quantum dots. However, conditions would not facilitate from ideal pairing in samples such as CdS, CdSe and ZnS which have comparatively small bulk exciton Bohr radius (~ 5 nm). In the past we had attempted with CdS but obtained large sized dots with broad size distribution although the same strategy was employed in the synthesis [16]. Moreover, for the PbS system, the effective mass ($m_h = m_e \sim 0.2 m_0$) and carrier mobility ($\mu_h \sim 620$ cm²/V-s, $\mu_e \sim 610$ cm²/V-s) for the holes and the electrons are comparable and thus, capable of facilitating interfacial carrier transfer more efficiently until perfect pairing is achieved. Previously, interfacial charge transfer was observed by various groups in heterogeneous and coupled quantum dot networks [17, 18]. Since the quantum dots generated from the two ligands of opposite chains and those generated from the same chains are interacting along their closest approach, the pairing is believed to be highly directional owing to interfacial charge transport mechanism. We speculate therefore, electric polarization sets up due to interfacial charge transfer along their closest proximity and make these quantum dots oriented.

4.1.4.7: TEM study of PbS/TiO₂ coupled quantum dot system

The TEM of image of as synthesized amorphous TiO₂ is presented in Fig.4.13 (A). The individual TiO₂ grains are of size 5nm but they are aggregated to make connectivity to stay behind as xerogel. This xerogel nature is a consequence of solgel synthesis. The pores could not be distinguished due to the resolution limitation of the microscope.

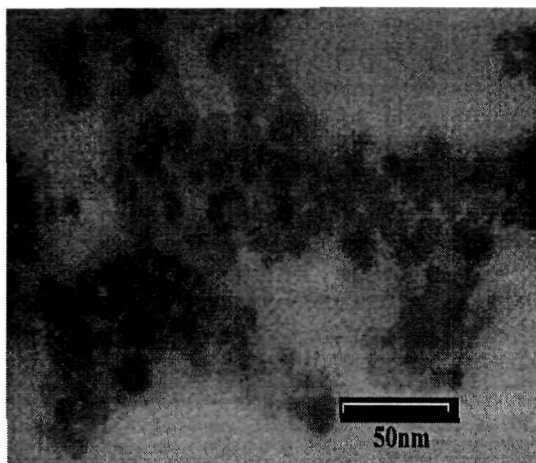


Fig4.13 (A) TEM of as-received TiO₂

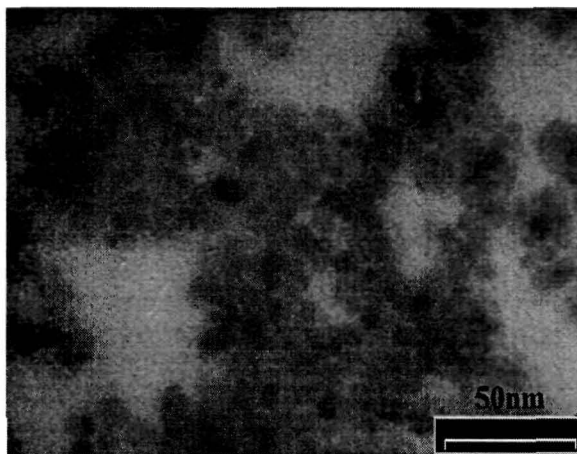


Fig4.13 (B) TEM of anatase TiO₂

The TEM image of anatase TiO₂ is presented in Fig4.13 (B) which was taken after the heat treatment as synthesised TiO₂.

On the other hand TEM of TiO₂ after the incorporation PbS is depicted by Fig.4.13 (A) and Fig.4.13 (B). But the image of PbS quantum dots which are entered in the pores of TiO₂ is not resolved in the micrograph. The grain size and distribution remained consistent after the incorporation of PbS also.

The TEM image of TiO₂ and sensitized with PbS after aging is shown in Fig.4.14 (A) and Fig4.14 (B) respectively. It was evident from the TEM images is that the rate of agglomeration in case TiO₂ over aging is more than PbS sensitized TiO₂. This observation infers that incorporation of PbS in the pores of TiO₂ contributed extra stability.

Fig.4.14(C) is the TEM image of properly sonicated PbS adsorbed TiO₂ xerogel. Selecting view on a particular grain and increasing magnification to 400KX we could resolve tiny PbS nanospheres sitting on the surface of the TiO₂ structure. The typical size of PbS particles was ~4nm.

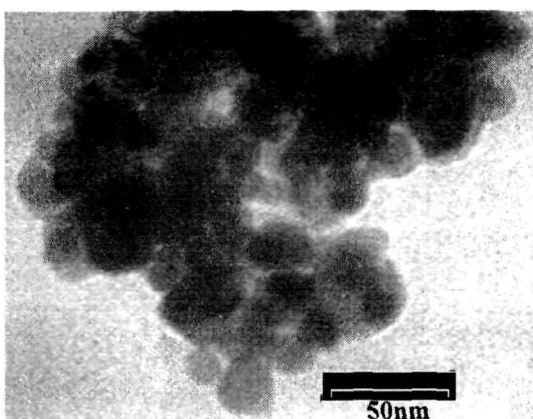


Fig.4.14 (A) TEM of as anatase TiO₂ after aging

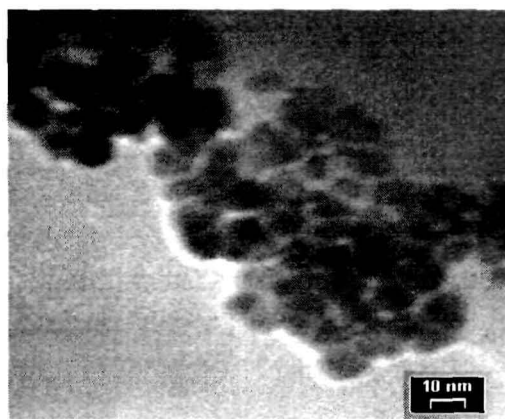


Fig.4.14 (B) TEM of PbS/ anatase TiO₂ after aging

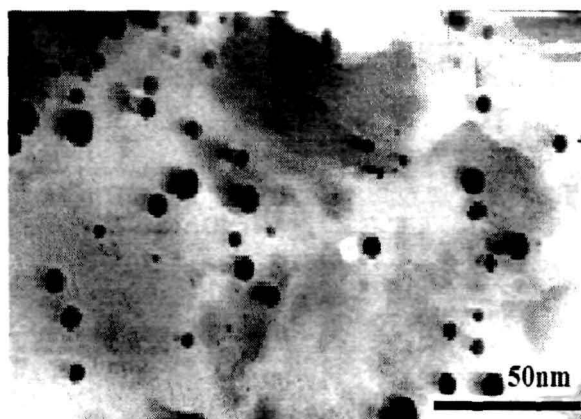


Fig.4.14(C) TEM of as anatase PbS quantum dots in TiO₂

4.1.4.8: TEM study of PbS quantum dots prepared through microemulsion route

TEM image of as synthesized PbS quantum dots and one year old PbS quantum dots is shown in the Fig.4.15 (A) and Fig.4.15 (B) respectively. It manifests the development of PbS quantum dot of with desired size, homogeneity and monodispersity. PbS quantum dots of size ~5nm are found to be well organized in the emulsion medium.

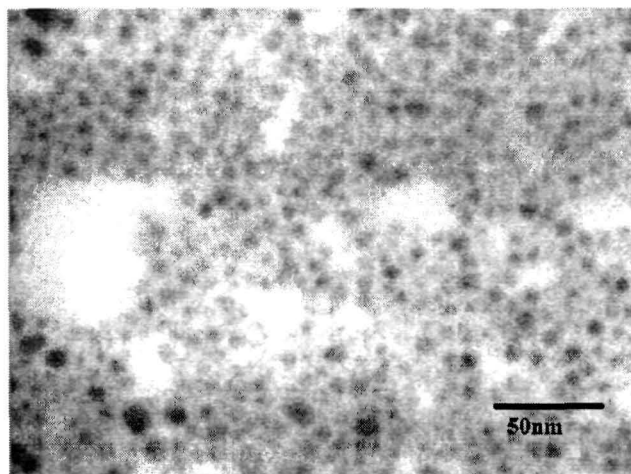


Fig4.15 (A) TEM image of PbS quantum dots in microemulsion of AOT and n-heptane

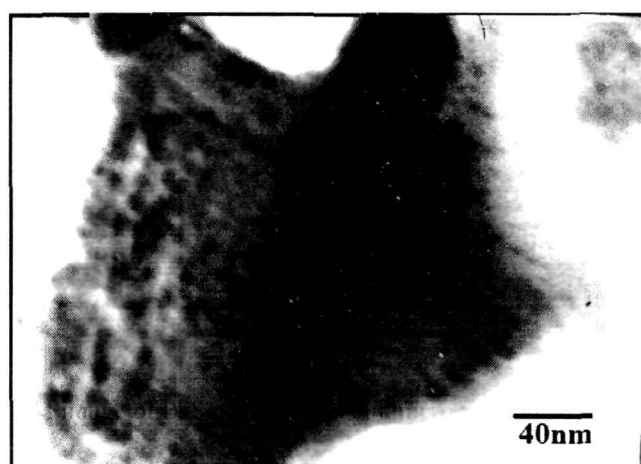


Fig4.15 (B) TEM image of PbS quantum dots in microemulsion after aging for one year

PbS quantum dots arranged in chain like configuration was noticed. The micelles provide an atmosphere supporting the dipole interaction between PbS quantum dots which is responsible for the chain like pattern. The system became more stable with time. Furthermore, PbS quantum dots were set to maintain a certain separation to minimize the potential energy of the microemulsion system which has protected them from agglomeration.

4.1.4.9: TEM study of nano material filled swift heavy ion induced ion tracks

Fig.4.16 (A), (B) and (C) are the TEM images of PbS filled etched track of PVOH films produced by SHI irradiation. Deviation from the exact spherical shape infers inhomogeneity in etching rate used in different cases. PbS nanoparticles fabricated in this method ranges from 10 to 25nm in size.

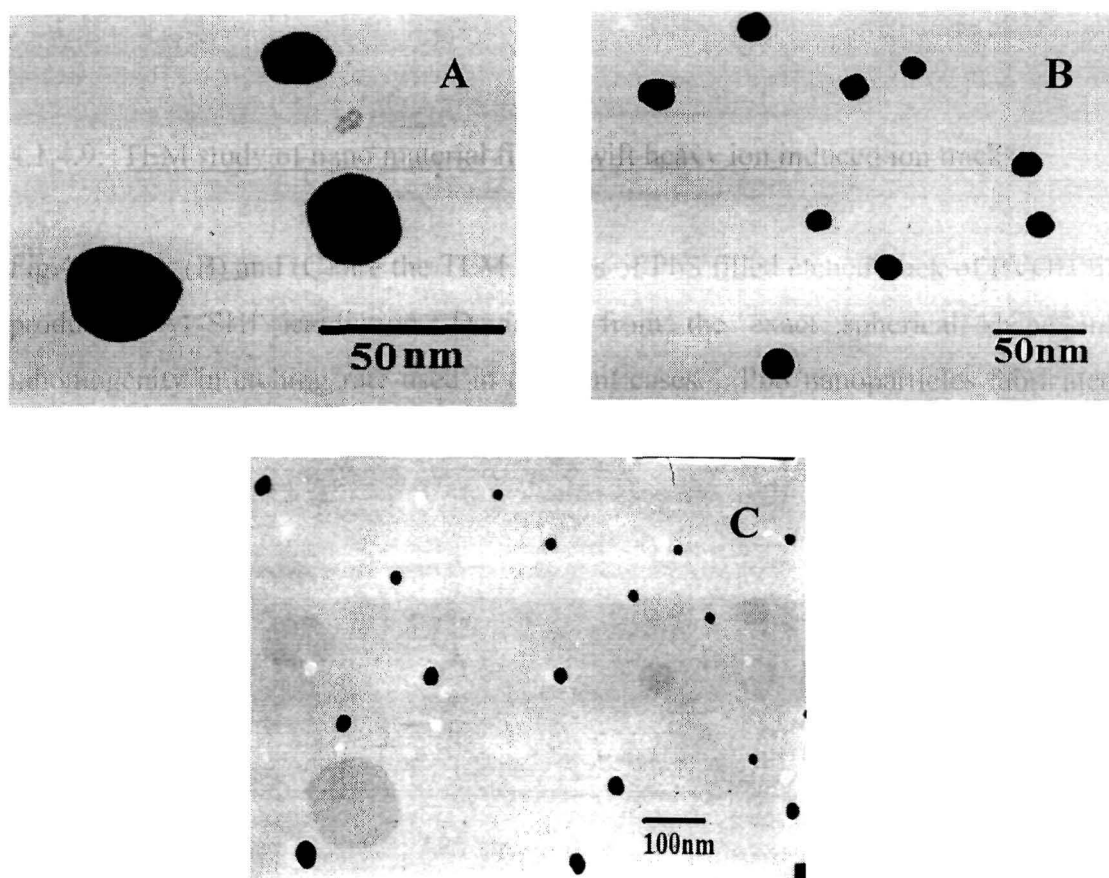


Fig.4.16: TEM image of PbS filled etched ion track

The size and shape of PbS quantum dots can be manipulated by controlling the etching rate of the latent ion tracks. Small and homogeneous voids were noticed in case low concentration of etchant with longer etching time where smaller and well organized PbS quantum dots had emerged. On the other hand, homogeneous and bigger size of the voids was created in case of using higher concentration of etchant and shorter

etching period. In the later case bigger and inhomogeneous PbS quantum dots are resulted. Fig4.16 (A) (B) and (C) signify the variation of size and shape of synthesized PbS quantum dots that have acquired better quality. The size and distribution of the PbS nanoparticles remained same after long aging interval. In this case PVOH films are behaving as stiff matrix holding PbS quantum dots efficiently by way of limiting the rate of agglomeration and minimizing the interaction between them.

4.2 X-ray diffraction (XRD) analysis of synthesized quantum dots

X-ray diffraction (XRD) is a versatile but non destructive technique exploited to recognize the crystal structure and composition of a material. In this method an X-ray beam is allowed to strike a target material and the beam is diffracted in much specific according to well known Bragg's law [19]. The characteristic of the target material is identified from the received diffraction pattern. In an X-ray diffraction measurement, a crystal is mounted and started rotating gradually while being bombarded with X-rays, producing a diffraction pattern of regularly spaced spots. The phase and other lattice parameters of the target are identified comparing available standard data. The other physical properties such as amount of crystallinity, stress, strain and defects are also investigated with this technique. XRD is used in nano scale characterization most importantly for determination of the particle size. A Debye-Scherrer formula [20] is used extensively in this characterization tool to estimate the particle diameter. The Debye -Scherrer formula is,

$$d = 0.9\lambda/\beta\cos\theta$$

Where, d is the particle diameter in nanometer.

λ is the wavelength of X-ray used.

β is the Full Width at Half Maximum(FWHM)

θ is the diffraction angle in radians.

The above parameters can be obtained from the X-ray diffraction pattern. The XRD analysis was carried out through Rigaku X-ray spectrometer.

4.2.1 : XRD of PbS quantum dots in PVOH matrix

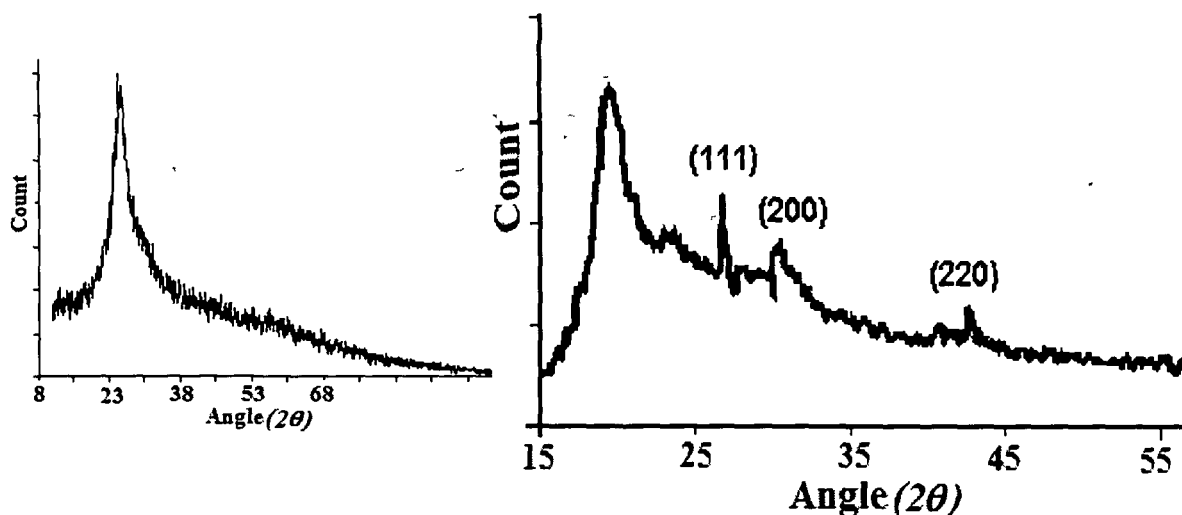


Fig.4.17 (A): XRD of PVOH matrix

Fig.4.17 (B) XRD of PbS quantum dots in PVOH matrix

Fig.4.17 (B) is showing the XRD pattern of as synthesized PbS quantum dots embedded in polymer matrix PVA. Developing diffraction peaks at $2\theta = 26^\circ$, 30.1° and 43° could ascertain the formation of PbS rock salt crystal structure which corresponds to its (111), (200) and (220) planes [21]. Presence of one more peak around 23° is attributed to the crystalline phase of the PVOH matrix [22]. It is expected that appearance of the distinct peak broadening is interrupted due to the interaction of PbS quantum dots and existence of a prominent peak due to PVOH.

4.2.2: XRD analysis of PbS quantum dots with acetonitrile surface passivation

XRD pattern of PbS quantum dots embedded in PVOH matrix with effective acetonitrile surface passivation is shown in Fig.4.18. The distinct characteristic peaks observable at $2\theta = 26^\circ$, 30.1° and 43° corresponded to PbS rock salt crystal structure.

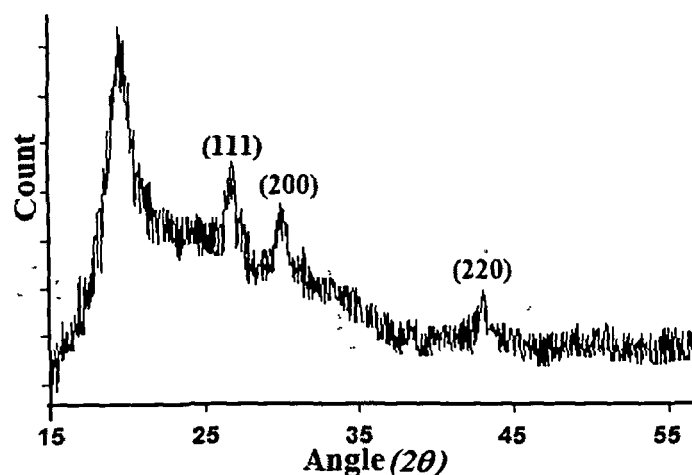


Fig.4 18. XRD of PbS in PVOH matrix with acetonitrile surface passivation

Considerable peak broadening compared to bared PbS quantum dots observed in this case which urge for significant surface passivation effect of acetonitrile. The size of the PbS quantum dots is estimated as 6.2nm approximately using Scherrer Formula.

4.2.3: XRD analysis of PbS quantum dots with Mn^{2+} incorporation

Referring to Fig.4.19 which shows a typical XRD pattern of PbS quantum dots with Mn^{2+} incorporation embedded in polyvinyl alcohol matrix. The XRD pattern contains Bragg's diffraction peaks corresponding to reflection from (111), (200) and (220) planes of PbS rock salt structure which suggest the formation of PbS quantum dots.

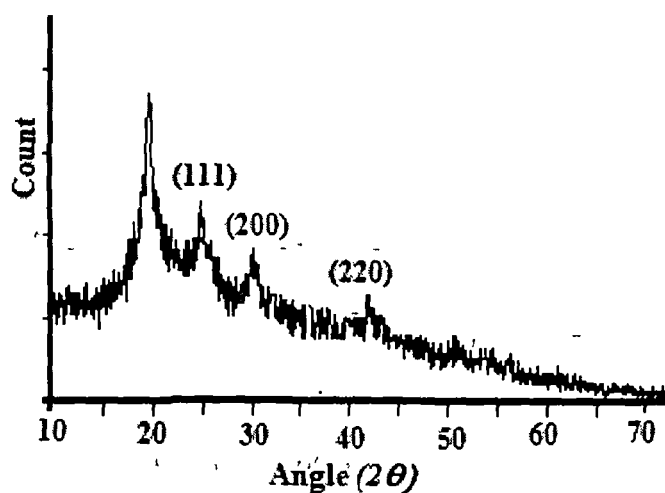


Fig.4.19: XRD of PbS quantum dots with Mn^{2+} incorporation

4.2.4: XRD analysis of PbS quantum dots coated with PVP

Fig.4.20 refers to XRD pattern of PbS quantum dots coated with PVP and dispersed in polyvinyl alcohol matrix.

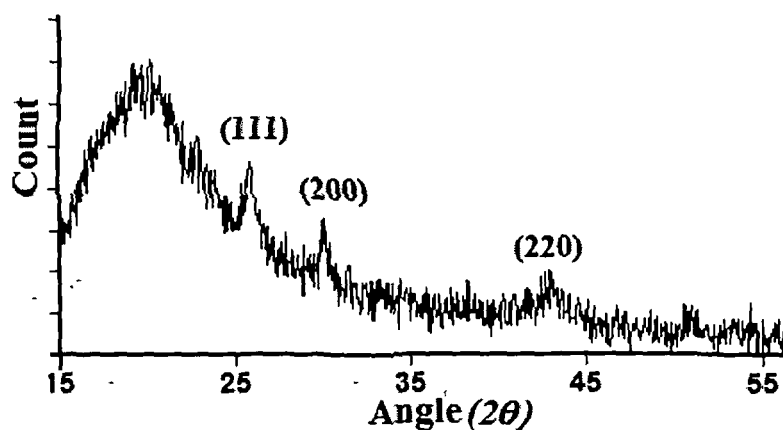


Fig4.20: XRD of PbS quantum dots with PVP coating

Existence of diffraction peaks emerging from the reflection from (111), (200) and (220) planes of PbS rock salt crystal ensures the formation of PbS quantum dots. The size has been estimated using Scherrer formulae and it is ~5 nm.

4.2.5: XRD analysis of PbS quantum dots by filling etched ion track

The XRD pattern of PbS quantum dots produced by filling etched ion track with PbS is shown in Fig.4.21. Subsequently, the existence of diffraction peak positioned at $2\theta = 26^\circ$, 30° and 43° corresponding to the reflection from (111), (200) and (220) planes.

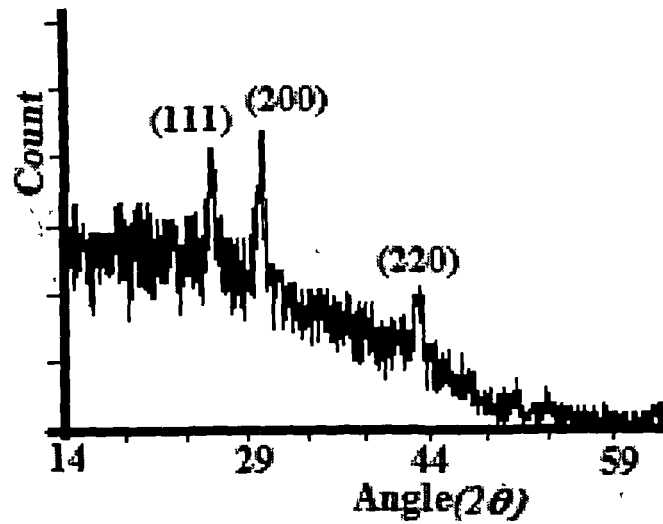


Fig.4 121: XRD of PbS filled etched ion track

This validates the development of PbS rock salt crystal structure. The size of PbS quantum dots has been approximated to be equal to 26.5nm.

4.2.6: XRD analysis of PbS quantum dots prepared through microemulsion route

Fig4.22 refers to XRD of PbS quantum dots in a microemulsion of AOT and n-heptane and dispersed in PVOH. The XRD pattern exhibits Bragg's diffraction peaks owing to reflection from (111), (200) and (220) planes that substantiate rock salt crystal structure of PbS.

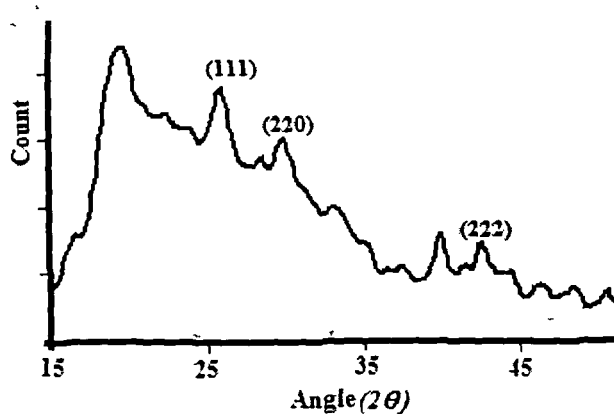


Fig.4.22: XRD of PbS quantum dots in a microemulsion of AOT and n-heptane dispersed in PVOH

The diffraction peak signal corresponds to weak intensity owing to low concentration of PbS. As a result the size of the PbS quantum dots could not be calculated due to non existence of sharp peak. An interaction between the micelles, PbS quantum dots and the matrix might have taken place. Though the distinct peak positions are obtained yet feasible broadening could not be evaluated from the XRD curves due to infiltration of noise.

4.2.7: XRD analysis of PbS quantum dots in SBR matrix

Fig 4.23(B) shows a typical XRD pattern of PbS quantum dots embedded in flexible SBR matrix. Fig4.23 (A) is representing XRD pattern of SBR latex. The XRD pattern contains prominent Bragg's diffraction peaks assigned to reflection from (111), (200) and (220) planes of PbS cubic rock salt structure. The average diameter has been estimated from the line width of the diffraction peaks using Scherrer formula and found to be ~8 nm.

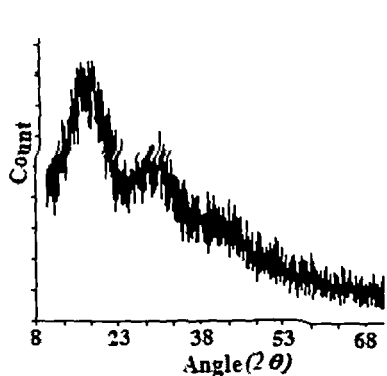


Fig4 23 (A) XRD pattern of SBR latex

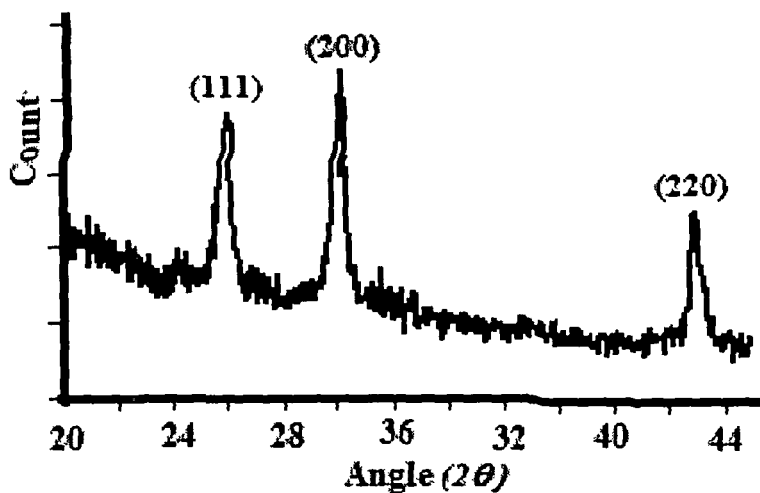


Fig4 23(B) XRD of PbS quantum dots in SBR latex

4.2.8: XRD analysis of PbS coupled quantum dots in SBR latex:

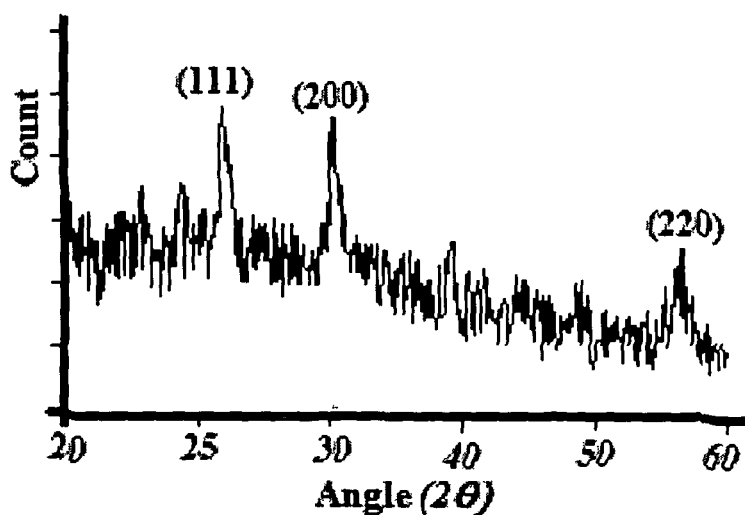


Fig4 24 XRD of PbS coupled quantum dots in SBR latex

The XRD pattern of PbS coupled quantum dots in SBR latex is depicted in Fig4.24 having distinct diffraction peaks at $2\theta = 26^\circ$, 30° and 43° owing to subsequent reflection

from (111), (200) and (220) planes thus confirming the development of PbS rock salt structures. Slight broadening of the diffraction peaks ensures the formation of PbS nano clusters. The size of the coupled quantum dots has been verified by using Scherrer Formula is $\sim 18\text{nm}$.

4.2.9: XRD analysis of TiO_2 and PbS/ TiO_2

The XRD pattern of as-synthesized nanoporous TiO_2 is presented in Fig4.25 (A). On the other hand, PbS sensitized nanoporous TiO_2 is depicted in Fig4.25 (B). The growth of crystal planes (111), (200), (220) and (311) assigned to diffraction peaks at $2\theta = 26^\circ$, 30° and 43° confirms the formation of PbS quantum dots inside nanoporous TiO_2 . The average diameter has been estimated from the line width of the diffraction peaks and to be $\sim 5\text{ nm}$.

The XRD patterns of nanostructured anatase TiO_2 developed after the heat treatment at 200°C for 12 hours is shown in the Fig 4.26(A) and on the other hand PbS incorporated TiO_2 is revealed in Fig 4.27(A). In consistency with the other reports, we notice that the diffraction peaks (101), (044), (200), (222) and (213) corresponding to various crystalline planes of TiO_2 [23]. Note that the diffraction peaks corresponding to PbS (which has typical cubic rock salt structure) are not resolved in PbS/ TiO_2 system Fig4.27 (A).

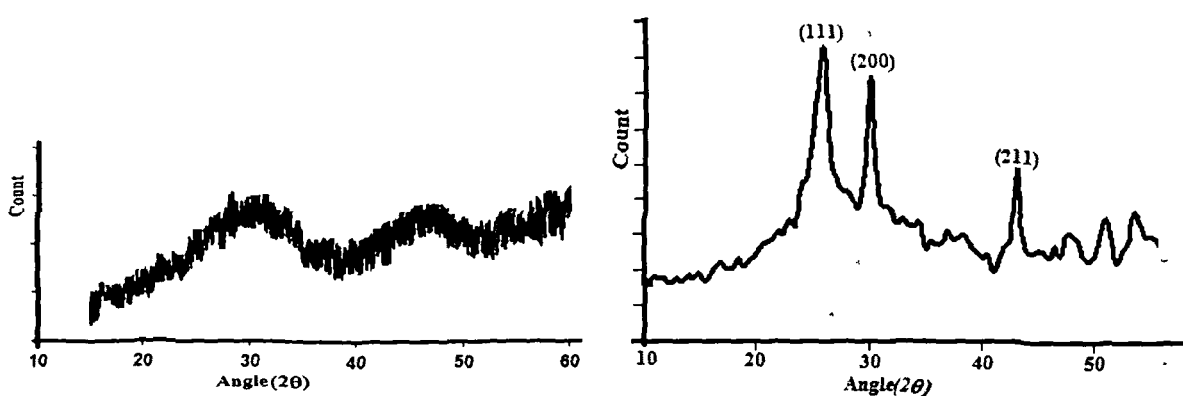


Fig 4.25 (A): XRD of as- synthesized TiO_2

Fig.4.25 (B): XRD of PbS/ as synthesized TiO_2

This could be due to the lower concentration of the adsorbed molecules and lesser chance of molecules staying on to TiO_2 surface. Further, the diffraction signals are

found to be weaker in PbS/TiO₂ system than TiO₂ system itself. Suppression in the full width at half maximum (FWHM) of the most prominent (101) peak from 0.048 radian to 0.039 radian signifies compactness of the TiO₂ nanostructured film owing to pore filling by PbS molecular adsorption.

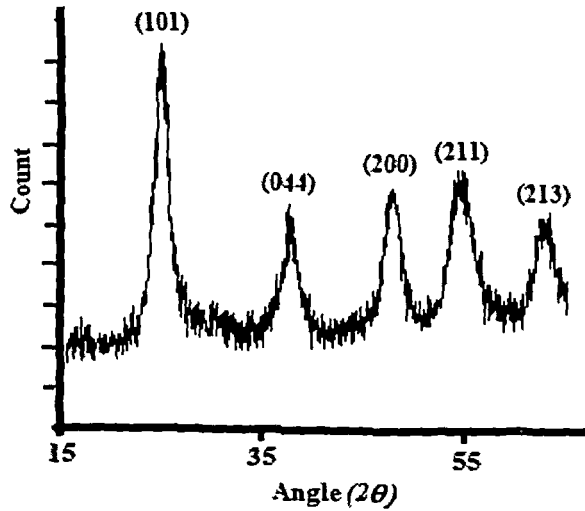


Fig 4 26 (A) XRD of anatase TiO₂

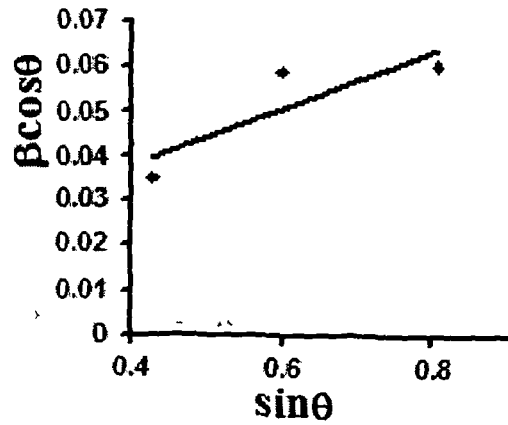


Fig 4 26 (B) Williamson-Hall plot of TiO₂

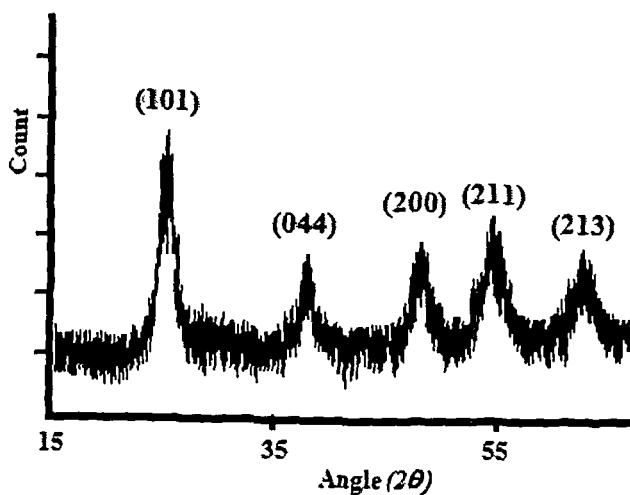


Fig 4 27 (A) XRD of PbS/ anatase TiO₂

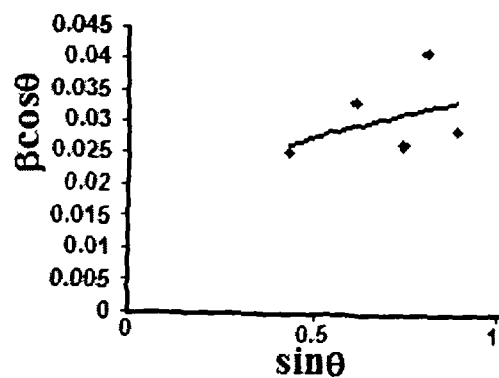


Fig 4 27(B) Williamson-Hall plot of PbS/ TiO₂

The microstrain of a particular sample was calculated using popular Williamson-Hall formula:

$$\frac{\beta \cos \theta}{\lambda} = \frac{1}{d} + \frac{\eta \sin \theta}{\lambda} \quad (4.1)$$

where β is the measured FWHM in radians, θ is the Bragg angle of the diffraction peak, λ is the x-ray wavelength, d is the average crystallite size, and η is the effective microstrain in the system [24]. The microstrain as calculated for TiO₂ and PbS/TiO₂ systems are found to be 0.035, and 0.1475; respectively. Increased microstrain in the later case ensures induction of stress due to PbS incorporation into TiO₂. This would certainly increase the rigidity of TiO₂. The Williamson-Hall plots for TiO₂ and PbS/TiO₂ are presented in Fig4.26 (B) and Fig4.27 (B); respectively.

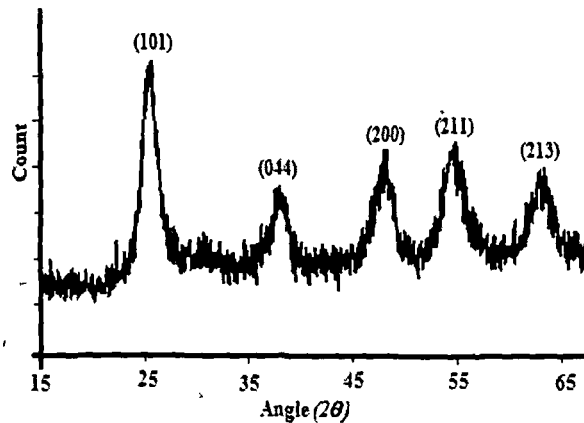


Fig 4 27(C) XRD of anatase TiO₂ (2nd type)

Fig. 4.27(C) represents the crystalline anatase phase of TiO₂ obtained through heat treatment of the gel form of TiO₂ at a temperature of 400⁰C for 6 hours. The nature of crystallinity is found to be similar in both the cases (i.e. at 200⁰C for 12 hours and 400⁰C for 6 hours). On the other hand spontaneous development of crystallinity is noticed while TiO₂ was kept for three months to study aging effect at room temperature [Fig.4.27 (D)].The development of crystalline phase is assumed as a consequence of enhancement of particle size resulting from grain growth.

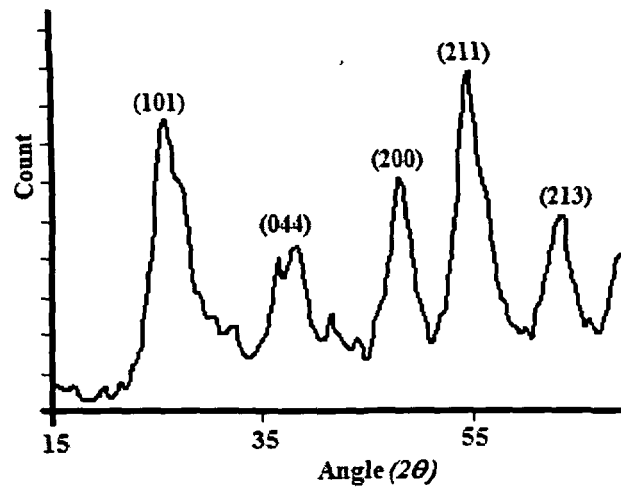


Fig 4 27 (D) XRD of anataseTiO₂ with

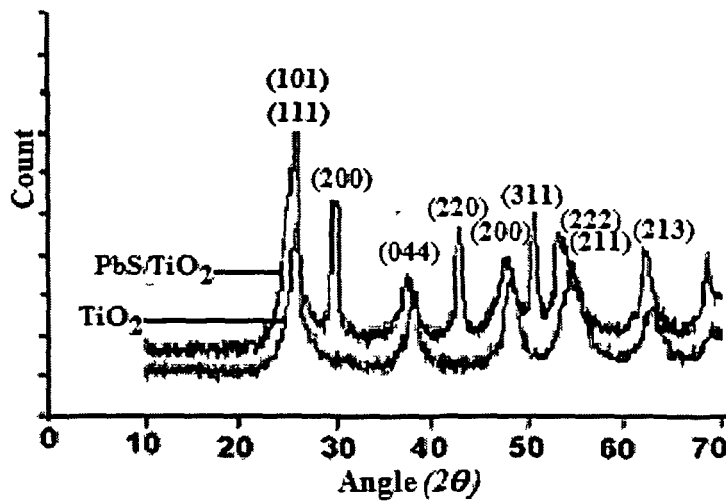


Fig.4.28 (A) Combined XRD of anataseTiO₂ and PbS/TiO₂

Fig4.28 (A) depicts combined XRD pattern of TiO₂ with PbS. Note that in this case the concentration of PbS becomes high in view of the fact that PbS has grown over the outer surfaces of TiO₂ also Slight shifting of peaks in nanoporous TiO₂ is observed after incorporation of PbS. This occurs because of strains developed between the planes of PbS and TiO₂ [25].

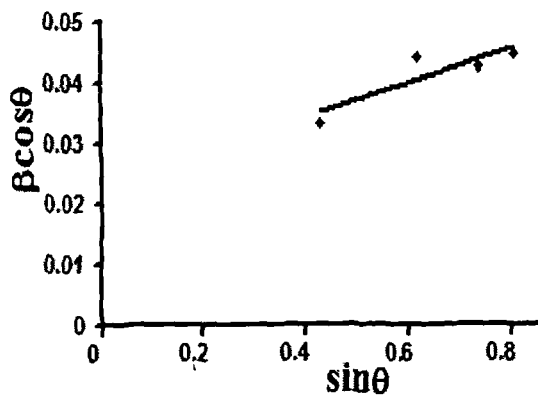


Fig4 28 (B) Williamson-Hall plot of TiO_2

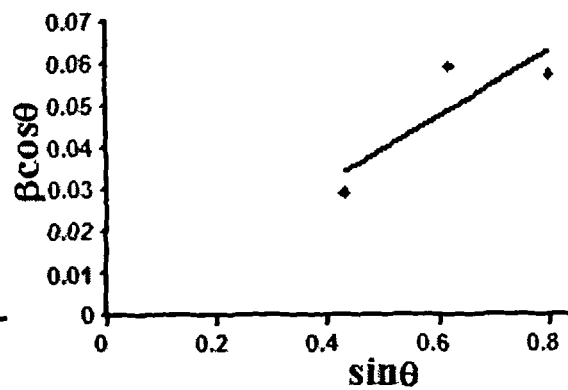


Fig4 28 (C) Williamson-Hall plot of PbS/TiO_2

A plot $\beta\cos\theta$ versus $\sin\theta$ [Williamson-Hall plot] for TiO_2 and PbS/TiO_2 is presented in Fig.4.28 (B) and Fig.4.28(C) respectively. The microstrains as calculated for TiO_2 is 0.16 and for PbS/TiO_2 system is 0.53. The average diameter has been estimated from the line width of the diffraction peaks using Scherrer formula and found to be 23.5 nm

4.3 Photoluminescence (PL) study

If spontaneous emission occurs from a material employing an optical excitation it is called as photoluminescence. When a substance absorbs energy in some form or other, a fraction of the absorbed energy may be re-emitted in the form of electromagnetic radiation in the visible or near-visible region of the spectrum and this phenomenon is called luminescence. The process of luminescence involves at least two steps: the excitation of the electronic system of the solid and subsequent emission of photons. According to nature of source (electron, heat, light) luminescence is divided into three types, electroluminescence, thermo luminescence and photoluminescence. Photoluminescence which has got the shortest emission life time [26]. Photoluminescence spectroscopy is a non-destructive characterization technique used to investigate optical properties of material systems. PL spectroscopy is a sensitive tool for probing discrete energy states. Nevertheless, the nature of surface, interface, and

impurity levels of a material can be studied through evaluating the emission features of a material. In addition, pulsed optical excitation provides a powerful means for studying transient phenomena. It depends only on radiative events and which is the fundamental limitation. Materials with poor radiative efficiency, such as indirect bandgap semiconductors having very low-quality emission are become very difficult to investigate through photoluminescence. Similarly, identification of impurity and defect states also depends on their optical activity.

Electronic excitations are created while light of sufficient energy is incident on a material efficiently and as a result photons are absorbed. Eventually, these excitations relax and the electrons return to the ground energy state if the relaxation occurs through radiative path-ways then PL becomes feasible. The emitted light is collected to analyze the photoexcited material. The excited electronic energy state is determined through the type of transition revealed from the photoluminescence spectrum. The intensity of PL emission is the measure of radiative and nonradiative recombination events. Further, variation of the PL intensity with external parameters like temperature and applied voltage etc. can be explored to categorise the underlying electronic states and bands. Photoluminescence generally depends on the nature of the optical excitation, penetration depth of the incident light and optical band gap of the material system

The strength and the nature of the PL signal also depend on the density of photoexcited electrons, while intensity of the incident beam can be adjusted to control those parameters. The transition of electrons depend not only the energy of the excitation wavelength but also upon the availability of the energy level in the excited state of the host material system for allowed transition. These transitions can be divided into two types: direct transition takes place in accordance with Franck-Condon principle whereas indirect transition or phonon assisted transition is mediated by violating Franck-Condon principle [27]. If the electronic transition takes place between the process E_1 and E_2 and if $E_2 > E_1$ then emission wavelength $\lambda = hc / E_2 - E_1$, where h is Planck's constant and c is the velocity of light. With a special reference to the emission wavelength, Stokes introduced the first law in the model of luminescence response which predicts that the wavelength of the emitted light in photoluminescence process is generally equal to or longer than that of the excited light (i.e. of equal or less energy). This difference in

wavelength is caused by a transformation of the exciting light, to greater or lesser extent through non-radiating vibration energy of atoms or ions. In some rare instances, the emitted light becomes shorter wavelength than the excitation wavelength when an intense laser light is used as the excitation source. This type of photoluminescence process is known as anti-Stokes photoluminescence or photoluminescence up conversion [28]. The quality of photoluminescence is assigned by the efficiency of photoluminescence or quantum yield which is the ratio of the emission energy to the excitation energy. A luminescent dye is also added with the host material to assist photoluminescence for some other reasons.

Often PL originates near the surface of a material. Since, surface of a material comprises of large number of defect states and these states act as long-lived trapping centres during the electron transition process consequently PL analysis has become an important tool in the characterization of surfaces. These trap states are explicitly known as surface states and classified into deep traps (high energy) and shallow traps (low energy)[29]. The usefulness of PL in the study of surface states is derived from its unique sensitivity of PL to discrete electronic states, many of these states lie near surfaces and interfaces. Discernable energy distribution and density of interface states can be ascertained by studying dependence of the intensity of PL spectrum on the excitation intensity. The presence of surface states influences the intensity of the PL signal. Having noticed the thermal activation process in temperature-dependent PL the depth of these surface states could be resolved. In fact, nonradiative interface states also exist and nonradiative traps dominate the transient PL signal at low carrier density. The overall carrier dynamics taking part in the luminescence process is estimated through time-resolved PL of radiative transitions in the material [30]. On the other hand, these transitions can also be considered as transition between highest occupied molecular orbital (HOMO) to lowest unoccupied molecular orbital [LUMO]

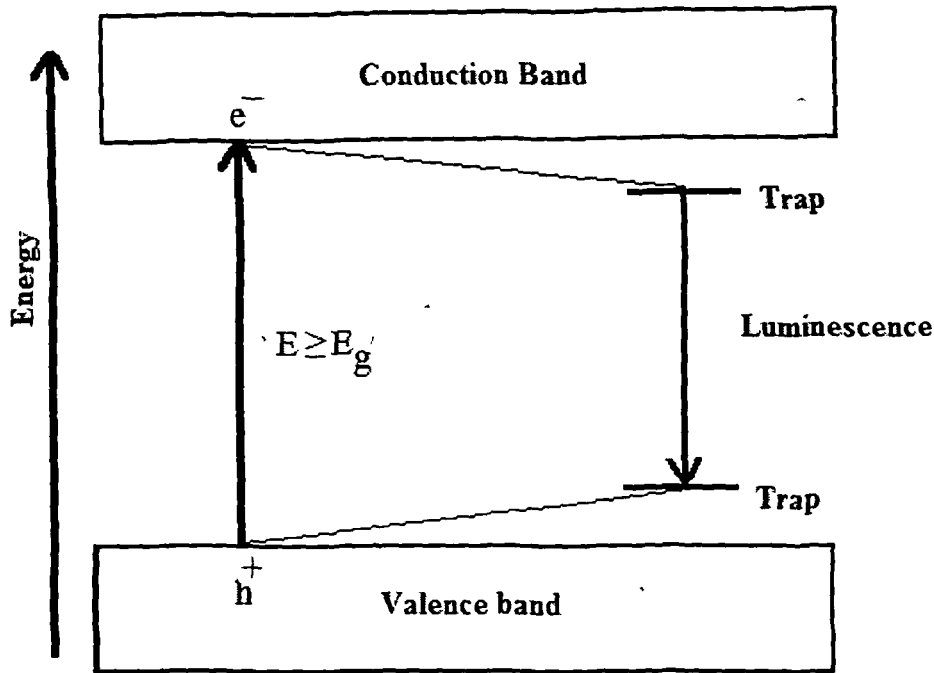


Fig 4.29 Schematic diagram photoluminescence

Since the excited electron stays temporarily in the high energy state leaving a hole in low energy state these electron hole pairs are termed as exciton and their characteristic actually plays the crucial part in the luminescence process. Another important factor which contributes to photoluminescence is the transition probability of carriers. The recombination of this exciton at band edge facilitates maximum energy known band edge emission.

The nature of photoluminescence of semiconductor quantum dots establishes some relations between many important parameters such as size dispersion, strength of electron phonon coupling etc. The impact of high surface to volume ratio, quantum dot possesses a large number of defect states or surface states associated with imperfections of nanocrystals which act as a radiative trap centres and promotes immense photoluminescence compared to its bulk counterpart. One of the fascinating facts is that, though some materials do not have photoluminescence features in bulk state can endorse photoluminescence in its low dimensional state [Nanoscale form] Since these energy states lie in between the forbidden gap therefore luminescence spectrum can also be tuned over a range by controlling these defect states The photoluminescence of semiconductor quantum dot system show and unique emission band which is

substantially red shifted as a result of quantum size effect. Quantum dots are left with a number of dangling bonds which aid more reactivity of surface and subsequently photoluminescence of this system is affected by the surrounding medium. On the other hand size dependent band edge emission is another important feature of the photoluminescence shown by semiconductor quantum dots. The PL measurements were carried out with Perkimelmer (*Model LS 55*) photoluminescence set up.

4.3.1 PL analysis of PbS quantum dots in PVOH matrix

PL spectra of PbS quantum dots embedded in PVOH matrix is shown in Fig4.30 (A). The fluorescence peak observed at 718nm while subjected to excitation of wavelength 450nm. The PL peak at 700nm is already reported [31]. The emission band has got a Gaussian distribution having FWHM of 140nm. The emission band is dominated by surface state emission. The photoluminescence spectra PbS quantum dot in PVOH matrix after the aging 60 days is depicted in Fig4.30 (B). The PL emission peak has shifted to 730nm as consequence of aging affect. This time FWHM has been found out to be equal to 60nm with relatively weak intensity.

The shape of the PL spectra is influenced by the factors such as size distribution and phonon coupling. The intensity of the PL spectra depends on the number of particles contributing to the e-h recombination emission process. The Gaussian distribution of the PL spectra ascribed to the polydispersity of quantum dot sizes [32]. But the PL spectra which was taken after 60 days suggests relatively uniform size distribution since the spectra ranges a small region of emission spectrum of 670nm to 830nm compared to the PL emission range of freshly prepared sample which ranges 630nm to 825nm.

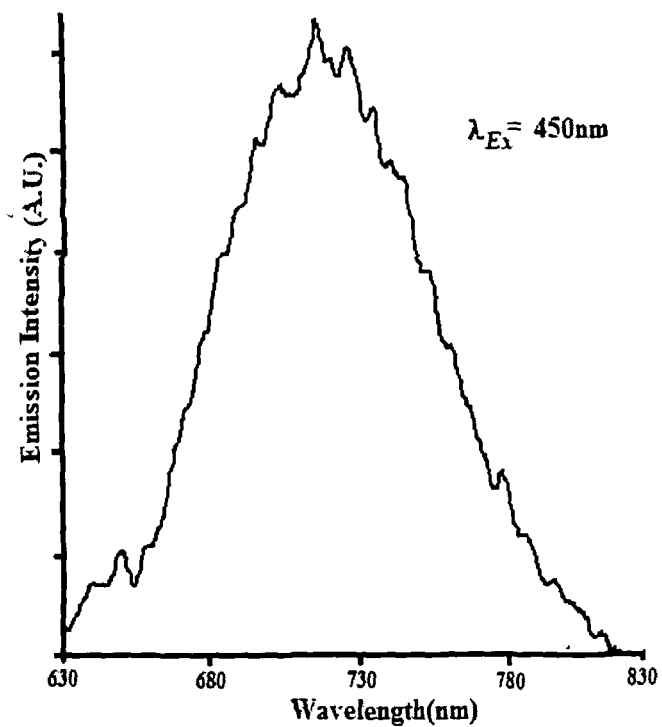


Fig 4 30 (A) PL spectra of PbS quantum dots in PVOH matrix

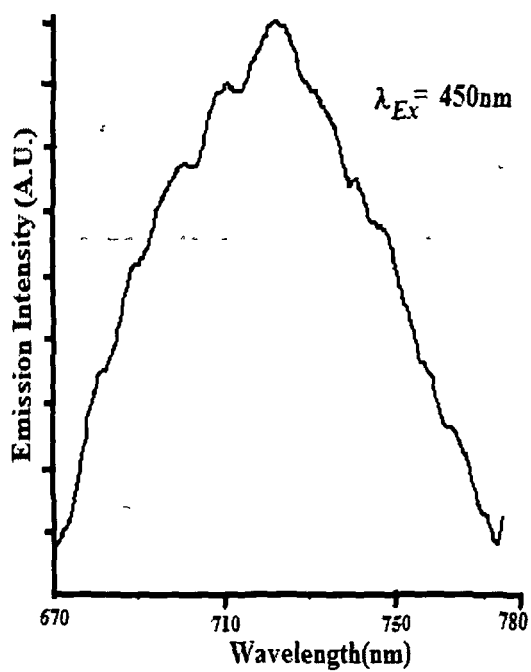


Fig.4.30 (B): PL spectra of PbS quantum dots in PVOH matrix after aging

The broadening PL bandwidth can be simulated by the following equation

$$I(E) = \sum \frac{1}{\sqrt{2\pi\gamma^2}} \frac{S^n}{n!} \exp\left(-\frac{[E - E_{zp} - n\hbar\omega_{LO}]^2}{2\gamma^2}\right) \quad (4.2)$$

where, S corresponds to the Huang-Rhys parameter, E and E_{zp} are energies of the emission and zero-phonon lines, $\hbar\omega_{LO}$ is the longitude-optical (LO) phonon energy, $S^n/n!$ is the probability for emission of n -photons and γ is a phenomenological broadening parameter, associated with the size distribution of the quantum dots. The Huang-Rhys parameter is known to be associated with the distortion of the e - h equilibrium distance at the excited state and the electron-phonon coupling, and is calculated according to the following equation.

$$S = \frac{e^2}{a} \frac{1}{\hbar\omega_0} \frac{1}{(2\pi)^2} \left(\frac{1}{k} - \frac{1}{k_0} \right) \quad (4.3)$$

Here, k , k_0 are high frequency and static dielectric constants and a is the electron (hole) radius [33]. The PbS quantum dot samples can have a number of imperfections (trap centres) which might have created during growth process. A large FWHM for this sample reflects profound phonon coupling with this trapped state. On the other hand, decrease in FWHM after aging indicates relatively less phonon coupling. The surface states diminished due to aging effect as a result electronic transitions were hindered that are responsible for photoluminescence. In this case band edge emission becomes dominating. After achieving saturated growth, PbS quantum dots of nearly equal size are produced and a narrow emission band of near band-edge exciton recombination.

4.3.2: PL analysis of PbS quantum dots with acetonitrile surface passivation

Fig.4.31 (A) shows the photoluminescence spectra of PbS quantum dots in PVOH matrix with effective acetonitrile surface passivation. The existence of dangling bonds changes the surface structure of nanocrystals which in turn affects photoluminescence. Surface passivation reduces shallow traps present near the band edge but the deep traps are supposed to have originated from the interstitial defect sites of PbS contribute significantly to in the luminescence. Small size of the PbS quantum dots resulting strong binding energy that renders the possibility of formation of large number of band edge excitons. Note that the energy difference between the band edge emission and deep trap state induced emission is sufficient to distinguish two peaks distinctly in the PL spectra. The first peak at 430nm is attributed to the recombination of band edge exciton and other at 446nm is assigned to the recombination at deep trap centres.

Photoluminescence of the same sample taken after one year aging is shown in Fig4.31 (B). The position of band edge exciton peak remained located at 430nm implies that stability of PbS quantum dots as a result of acetonitrile surface passivation. We believe that some of the interstitial defects might have vanished as a result of formation of PbO (PbO phase was noticed in XRD of concerned sample). The line shape of the emission band implies involvement of phonons. The band structure of PbS also supports indirect transitions or phonon assisted transition. Band edge exciton recombination can also be associated with phonons. UV excitation of wavelength 325 nm was used to obtain luminescence in both the cases. The emission peak at~ 434 nm has been reported previously in PbS nanocubes [34].

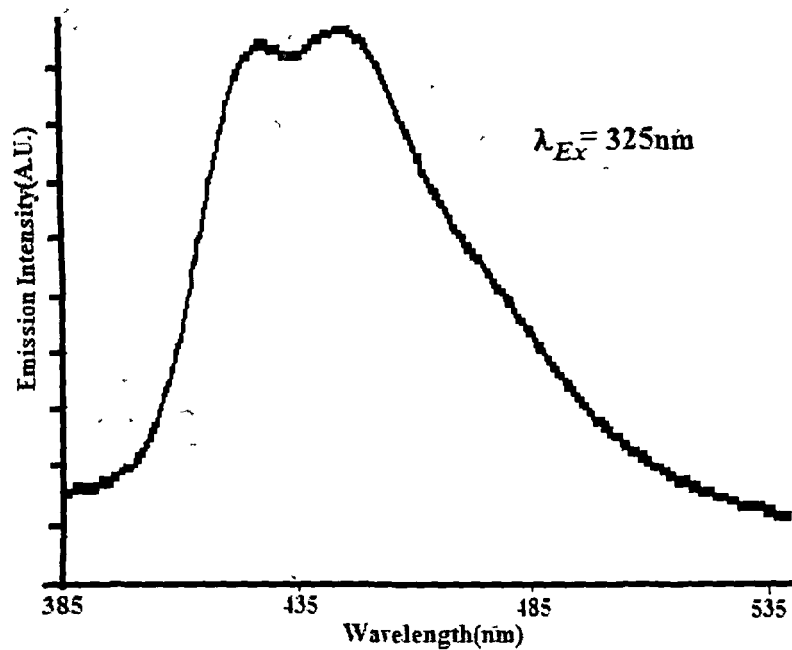


Fig4.31 (A): PL of PbS quantum dots with effective surface passivation

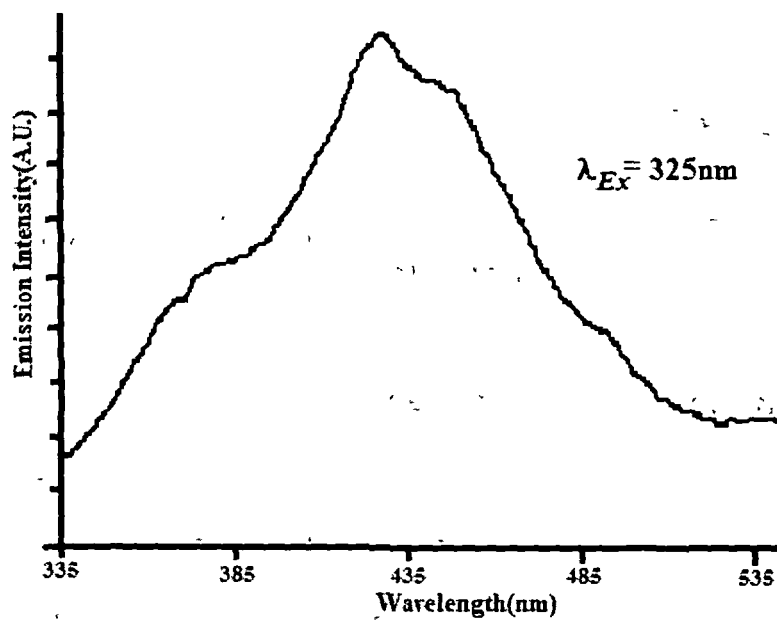


Fig4.31 (B): PL of PbS quantum dots with effective surface passivation after aging of one year

4.3.3: Photoluminescence of PbS quantum dots with Mn^{2+} incorporation:

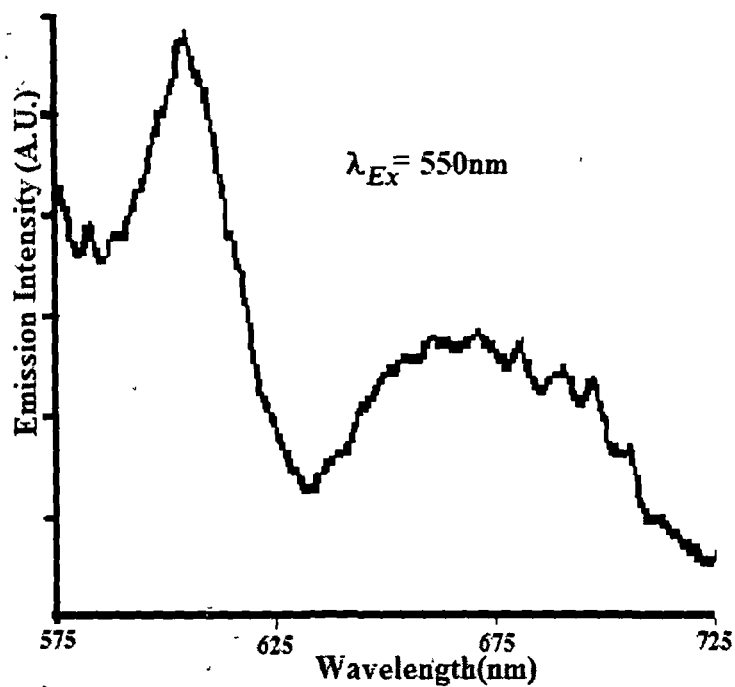


Fig4.32 (A): PL spectra of PbS quantum dots in PVOH matrix with Mn^{++} incorporation

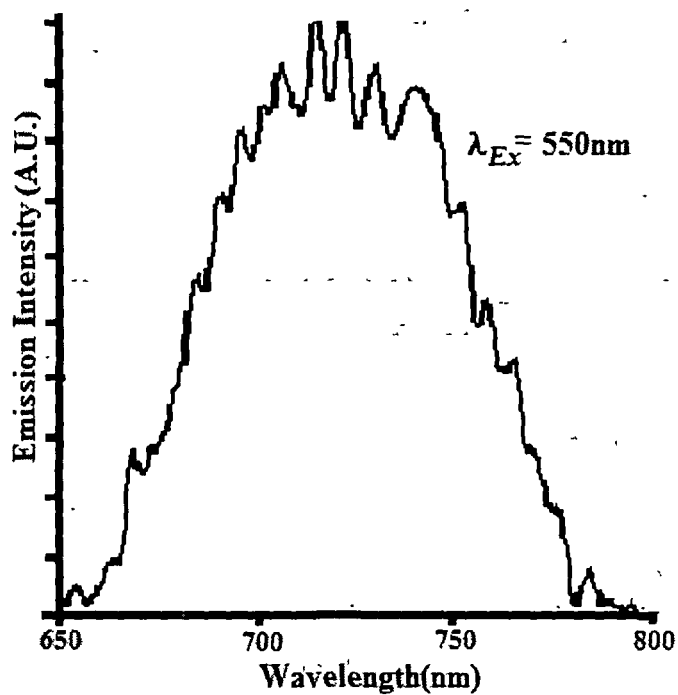


Fig4.32 (B): PL spectra of PbS quantum dots in PVOH matrix with Mn^{++} incorporation after aging

Fig4.32(A) shows the photoluminescence spectra of PbS quantum dots with Mn^{2+} incorporation for freshly prepared sample. Two distinct emission bands are noticed, a narrow band peaking $\sim 600\text{nm}$ is attributed to Mn^{2+} induced surface state emission [35]. There could be a surface states coupled the impurity level states of the host material. The second one which is reasonably broad emission band and peaking at $\sim 670\text{nm}$ is ascribed to surface trap emission of PbS. The presence of 'd' orbital of Mn^{2+} promotes exchange interaction with the excitons of the host material.

The PL spectra of the same sample taken after the aging is shown in Fig4.32 (B). One emission band peaking at $\sim 725\text{ nm}$ is observed instead of two emission band. The emission band could be for PbS only. The emission induced by Mn^{2+} might have disappeared as a result of formation of MnO_2 and provided surface passivation which has protected further growth. The shifting of this peak from $\sim 670\text{nm}$ to $\sim 725\text{ nm}$ suggest growing PbS quantum dots due to Ostwalds ripening till surface passivation of MnO_2 has become effective. An excitation wavelength of 550nm was used in both the cases.

4.3.4: PL analysis of PVP coated PbS quantum dots

The PL spectra of freshly prepared PbS quantum dots with PVP coating is depicted in Fig4.33 (A). and taken after aging is shown in Fig4.33(B). A broad emission peak signifies considerable size distribution and involvement of plenty surface traps. The interaction of quantum dots with matrix generates a large number of surface states near the interface of quantum dot and the matrix. The peak of the emission band was located at $\sim 500\text{nm}$ and $\sim 516\text{nm}$ respectively for the samples where a shifting of $\sim 15\text{nm}$ is observed.

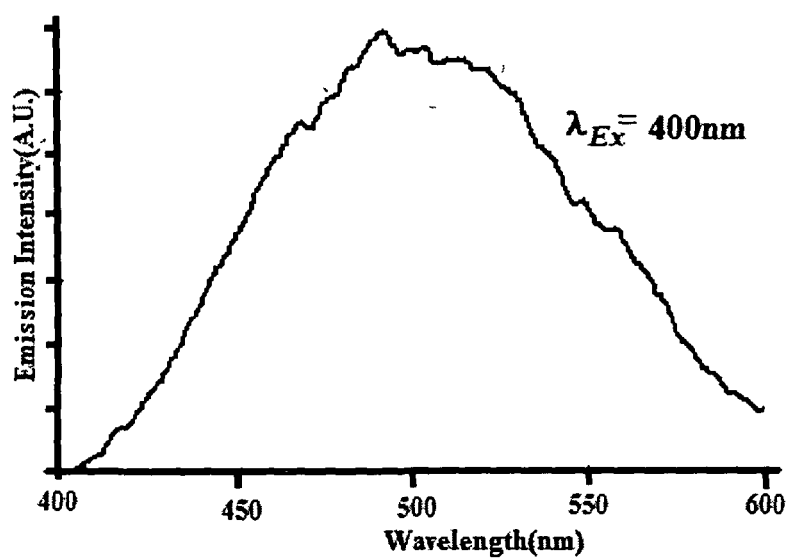


Fig 4 33 (A) PL spectra of PVP coated PbS quantum dots

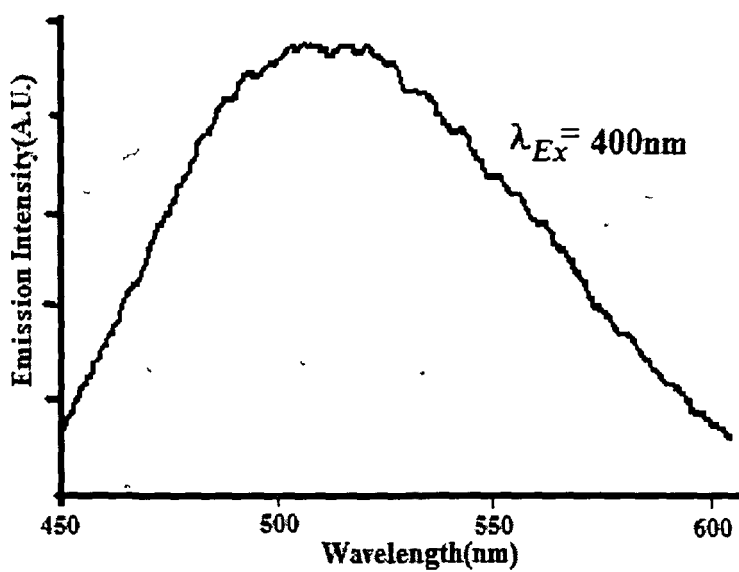


Fig 4 33 (B) PL spectra of PbS quantum dots after the effect of aging

Interestingly, the FWHM of the emission band have been found as $\sim 110\text{nm}$ and $\sim 125\text{nm}$. The shifting of peak and increase of FWHM was found to be equal and it is nearly 15nm . The evaluated photoluminescence data suggests the photoluminescence of the system is predominated by surface state emission. The major contribution of photoluminescence of this system might have come from radiative recombination at the trap centres of the interfaces of PVP and PbS quantum dots. Both the samples were given an excitation of wavelength 400nm to obtain photoluminescence responses.

4.3.5: PL analysis of PbS quantum dots prepared through microemulsion route

The PL spectra of PbS quantum dots in microemulsion medium of AOT and n-heptane before and after aging are represented in Fig.4.34 (A) and Fig.4.34 (B) respectively. The PL spectra describes reasonably narrow emission band observed with maximum emission peak at 536nm for freshly prepared sample and 545nm after aging respectively.

The nature of the emission band with a narrow FWHM of $\sim 16\text{nm}$ implies the signature of uniform size distribution. The emission associated to the band edge exciton recombination predominates the PL of freshly prepared samples. Since no additional coating is used so PbS quantum dots might have suffered from the particle growth to some extent that results in small broadening of the PL spectra and increase of FWHM of $\sim 40\text{nm}$. The shifting of maximum emission peak renders the size dependent band edge exciton recombination in nanograins. The photoluminescence was obtained while the sample was excited at a wavelength of 500nm .

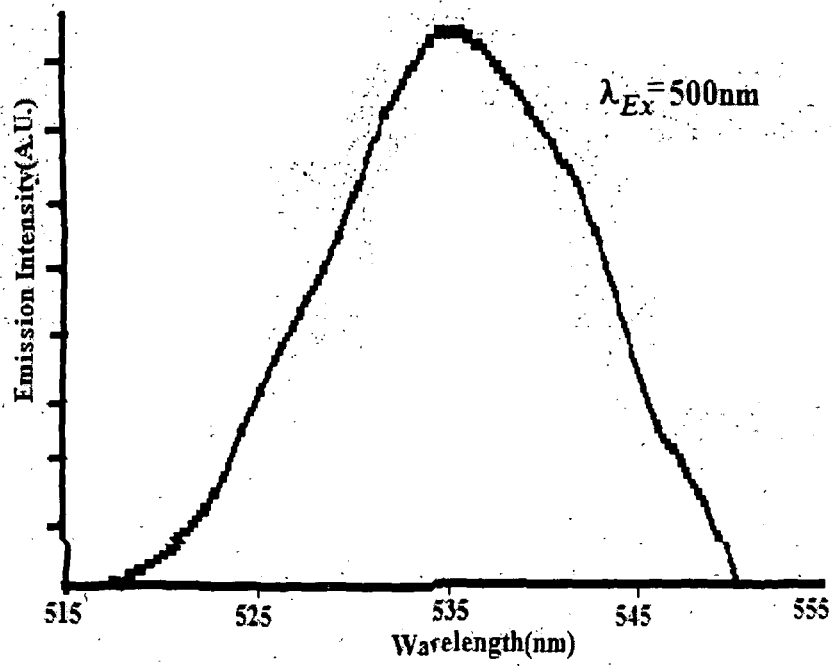


Fig.4.34 (A): PL spectra of PbS quantum dots in microemulsion

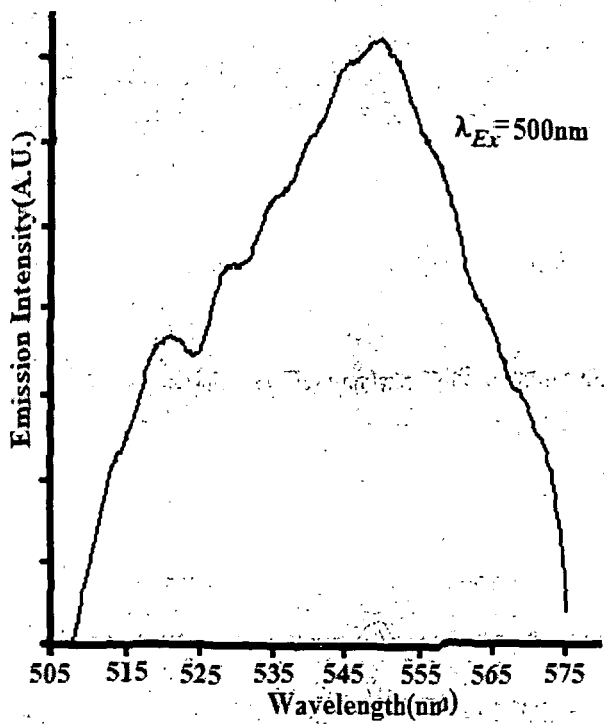


Fig.4.34 (B): PL spectra of PbS quantum dots in microemulsion after aging

4.3.6: PL analysis of PbS quantum dots in SBR latex

The PL study of the PbS sample reveals three emission peaks corresponding to 573 nm and 617 nm and 825 nm respectively is represented in Fig.4.35(A). These emission peaks have been perceived using excitation wavelength 450nm. The peak at 573 nm is attributed to the band edge emission corresponding to band edge exciton recombination of the PbS quantum dots. The second peak is the excitonic peak observable at 617 nm is analogous to recombination at deep trap centres. Normally, for other binary semiconductor systems (e.g. CdS) excitonic emission is rarely observable as it is very close to the band edge emission with energy spacing of the order of a few meV only. On the other hand, in PbS system, up to ~ 10 fold energy gap enhancement might provide an opportunity to notice visible excitonic emission. In our case, band edge emission ($\lambda=573 \text{ nm}$, $E=2.171 \text{ eV}$) and exciton emission ($\lambda=617 \text{ nm}$, $E=2.016 \text{ eV}$) are well separated by an energy spacing 155 meV, which is the binding energy of our PbS quantum dots. The result of the calculation of excitonic energy in consistency with earlier reports [36]. Here the exciton energy is 2eV. Although effective mass approximation (EMA) is not valid reasonably in case of PbS however since E_b is less than 100 meV, then the combination of small effective mass and large dielectric constant makes the EMA useful in case of bulk PbS [37] so using the formula $E_b=Ry m^*/\epsilon^2$, the exciton binding energy (E_b) for PbS bulk system has been calculated [where Ry is the Rydberg energy, m^* is effective mass of electron and ϵ is the high frequency dielectric constant] to be 0.014 eV. In our PbS quantum dot system, E_b (0.155 eV) has been increased by over 10 fold due to significantly large energy gap more than 10 times due to the huge energy gap enhancement (from 0.29 eV to 2.15eV) while undergoing transition from bulk to molecular system. The third peak was visible at 825 nm, due to shallow surface state led recombination emission. Envelope function calculation of the electronic structure of PbS quantum dots also provides the energy spectrum as well as gives selection rules for different transitions in quantum dots of smaller diameters [38]. Such calculations indicate that better emissive property of PbS quantum dots is assured by the number of excitons staying at higher energy states.

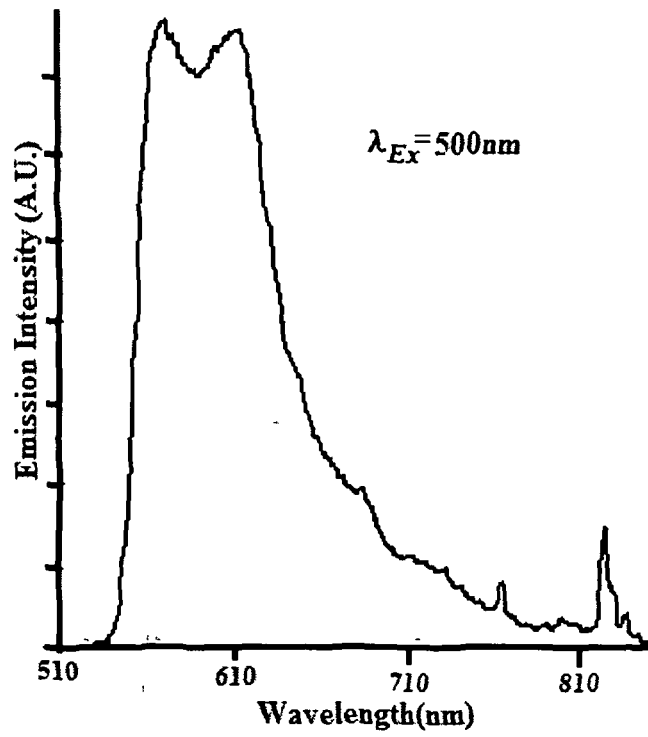


Fig.4.37 (A): PL spectra of PbS quantum dots in SBR latex

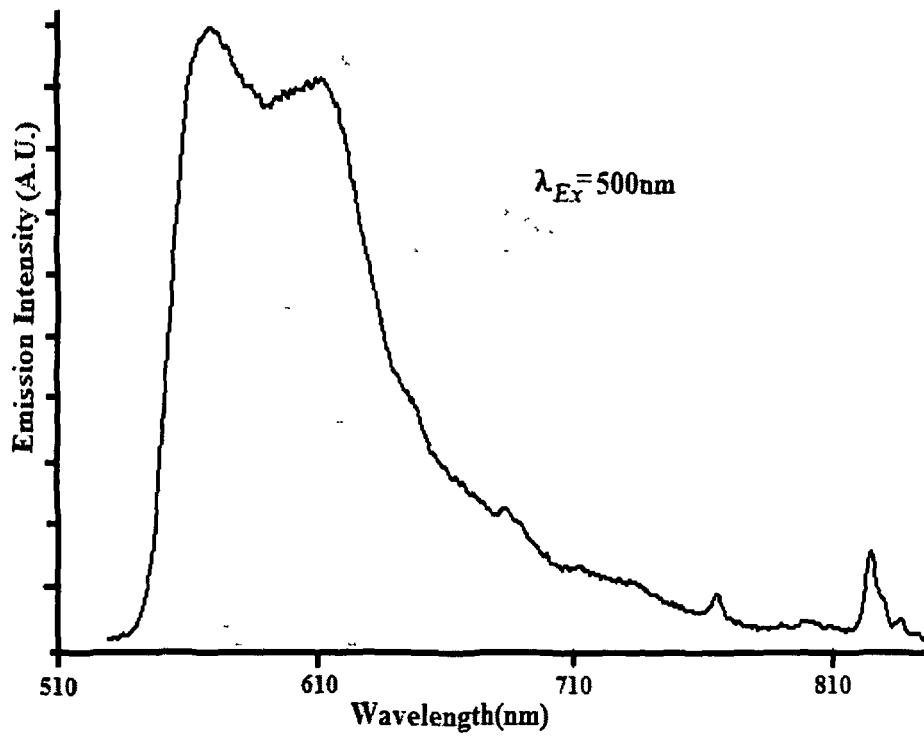


Fig.4.37 (B): PL spectra of PbS quantum dots in SBR latex after aging of one year

However, the highest energy state of the excitons is the band edge. But for better emissive properties one requires maximum numbers of excitons staying at the higher energy states [40]. Combination of strong quantum confinement and high dielectric constant of PbS quantum dot system enables observation of such distinct excitonic emission peaks related to the higher energy states. Thus, the PL spectra of PbS quantum dots in SBR latex has efficiently isolated band edge exciton emission from other surface state exciton emission.

The PL spectra of the same sample was taken after aging and is shown in Fig 4.35 (B). Although the peaks of the emission band remained consistent but the intensity of the second peak has dropped by a substantial amount. A slight broadening of the emission band is noticed in this case which indicates the involvement of phonons but predominance of band edge exciton recombination is still present. The diminishing intensity infers condensation of the number of deep traps induced by Pb^{++}

4.3.7: PL analysis of PbS coupled quantum dots in SBR latex

The PL spectra of PbS coupled quantum dots figured a prominent emission band with maximum at ~565nm in Fig.4.36 (A) and which is attributed to combination of deep trap as well as shallow trap state and band edge recombination emission. The band edge exciton recombination might have subsided as a result of strong coupling between the quantum dots. Simultaneous creation of large number of exciton near the conduction band obstructs the path of radiative recombination.

On the other hand, number of deep traps become more than their individual state. Subsequently, two individual peaks have appeared in case of isolated PbS quantum dots that have merged to a single peak. The aging effect has also been noticed in PL spectra where shifting of the peak position to ~600nm is evident from Fig4.36(B). The deep traps are subsiding substantially and shallow surface state emission is also prevailing. An excitation wavelength of ~ 500nm was used in both the cases

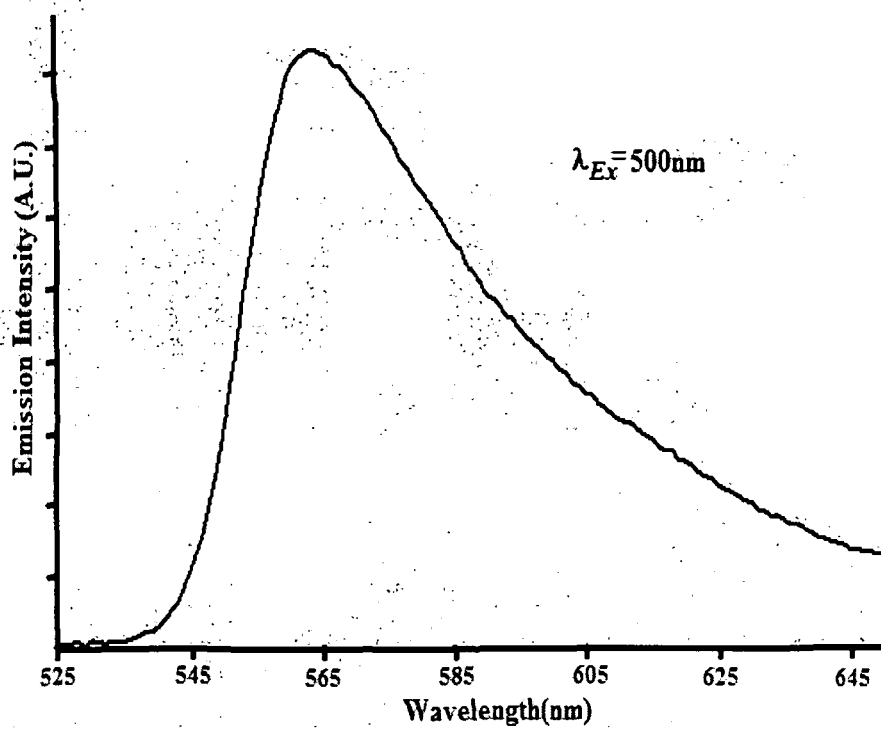


Fig.4.36 (A): PL spectra of PbS coupled quantum dots in SBR latex

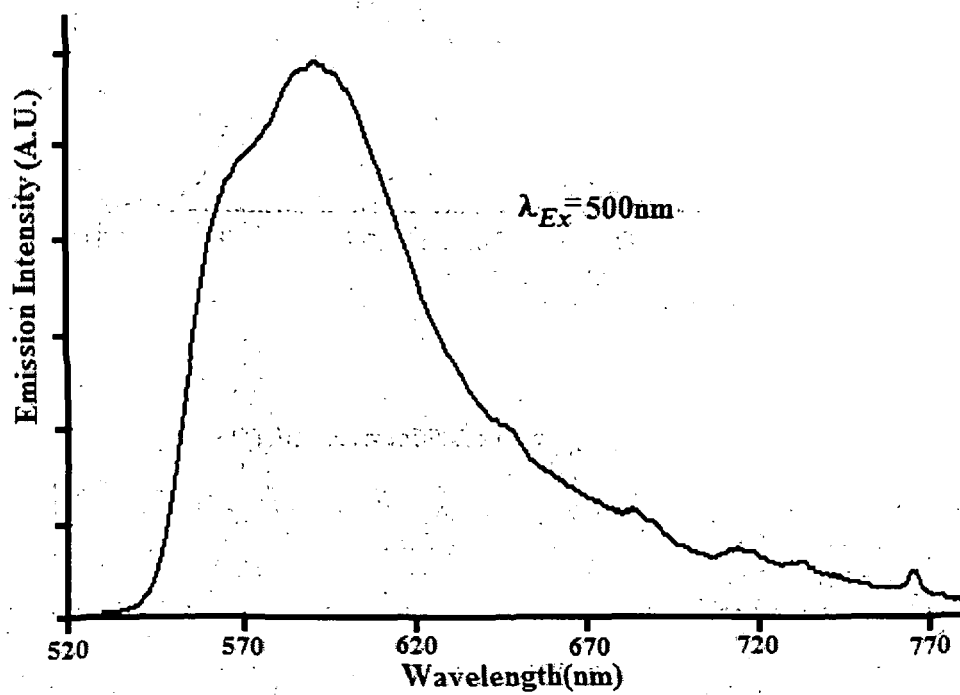


Fig.4.36 (B): PL spectra of PbS coupled quantum dots in SBR latex after aging

4.3.8 PL analysis of PbS filled SHI induced ion tracks

Photoluminescence spectra of PbS filled SHI induced ion tracks is shown in the Fig.4.37(A) and PL of the same sample after one year aging is shown in Fig.4.37(B) . Both the emission bands are peaking at $\sim 750\text{nm}$ where a wavelength of 550nm was used for excitation. Consistency of peak position signifies stability of the synthesized the nanocrystal product. Observing various PL spectra of nanocrystals embedded in a matrix fabricated by us it could be speculated that most of the low energy surface states are created due the interaction of nanocrystal with the matrix interface.

But this synthesis procedure has provided a balanced approach with regard to growth of PbS nanocrystals along with aging effects. Subsequently, the shallow surface states turned into the localized level and made emission energy consistent with time. A small increase of FWHM is noticed after aging which results from the involvement of more number of phonons compared to the fresh sample. It could be interpreted as raising energy of the individual energy state of nanocrystals due lattice vibration and consequently new radiative recombination centres were created which also contributed in luminescence process without affecting the original transition.

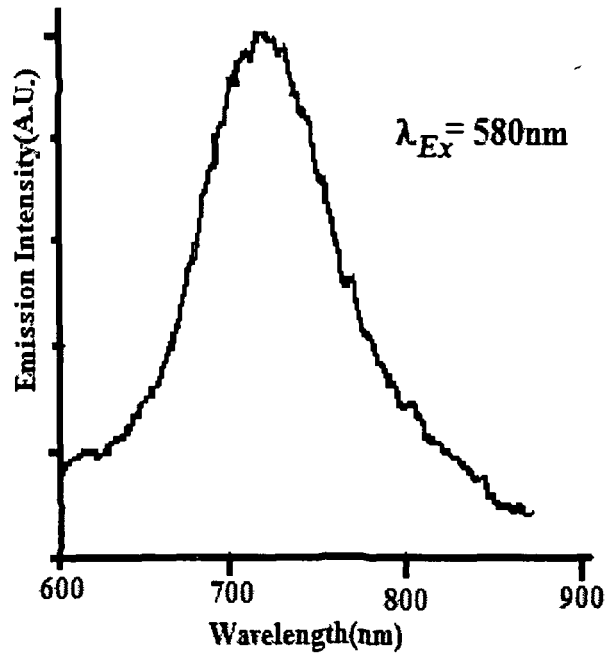


Fig 4 37 (A) PL spectra of PbS filled SHI induced ion track

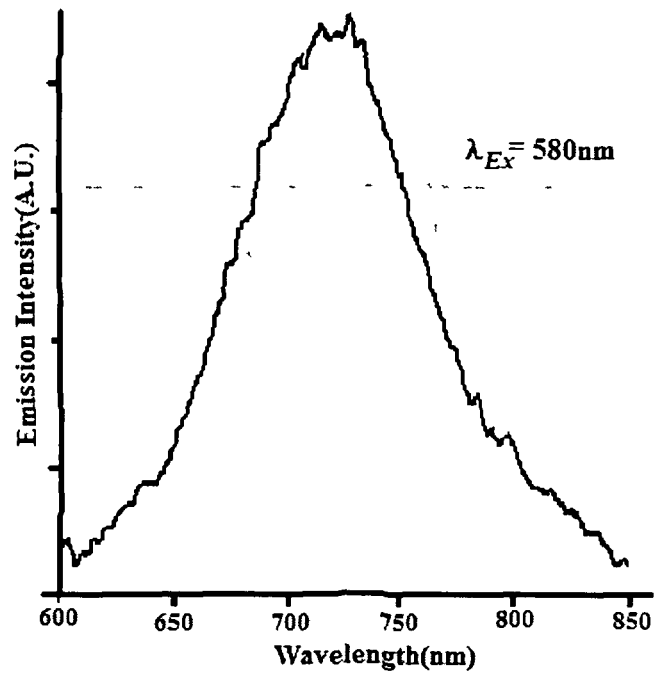


Fig 4 37 (B) PL spectra of PbS filled SHI induced ion track after aging

In this chapter, the description of characterization techniques such as TEM, XRD, PL SEM, EDS, and AFM exploited in this work to characterize synthesized quantum dots and obtained results are elaborately presented.

TEM results confirm formation stable PbS quantum dots of size 5-10 nm in both rigid matrix PVOH and flexible matrix SBR. Chain like organized structure is noticed in case of acetonitrile treated surface passivation in PVOH matrix. PbS coupled quantum dots are developed in the flexible matrix like SBR latex. The filling up of SHI induced tracks with PbS is also substantiated through TEM. Further it validates formation of nanoporous TiO₂ network and PbS/TiO₂ coupled quantum dot system.

Next, XRD results also substantiate development of PbS quantum dot in PVA matrix in SBR matrix and PbS coupled quantum dots SBR matrix and filling of SHI induced tracks with PbS. The development of nanoporous TiO₂ and PbS/ TiO₂ is also confirmed from XRD. These studies are further assisted by EDS analysis in some cases. SEM gives visible evidence of etched tracks and TiO₂ networks. AFM is able to furnish a good morphological analogy of PbS quantum dot, coupled quantum dots and PbS/ TiO₂ coupled quantum dot system.

PL analysis of prepared PbS quantum dots are able to emit in a wide emission range from visible to near infra red of the electromagnetic spectrum. Different contributors of the luminescence and their participation are also described well in pertinent places in the discussions. Specially, in case of isolated PbS quantum dots in SBR matrix, we have been able to efficiently distinguish band edge exciton emission from excitonic emission. Further, the binding energy of the excitons is also evaluated.

References

- [1] R. Egerton, *Physical Principles of Electron Microscopy*, Springer (2005)
- [2] I. T. Jolliffe, *Principal Component Analysis*, Series: Springer: Series in Statistics 2nd ed., Springer, NY, **XXIX 487** (2002) 28
- [3] P. Eaton, P. West, *Atomic Force Microscopy*, Oxford (2010)
- [4] D. B. Williams, C. B. Carter, *Transmission Electron Microscopy A Textbook for Materials Science (4-Vol Set)*, Springer (2004)
- [5] L. Ying, K. Kendra, S. Walid, R. K. Prud'homme, *Phys Rev Lett* , **98** (2007) 036102
- [6] Z. Tang, A. N. Kotov, M Giersig, *Science*, **297** (2002) 237
- [7] F. B. Li, H. Bremner, A.E. Burgess, *Corrosion Sci* , **41** (1999) 2317
- [8] S. Kelvin, Z. Y. Leung, *Inorg. Chem. Commun* **2** (1999) 498
- [9] D. Mohanta, H. Bora, N. Dutta, A. Choudhury, *Eur. Phys. J. Appl. Phys* **41** (2008) 129
- [10] S.C. Erwin, Lijun Zu, M. I. Haftel, A. L. Efros, T. A. Kennedy, D. J. Norris, *Nature* **436** (2005) 91
- [11] K. K. Nanda A. Maisels, F.E. Kruis, H. Fissan, S. Stappert, *Phys Rev Lett*, **91**(2003)106102
- [12] I. A. Ovid'ko, *Science*, **295** (2002)2386
- [13] M. Futamata, Y. Maruyama, *Analytical and Bioanalytical Chemistry*, **388**(2009)89
- [14] L. Kouwenhoven, C Marcus, *Phys World* **35** (1998)
- [15] <http://www.sandia.gov/media/NewsRel/NR1999/quantum.htm> News release August 9 (1999)
- [16] D. Mohanta, A. Choudhury, *Materials Lett* , **58** (2004) 3694
- [17] D. Mohanta, M. Deka, A. Choudhury, *J Appl. Phys.* **101**(2007)044302
- [18] R. Vogel, P. Hoyer, H. Weller, *J Phys Chem.* **98** (1994)3183
- [19] H. P. Klug E Alexander, *X-ray Diffraction Procedures Wiley NewYork*, (1974)
- [20] A. V. Dijken, A. H. Janssen, M. H. P. Smittsmans, D. Vanmaelbergh, A. Meijerink, *Chem matter* **10**(1986)2555
- [21] K. Suresh Babu C. Vijayanb, R. Devanathan, *Materials Letters* **58** (2004), 1223
- [22] Ma Xiao-Dong, Qian Xue-Feng, J. Yin ZiKang Zhu, *J. Mater Chem* **12**(2002)663
- [23] M. I. B. Bernardi, E. J. H. Lee, P.N. Lisboa-Filho, E.R. Leitea Longo, J. A. Varela, *Materials Research*, **4** (2001) 223-226

- [24] S. B. Qadri, E. F. Skelton, D. Hsu, A. D. Dinsmore, J. Yang, H. F. Gray
B. R. Ratna *Physical Review B* **60**, (1999-I) 9191
- [25] Hansen, F. Bensing, A. Waag, *Thin Solid Films*, **367** (2000)85
- [26] International Union of Pure and Applied Chemistry.
"Photochemistry". *Compendium of Chemical Terminology* Internet edition
- [27] J. T. Devreese, V. M. Fomin, V. N. Gladilin S. N. Klimin, *Phys. Stat Sol.*
224 (2001) 609
- [28] H. M. Cheong, B. Fluegel, M.C. Hanna, A. Mascarenhas, *Phys. Rev. B.*
58 (1998) R4254
- [29] M. Tanaka, J. Qi, Y. Masumoto *Journal of Crystal Growth*, **214**(2000) 410
- [30] K. Wakita, N. Nakayama, G. Hu, *Thin Solid Films* **431**(2003)181
- [31] S. Chen, L.A. Truax, J.M. Sommers, *Chem Matter.*, **12**(2000)3864
- [32] T. R. Ravindran, Akhilesh K. Arora, B. Balamurugan,
B. R. Mehta, *Nanostructured Material*, **11**(1999) 603
- [33] A. Sashchiuk, E. Lifshitz, R. Reisfeld, T. Saraidarov, M. Zelner,
A. Willenz, *Journal of Sol-Gel Science and Technology*,**24** (2002) 31
- [34] H. Cao, G. Wang, S. Zhang, X. Zhang, *Nanotechnology*, **17** (2006) 3280
- [35] S. Kar, S. Biswas, *J. Phys. Chem. C*, **112**(2008) 11144
- [36] K. K. Nanda, S.N. Sahu, *Advanced Material*, **13**(2001)280
- [37] R. E. Hummel and P Weissmen, *Hand book of optical properties of small
particles and interfaces*, **II** New York (1997)
- [38] K. Kang, K. Daneshvar , *Journal of Applied Physics*, **95** (2004) 4747
- [39] I. Kang, F. W Wise *J Opt. Soc. Am. B*, **14** (1997) 1632
- [40] A. Henglein, *Chem Rev.* **89**(1989) 1861

CHAPTER 5

Study of surface-interface phenomena of PbS/TiO₂ coupled quantum dot system

When one nanoparticle system is clubbed with another nanoparticle system in such a manner that they are separated by distance of few Å only then it is most likely that electron can tunnel from one system to the other. Further, anatase TiO₂ is porous and its pores play vital role in surface-interface kinetics. In this chapter the surface interface kinetics of the heterogeneous system of PbS/TiO₂ is investigated extensively. N₂ adsorption/desorption study was carried out on TiO₂ and PbS/TiO₂ networks independently to ascertain (i) the extent of pore filling and (ii) the kinetics of molecular adsorption. Investigation of pore filling mechanism and creating coupled heterogeneous nanostructured system would help us to understand the underlying mechanism of charge leakage phenomena in nanoelectronic junctions and circuits. The interfacial charge transfer mechanism is further substantiated by optical probing through photoluminescence analysis of PbS/TiO₂ and also with suitable electrical characterization.

In recent years, composite and heterogeneous nanostructures have emerged as technologically important candidates for application in photovoltaics, catalysis and optoelectronic sensors [1]. Production of heterogeneous nanocomposites is governed by surface and interface properties of the associated molecules that make up a coupled system. The large specific area of nanostructured TiO₂ can have direct relevance in photocatalytic activity, sensitized solar cell etc. [2]. Its pores can also be used in controlled growth of the other nanoparticles [3]. The mesoporous TiO₂ is not only suitable for controlled growth of the other materials but also useful for understanding several interfacial properties including growth kinetics and charge leakage events. Such phenomena are particularly important when a narrow band gap material is grown into the pores of a wide band gap system. In fact, a large number of oxygen vacancies are expected in TiO₂ network leading to the creation of many surface states [4]. The surface states of TiO₂ acts as trapping and recombination sites which could influence directly on its electrical and optical properties [5].

Here, the mobility of charge carriers in between the surface traps is given by

$$\mu = \frac{2v_a}{lE} \exp\left(-\frac{\varepsilon}{kT}\right) \sinh\left(\frac{eE_a}{2kT}\right) \quad (5.1)$$

Where, v is the attempt-to-jump frequency, a is the average distance between the traps, l is the number of equivalent neighbouring sites to which the carrier is allowed to jump [6], E is the applied field, ε is the trap depth ~activation energy, e is the elementary charge, k is the Boltzmann constant and T is the absolute temperature[7]. This surface conductivity can be used in photoconduction.

On the other hand, PbS is a narrow band gap semiconductor having a band gap of 0.41eV at 300 K. PbS incorporated TiO₂ system offers an ideal system to know molecular adsorption, growth kinetics and the pore filling mechanism. It was reported previously that owing to the substantial difference in lattice parameters (~1.3Å) between TiO₂ and PbS, the carrier transport can become energetically favourable across the interface [8].

5.1 Nitrogen Adsorption Studies

The morphology of ceramic materials is characterized by studying adsorption of gases onto the porous solids [9]. Most importantly the morphological parameters of a system can be evaluated by analysing the relationship between the volume of the gas adsorbed and the relative pressure of the physically adsorbing gas. Note that the relevant calculations and estimations that depend significantly on the models are assumed to represent the pores and the equations employed are to relate the relative pressure to the state of the physisorbing gas. The "monolayer concept" of adsorption was started with Langmuir [10]. Next, Brunauer-Emmett-Teller (BET) theory has appeared and it provided a theoretical basis to understand the stage of monolayer completion and the beginning of multilayer development. Identification of different physisorption isotherms is another important contribution of the BET theory which served as the basis for a more complete classification proposed later by the IUPAC [11]. In IUPAC

classification, type-IV adsorption isotherm characterizes mesoporous adsorption hysteresis and its analysis is the basis of obtaining properties of mesoporous structure. Presently, Barrett-Joyner-Halenda (BJH) method [12] and Dollimore-Heal (DH) method [13] are generally used on the basis of macroscopic condensation theory. Porosity of a porous material is the most important morphological characteristic and a number of methods can be used to calculate pore size and distribution from the results of gas adsorption measurements[14]. For example, the method of calculation described by Barrett, Joyner and Halenda (BJH) employs the Kelvin equation and involves an emptying of condensed nitrogen in the pores in a stepwise manner as the relative pressure is equally applicable either following the adsorption or the desorption branch of the isotherm. The Kelvin equation [15] comprised the correlation between pore critical radius and relative pressure (P/P_0) at capillary condensation. Originally, Kelvin's equation provided the relation of capillary radius and saturated vapour pressure of the adsorbate on spherical meniscus without consideration of the adsorbed film thickness. The adsorbed film was first formed on the pore wall during the adsorption and then gradually became thick until the films joined together. Thus, the formation of the adsorbed films in confined pores have greatly affected the capillary condensation, and the evaluation of the film thickness, pore critical radius at capillary condensation was believed to be a key problem [16]. Capillary condensation is characterized by a typical step in adsorption isotherms in the vast majority of systems which is associated with a pronounced hysteresis. The adsorption/desorption isotherms are associated with the hysteresis which results from the metastability of the gas like configuration in a single pore and hysteresis exhibits a dependency on the nature of both the adsorbent and the adsorptive, and on the temperature. The main arguments raised by this phenomenology are; phase transition associated with capillary condensation in disordered materials, the connection between the transition and the observed hysteresis etc. The origin of hysteresis behaviour and some of its features are described and interpreted in terms of the physical processes involved with the help of hysteresis phase diagram linked to the recent theories of capillary condensation. Capillary condensation of a gas inside a mesoporous material refers to the rapid change to a liquid like state that occurs at a pressure (or chemical potential) lower than the bulk saturation value [17]. This phenomenon is often considered as consequence of shifting of gas-liquid transition. Theoretical studies of fluids confined in single pores of ideal geometry have clarified the mechanism for such a shifted transition and introduced the concept of capillary

criticality that describes the fact that the liquid-vapour critical point in a pore occurs at a lower temperature than the bulk [18, 19]. However, the situation in real mesoporous materials is different where most of these systems consist of an interconnected network of pores of varying shape, curvature, and size. Generally by determining the adsorption isotherms, the morphology of a porous material is characterized. The adsorption-desorption curves represent the mass of the gas at liquid nitrogen temperature, adsorbed onto a substrate as a function of the equilibrium vapour pressure of the surrounding vapour, typically nitrogen (N_2) or Argon (Ar) is used in this purpose. Porous materials exhibit two main features: (i) a sharp increase in the amount of adsorbed gas well below the liquid-vapour coexistence pressure P_0 of the bulk adsorbate, which is explained in terms of capillary condensation in the small pores, and (ii) a hysteresis loop between the adsorption (gas is added to the sample cell) and the desorption (gas is removed from the sample cell) branches. Condensation occurs at a pressure P_{ads} and which is larger than the pressure of evaporation P_{des} . As pore diameter increases, P_{ads} moves closer to P_0 , Critical value. From the shape of this loop it is possible to derive information about the pore size, shape and distribution and connectivity. The influence of pore blocking and percolation process also comes in the picture of the observed hysteresis grounds. In spite of its ordinary occurrence, the origin of the hysteresis phenomenon is still a matter of debate. In particular, it is not clear whether hysteresis of the adsorption arises solely as a consequence of fluid behaviour in a single pore, or the role of the pore network is a dominant factor. Pore blocking effects, which occur as a result of the interconnected nature of the pore space, may give rise to hysteresis even in the absence of irreversibility in a single pore [20]. Whereas adsorption is controlled by capillary condensation, desorption is not equivalent but becomes a percolation process throughout the network. It could be speculated that this phenomenology can only bring satisfactory explanation of the observed hysteresis in case of TiO_2 network. In this hypothesis the effect of temperature cannot be neglected. The contour of the hysteresis and subsequently the area under the hysteresis loop changes with temperature. According to macroscopic thermodynamic arguments hysteresis is usually explained in terms of the different shape of the vapour/adsorbate interface during adsorption and desorption in a pore open at both the ends [21]. In this regard, Cohan et al first tried to explain it with the help of the relation between the meniscus of the adsorbed liquid and the pore shape [22]. But Kelvin gave a better interpretation through a formulation of occurrence of adsorption and desorption at

different relative pressure. Frenkel-Halsey-Hill (FHH) has modified this equation. After a while of the air exposure of a porous solid, the gas phase changed to the vapour phase and then it condenses in the pores and finally transforms to a liquid like dense state. This phenomenon is known as capillary condensation. Adsorption-desorption isotherms form a reproducible hysteresis loop and the shape of which depends on the eccentricity (peculiarity) of the pore structure. As a development of such ideas, the hysteresis was associated to the stability of multilayers adsorbed in cylindrical pores. Various techniques, namely mean density functional theory, molecular dynamics simulations of adsorption and desorption by diffusive mass transfer into model pores, and grand canonical Monte-Carlo simulations confirmed this classical picture of the adsorption in a single pore [23]. In a later approach, the pores are modelled as an ensemble of segments with different diameters and cavities. The main constraint in this system is the effect of dependence on the neighbouring domains as the condensation and evaporation pressures are influenced by the nearby domains at large. Nitrogen adsorption study is generally exploited to analyse pore size distribution and evaluation of the pore volume. A number of workers Chang et al, Boer have tried to rationalize this aspect giving good theoretical support. The same material can show different behaviour before and after heat treatment which confirms the dependence of hysteresis configuration on pore volume that changes with nature of the porosity [24].

N₂ adsorption/desorption study was performed on both nanoporous TiO₂ and PbS sensitized TiO₂ systems. The pore size distribution profiles of TiO₂ and PbS/TiO₂ systems are shown in Fig.5.1(A),(B) as per Barrett–Joyner–Halenda (BJH) model .

Note that Fig.5.1(A) is characterized by two prominent envelopes, representing two distinctly different pore types in the anatase TiO₂ network. The first kind is having a pore dia ~3.6 nm where as the second kind has an average dia of 8.8 nm. Conversely, the desorption vs. pore dia trace for PbS/TiO₂ system is characterized by a single envelope peaking around 4.6 nm (Fig.5.2 (B)).

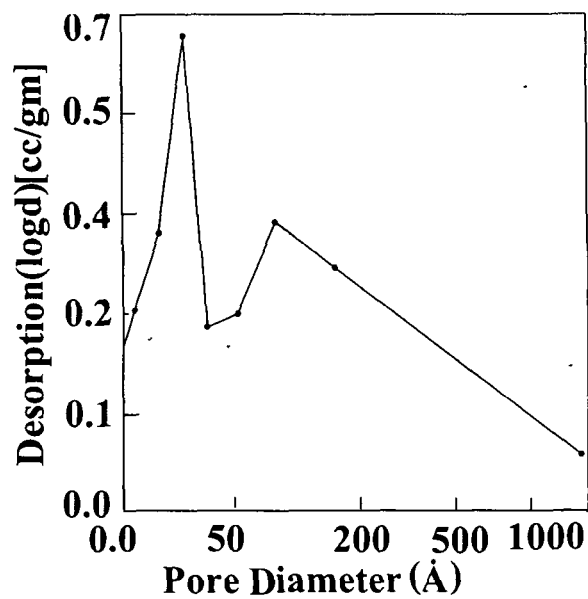


Fig.5.1 (A): Analogy of pore geometry of TiO₂

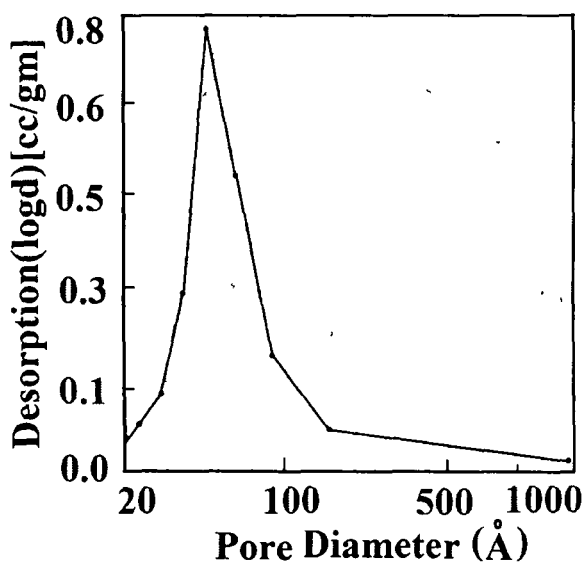


Fig.5.1 (B): Analogy of pore geometry of PbS/TiO₂

The absence of second envelope in the specimen clearly indicates that the pores of larger dia have been largely filled with PbS molecules.

Furthermore, it suggests that ultra small pores cannot be filled by the respective PbS molecules. Note that the bulk Bohr exciton size of anatase TiO₂ is 3.1nm [25]. Pores comparable to the Bohr exciton size are not permitted due to strong carrier (electron/hole) confinement effect along with increased surface energy at the interface. Since surface adsorption is hindered by charge the imbalance within the pores at large most likely, smaller pores will remain empty. The pores of intermediate size may be partially filled and that is why we noticed a shifting of the peak position from 3.6 nm (small pore in TiO₂) to 4.6 nm (small pore in PbS/TiO₂).

The surface area of TiO₂ and PbS/TiO₂ pores as estimated from overall surface absorption data are found to be 328.6 m²/g, and 217m²/g; respectively [Fig.5.1(C, D)]. Noting that N₂-adsorption is directly proportional to the available surface area, the average pore-depth can be calculated and is found to be to be ~ 765nm.

The incorporation of PbS into TiO₂ nanopores is also evident from the N₂ adsorption-desorption isotherms. In fact, the pore statistics which infer the N₂ adsorption/desorption in TiO₂ and TiO₂/PbS represents a collective phenomena governed by several mechanisms. Langmuir type of adsorption occurs in small pores where one monolayer is sufficient to fill the pores. On the other hand, the pore filling process in the pores having larger dia can be explained by BET theory [26]. Note that the adsorption/desorption largely depends on the surrounding environment i.e , relative gradient in surface tension, chemical potential, concentration of the adsorbent/adsorbate, temperature etc. As many of these parameters are different in the unfilled and PbS filled TiO₂ networks, noticeable variation in the half widths of the curves representing the pore geometry is justified (Fig. 5.1(A, B)).

Considering optimum pressure variations, as can be seen from Fig.5.1(E, F) the nitrogen adsorption has been reduced from 254.4 cc/g to 167.3 cc/g for TiO₂ and PbS/TiO₂ system, respectively. The reduction in the adsorbed volume indicates that about 34 % of the total number of pores in the TiO₂ network has been filled by PbS molecules.

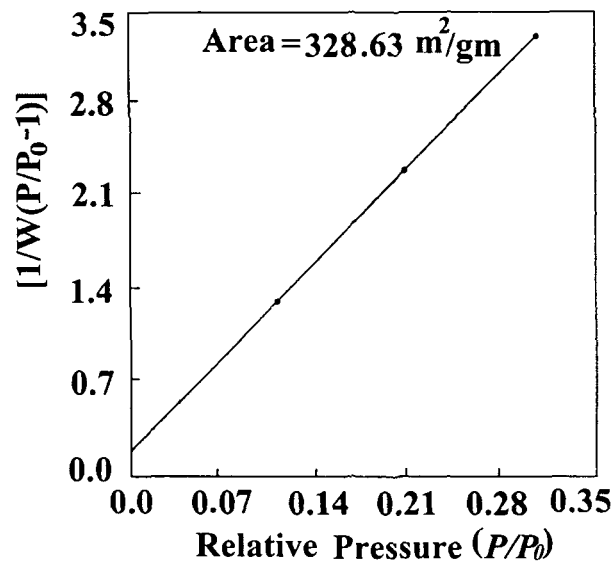


Fig 5 1(C) Surface area analogy of TiO₂

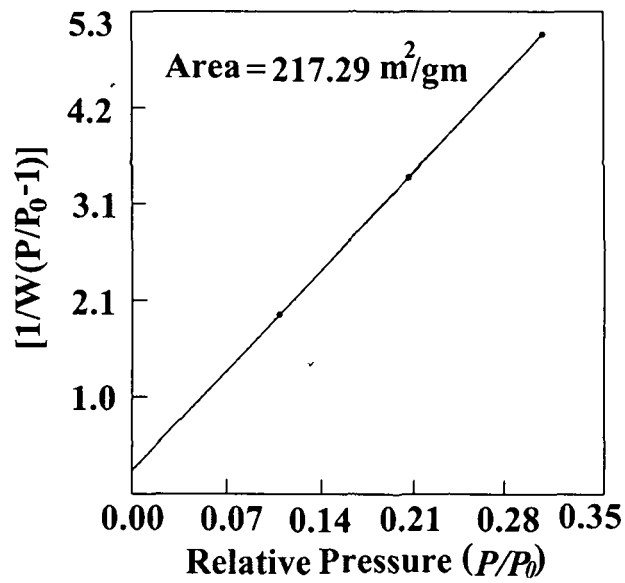


Fig 5 1 (D) Surface area analogy of PbS/TiO₂

Eventually, upon PbS incorporation, the unfilled space get reduced. Reduced amount of N₂ adsorption is a consequence of reduction in unfilled the space. The adsorption/desorption isotherms in both the systems exhibit hysteresis configuration beyond a critical pressure.

As the hysteresis loop is expanded in case of PbS/TiO₂ specimen compared to its counterpart (i.e., TiO₂ system), two important conclusions can be drawn. First, the desorption becomes slower in the PbS/TiO₂ system owing to pore filling and the second the introduction of a heterogeneous system. The pores of smaller dia did not participate in hysteresis configuration. Moreover, the slope of the isotherm (from the linear regime of Fig.5.1 (E, F) corresponding to PbS/TiO₂ system has a value half of its value for the TiO₂ system. This indicates that nitrogen adsorption-desorption process is relatively slow for a heterogeneous system above a critical pressure ($0.41 P_0$).

The area under the hysteresis for PbS incorporated TiO₂ system, is about 2.5 times larger than the corresponding TiO₂ network. In case of a PbS filled TiO₂ network, it is expected that owing to the drastic variation in the rates of adsorption and desorption the area under the hysteresis has been increased significantly.

The hysteresis occurs as a result of the differences in the rates of adsorption and desorption process in a particular system. The pores having larger dia (> 4.0 nm) only shows hysteresis in consistency with the other reports [27]. Essentially, the pore filling with N₂ adsorption occurs as a result of capillary condensation whereas pore emptying (N₂ desorption) is a result of the abrupt evaporation due to the relative pressure gradient.

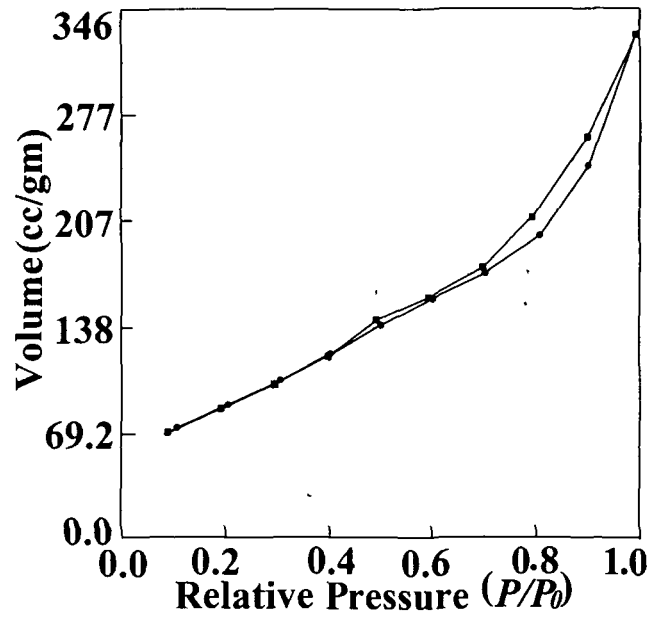


Fig.5.1(E): N₂ adsorption isotherm of TiO₂

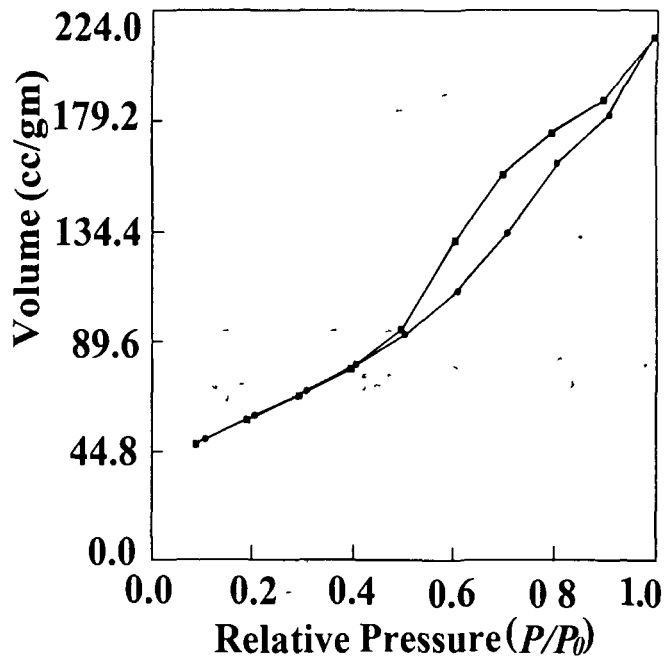


Fig.5.1(F). N₂ adsorption isotherm of PbS/TiO₂

This can also be described with the help of popular Kelvin's equation [28]

$$\ln \frac{p}{p_0} - \frac{2\gamma V_m}{rRT} = 0, \quad (5.2)$$

where p and p_0 are the actual and saturated vapour pressures, γ is the surface tension of liquid N_2 , V_m is the molar volume, and r being the radius of the droplet. Here, R is the universal gas constant (8.31 SI units), and T is working temperature (77 K).

As shown, (Figure 7; V_m (TiO_2) =125cc/gm; and V_m (PbS/TiO_2) =79.15cc/gm) the respective molar volumes consumed at critical pressure ($0.41P_0$) are found to be different for different systems. In case of PbS/TiO_2 , V_m falls by 37 % compared to its value for TiO_2 system. Interestingly, the dia ($2r$) of the N_2 droplet (close to the second kind pore dia) that would desorb out of the pores is found to be 12.3 and 8.0 nm for TiO_2 and PbS/TiO_2 systems; respectively. Since untreated TiO_2 has wide distribution of pores, the model predicted the value which is some what larger than the corresponding experimental value. On the other hand, in PbS/TiO_2 case, owing to appreciable pore filling by heterogeneous molecular aggregates the desorption of N_2 would take place in a more controlled manner. Consequently, the experimental value of larger sized pores (~8.8 nm) matches reasonably well with that of the theoretically predicted size of the desorbed N_2 droplet (~8.0 nm).

In order to visualize further, we consider the percolation mechanism in our systems of interest [29]. Note that the anatase TiO_2 has a cage like network and adsorption/desorption phenomena depends on the interconnection between the pores known as percolation. It favours uniformity by maintaining adsorption and desorption area equal. The pores are connected through narrow internal channels. Prior to PbS incorporation, the interlinks were supposed to be smooth that make all the pores accessible for adsorption. PbS molecules generally grow inside the pores as well as outside the pore walls and initiate pore blocking as a result of which adsorption/desorption process gets hindered. In these pores, adsorption/desorption would not proceed independently owing to percolation via pore interlinks. Further, spontaneous nucleation of N_2 gas bubbles namely cavitation facilitates desorption mechanism [30]. We speculate that the PbS aggregates would stop cavitation and obstruct fast desorption in PbS/TiO_2 system. Consequently, desorption path would follow a slowly varying path resulting a relatively wider hysteresis loop. Substantial amount of departure from the narrow hysteresis loop (as seen for TiO_2 system) is ascribed to the constrained percolation and cavitation within the pore-filled networks. As these effects are very strong in TiO_2 nanostructured systems, sometimes this would lead to the disappearance of hysteresis in TiO_2 . The existence of wider hysteresis loop PbS/TiO_2 system ensures incorporation of PbS into the TiO_2 pores. The PbS sensitized

TiO₂ system forms an ideal coupled semiconductor system to understand interfacial charge leakage phenomena that can be applied to nanoelectronic components and junctions [31]. The PbS/TiO₂ system has also potential application in dye sensitized photovoltaic cells [32].

5.2 Optical probing of interfacial charge transfer:

Fluorescence spectroscopy has been explored to probe electron injection from PbS quantum dots to TiO₂. Photoluminescence spectra of nanoporous TiO₂ and PbS sensitized TiO₂ has been taken. Note that incorporation PbS effectively changes the photoluminescence intensity of TiO₂ efficiently while investigating for different concentration of PbS incorporation. The PL spectra of PbS sensitized amorphous TiO₂ is shown in Fig.5.2. PL spectra of anatase TiO₂ incorporated with PbS (*Type I*) is shown in Fig.5.5(A) and PL spectra of anatase TiO₂ sensitized with PbS (*Type II*) is depicted 5.5.(B) respectively. Since, intensity of luminescence depends on number of particles participating in the luminescence process therefore it could be explained that the origin of emission process in TiO₂ has subsided by incorporation of PbS. This is a consequence of interfacial charge transfer.

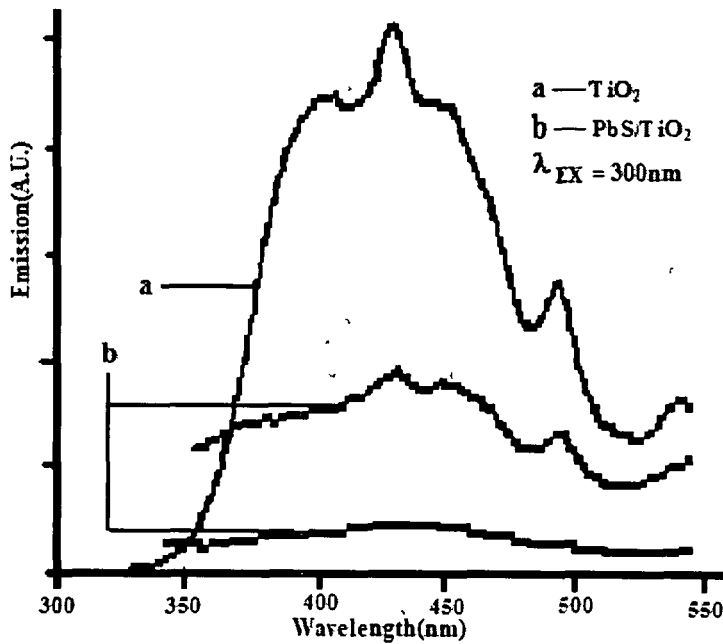


Fig 5.2 PL of TiO₂ and PbS/TiO₂

Let us consider the band structure of PbS and TiO_2 and which would help in understanding the interfacial charge transfer and its effect on photoluminescence. The structure of band gap in the surface of each material is different from its bulk counterpart and the same view is valid for nanomaterial also [33]. Both PbS and TiO_2 are n-type semiconductors in which surface states always lie near the bottom of the conduction band. The Fermi level of p-type semiconductor is filled up to the surface state level. The arbitrary band structure of PbS and TiO_2 and interface of PbS/ TiO_2 are shown in Fig.5.3 (A) Fig.5.3(B) and Fig.5.4 respectively. Since electron affinity of PbS(4.5eV) wrt vacuum is less than the electron affinity of TiO_2 (5.2eV) (34) wrt vacuum, thus electron transfer from PbS to TiO_2 is highly favourable when ideal conditions are met. The detailed analysis of the development of potential difference will be explained while discussing electrical properties

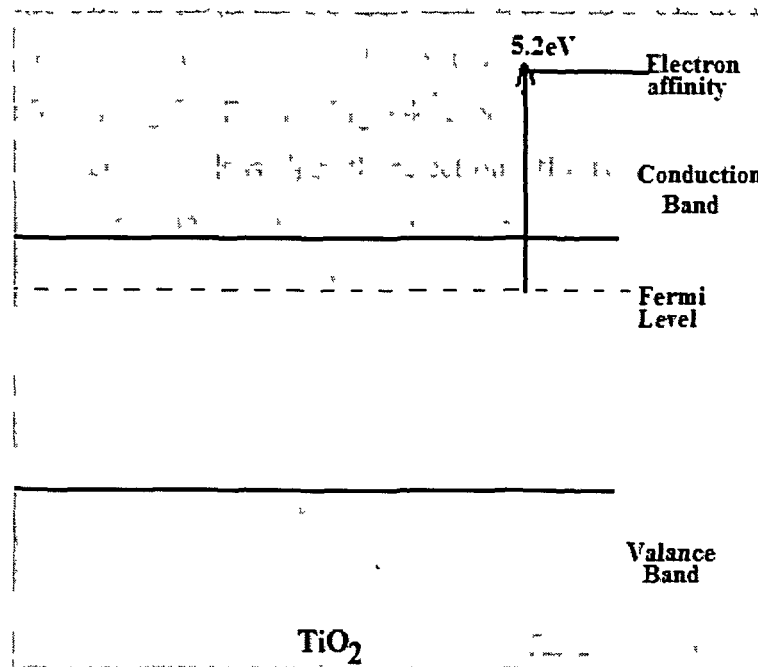


Fig5 3 (A) Schematic representation of TiO_2

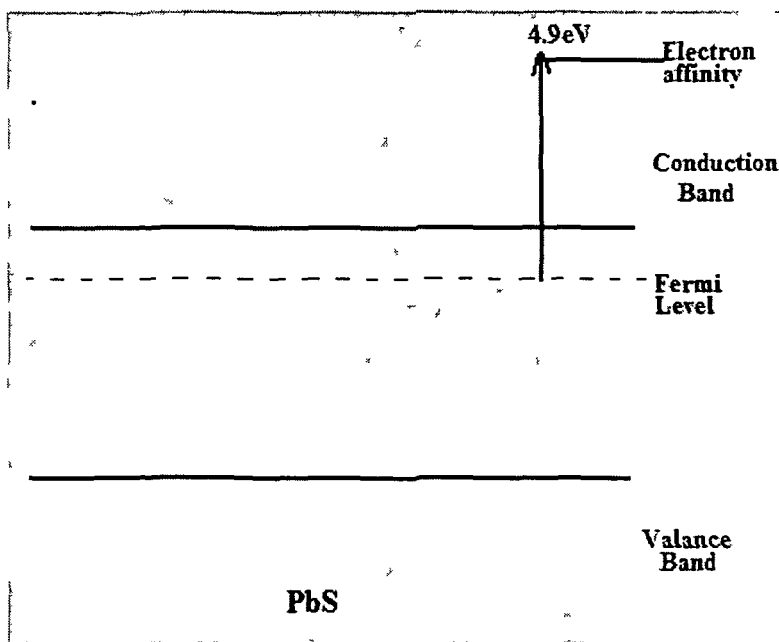


Fig 5 3 (B) Schematic representation of PbS

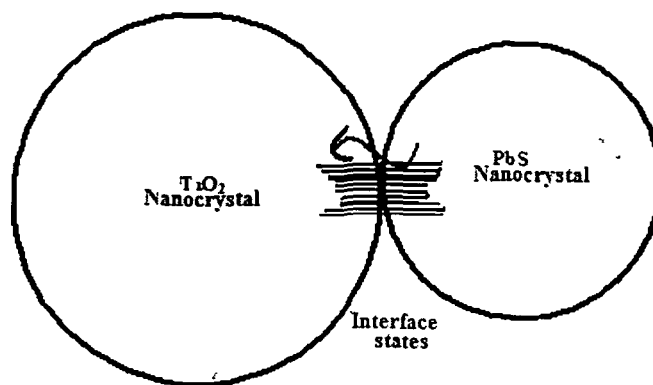


Fig5 4 Scheme of interfacial charge transfer

Due to transfer of charge carrier from PbS to TiO_2 , the density of the exciton increases near the conduction band which further minimizes binding energy of the excitons in TiO_2

Many radiative luminescence centres had converted to non radiative centres as a consequence of charge leakage through the interfaces. As a result, the number of exciton formation becomes lesser. Since excitons are responsible for performing photoluminescence of semiconductor material therefore its number plays vital role in enhancing or suppressing the intensity. The amorphous TiO_2 contains a large number of surface traps alongwith large number of empty space to accommodate charge carriers. This condition facilitates charge transfer more effective and suggests the change in intensity with different rate of charge transfer. On the other hand, the empty spaces diminish with heat treatment owing to development of degree of crystallinity. The charge transport is most improving in case of PbS which has grown inside the pores of the TiO_2 . Therefore, a discernable change in intensity is noticed in PbS sensitized amorphous TiO_2 .

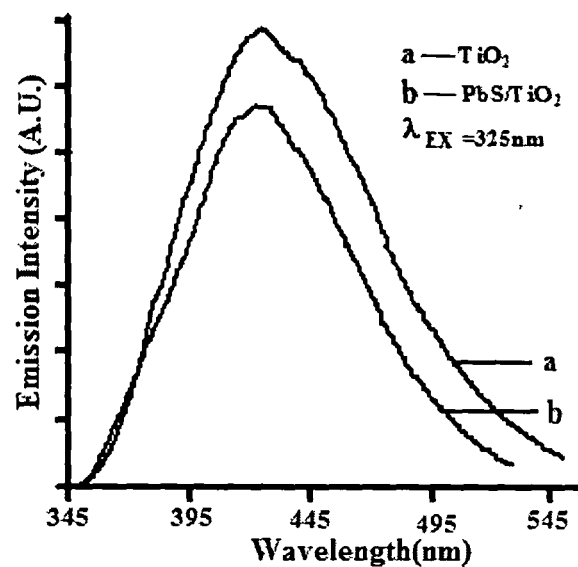


Fig 5 5 (A): Effect of PbS on PL of PbS/TiO_2 (Type1)

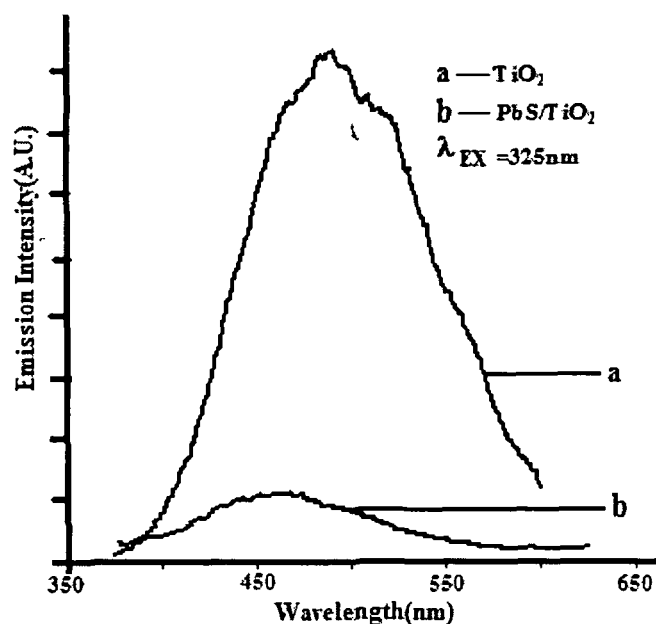


Fig5.5 (B): Effect of PbS on PL of PbS/TiO₂ (TypeII)

Anatase TiO₂ also supports the interfacial charge transport. But in the last case, the difference in intensity was found smaller from the previous cases. This could be due to the diminishing effect of smaller pores in TiO₂ where PbS has grown over the surfaces of TiO₂ but not able to take part in charge transport fully. But lessening of FWHM could be distinguished from the observed PL spectra inferring dropping the number of surface states.

5.3 Electrical properties of TiO₂/PbS

The probing of interfacial charge transfer in coupled quantum dot through electrical measurements was reported previously [35]. The current generation due to the charge transport through the interface becomes detectable while connected to an external biasing source. The PbS/TiO₂ system is promising heterogeneous coupled quantum dot

system which offers deep insight to interfacial charge transport evidence at room temperature.

I-V measurements on TiO_2/PbS were carried out with the help of Keithley conductivity meter. Two types of connection were made to observe the electrical properties this system. One of which is gap type where connection is made on glass substrate and other is a sandwich type where connection were made on ITO (Indium-Tin-Oxide) coated glass substrate. While making this connection the work functions of glass, ITO coating as well as TiO_2 and aluminium have been checked to get non rectifying Ohmic contacts. A thin aluminium layer is coated on the PbS/TiO_2 thin film using a thermal evaporation method (HIND HIVAC, Model:12A4D). The current voltage characteristic of the TiO_2/PbS system in gap type of connection is shown in Fig.5.7 (A) and evaluation curve of its nature is depicted in Fig.5.7 (B). The I-V characteristic in sandwich type connection along with its nature evaluation curve is depicted in Fig5.8 (A) and Fig5.8(B) respectively. This I-V characteristic shows linear dependence of current with respect to voltage i.e. diode nature in both the cases. Dark current was avoided in either of the cases. This instrument set up has an automatic adjustment tool which only considers the signals coming from the sample being measured.

This works up to a temperature limit 30°C . Another advantage of this instrument is that it can measure current or voltage value which falls in the range of nanometer scale.

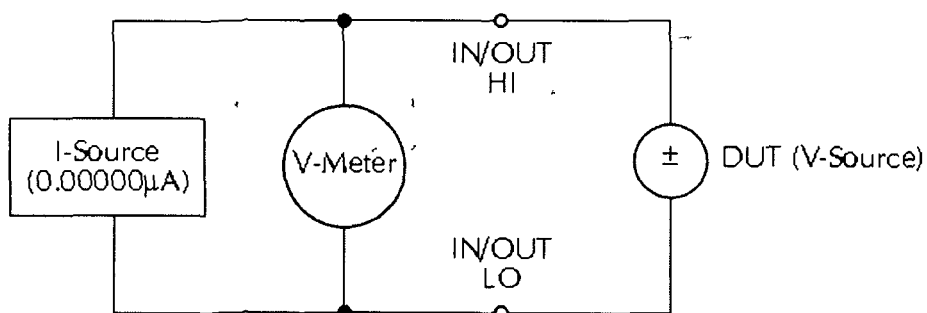


Fig5 6 Schematic diagram of the source meter used for I-V measurements

The behaviour of the current suggests Pool-Frenkel type of conductivity [36^a]. A potential is developed between the two particles of lead sulphide(PbS) and titanium-dioxide(TiO₂) which is responsible for current conduction offered by this system. In Pool-Frenkel conductivity, a built in potential gradient is developed due to unequal distribution of charges between two adjacent particles in polycrystalline semiconductor material. Note that nanomaterial possesses a number of interface states where electrons are trapped. Actually, some of the electrons become free due to some thermal disturbance for small interval of time and they can move in the conduction band i.e. can move from one location to other until they become trapped again in these trap sites [37]. While moving from place to place electrons produces a concentration gradient among the particles which further resist their own movement. But this barrier potential could be lowered with an application of an external electric field so that charge conduction takes place again.

The nature of Pool-Frenkel type of conductivity [36^b] can be realized with help of characteristic *I-V* behaviour a material. This conductivity is similar as forward biased diode characteristic. In our case also current vs. voltage is given by Pool Frenkel type expression.

$$\ln \sigma_i(E) = \ln C + \frac{\beta_{pf}}{kT} \cdot F^{1/2} \quad (5.2)$$

$$\Rightarrow \ln \sigma_i(E) = mF^{1/2} + c$$

where, right hand side contains natural logarithm of conductivity (σ) at a particular temperature and left hand side contains square root of applied field i.e. applied voltage (F). Using the following Equation (5.2), a straight line plot is obtained. This conductivity resembles the forward biased diode characteristics.

Fig.5.7 (A), (B) current vs voltage plot of PbS/TiO₂ its respective Pool-Frenkel behaviour is shown for gap type connection. In contrast, the similar I-V plot along with Pool-Frenkel behaviour of PbS/TiO₂ for sandwich type of connection is shown in Fig.5.8 (A), (B). This conductivity is sensitive to temperature because the charge transport depends on thermal agitation.

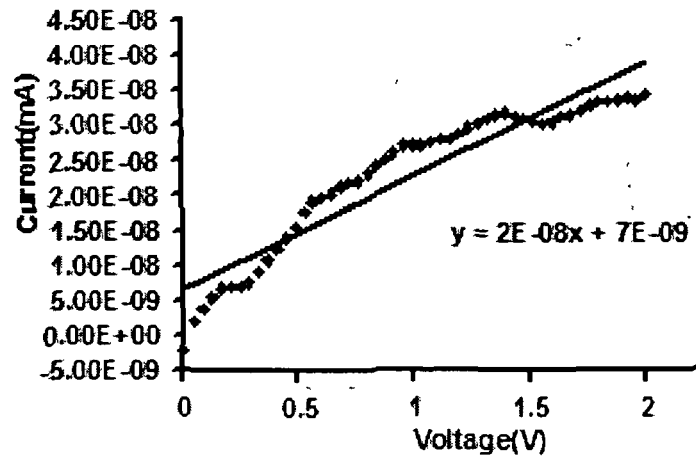


Fig5.7 (A) I-V plot for PbS/TiO₂ for gap type connection

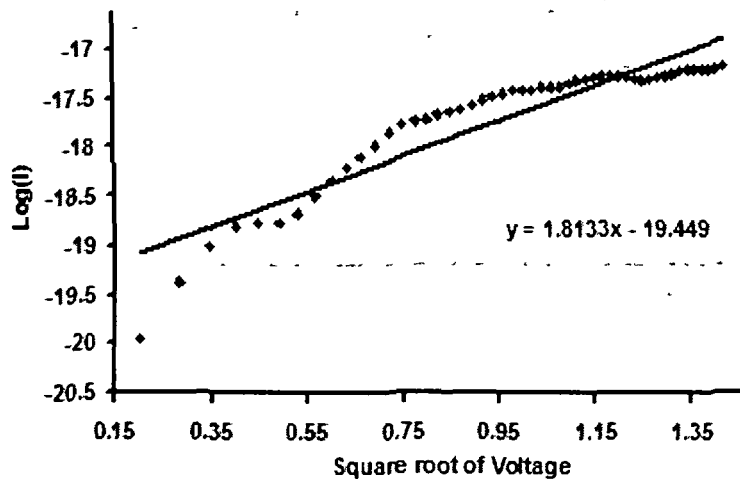


Fig5.7 (B): Evaluation of I-V plot

Therefore if we plot the logarithm of conductivity with respect to square root of applied field i.e. applied voltage (F) and if it satisfies the equation of a straight line then the concerned conductivity should be of Pool-Frenkel type which is a direct evidence of charge conduction through interface states between two nearby grains. β_{pf} is known as Pool-Frenkel coefficient. The strength of Pool-Frenkel conductivity could be evaluated with help of evaluation of Pool-Frenkel coefficient for that material at that particular temperature.

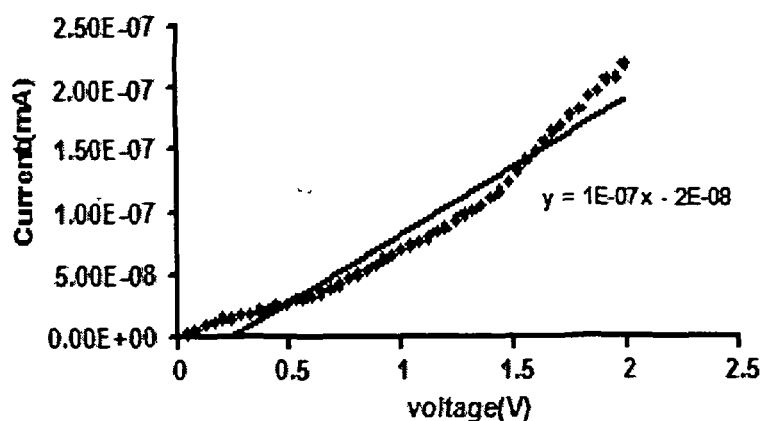


Fig5.8 (A). I-V plot for PbS/TiO₂ for sandwich type connection

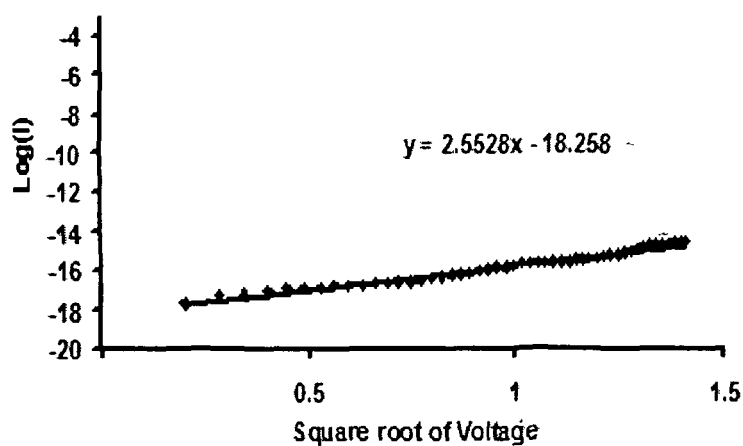


Fig. 5 8(B): Evaluation of I-V plot

The nature of these plots clearly signifies occurring of Pool-Frenkel type of conduction in PbS/TiO₂ heterogeneous coupled quantum dot system. Since Pool-Frenkel type of conductivity itself indicates conductivity due to surface charge therefore conduction of charges through the interfaces of PbS and TiO₂ has been verified.

Explicit sensitization of TiO₂ pores with PbS molecular adsorption has been demonstrated and the interfacial charge transfer phenomena between coupled nanostructured systems is being investigated. We have also tried to bring a new idea of optical probing of interfacial charge transfer in a heterogeneous network of PbS/ TiO₂ coupled quantum dot system. Further, it has been supported by electrical measurements.

References:

- [1] P. V. Kamat, *Chem. Rev.* **93** (1993) 267
- [2] Y. Wang, S. Zhang, X. Wu, *Nanotechnology*, **15** (2004)1162
- [3] J. Bisquert, A. Zaban, P. Salvador, *J. Phys. Chem. B*, **106** (2002) 8774
- [4] D. Bahnemann, A. Henglein, J. Lilie, L. Spanhel, *J. Phys. Chem.* **88** (1984) 709
- [5] P. Hoyer, R. Konenkamp, *Appl. Phys. Lett.* **66**(1995)349
- [6] L. A. Dissado, J. C. Fothergill, *Electrical Degradation and Breakdown in Polymers*
Peter Peregrinus, London, (1992)
- [7] J. A. Anta, J. Nelson, N. Quirke, *Phys. Rev. B* , **65**(2002) 125324
- [8] P. Wang, L. Wang, B. Ma, B. Li, Y. Qiu, *J. Phys. Chem. B*, **110** (2006) 14406
- [9] A. Dais, V. S. T. Ciminelli, *Ferroelectrics*, **241** (2000) 9
- [10] I. J. Langmuir, *J. Amer Chem. Soc.*, **40** (1918)1361
- [11] J. Rouquerol, D. Avnir, C.W. Fairbridge, D.H. Everett, J.H. Haynes, Penicone,
J. D. F. Ramsay, K. S. W. Sing, K. K. Unger, *Pure Appl. Chem.*, **66**(1994)1739
- [12] E.P. Barrett, L.G Joyner, P.P. Halenda, *J. Am. Chem. SOC.* **73** (1951)373
- [13] A. Touzik, M. Hentsche, R. Wenzel, H. Hermann, *J. Alloys and Compounds*
426(2006)272
- [14] W. D. Machin, *Langmuir*, **10**(1994) 1235
- [15] S. J. Gregg and K. S. W. Sing, *Adsorption, Surface Area and Porosity*, London:
Academic Press (1982)
- [16] F. Casanova, C. E. Chiang, C-P Li, I. K. Schuller, *Applied Physics Letters* ,
91 (2007) 243103
- [17] A. V. Neimark, P. I. Ravikovitch, A. Vishnyakov, *Phys. Rev. E*, **62**(2000) R1493
- [18] E. A. Ustinov, D. D. Do, *J. Phys. Chem. B* **109** (2005) 11653
- [19] K. Morishige , N. Tateishi *Journal Of Chemical Physics* **119**(2003) 2301
- [20] G. Mason, *J. Colloid Interface Sci.*, **88** (1982) 36
- [21] L. Bruschi, G. Fois, G. Mistura, K. Sklarek, R. Hillebrand, M. Steinhart,
Ulrich Gosele, *Langmuir* **24** (2008) 10936
- [22] L. H. Cohan, *J. Am. Chem. SOC.* **60** (1938) 433
- [23] L. D. Gelb, *Mol. Phys.*, **100**(2002)2049
- [24] Z.-M. Wang, R. Kato, K. Hotta, K. Miyazawa, *Journal of Physics: Conference*
Series, **159** (2009) 012013
- [25] C. Kormann, D. W. Bahnemann, M. R Hoffmann, *J. Phys. Chem.* **92** (1988) 5196

- [26] S. Brunauer , L. Deming , S. Deming, W.E. , E. Teller, *J. Amer Chem. Soc.*, **57** (1940) 1754
- [27] P. C. Ball, R. Evans, *Langmuir*, **5**(1989)714
- [28] Y. Zhanga, F. Leung-Yuk Lamb, Z.F. Yana, X. Hub,
Chinese Journal of Chemical Physics, **19** (2006) 102
- [29] S. Muhammad, S. Sahimi, M. Sahimi, *Application of Percolaion Theory*,
CRC Press (1994)
- [30] K. Morishige, M. Ishino, *Langmuir* **23** (2007) 11021
- [31] C. Longo, M-A De Paoli, *J. Braz. Chem. Soc.*, **14** (2003) 889
- [32] P. Hoyer, R. Konenkamp, *Appl. Phys. Lett*, **66**(1995)349
- [33] Al. L. Efros, M. Rosen, *Annu. Rev Mater. Sc*, **30**(2000)475
- [34] B-R Hyun, Y-W Zhong, Bartnik A. C. , L. Sun, Abrun D.H., F. W. Wise,
D. Jason , Goodreau, J. R. Matthews, T. M. Leslie, N. F. Borrelli,
ACS Nano **2** (2008) 206
- [35] D. Mohanta, M. Deka, A. Choudhury, *J. Appld. Phys.* **101**(2007) 044302
- [36^a] R. L. Perritz, *Physical review* **97**(1956) 322
- [36^b] J. G. Simmons, *Phys. Rev. B* **166**(1968)912
- [37] R. D. Gould, C. J. Bowler, *Thin Solid Films* **164** (1988) 281

CHAPTER 6

Investigation of nonlinear optical properties of PbS nanocrystalites through two photon excitation fluorescence (TPEF) and second harmonic generation (SHG) studies

Since PbS is better suited in the strong-confinement limit (because of large exciton Bohr radius), large optical nonlinearities are expected in PbS quantum dots. This opens tremendous potential applications in nanophotonics, nonlinear optics and spectroscopy. The fascinating aspects were perceived while studying its nonlinear optical properties.

Thus, a detailed study of nonlinear optical properties of PbS quantum dots was included in our next plan. Nonlinear optics is a phenomenon in which a nonlinear response of the field component is induced while sufficiently intense light (10^6 volt/m) is allowed to interact with a material system. The study of nonlinear optics was first developed with the use of a laser after the work of Maiman in 1960 [1]. But it was first explored by Franken and co-worker by their classic experiment of second-harmonic generation who demonstrated in quartz crystal with the use of a ruby laser [2]. In this chapter we discuss two photon excitation fluorescence (TPEF) and imaging, second harmonic generation (SHG) study through SHG imaging of ~ 5 nm sized surface passivated PbS quantum dots.

In recent years, there has been a great deal of research interest in the nanoscale narrow band gap semiconductors owing to scope for tunable light emission over a wide electromagnetic spectrum. Schmitt-Rink et al. [3] have argued that the resonant nonlinear optical properties would be strongest for the nanocrystals of size (R) smaller than the bulk Bohr excitonic radius [4]. As PbS nanoparticles in the strong quantum confinement limit can be suitably fabricated with advanced synthesis protocols, it is better opted for various studies in the said regime. Ordinarily, the optical properties of a material do not depend on the intensity of the light, and as a result, light beams do not interact with each other. However, at high enough intensities, materials become nonlinear; the light changes the material properties [5]. Optical nonlinearities are generally strongest when the photon energy matches an optical transition in the solid; this property is referred to resonant enhancement of the nonlinearity [6]. Since

nanoscale materials, in the strong confinement regime display resonantly enhanced optical nonlinearities with their strong absorptions therefore in order to use such quantum confined solids for lasing, frequency modulation and bioimaging purposes, it is extremely important to explore upconversion of light, harmonic generation, and saturation absorption characteristics [7]. Optical nonlinearities can be implemented in various applications based on light energy, which are potentially much faster than electrical switches. Thus, these materials can become potential candidates for fast optical switching [8] and information processing [9]. A pump laser can induce transient asymmetry in the crystalline structure, capable of exciting dipoles that oscillate in a way to give rise to the second order nonlinear optical phenomena. The relaxation to the ground state from the excited states can be accompanied by the radiation of photons with frequency doubled [10]. As far as nonlinear optical studies are concerned, earlier researchers have used either *z-scan* method [11] or four wave mixing technique [12] for determining nonlinear refractive index (consequently, nonlinear susceptibility) and in order to assess the figure of merit of the nonlinear device. Conversely, much attention has not been given to imaging fluorescent nanoparticles by direct excitation or via two photon excitation processes. Traditional fluorophors, e.g., organic dyes and fluorescent proteins are limited by their narrow absorption range, broad emission spectra along with weak photostability. Observation of fluorescence from single PbS quantum dots using confocal microscopy [13] and water-soluble PbS quantum dots for *in vivo* biological imaging [14] that absorb and emit in the near IR regime have been reported previously. Here, we discuss two photon absorption events and corresponding nonlinear optical imaging of surface passivated PbS nanocrystals using confocal laser scanning spectroscopy with Ti:Sapphire as the excitation source. A correlation of excited nanoparticles and spots depicting particle assemblies has also been highlighted. Advances in molecular engineering have enabled the design of molecular structures of various resonances and symmetries with optimized one and two-photon absorption cross sections or combining different optical properties such as luminescence and second harmonic generation (SHG). Semiconductor nanocrystals in a transparent matrix have attracted recent interest due to their potential in applications in nonlinear optics such as photonic switching [15]. Hence, two-photon excited fluorescence TPEF and second harmonic generation SHG has become an important tool for characterization of nanocrystals grown in amorphous matrix such as polymers. TPEF is an incoherent process allowed in centrosymmetric and noncentrosymmetric media, which exhibits a

specific anisotropy depending on the medium symmetry. Conversely, SHG is the signature of a crystalline noncentrosymmetric phase in the sample, with sensitivity down to the nanometric scale [16]. In addition, macro arrangements have been optimized using tensorial oriented gas model, which predicts that an enhancement of the SHG efficiency is expected from the noncentrosymmetric crystalline arrangement of efficient nonlinear molecules. Nonlinear microscopy may be broadly divided into two classes: incoherent or coherent. Incoherent microscopy produces signals whose phase is random and whose power is proportional to the concentration of radiating molecules. Fluorescence is a common example of an incoherent signal. Nonlinear versions of fluorescence microscopes are based on the simultaneous absorption of two or more photons, the most well known being two-photon excited fluorescence (TPEF) microscopy. In general, SHG microscopy is combined with TPEF microscopy in the same instrument. Both contrasts can be derived from the same laser excitation, exhibit the same intrinsic 3d resolution, and are often. Despite their similarities, however, TPEF and SHG constitute very different signals. The first is fluorescence, meaning it can provide molecular specificity since the fluorescence wavelength depends on the molecule species. The second is scattering, which cannot provide molecular specificity, but specifically reveals mesoscopic organization in the sample. As such, the signals are complimentary. By far, the most common excitation source in TPEF or SHG microscopy is the mode-locked Ti:sapphire laser, which is robust and tunable over a wide range of wavelengths spanning 700nm to 1000nm.

6.1.1 Two photon absorption studies

Absorption and emission of two or several photons can occur stepwise or simultaneously. The stepwise and simultaneous absorption of photons are represented pictorially by Fig6.1.

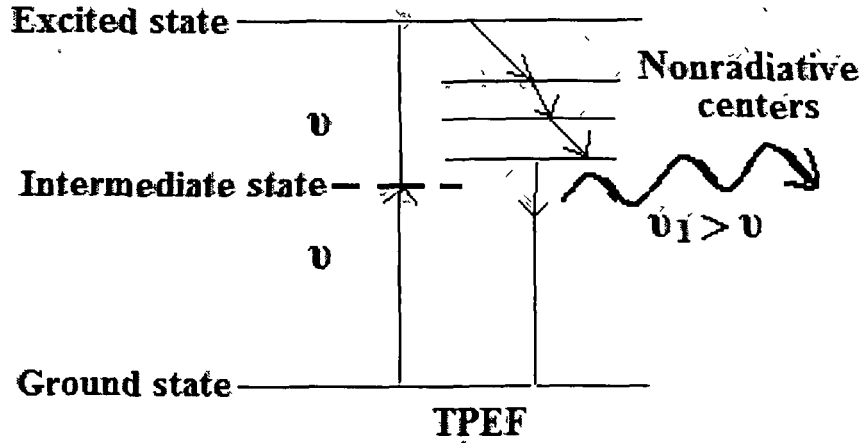


Fig6.1: Schematic representation of TPEF

Absorption via an intermediate energy state or without may occur as coherent interaction between light and the transition dipole moment. Using rate equation, the two photon transition probability from the state 'l' to the state 'm' can be described as [17]

(1) two-photon absorption from l to m ($N_l \rightarrow N_m$)

$$\frac{\partial N_l}{\partial t} = -\sigma_{l,m}^{(2)} I_1 I_2 N_l \quad \text{and} \quad \frac{\partial N_m}{\partial t} = +\sigma_{l,m}^{(2)} I_1 I_2 N_l \quad (6.1)$$

(2) two photon emission from m to l ($N_m \leftarrow N_l$)

$$\frac{\partial N_l}{\partial t} = +\sigma_{m,l}^{(2)} I_1 I_2 N_m \quad \text{and} \quad \frac{\partial N_m}{\partial t} = -\sigma_{m,l}^{(2)} I_1 I_2 N_m \quad (6.2)$$

The photon transport equation is given by,

$$\frac{\partial I}{\partial z} = -N_{total} \sigma^2 I_{exe}^2 \quad (6.3)$$

which can be integrated to give ,

$$I(z) = I_0 \frac{1}{1 + \sigma^{(2)} N_{total} I_0 z} \quad (6.4)$$

With the incident exciton intensity I_0 at $z=0$ and the total number of absorbing particles N_{total} .

A theoretical modelling of two photon processes can be illustrated as combined successive transition from the ground state $|g\rangle$ to virtual state $|v\rangle$ to upper state $|u\rangle$ representing the transition from the second photon. The transition state is then represented by the linear combination of the wavefunctions of all real energy states of the of the matter which have allowed single photon transitions from the ground state and the transition probability for this transition results from the sum of all these single transition probabilities. The second transition is treated in the same manner and thus the final transition results from the product of these two single step transition probabilities.

Therefore, the two photon process is associated with specific selection rules. Compared to the single photon transitions which are allowed between the states of opposite parity, two photon transitions are strong between the states of the same parity.

Allowed single photon transitions:

even \longrightarrow odd and odd \longrightarrow even

Allowed two photon transitions

even \longrightarrow even and odd \longrightarrow odd

and thus with two-photon spectroscopy states can be reached which are forbidden in conventional spectroscopy. If the two photon transition occurs almost resonantly via a real energy level of the sample then the transition probability is strongly enhanced and reaches values of the usual single photon transitions.

6.1.2 Second harmonic generation (SHG) studies

When a material medium is subjected to one or more electromagnetic waves, the atoms and molecules of the medium oscillate not only at the frequencies of the electric fields associated with the *em* oscillation but also with different combinations of those frequencies owing to nonlinear responses of the medium. Consequently, atoms of the medium experience a displacement from their respective mean positions. Subsequently dipoles are created as a result of separation of the positive and negative charges while responding the applied field. The resultant dipole moment per unit volume describes the induced polarization of the medium. When the applied electric fields are sufficiently small, the electric polarization is approximately linearly proportional with the applied electric field *E*

$$P = \chi E \tag{6.5}$$

Where χ is called the polarizability or dielectric susceptibility or electric susceptibility tensor of the medium and is constant only in the sense of being independent of *E*; where magnitude is a function of frequency. This is the situation of linear optics. However, when the applied electric fields are high enough, the induced polarization has a nonlinear dependence on these electric fields

$$\begin{aligned} P &= \chi^{(1)} E + \chi^{(2)} EE + \chi^{(3)} EEE \dots \\ &= P^{(1)} + P^{(2)} + P^{(3)} + \dots \\ &= P^{(1)} + P^{NL} \end{aligned} \tag{6.6}$$

where $\chi^{(1)}$ is the linear susceptibility, $\chi^{(2)}$ is the second order nonlinear susceptibility, and $\chi^{(3)}$ is the third order nonlinear susceptibility. The term $\chi^{(1)}$ is responsible for linear absorption and refraction and it reflects linearity between the induced polarization and the incident field. The term $\chi^{(2)}$ exists only in case of noncentrosymmetric materials, i.e. materials without inversion symmetry.

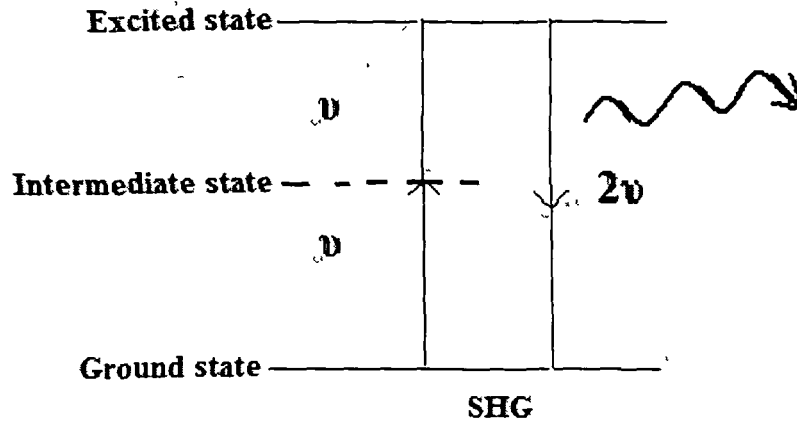


Fig6.2: Schematic representation of SHG

The induced polarization can be integrated to get the following in 3D

$$P^{(2)}(x,t) \propto E_1^{n_1} E_2^{n_2} e^{i(\omega_3 t - (m_1 \bar{k}_1 + m_2 \bar{k}_2) x)} \quad (6.7)$$

At each position x , the oscillating second-order polarization radiates at angular frequency ω_3 and a corresponding wavevector, $\bar{k}_3 = n(\omega_3)\omega_3 / c$. A constructive interference, and therefore, a high intensity ω_3 field, will occur only if

$$\bar{k}_3 = m_1 \bar{k}_1 + m_2 \bar{k}_2 \quad (6.8)$$

The above equation is known as the phase matching condition [m_1, m_2 are constant] Nonlinear effects exhibit the optimal response when this phase matching condition is met [18]. Correspondingly the efficiency of SHG signals is also obtained in this condition. The phase matching conditions can be evaluated by adopting some procedures relevant to a particular nonlinear media which will be discussed later.

6.1.3.1 Confocal microscopy

Confocal microscopes allow only the signals from the focal plane for imaging and reject all signals coming out from planes beyond the focal plane [19]. However, this microscope is usually operated in the reflection mode where optical sectioning of the planes can be obtained. Light reflected from parts of the objects lie in the focal plane of the objective lens, focused on to the pinhole and a large signal is detected. In contrast, light reflected from the parts of the object that lie outside the focal plane forms a defocused spot at the pinhole and hence, its contribution is avoided by the pin-hole arrangement. Thus, in-focus detail is efficiently imaged in a confocal microscope. On the other hand in second harmonic confocal microscopy the resolution is determined by the wavelength of the second harmonic radiation that leads to a higher resolution.

6.1.3.2 Set up based on laser scanning microscope

For imaging based on two photon excitation fluorescence (TPEF) and second harmonic generation (SHG), we have used a confocal spectral laser scanning microscope (Model:Leica TCS SP) of power 400mW. The objective has a magnification of 10X with 0.37 NA. We have used the infrared port on the microscope for obtaining images corresponding to multiphoton excitation. The excitation source was a 80 fs pulsed, 80 MHz, Tsunami Ti:Sapphire laser, tunable in the range 700 - 850 nm, but stabilized at ~706 nm for the purpose of our experiment. For the multiphoton excited fluorescence, we collected optimum signal in the epi-direction (the back-scattered signal) by appropriate pinhole adjustment. In second harmonic generation microscopy, the signal was collected in the forward direction.

While using the spectral confocal scanning microscope, the detector was first set for detecting at one wavelength and then the microscope was allowed to scans over a complete image- frame of an optical section fixed at a particular depth to image the sample's fluorescence for the corresponding wavelength. Subsequently, the next fluorescence images from the same image-frame were detected by setting the detector to detect at consecutive wavelengths separated by a difference of 4 nm. Although the microscope had the provision for scanning image-frames at different regions of the

same optical section or other optical section at different depths of the sample, the images described in this work were taken at the same region for one particular optical section.

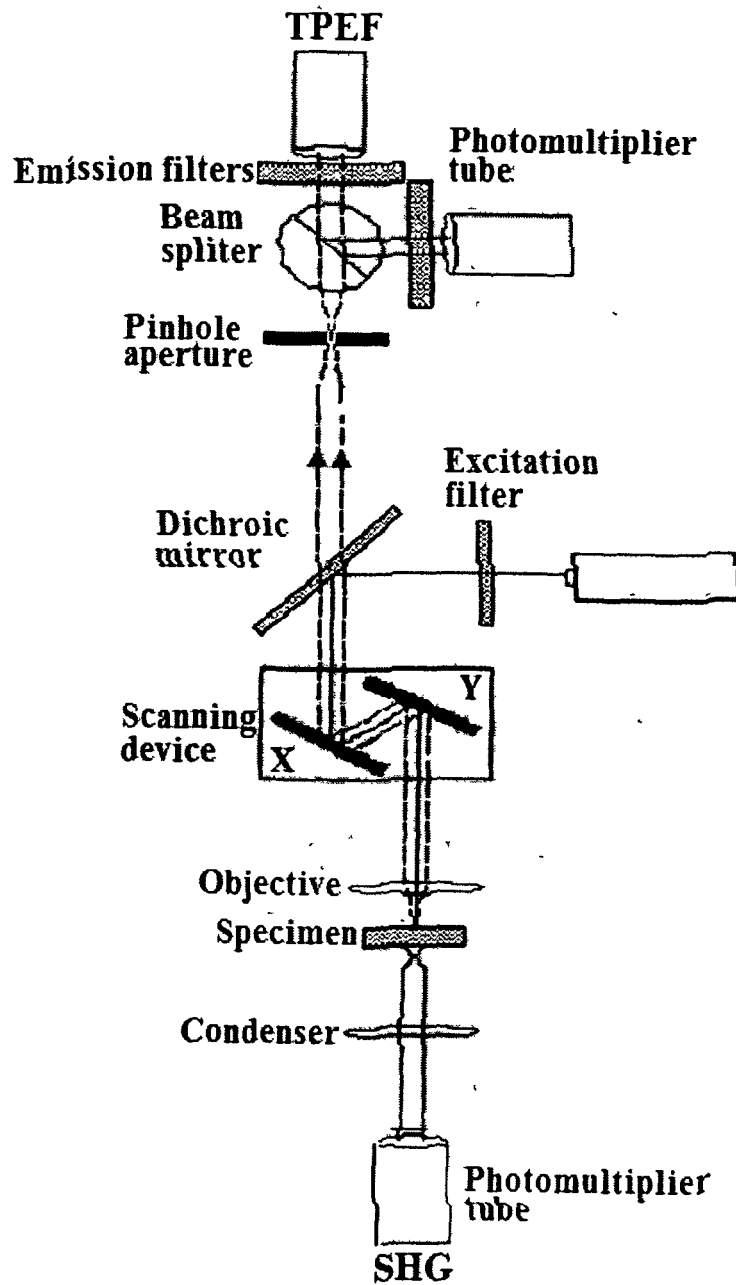


Fig6.3: Schematic representation of confocal microscope

6.2 Two photon excitation fluorescence spectra and imaging of PbS quantum dots

It was known that the two photon excitation fluorescence (TPEF) is associated with the simultaneous absorption of two photons of same or different energy and corresponds to the emission of a photon of energy higher than that of the absorbed photons. The illustration of TPEF spectra and is presented in Fig6.4. The use of a near-IR as excitation source ($\lambda \sim 706$ nm) would reduce unwanted scattering effect, whereas extremely short pulse (~ 80 fs) facilitates simultaneous absorption of near-IR photons. The high power and short pulses of the laser source enforce the PbS nanoparticles to capture several photons simultaneously.

The TPEF spectra show two distinct emission features. The first one is sharp, relatively symmetric and peaking at ~ 456 nm with a full width half maximum (FWHM) of ~ 0.408 eV and is ascribed to the band edge emission. In a typical fluorescence activation process, the band edge emission peak corresponds to the highest energy [20].

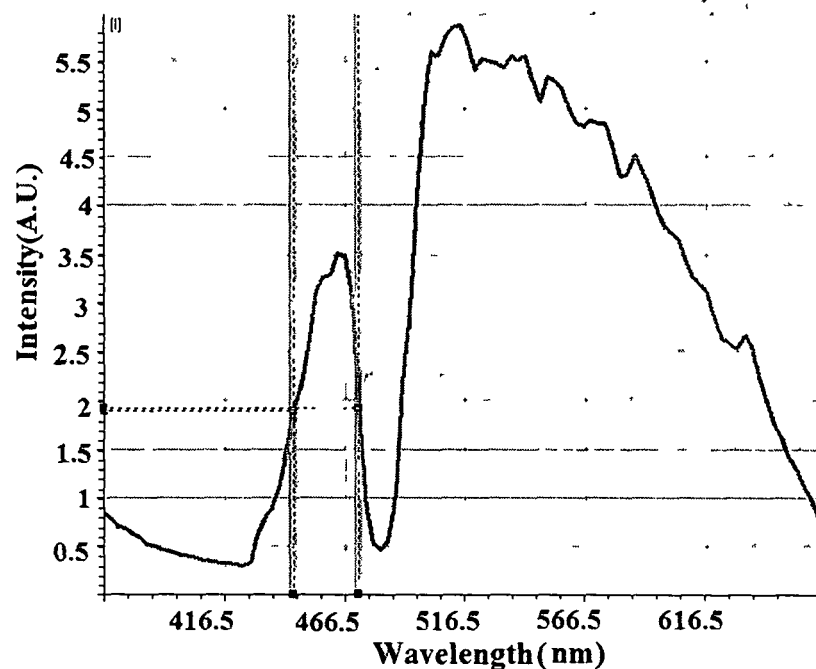


Fig6.4 TPEF spectra of PbS quantum dots

The second band within 516.5-665.5 nm is broad, asymmetric and represents the trap-related emission. The surface traps on the nanoparticles would act as the nonradiative centres for subsequent retrapping and recombination emission. They supply some virtual intermediate states which could facilitate two photon emissions. The asymmetry nature of the broad band could have arisen due to the one or more reasons e.g., unequal energy spacing between subsequent surface traps within the forbidden energy gap, unequal probability of the radiative process via nonradiative pathways and similar reasons based on the size dependent effects.

The high resolution TPEF images and their graphical representation are shown in Fig.6.6 and Fig.6.5. Here each of the images corresponded to the emission response of PbS nanoparticles owing to the laser scanning area of $1 \times 1 \text{ mm}^2$ at a designated wavelength. The first sets of images [Fig.6.6 (e, f)] are related to the near band edge emission events. Referring to Fig.6.4, the TPEF response is found to be weaker at the bottom and base parts [Fig.6.6 (a, b, g)] than the upper parts of the main peak [Fig.6.6 (c, d)]. The images Fig.6.6 (h-k) are corresponding to trap related emission. Owing to the low scattering events of IR photons compared to the UV photons, the former provide the opportunities for high resolution imaging when appropriate conditions are met. In addition, they require higher damage threshold in a given focal volume of the specimen. In fact, the probability of fluorescence emission of inorganic fluorophor increases quadratically with the excitation intensity.

With the average laser power of 400 mW and the beam dia of $\sim 1.2 \text{ }\mu\text{m}$, the incident power received at the sample was estimated to be $\sim 35.4 \text{ GW/cm}^2$. The laser wavelength was stabilized at 706 nm and a pulse of duration $\Delta t \approx 80 \text{ fs}$ with a repetition rate of 80 MHz was used in the experiment and therefore, every pulse was carrying as high as $\sim 1.1 \times 10^5$ photons altogether. Such an intense beam would largely facilitate two photon absorption process within a maximum thickness $\Delta z = c\sqrt{2} \Delta t$ of the sample, where c is the velocity of light [21]. In our case, Δz is found to be $\sim 29.6 \text{ }\mu\text{m}$ which is comparable to the thickness ($\sim 30 \text{ }\mu\text{m}$) of the solid film that contained isolated PbS nanoparticles. In other words, the probability of simultaneous photon absorption condition is adequately provided to each of the PbS nanoparticles.

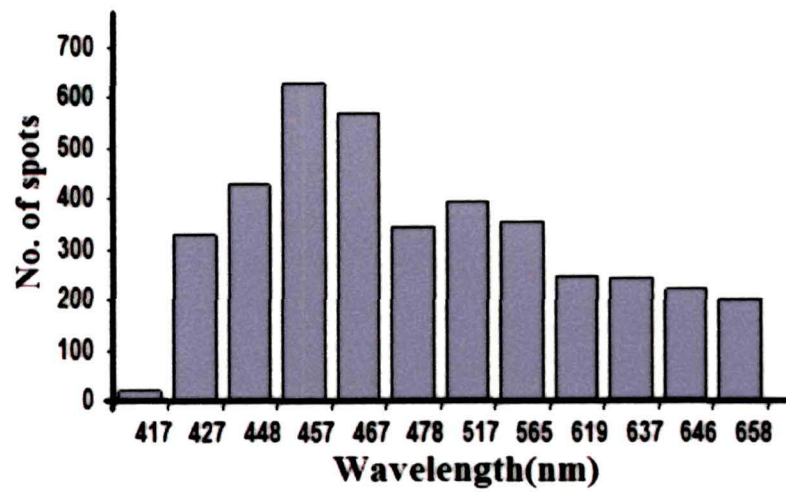
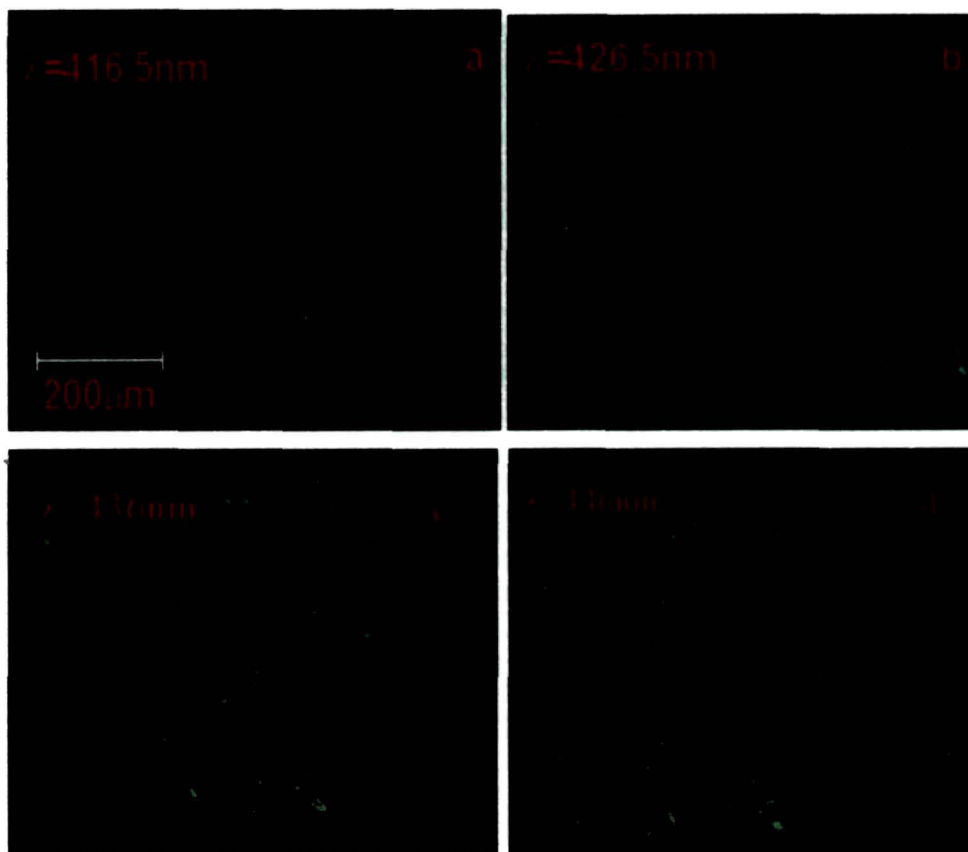
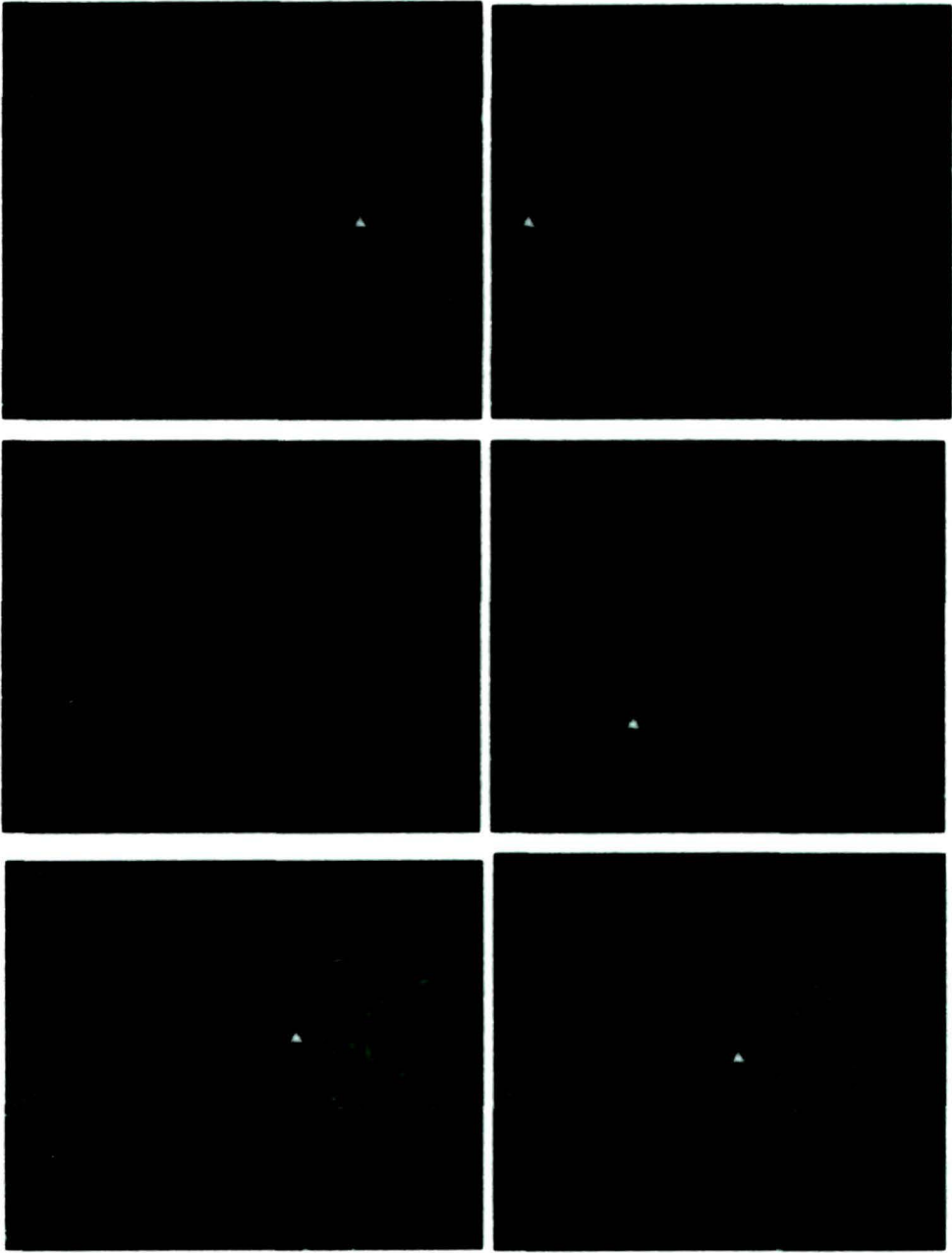


Fig 6.5: Graphical representation of TPEF





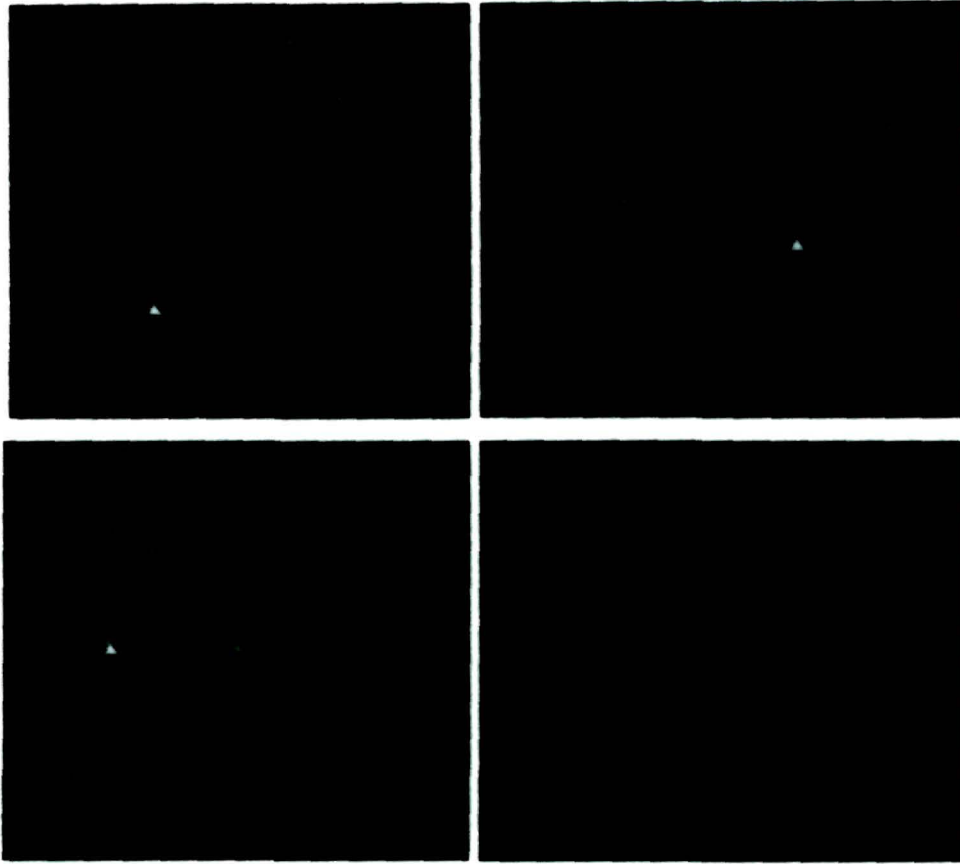


Fig6.6(a-n). Fluorescence images of a specific region ($1 \times 1 \text{ mm}^2$) obtained as a result of TPEF process corresponding to different wavelengths. The figure insets in g, i, and k represent TPEF images from chain like assemblies of nanoparticles.

Further, for nonlinear optical studies, we ensured that the experiment was performed in the safe-limit of the PbS system. The energy carried by each pulse ($\sim 3.2 \times 10^{-14} \text{ J}$) is relatively smaller than the critical value of the damage threshold energy ($E_{th} = 353.9 \times 10^{-14} \text{ J}$) for PbS system as calculated using following equation [22]

$$E_{th} = \frac{I_{th} \tau \lambda^2}{(NA)^2 + I_{th} \frac{\lambda^2}{P_{cr}}} \quad (6.9)$$

with critical power given by,

$$P_{cr} = \frac{3.77 \lambda^2}{8\pi n_0 n'_2} \quad (6.10)$$

Here, τ is the pulse duration, NA the numerical aperture, λ the laser wavelength and n_0 and n'_2 representing linear and nonlinear refractive indices for PbS, respectively [23,24]. In order to validate TPEF response of individual or cluster of particles we calculated the number of isolated spots present in individual images Fig6.6 (a-n). The wavelength vs. no. of distinct spots is being presented in Fig 6.5. With a nanoparticle size dispersion $\sim 4.3 \times 10^{11} / \text{cm}^2$, and knowing the beam *dia* $\sim 1.2 \mu\text{m}$, we predicted that each of the pulse would enforce about 4860 particles to participate in the multiphoton absorption process. Since the TPEF signals were obtained by scanning over the sample of area $1 \times 1 \text{ mm}^2$ and because of the fact that closely situated particles associated to the interfering fluorescence, a maximum value of 630, corresponding to $\lambda_{em} = 456.5 \text{ nm}$ has been observed (Fig.6.6(e)). We argue here that each bright spot could be as a result of collective TPEF signals generated from many closely spaced independent PbS nanoparticles. Depending on the arrangement and geometry of a set of particles, we notice spots of varying symmetry. The asymmetry varies from the oblate to triangular, rectangular to spheroidal, depending on the distribution of the particles in a given configuration. Non-overlapping chain like distributions is visible in consistency with TEM results. It is therefore, ascertained that each of the isolated PbS nanoparticles is capable of giving fluorescence independently. The faint spots can be ascribed to the nanoparticle emission response in underneath planes. The two photon emission response, corresponding to $\lambda = 516.5 \text{ nm}$, is characterized by a significantly large no. of spots which gradually decreases with increase in wavelength. The no. of spots observed has decreased from nearly 315 to 200 within an emission wavelength range 516.5-666.5 nm. Therefore is possible that the closely spaced PbS nanoparticles (with spacing close to the lattice parameter) are losing energy initially through the non-radiative pathways and finally by abrupt emission of photons [Fig.6.1] [25]. Owing to the large surface-to-volume ratio of the ultra small PbS nanoparticles ($\sim 5 \text{ nm}$), there is a significantly higher probability of trap-related emissions compared to the band edge emission and that is why we notice prominent TPEF signals in the former case

Further, along the forward direction [Fig.6.3], the encapsulated PbS nanoparticles are capable of producing significant second harmonic signals ($\lambda=352\text{nm}$). We know that the efficiency of SHG depends on the phase matching condition ($\Delta k = 0$, k being propagation vector) which is related to the phase coherence length L_c given by,

$$L_c = \frac{\pi c}{2\omega(n_2 - n_1)} \quad (6.11)$$

In our experiment, taking $n_1=2.78$ and $n_2=4.56$ as the refractive indices at the respective wavelengths of 706 nm and 352 nm we have estimated L_c to be $\sim 10^{-7}$ m. Here, ω is the frequency analogue of incident $\lambda=706$ nm. Since the second harmonic power increases almost quadratically with particle dimension (d) smaller than the coherence length (L_c) [26], one could observe adequate SHG signals in the present case (with $d\sim 5$ nm and $L_c\sim 100$ nm).

The last image of Fig6.7 represents SHG image obtained from the same PbS specimen. It depicts distribution of intense spots corresponding to the light emission feature of the isolated PbS nanoparticles, at the half wavelength of the incident beam (i.e., 352 nm), obtained along forward direction. It is worth mentioning here that the two photon microscopy involves rotation of linearly polarized incident IR light beam and recording TPEF and SHG signals along two mutually perpendicular polarization directions for each of the isolated nanoparticles.

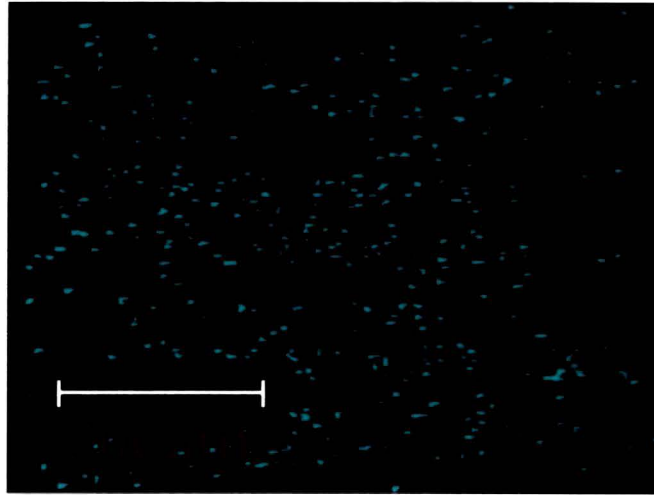


Fig. 6.7: SHG image of the region under investigation

Due to the incoherent radiation nature of TPEF process, we could image PbS nanoparticles over a large spectral range (366.5- 670 nm) with relevant imaging in the symmetric band-edge regime. The trap related emission is associated with the nonradiative centres with uneven energy spacing, and hence observed as a broad asymmetric emission in the larger wavelength regime.

In order to make a comparison between the intensity distribution profiles of TPEF (at 366 nm, along backward direction) and SHG (at 352 nm, along forward direction) images, we used the MATLAB[®] program and the results are plotted in Fig.6.8. Each of the bright spot in the left hand side figure corresponds to a vertical line in the right hand side intensity distribution plot. The length of the vertical line describes the intensity of a given spot. It is a matter of fact that at resonance (~352 nm), the SHG signal (along forward direction) is highest and TPEF (along backward direction) is minimum. That is why we have put TPEF response at off-resonance position. In the present case, the SHG response is nearly 34% stronger than its TPEF counterpart. It ensures that our sample is capable of producing very high quality SHG image.

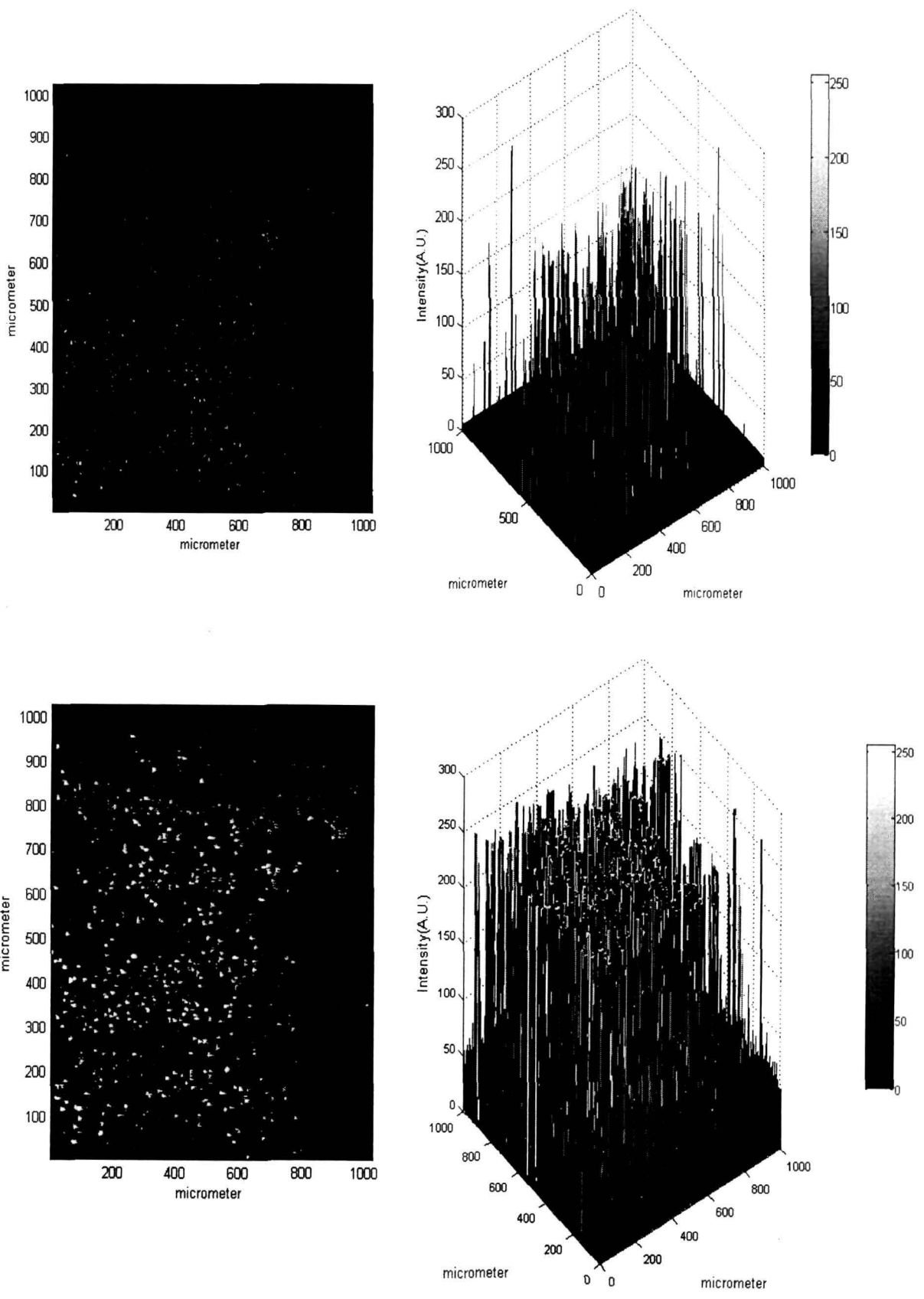


Fig.6.8: Matlab image of TPEF & SHG

In case of SHG image, the no. of spots (each corresponding to a nanoparticle assembly) is calculated to be 315 and the total number of nanoparticles is close to that were excited all at once by the ultra small laser pulse.

A close look on the SHG image tells us that there is an impression of stretched bright spots that could be aroused due to temporal overlapping of single wavelength emission response from the adjacent nanoparticles. As the acetonitrile treated ~5 nm quasi-spherical particles can undergo surface charge oscillation under the influence of an intense *em-field*, there could be appreciable displacement of atoms that constitute a molecular solid. A slightest departure from the rock-salt symmetry allows the system to behave as non-centrosymmetric one. In other words, ultra small size, departure from the perfect spherical shape, use of intense *em-field* alongwith surface treatments play major roles in inducing non-centrosymmetry. As a result, isolated nanoparticles could display substantial SHG signals. Furthermore, PbS has a relatively higher refractive index value ($n_{\text{PbS}}=4.5$) compared to the host polymer matrix ($n_{\text{PVOH}}=1.3$). Therefore, the materials will respond differently to the incident light as per the equation $I=P/A = (n_0/2\mu_0c) E^2$ with symbols have their usual meanings [27]. The situation can be equivalent to the case of presence of a dielectric sphere in a uniform electric field. Under the influence of a transient *em-field*; the interface separating the two media has a large field gradient ($\sim 9.3 \times 10^6$ V/cm) leading to the formation of dipoles on the surfaces of the PbS particles. These dipoles would oscillate in such a way that the polarization so induced can vary with the applied field in a nonlinear way. Recently, a strong Kerr signal as a result of transient anisotropy in a dispersed nanoparticle system has been reported by our group [28]. It was suggested that the even the low power lasers could result in induced polarization that can lead to a transient anisotropy in the individual nanoparticles. In contrast, high power pulsed lasers are more promising for generating and detecting second harmonic signals when ideal conditions are met. Quantum dots were introduced to cell biology as alternative fluorescent probes in recent years. Earlier, PbS nanocrystals entrapped in the hollow core of apoferritin protein cages ensured the development of near-infrared fluorescent composites [29]. Similarly, the use of PbS quantum dots as bioconjugates for near infrared (NIR) contrast agents for targeted molecular imaging with expanded emission wavelengths beyond 1 μm has also reported [30]. In this context, our TPEF and SHG results on PbS nanoparticle can be promising for imaging tissues, infected cells and other such biological specimens.

In this chapter, we have discussed about the efficient detection of SHG and TPEF signals from acetonitrile treated PbS nanoparticles. The photoluminescence study through TPA events have revealed intense emission. TPEF spectra observed by us at room temperature, opens up the possibility of imaging and sensing nonfluorescent biomolecules that can bind to such nanoparticles. Imaging by nonlinear spectroscopy can help in understanding structure, organisation, and conformational dynamics of the bioconjugates with high specificity and selectivity.

References

- [1] T. H. Maiman, *Nature*, **18** (1960) 493
- [2] P. A. Franken, A. E. Hill, C. W. Peters, G. Weinreich, *Phys. Rev. Lett.*, **7**(1961)118N
- [3] Schmitt-Rink, S. Miller, D. A. B. Chemla, *Phys. Rev. B*, **35**(1987) 8113
- [4] A. Lipovskii, E. Kolobkova, V. Petrikov, I. Kang, A. Olkhovets, T. Krauss, M. Thomas, J. Silcox, F. Wise, Q. Shen, S. Kycia, *Appl. Phys. Lett.* **71** (1997) 3406
- [5] M. Müller, J. Squier, R. Wolleschensky, U. Simon, G. J. Brakenhoff, *J. Microsc.* **191** (1998) 141
- [6] Y. Wang, *Ace. Chem. Res* , **24**(1991)133
- [7] N. Bloembergen, *Nonlinear Optics*, World Scientific Publishing, Singapore (1996)
- [8] J. Zyss, *Molecular Nonlinear Optics Materials*, Physics, and Devices, Academic Press, London (1994)
- [9] Schmitt-Rink, S. Miller, D. A. B. Chemla, *Phys Rev. B* **32** (2005)6601
- [10] W. Denk, J.H. Stricker, W.W.Webb: *Science* **248**(1990)73
- [11] J. Yumoto, H. Shinojima, N. Uesugi, K. Tsunetomo, H. Nasu, Y. Osaka, *Appl. Phys. Lett.* **57** (1990) 2393
- [12] G. Fu, T. Yoda, K. Kasatani , H. Okamoto, S. Takenaka, *Synthetic Metals* **155** (2005)68
- [13] J. J. Peterson, T. D. Krauss, *Nano Letters* **6** (2006) 510
- [14] L. Bakueva, I. Gorelikov, S. Musikhin, X. S. Zhao, Sargent, E. H. Kumacheva, *Adv. Mater.* **16** (2004) 926
- [15] Y. Wang, W. Mahler, *Opt. Commun.*, **61**(1987)233
- [16] S. Brasselet, V. Le Floch, F. Treussart, J. F. Roch, J. Zyss, *Phys. Rev. Lett.* **92** (2004)207401
- [17] R. Menzel *Photonics*, Springer, New Delhi (2004) 161
- [18] B. B. Loud, *Laser and Nonlinear Optics*, New Age International (P) Ltd. (2000)
- [19] S.J. Hewlett, T. Wilson, *Machine Vision and Applications* **4** (1991) 233
- [20] J. Hu, *et al.*, *Science*, **292** (2001) 2060
- [21] W. H. Glenn, *IEEE Jour. Quant Electr* , **6** (1970) 510
- [22] C. B. Schaffer, A. Brodeur, and E. Mazur, *Meas. Sci. Technol.*, **12** (2001)1784

- [23] R. Xie, A. E. Dongsheng, Li Deren, A. E. Yang, M Jiang, *J. Mater Sci.* **42** (2007) 1376
- [24] C. Li, G. Shi, H. Xu, S. Guang, R. Yin, Y. Song, *Mater. Lett.*, **61**(2007) 1809
- [25] A. M. Agal'tsov, V. S. Gorelik, and I. A. Rakhmatullaev, *Semiconductors*, **31**(1997) 1228
- [26] A. Ghatak, K. Thyagarajan *Optical Electronics*, Cambridge University Press New Delhi (1996) 574
- [27] A. Ghatak, K. Thyagrajan, *Introduction to Fibre optics* Cambridge University Press, New Delhi, (1999)
- [28] D. Mohanta, S. Biswas, A. Choudhury *Eur. Phys. J. D.*, **55** (2009) 679
- [29] J. Sun, M. Zhu, K. Fu, N. Lewinski, R. A Drezek , *International Journal of Nanomedicine*, **2** (2007) 235
- [30] B. Hennequin , L. Turyanska , T. Ben , A. M. Beltran, S. I. Molina , Mei Li , S. Mann, A. Patane, N. R. Thomas *Adv. Mater* **20** (2008) 3592

CHAPTER 7

Conclusion and Future directions

7.1 Thesis Conclusion

We have been able to prepare PbS nanoscale particles (quantum dots) in polymer matrix such as PVOH and SBR. The synthesized quantum dots are found to be stable against environment attack and have shown stability up to one year. The average size range of the prepared quantum dots was found to be within 5-10 nm which was confirmed from TEM and XRD measurements. Significant chain like structuring was noticed in case of acetonitrile surface passivation.

We have also prepared PbS coupled quantum dots in SBR matrix. The coupled dots are also shown to possess good stability against environmental interference. The size of the prepared quantum dots is within 10-15 nm and was confirmed from TEM and XRD studies.

In reference to heterogeneous system, we have also derived an efficient method of preparing PbS/TiO₂ coupled quantum dots using solgel chemistry.

Apart from sol-gel routes, we have been able to prepare PbS quantum dots of average size ~5nm using standard microemulsion technique. The size of the as-prepared quantum dots was confirmed from electron microscopy studies.

Further, we have proficiently filled the SHI induced ion tracks with PbS. The size of the prepared quantum dots was found to be varied between 15 to 25 nm and was confirmed from TEM and XRD measurements.

As a means of optical characterization, photoluminescence study of the synthesized quantum dots have been performed extensively. The synthesized quantum dots emit in the range of visible to near IR of the electromagnetic spectrum. The PbS quantum dots synthesized in SBR matrix show unique photoluminescence characteristics where, distinct near band edge emission from the excitonic emission were noticed. This work

opens a new idea of using photoluminescence as probe of investigating interfacial charge transfer between coupled quantum dot systems. In this work, we have adequately demonstrated the interfacial charge transfer in PbS/TiO₂ coupled quantum dot system.

We believe that the Pool-Frenkel type of conductivity is dominant in semiconductor quantum dot systems, it is established through electrical characterization of the PbS/TiO₂ coupled quantum dots.

The theoretical interpretation behind the enhancement of band gap in semiconductor (of size in the nanoscale regime) was attempted by use of Bloch functions. To own best possible effort, with the help of three basic models Kronig-Penney, Free electron model and LCAO, the band gap enhancement of PbS nanocrystal was rationalised to large extent.

For the first time, the nitrogen adsorption study was performed in a nanoscale heterogeneous system (such as PbS/TiO₂) to investigate incorporation of PbS in the pores of TiO₂ through pore-filling mechanism.

The TPEF study has brought a new insight in the characterization of nanomaterials as the results of TPEF could be correlated with particle assemblies.

The detection of SHG signals from nanoscale PbS is also an important contribution as far as NLO properties are concerned. Acetonitrile surface passivated PbS quantum dots are efficiently imaged with the help of SHG microscopy.

Both TPEF and SHG spectroscopy have been promising tools in characterizing the synthesized PbS quantum dots which have provided important ideas about the PbS quantum dot assemblies contributing to nonlinear optical emission events.

7.2 Future directions

Different matrices were tried at particular temperature and pH. The parameters (pH, temperature, concentration of the reactants etc) can be varied further to assess if they could influence size, shape, monodispersity. Most importantly, formation of organized assemblies can be achieved. Incorporation of Mn^{2+} by adopting doping route has got significance for selective emission and it can be studied a further connecting magnetic properties. In this work, though a physical interpretation of couple formation was tried yet, a theory can be modelled alongwith computer simulation to explain PbS couple quantum dot formation in a flexible matrix such as SBR.

The HRTEM studies that are capable of providing information about the crystal plane growth in PbS quantum dots will be more helpful in understanding the internal structure and lattice defects of PbS quantum dots. Similarly, scanning transmission electron microscopy (STEM) will be more beneficial in the study of PbS/TiO₂ system because it could resolve the information of incorporation of PbS in the mesopores of TiO₂

We expect that the synthesized PbS quantum dots are able to emit beyond 800nm i.e. in the range of 1200nm to 1500nm but due to the limitation of the detectors response, this range of investigation was unexplored.

Significant phonon contribution was observed in photoluminescence spectrum of the PbS quantum dots. Raman spectroscopy for these samples will definitely bring clearer picture of the vibrational modes.

Time resolved photoluminescence (TRPL) study of quality PbS quantum dots and PbS/TiO₂ coupled quantum dot system will provide more information with regard to carrier life time aspects. The radiative emission and relaxation response could explain reasonably strong exciton dynamics. Further, life time of the exciton could be controlled in these systems after proper investigation of TRPL.

The SHG and TPEF studies were performed for a specific excitation wavelength and these studies could be extended to two more wavelengths. Bioconjugation of these PbS quantum dots with non luminescent biomolecules can be experimented further.

The application potential of PbS quantum dots, PbS coupled quantum dots, and PbS/TiO₂ coupled system and PbS filled ion tracks can be considered for biosensing and bioimaging purposes.

The rheological properties of PbS quantum dots synthesized through microemulsion technique can also be investigated if it can be functionalised as a nanofluid [1]. This kind of nanofluid will be more advantageous because the prepared nanoparticles are received in already dispersed form and no additional effort is required to get it phase separated.

7.3: Prospective application arena

The possibility of obtaining stable excitons is indicated by PL spectra. It may be explored as regard to its origin and tunability over a given spectrum. PbS is able to emit in the range of visible to near infrared and photoluminescence of this system covers a wide range of emission spectrum. Therefore it can be used for designing various kinds of optoelectronic components where a broad emission range is required. The PbS quantum dots in the form of array, coupling can be useful as optical sensors which are based on the principle of photoluminescence [2]. Promising exciton dynamics has also been shown in optical switching [3]. Increase in available number of excitons in PbS quantum dot system brings the promise of population inversion leading to realization of quantum dot laser. Further, PbS quantum dots can be explored for generating emission extended to IR region, which would find scope in making detectors operated at IR and telecommunication wavelength.

The PbS coupled quantum dots can also be explored as qubits in quantum information network which has already received worldwide popularity.

The heterogeneous coupled quantum dot system of PbS/TiO₂ will be beneficial for the application in the field of electronics as well as optics providing conditions for interfacial charge transfer and its impact in photoluminescence. The electrical properties

also suggest that the photovoltaic properties can be explored in a greater detail as an alternate candidate for solar cell [4].

The TPEF spectra observed by us at room temperature, opens up the possibility of imaging and sensing nonfluorescent biomolecules that can bind to such nanoparticles. Imaging by nonlinear spectroscopy can help in understanding structure, organisation, and conformational dynamics of the bioconjugates with greater accuracy.

References

1. J. Buongiorno, *Journal of Heat Transfer*, **128**(2006)240
2. V. Mulloni , L. Pavesi, *Appl. Phys. Lett.*,**76**(2000) 2523
3. S. V. Frolov, M. Liess, P. A. Lane, W. Gellermann, Z. V. Vardeny, M. Ozaki
K. Yoshino, *Phys. Rev. Lett.* **78**(1997) 4285
4. J. Simiyu, B. O. Aduda , J. M. Mwabora , *Progress in Colloid and Polymer Science*
,Springer Berlin / Heidelberg, **125**(2004) 34

Appendix

Parameters Related to SHI Irradiation

Fluence. It is defined as the total number of irradiating ions incident per square centimetre (ions/cm^2) of the sample. It varies from sample to sample depending upon its size and material.

Fluences are calculated using the following formula

$$\text{Fluence}(\varphi) = (\text{Time}(t) \times \text{Beam Current} \times \text{pnA}) / (\text{Charge state})$$

Beam currents for this ion irradiation experiments are usually taken as 7 pnA.

$$1 \text{ pnA (particle nano - ampere)} = 10^{-9} \text{ Coulmb/s} / 1.6 \times 10^{-19} \text{ Coulmb} = 6.25 \times 10^9 \text{ s}$$

During ion irradiation process, fluences are recorded by using a counter. Following relation relates the counts and fluences.

$$\text{Counts} = \varphi q e / S$$

where, φ is the fluence,

q is the charge state of ion beam,

e is the electronic charge (1.6×10^{-19} coulmb),

S is the scale of the counter.

List of publications

- [1] N. Dutta, D. Mohanta, A. Choudhury “Synthesis and characterizations of quality PbS quantum dots” *Indian J. Phys* 82 (3), 327-331 (2008).
- [2] D. Mohanta, H. Bora, N. Dutta and A. Choudhury “Development principles and production of paired quantum dots” *European Physics J Applied Physics A-I* (2), 129-132 (2008).
- [3] Nabanita Dutta, Dambarudhar Mohanta, Indra Sulania, Amarjyoti Choudhury “Studies of optical properties and SHI irradiation on PbS sensitized nanoporous TiO₂ network” *J Opt* , 38 (3) (2009)169–176
- [4] N. Dutta, G. A. Ahmed, D. Mohanta, A. Choudhury and F Singh, “Nanomaterial Filled SHI Induced Ion Tracks and their Application in Nanodevices” *Annu Report , Inter University Accelerator centre*, 2008-2009, 233-234
- [5] N. Dutta, D. Mohanta, A. Choudhury, “Optical Probing on Interfacial Charge Transfer Phenomena in TiO₂/PbS Quantum dot System” *Contemporary Optics and optoelectronics, Proceedings of the XXXIII Optical Society of India (OSI) Symposium Tata Mcgraw–Hill Publishing Company Limited , New Delhi 2007*

Conference Paper presented

- [1] N. Dutta, D. Mohanta, A. Choudhury, *Synthesis and characterization of PbS quantum dots in flexible SBR matrix*, CMDAYS-2006, Tezpur University, Aug 28-29, 2006
- [2] N. Dutta , D. Mohanta, A. Choudhury “*Optical Probing on Interfacial Charge Transfer Phenomena in TiO₂/PbS Quantum dot System*” National Symposium of OSI India, Tezpur University , Dec 18-20, 2007
- [3] N. Dutta, G. A. Ahmed, D. Mohanta, A. Choudhury and F Singh, *Nanomaterial SHI induced Ion Tracks*, AUC-2007, National Conference, IUSC, New Delhi, 2007

[4] H. L. Das and N. Dutta, *Energy band calculation in nanocrystals with the help of the LCAO method*, 54th Annual Technical Session of Assam Science Society, Tezpur University, 4th Feb. , 2009

[5] N. Dutta, D. Mohanta, G. A. Ahmed, A. Choudhury, R. Hristu, S.G. Stanciu, G. A. Stanciu, *A qualitative Second harmonic generation study in nanostructures with Ti sapphire Laser*, NSPQS- 2009, National seminar on photonics and quantum structures Tezpur University , Nov 4-6, 2009